Technische Universität München
Ingenieurfakultät Bau Geo Umwelt
Fachgebiet Hangbewegungen

Predicting the mechanical stability of degrading permafrost rock slopes:

Geophysical and geotechnical field reconnaissance, laboratory testing and numerical modelling

Dipl.-Geogr. Philipp Mamot

Vollständiger Abdruck der von der Ingenieurfakultät Bau Geo Umwelt der Technischen Universität München zur Erlangung des akademischen Grades eines

Doktors der Naturwissenschaften (Dr. rer. nat.)

genehmigten Dissertation.

Vorsitzender:	Prof. Dr. Kurosch Thuro
Prüfende der Dissertation:	1. Prof. Dr. Michael Krautblatter
	2. Prof. Dr. Oliver Sass
	3. Prof. Dr. Jürgen Geist

Die Dissertation wurde am 24.02.2021 bei der Technischen Universität München eingereicht und durch die Ingenieurfakultät Bau Geo Umwelt am 17.08.2021 angenommen.

Abstract

High-mountain infrastructure, tourism and local populations are endangered by a rising incidence of rock slope failures, rockfalls and subsidence. The climate-induced warming and thawing of bedrock permafrost is observed to be one of the key drivers of the current increment of rock slope failures in high-mountain areas. Mountain surface air temperature is projected to continue increasing at an average rate of 0.3 °C per decade until 2050. Correspondingly, European mountain ranges are predicted to perceive an overall warming of permafrost and irreversible thaw layer deepening up to the end of the 21st century. While the thermal regime of permafrost degradation in high-mountain rock slopes has been intensively investigated, the mechanical consequences on rock slope stability are still poorly understood, and have so far not been simulated in numerical models. Previous laboratory studies and conceptual models argue that warming and thawing decrease rock and discontinuity strength and promote deformation. The understanding of permafrost rock destabilisation is a key requirement for early warning, structural interventions and other risk reduction measures.

The presented thesis takes this research gap up, and is structured in three parts: An unstable permafrost rock slope was mechanically and thermally characterised by multiple field methods (Part I). The study site was used to constrain rock-ice-mechanical experiments in the laboratory, which provides novel data and findings on the mechanical response of frozen rock and ice-filled rock joints to warming or thawing (Part II). Both the results from the field and from the laboratory were combined to develop, for the first time, a 2D numerical discontinuum stability model for a warming permafrost rock slope which includes coupled thermo-mechanical information (Part III). This manuscript is a publication-based dissertation, and as such it includes three research articles accepted for publication in the international peer-reviewed journals “The Cryosphere” and “Earth Surface Dynamics”.

In Part I, the thermal regime and the mechanical stability of the permafrost-affected Zugspitze summit crest were investigated (2900 m a.s.l., Germany). Two electrical resistivity tomographies (ERT) and three seismic refraction tomographies (SRT) were performed between 08/2014 and 08/2016. Near-surface rock temperature (NSRT) between 08/2015 and 08/2019 was continuously monitored due to ten iButton loggers instrumented in a depth of 10–80 cm. These techniques were successfully combined to constrain the current extent of permafrost to the core of the Zugspitze summit crest and the rock layers below 5 m at the north-face. Combined geotechnical mapping, kinematic analysis and 3D point cloud analysis (derived from UAV (Unmanned Aerial vehicle) -based photogrammetry) allowed to (i) characterise the discontinuity network, (ii) identify main shear planes, (iii) derive a complex combination of both a plane and a wedge failure, and (iv) estimate a potentially failing rock mass volume of $2.9 * 10^4$ m³. Fracture displacements were measured due to a portable tape extensometer from 09/2013 to

07/2019, and showed an annual mean absolute displacement of 2.1 mm y^{-1}. The rock mass is highly fractured, and the main shear zones show a high level of joint persistence and trace lengths. One of these shear zones runs in depths not greater than 20 m and reveals ice-filled fractures. Therefore, the rock slope is assumed to be close to or at the advanced stage of destabilisation, which is controlled by rock-ice-mechanical processes along persistent joints being ice-filled in frozen rock mass sections.

In Part II, the influence of warming or thawing on the mechanical properties of frozen rock and ice-filled rock joints was studied. All tested rocks were taken from the study site at the Zugspitze, and two other permafrost sites in the Swiss and Norwegian Alps. The shear strength of ice-filled rock joints was analysed in 261 shear tests with rock-ice-rock "sandwich" samples. Tests were performed at (i) constant strain rates (10^{-3} s^{-1}) which provoke ice fracturing and simulate the accelerated failure stage, (ii) rock temperatures from -10 to -0.5 °C typical for recent observed rock slope failures in alpine permafrost, and (iii) normal stresses ranging from 100 to 800 kPa (corresponding to a rock overburden of 4–30 m). These conditions are in accordance with the observations at the field site. The test results allowed us to develop a new Mohr-Coulomb based brittle failure criterion for the shear strength of ice-filled rock joints, which involves the fracturing of ice fillings and rock-ice-contacts. The tests showed that the shear strength generally decreased upon unloading (decreasing normal stress), and the cohesion and friction angle reduced by 12 % $°C^{-1}$ and 10 % $°C^{-1}$ at warming. The novel failure criterion is transferable to a wide variety of rock types relevant for permafrost rock slope failures in the Alps.

A further extensive set of laboratory tests on frozen and unfrozen intact rock and rock joints was performed to provide temperature-dependent rock-ice-mechanical input parameters for the numerical model. The experiments encompassed 110 tilt tests, Schmidt hammer tests on 7 distinct samples, 90 density tests, 28 uniaxial compressive strength tests, 60 indirect tensile strength tests and 60 ultrasonic tests. The results show that the mechanical strength of frozen intact Wetterstein limestone decreases up to 22 % upon thaw, while its deformability increases up to 22 %.

Part III deals with the set-up of a discontinuum stability model and the subsequent numerical calculations. While the geometry, the fracture network and the subsurface thermal field were derived from reconnaissance of the field site, temperature-dependent mechanical rock and rock joint properties were obtained from the laboratory tests. Intact rock properties were converted to rock mass characteristics using internationally standardised mathematical equations. The model contains a subsurface temperature field, characterised by rock layers with varying temperature-dependent mechanical properties, and a procedure of gradual warming. An instruction for the implementation of temperature-dependent mechanical data, the model set-

up and the modelling strategy was proposed, and can be used for any permafrost-affected rock slope across the globe, which is subjected to warming and thawing.

Numerical modelling of the mechanical stability of the Zugspitze summit crest demonstrated that warming decreased rock slope stability to a critical level, while thawing initiated failure. A sensitivity analysis of the model with simplified geometry and warming trajectory below 0 °C resulted in the first numerically derived critical stability thresholds for permafrost rock slopes with ice-filled fractures: successive rock mass warming close to melting initiates instability above a slope angle of 50–62°, dependent on the orientation of the fracture network versus the slope face. The increase in displacements intensifies for warming steps closer to zero degree. The simulated rock mass temperatures and calculated critical slope angles agree with documented rock slope failures in the European Alps, which mostly occurred in permafrost areas and often showed large amounts of residual ice in the rockfall scars.

Overall, this thesis presents (i) novel laboratory data on the mechanical response of frozen rock and rock joints upon warming, (ii) a new temperature- and stress controlled failure criterion for ice-filled rock joints, and (iii) a geotechnical and geophysical study of an unstable permafrost rock slope at the Zugspitze summit. These techniques were combined to parameterise, develop and implement the first mechanical, temperature-dependent numerical model which is capable of supporting scientists and engineers to perform stability analyses of degrading permafrost rock slopes affected by a warming climate. The derived critical stability thresholds make it possible to identify rock slopes susceptible to failure.

Zusammenfassung

Gleitungen, Stürze und Sackungen in Felshängen im Hochgebirge nehmen zu und gefährden Siedlungen, Infrastruktur, und Tourismus. Die klimatisch bedingte Erwärmung und das Auftauen von Permafrost in Festgestein gehören zu den bedeutendsten Einflussfaktoren auf die aktuelle Zunahme an Felshangversagen im Hochgebirge. Es wird prognostiziert, dass die Oberflächentemperatur im Hochgebirge bis zum Jahr 2050 weiter steigen wird, im Mittel um 0.3 °C pro Jahrzehnt. Hiermit verbunden wird in Europäischen Gebirgen bis zum Ende des 21. Jahrhunderts eine Erwärmung des Permafrosts sowie eine irreversible Vergrößerung der jährlichen Auftauschicht erwartet. Während das thermische System der Permafrostdegradation in Hochgebirgsfelswänden bereits intensiv untersucht ist, wurden die mechanischen Auswirkungen auf deren Stabilität bisher kaum beachtet. Laborstudien und konzeptionelle Ansätze zeigen, dass Erwärmung und Auftauen zu einer Festigkeitsabnahme im Gestein und entlang von Felsklüften führen und Verformungen begünstigen können. Das Wissen über die Destabilisierung von Felshängen im Permafrost ist eine Grundvoraussetzung für Frühwarnung, bautechnische Eingriffe und andere Maßnahmen der Risikominderung.

Die vorliegende Doktorarbeit greift die beschriebene Forschungslücke auf. Sie ist in drei Teile gegliedert: Ein instabiler Felshang im Permafrost wurde mit einer Fülle verschiedener Feldmethoden mechanisch und thermisch untersucht (Teil I). Das Untersuchungsgebiet diente zur genauen Abgrenzung der Randbedingungen für eine Reihe von mechanischen Labortests, die neue Daten und Erkenntnisse zur mechanischen Reaktion intakten Gesteins oder eisgefüllter Felsklüfte auf Erwärmung liefern (Teil II). Die Ergebnisse der Feld- und Laborarbeit wurden kombiniert, um erstmals ein numerisches Diskontinuum-Stabilitätsmodell eines sich erwärmenden Permafrost-Felshangs in 2D zu entwickeln, welches gekoppelte thermisch-mechanische Informationen enthält (Teil III). Die vorliegende Dissertationsschrift ist publikationsbasiert. Sie beinhaltet drei akzeptierte Veröffentlichungen in den internationalen, peer reviewed Journals „The Cryosphere“ und „Earth Surface Dynamics“.

Im ersten Teil dieser Arbeit wurden das thermische Regime und die mechanische Stabilität des durch Permafrost beeinflussten Gipfelgrates der Zugspitze (2900 m. ü. NN, Deutschland) untersucht. Zwei elektrische Resistivitäts-Tomographien (ERT) und drei Seismische Refraktionstomographien (SRT) wurden zwischen 08/2014 und 08/2016 durchgeführt. Oberflächennahe Felstemperaturen wurden im Zeitraum von 08/2015 und 08/2019 kontinuierlich anhand von iButton-Loggern in Tiefen von 10–80 cm gemessen. Diese Methoden wurden erfolgreich genutzt, um die aktuelle Permafrostverbreitung im Zugspitzgrat auf seinen Kern und die Gesteinsschichten unterhalb von 5 m auf der Nordseite einzugrenzen. Eine Kombination aus geotechnischer Kartierung, kinematischer Analyse und 3D-Punktwolken-Analyse (hergeleitet

aus Fotogrammetrie, die auf einer Drohnenbefliegung basierte) ermöglichte es (i) das Trennflächensystem zu charakterisieren, (ii) die Hauptscherflächen einer Felsgleitung zu identifizieren, und (iii) daraus eine komplexe Kombination aus planarem Versagen und Keilversagen abzuleiten, sowie das Volumen der Felsmasse bei einem potentiellen Versagen auf eine Größe von $2.9 * 10^4$ m³ abzuschätzen. Kluftbewegungen wurden mittels mobilem Drahtextensometer zwischen 09/2013 und 07/2019 erfasst. Die Ergebnisse zeigten eine mittlere, absolute Bewegungsrate von 2.1 mm pro Jahr. Die Felsmasse ist stark zerklüftet, die Hauptscherzonen zeigen eine hohe Trennflächenpersistenz. Eine dieser Scherzonen verläuft in einer Tiefe von weniger als 20 m und ist stellenweise eisgefüllt. Es wird daher angenommen, dass sich der Felshang kurz vor oder bereits in einer fortgeschrittenen Destabilisierungsphase befindet. Diese wird durch fels-eis-mechanische Prozesse entlang von persistenten Klüften kontrolliert, welche in gefrorenen Bereichen der Felsmasse eisgefüllt sind.

Im zweiten Teil der Arbeit wurde der Einfluss von Erwärmung oder Tauen auf die mechanischen Eigenschaften von gefrorenem Gestein und eisgefüllten Felsklüften untersucht. Die Gesteine für die Tests wurden vom Untersuchungsgebiet an der Zugspitze sowie von zwei weiteren, von Permafrost betroffenen Standorten in den Schweizer und norwegischen Alpen bezogen. Die Scherfestigkeit von eisgefüllten Klüften wurde in 261 Schertests analysiert. Hierfür wurden Proben aus zwei Gesteinszylindern verwendet, die durch eine Eisschicht miteinander verbunden waren. Die Tests wurden unter Bedingungen durchgeführt, die den Beobachtungen im Untersuchungsgebiet entsprechen: (i) mit einer konstanten Scherrate von 10^{-3} s^{-1}, die das Brechen von Eis auslöst und die beschleunigte Versagensphase simuliert, (ii) mit Felstemperaturen zwischen -10 und -0.5 °C, die für aktuell beobachtete Hangversagen in alpinem Permafrostgestein typisch sind, und (iii) bei Normalspannungen von 100–800 kPa, die einer Felsauflast von 4–30 m entsprechen. Die Testergebnisse ermöglichten die Entwicklung eines neuen, auf Mohr-Coulomb basierten Bruchkriteriums, welches die Scherfestigkeit eisgefüllter Klüfte beschreibt und das Brechen im Eis sowie entlang von Fels-Eis-Kontakten beinhaltet. Bei einer Reduktion der Auflast zeigten die Tests eine allgemeine Abnahme der Scherfestigkeit. Außerdem nahmen Kohäsion und Reibungswinkel bei einem Anstieg der Felstemperatur um jeweils 12 % bzw. 10 % pro °C ab. Das neue Bruchkriterium ist auf eine große Bandbreite an Gesteinstypen übertragbar, die in aktuelle Hangversagen im Permafrostgestein in den Alpen einbezogen sind.

Weitere umfangreiche Labortests wurden mit gefrorenem und ungefrorenem intakten Gestein und an Felskluftoberflächen durchgeführt, um temperaturabhängige, fels-eis-mechanische Eingabeparameter für das numerische Modell abzuleiten. Die Experimente umfassten 110 Kipptests und Schmidt Hammer Tests an 7 verschiedenen Proben, 90 Dichtemessungen, 28 einaxiale Drucktests, 60 indirekte Spaltzugversuche und 60 Ultraschalltests. Die Ergebnisse

weisen darauf hin, dass die mechanische Festigkeit von gefrorenem, intaktem Wettersteinkalk durch Tauen um bis zu 22 % abnimmt, während seine Verformbarkeit um bis zu 22 % zunimmt.

Der dritte Teil dieser Arbeit bestand aus dem Aufbau eines Diskontinuum-Stabilitätsmodells sowie den numerischen Modellberechnungen. Geometrie, Trennflächennetzwerk und Temperaturfeld im Untergrund wurden aus den Geländeuntersuchungen am Zugspitzgrat bezogen. Die Labortests lieferten die temperaturabhängigen, mechanischen Gesteins- und Klufteigenschaften. Die Eigenschaften des intakten Gesteins wurden mittels international standardisierter mathematischer Gleichungen in Eigenschaften der Felsmasse konvertiert. Das Model enthält ein Temperaturfeld für den Untergrund, welches durch Gesteinsschichten mit unterschiedlichen temperaturabhängigen, mechanischen Eigenschaften repräsentiert wird. Außerdem beinhaltet das Modell ein Verfahren der schrittweisen Erwärmung. Eine Anleitung wurde für die Implementierung temperaturabhängiger mechanischer Daten, den Aufbau des Modells sowie die Vorgehensweise bei der Modellierung vorgestellt. Diese kann für jeden beliebigen Felshang auf der Welt genutzt werden, der unter dem Einfluss von Permafrostdegradation steht.

Anhand der numerischen Modellierung der mechanischen Stabilität des Zugspitz-Gipfelgrats konnte gezeigt werden, dass eine Erwärmung der gefrorenen Felsmasse die Hangstabilität bis zu einem kritischen Niveau herabsetzen kann. Auftauen kann das Versagen des Felshanges in Gang setzen. Eine Sensitivitätsanalyse dieses Modells mit einer vereinfachten Geometrie und einem Erwärmungsmuster unter 0 °C lieferte die ersten numerisch abgeleiteten, kritischen Schwellenwerte für die Stabilität von Felshängen im Permafrost und mit eisgefüllten Klüften: die schrittweise Erwärmung der Felsmasse kurz unterhalb des Taupunktes initiiert Instabilität bei Felshängen mit einem Gefälle von 50–62°. Innerhalb dieses Bereichs ist das Einsetzen von Hangdeformationen abhängig von der Orientierung des Trennflächengefüges im Verhältnis zur Orientierung der Hangfläche. Je näher die simulierte Felstemperatur am Taupunkt liegt, desto stärker wird die Zunahme der Bewegungen. Die simulierten Temperaturen der Felsmasse und der berechneten, kritischen Hangwinkel stimmen mit denen dokumentierter Felshangbewegungen in den Europäischen Alpen überein, welche mehrheitlich aus Permafrostgebieten entsprangen und oft große Mengen an Eis an den Abrisskanten offenbarten.

Zusammenfassend präsentiert diese Doktorarbeit (i) neue Labordaten zur mechanischen Reaktion von gefrorenem Gestein sowie Felsklüften auf Erwärmung, (ii) ein neues temperatur- und spannungsabhängiges Bruchkriterium für eisgefüllte Klüfte, und (iii) eine geotechnische und geophysikalische Untersuchung eines instabilen Permafrost-Felshangs am Zugspitzgipfel. Diese Methoden wurden miteinander kombiniert, um erstmalig ein mechanisches sowie

temperaturabhängiges, numerisches Modell zu parametrisieren, zu entwickeln und anzuwenden, welches Wissenschaftler*innen und Ingenieur*innen dabei unterstützen kann, Stabilitätsanalysen für degradierende Permafrost-Felshänge in einem sich erwärmenden Klima durchzuführen. Die abgeleiteten kritischen Schwellenwerte erlauben die Identifizierung von Felshängen, die anfällig für ein Versagen sind.

Declaration of authorship

I, Philipp Mamot, hereby declare that the dissertation entitled "*Predicting the mechanical stability of degrading permafrost rock slopes: Geophysical and geotechnical field reconnaissance, laboratory testing and numerical modelling*", and the research it is based on, are both my own original work undertaken in fulfillment of the requirements for the doctoral degree. I confirm, that I have made no use of sources, materials or assistance other than those indicated in the text and in the reference list.

The presented dissertation was written according to the TUM regulations for publication-based dissertations. Accordingly, it includes two research articles published in the international, English language, peer-reviewed journal "The Cryosphere" (Impact factor: 4.7), and one research article published in the international, English language, peer-reviewed journal "Earth Surface Dynamics" (Impact factor: 3.9). As defined by the TUM regulations, these papers were designed and written as first author:

Mamot, P., Weber, S., Schröder, T. and Krautblatter, M. (2018): A temperature- and stress-controlled failure criterion for ice-filled permafrost rock joints, The Cryosphere, 12, 3333–3353, doi: 10.5194/tc-12-3333-2018.

Mamot, P., Weber, S., Lanz, M. and Krautblatter, M. (2020): Brief communication. The influence of mica-rich rocks on the shear strength of ice-filled discontinuities, The Cryosphere, 14, 1849–1855, doi: 10.5194/tc-14-1849-2020.

Mamot, P., Weber, S., Eppinger, S. and Krautblatter, M. (2021): A temperature-dependent mechanical model to assess the stability of degrading permafrost rock slopes, Earth Surface Dynamics, 9, 1125–1151, doi: 10.5194/esurf-9-1125-2021.

The following articles were written in the context of my dissertation and published in proceedings or abstract books of national and international scientific conferences:

Mamot, P. and Krautblatter, M. (2016): Towards a mechanical failure model for degrading permafrost rock slopes representing changes in rock toughness and fracture infill, in: Book of abstracts of the XI. International Conference on Permafrost (ICOP), edited by Günther, F. and Morgenstern, A., pp. 64-65, Potsdam, Germany, 20.-24.06.2016.

Mamot, P., Weber, S. and Krautblatter, M. (2017): Laboratory shear tests on temperature dependent fracturing along ice-filled rock joints, in: Tagungsband Fachsektionstage Geotechnik, Forum für Junge Ingenieurgeologen, edited by the DGGT, pp. 352-355, Würzburg, Germany, 06.-08.09.2017.

Mamot, P., Weber, S. & Krautblatter, M. (2018): A temperature- and stress-controlled failure criterion for ice-filled permafrost rock joints, in: Book of Abstracts of the 5th European Conference on Permafrost (EUCOP), edited by: Deline, P. et al., pp. 930-931, Chamonix Mont-Blanc, France, 23.06.-01.07.2018.

Mamot, P., Krautblatter, M., Scandroglio, R. and Eppinger, S. (2019): A thermo-mechanically coupled failure model for degrading permafrost rock slopes based on laboratory and field data, in: EGU General Assembly Geophysical Research Abstracts, Vol. 21, EGU2019-5291, Vienna, Austria, 07.-12.04.2019.

Pläsken, R., Groß, J., Krautblatter, M. and Mamot, P. (2020): Stress- and temperature dependent application of joint-constitutive-models for rock-ice mechanical systems and its implementation in a comprehensive distinct element code, in: EGU General Assembly Conference Abstracts, Vol. 22, EGU2020-18754, Vienna, Austria, 04.-08.05.2020.

Beyond that, I contributed to the following peer-reviewed research article as co-author which has not been considered in this thesis:

Knapp, S., Mamot, P., Lempe, B. and Krautblatter, M. (2020): Impact of an 0.2 km^3 Rock Avalanche on Lake Eibsee (Bavarian Alps, Germany) – Part I: Reconstruction of the paleolake and Effects of the Impact, Earth Surface Processes and Landforms, doi: 10.1002/esp.5024

Acknowledgements

The following list of acknowledgements is directed to all persons who helped or supported me to realise this dissertation: I would like to thank…

…my supervisor, Michael Krautblatter, for having asked me to work for the Chair of Landslide Research and to put your confidence in me. You gave me the opportunity to work on highly interesting topics for six years. I appreciate your good scientific ideas and your remarkable ability to encourage people. I thank you for your friendship.

…Oliver Sass and Jürgen Geist for reviewing and grading this dissertation and the related oral examination.

…Kurosch Thuro for providing a really comfortable working atmosphere as well as the good and simple collaboration with the Chair of Engineering Geology. I am looking back to a really great time that I spent with all members of the Chair of Engineering Geology, for example in the coffee room, at excursions or events like Geolaus or barbecues in the summer. I thank you, Kurosch, for your good advice whenever I needed some.

…all my colleagues of the Landslides Research Group I worked with (Andreas Dietrich, Lukas Paysen-Petersen, Benjamin Jacobs, Sibylle Knapp, Johannes Leinauer, Tanja Schröder, Saskia Eppinger, Riccardo Scandroglio, Daniel Dräbing, Anne Voigtländer, Theresa Frimberger, Regina Pläsken, Doris Hermle, Verena Stammberger, Kerry Leith, Hailiang Jia and Milos Marjanovic). Luckily, I look back to a lot of fun, a very good team work and interesting scientific discussions in the office, laboratory, field, excursions, conferences, coffee room and other social events.

…Samuel Weber for many very interesting and productive scientific discussions, for a really good collaboration in the context of three research articles that we published as a team of authors, for a good time sharing the same office, and for your hospitality and friendship.

…my former colleague Kerry Leith for valuable talks and your helpful and critical scientific input.

…all my colleagues of the Chair of Engineering Geology, especially Florian Menschik and Bettina Menschik, for many very funny moments, but also for your scientific support and help in performing field work at the Zugspitze.

…Friedrich Ettl for preparing rock samples for the laboratory experiments.

…my former B.Sc. and M.Sc. students Tanja Schröder, Saskia Eppinger, Maximilian Rau, Maximilian Lanz, Christina Utz and Christoph Körner for supporting my studies at the Zugspitze or in the laboratory.

…the team of the research station Schneefernerhaus at the Zugspitze (in particular Hannes Hiergeist and Till Rehm) who supported us so much to realise field work at the Zugspitze crest and in the Kammstollen.

…Johann Müller, Samuel Weber and Andreas Dietrich, who agreed to read and revise parts of this thesis, and thus, contributed to improve the overall performance of it.

A special thanks goes to my wife Elisabeth for her numerous good ideas, help, pragmatism, realism, patience and love! Fortunately, our sons Anton and Joscha diverted me from my work at the TUM during particularly demanding times. Finally, I regret profoundly that my father was not lucky to live to see the finalisation of this work.

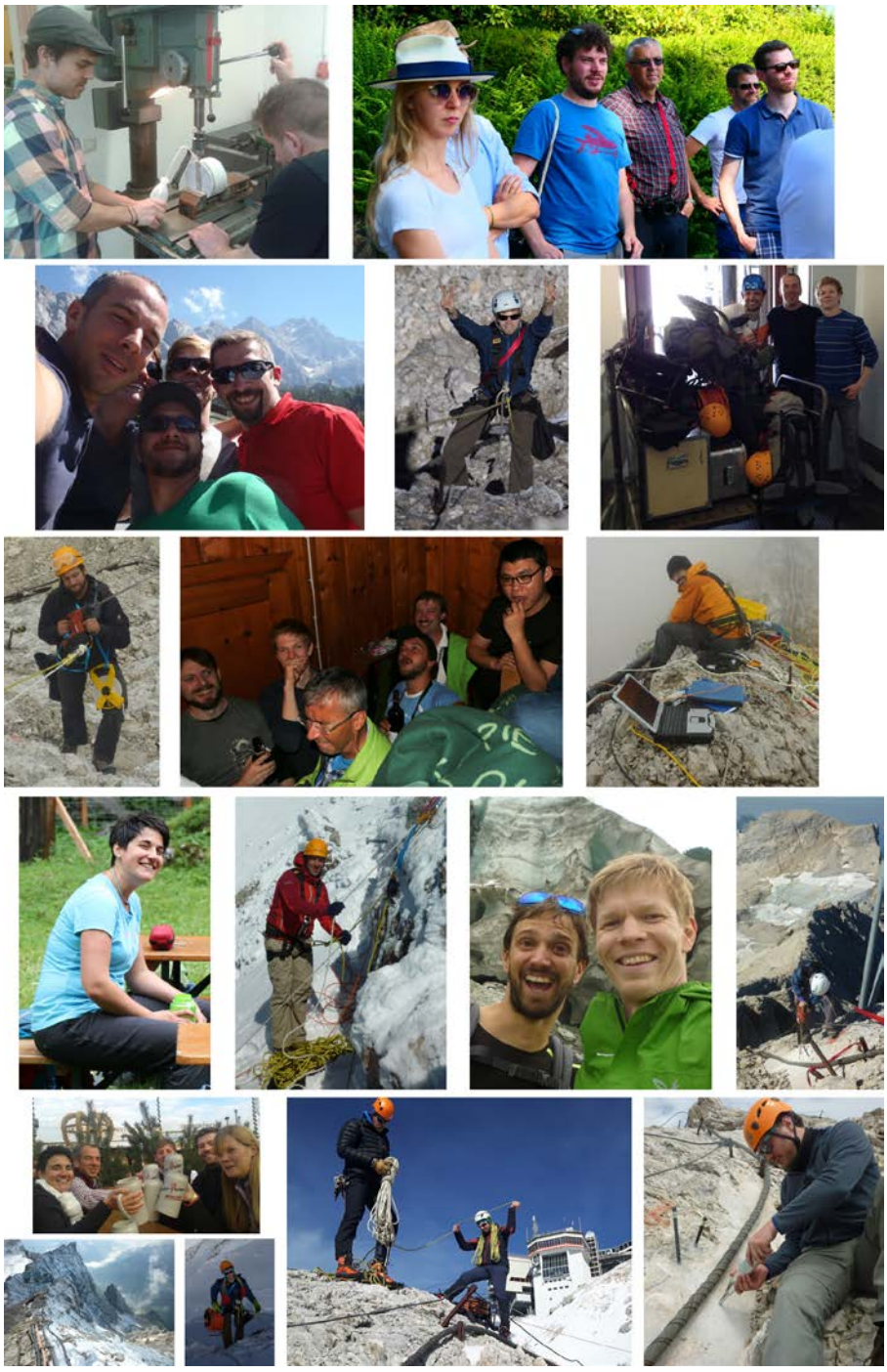

Table of contents

1. Introduction

1.1. Motivation and research gap

Rock slope failures in high mountain areas potentially endanger settlements and infrastructure for transportation, energy or tourism. The collapse of a rock slope can result in huge destruction when it turns into a cascading event with a long run-out by triggering a flood wave that reaches a lake or by transforming into a highly mobile debris flow (Clague and O'Connor, 2015; Huggel et al., 2012a; Walter et al., 2020). Human settlements and activities progressively extend towards endangered zones in many mountain regions, and thereby, expose themselves to dangerous mass movements. To reduce damage to human life and property, monitoring of slope displacements, early warning systems, structural interventions and other risk reduction measures have to be taken into account. In this context, it becomes increasingly important to improve the understanding of the potential impact of the ongoing climate change on high mountain slope stability (Etzelmüller, 2013; Fischer et al., 2012; Huggel et al., 2012a). The climate-induced degradation of bedrock permafrost can considerably affect the stability of alpine rock slopes (Fischer et al., 2006; Gruber et al., 2004a; Ravanel and Deline, 2015). This specific link has been clearly demonstrated by rock slope failure inventories in high-mountain areas of the European central Alps, where the majority of the events have been related to the degradation of bedrock permafrost and ice-filled discontinuities (Fischer et al., 2012; Huggel et al., 2012a; Ravanel et al., 2010; Ravanel et al., 2017).

Mountain permafrost warmed globally by 0.19 °C between 2007 and 2016 (Biskaborn et al., 2019). Simulations of long-term permafrost evolution in Swiss, German and Norwegian mountain ranges show an overall warming of permafrost and irreversible thaw layer deepening up to the end of the century (Gallemann et al., 2017; Hipp et al., 2012; Marmy et al., 2016). As a result of this warming trend, permafrost degradation may become a more frequent trigger of rock slope failures (Gobiet et al., 2014; Huggel et al., 2012a). This evolution is currently observed by an increasing number of failure events of all magnitudes in permafrost-affected rock walls all over the world. For instance, the 2014 Piz Kesch rock slope failure (0.15 Mio m^3; Phillips et al., 2017) and the 2017 Pizzo Cengalo failure with 8 fatalities (3–4 Mio m^3; Walter et al., 2020) in Switzerland, the 1987 Val Pola debris avalanche in the Italian Alps (33 Mio m^3; Dramis et al., 1995), the 2005 Mt. Steller rock-ice avalanche in Alaska (40–60 Mio m^3; Huggel et al., 2010) and the 2002 Kolka/Karmadon rock-ice avalanche with 140 fatalities in the Russian Caucasus (100 Mio m^3; Huggel et al., 2005) have all partially been traced back to permafrost degradation.

While the thermal regime of permafrost degradation in high-mountain rock slopes has been intensively investigated, the mechanical consequences on rock slope stability are still poorly understood. Laboratory studies and conceptual models have argued that warming below zero

degree or thawing decrease the strength of rock and discontinuities and thereby promote deformation (Davies et al., 2001; Gruber and Haeberli, 2007; Krautblatter et al., 2013). All rock-ice-mechanical laboratory test series are able to demonstrate a temperature-dependent strength reduction at warming below zero degree or thawing (Arenson and Springman, 2005a; Dwivedi et al., 2000; Glamheden and Lindblom, 2002; Inada and Yokota, 1984; Kodama et al., 2013; Krautblatter et al., 2013; Mellor, 1973; Schulson and Duval, 2009; Yamamoto and Springman, 2014). However, for instance, the brittle failure of ice-filled rock joints has only been observed in a small number of experiments by Davies et al. (2000) and Günzel (2008) and is still poorly understood. Nevertheless, its potential influence on rock slope stability has been highlighted in many studies yet (Davies et al., 2001; Gruber and Haeberli, 2007; Krautblatter et al., 2013; Luethi et al., 2015).

So far, the attempt to study the effect of warming or thawing on the mechanical response of an entire rock slope has been generally neglected (Etzelmüller, 2013). The only studies focusing on this scale are summarised in the following: Davies et al. (2001) developed a laboratory centrifuge model to simulate a full rock slope and estimated the factor of safety for unfrozen joints and for ice-filled joints at different temperatures close to 0 °C. In addition, Krautblatter et al. (2013) introduced the first comprehensive failure criterion for thawing permafrost rock slopes which includes rock- and ice-mechanics operating at different spatial and temporal scales.

A big challenge is to transfer these conceptual models and findings about single rock joints and intact rock samples at the laboratory scale to the rock mass of an entire slope. Here, geometry, stress conditions, non-linear behaviour, anisotropic properties, the fracture network and coupled processes like seismic loading, make the system more complex (Barton, 2013; Cai et al., 2004; Stead et al., 2006; Wyllie, 2018). These complexities can be addressed by means of numerical modelling, which is a powerful and common tool to assess rock slope stability and to characterise failure, deformation and influencing factors. Discontinuum discrete-element codes, for instance, simulate the deformation behaviour of fractured rock masses and consider the influence of discontinuities (Stead et al., 2006). A first and notable step towards a numerical discontinuum analysis for a permafrost-affected rock slope was realised by Fischer et al. (2010), who performed hydro-mechanical, numerical modelling of the 1988 Tschierva rock slope failure (Switzerland). Though, the implemented hydro-mechanical input parameters solely referred to the unfrozen rock mass and unfrozen rock joints.

The rock-ice-mechanical failure criterion after Krautblatter et al. (2013) is not yet embedded in a numerical model environment. Further, no numerical discontinuum model has been developed yet that combines thermal and mechanical data to analyse the effect of thawing or warm-

ing permafrost bedrock on the mechanical stability of an entire rock slope. However, to anticipate failure in a warming climate, and to reduce damage to human life and property, we need to understand how rock-ice mechanical processes control destabilisation at the slope scale and how failure close to melting, and at thawing, can be mechanically expressed in models.

Therefore, the presented thesis tries to address the gap between the thermal anticipation of future permafrost evolution in high-mountain rock slopes and the related consequences on the mechanical stability and deformation behaviour. The aims of this thesis are to

(i) constrain mechanical and thermal conditions relevant for destabilisation processes in permafrost rock slopes in the field,
(ii) produce novel laboratory data and findings on the effect of (a) subzero warming on the shear strength of ice-filled rock joints and (b) thawing on the mechanical response of frozen rock,
(iii) develop, for the first time, a 2D numerical discontinuum stability model for warming permafrost rock slopes which includes coupled thermo-mechanical input data derived from field and laboratory work, and
(iv) take the first step towards upscaling the novel model to other permafrost sites in the Alps.

By this, the presented work is supposed to contribute to the improvement of the stability assessment for permafrost rock slopes in the direct vicinity of potentially endangered mountain infrastructure or settlements.

1.2. Methodological approach and research questions

The research questions of this dissertation are related to each other as follows (see also Figure 1.1):

1) How can we constrain relevant mechanical and thermal conditions of permafrost rock slope instability, using the example of the Zugspitze summit crest?

The summit crest of the frequently visited Zugspitze (2962 m a.s.l.), Germany, was proposed as benchmark or real-world example to constrain the geometrical, thermal and stress-conditions for (i) the mechanical laboratory experiments on ice-filled rock joints and (ii) the simulation of the destabilisation of a permafrost rock slope in a numerical model. Hence, the suitability of the Zugspitze site as benchmark analogue and test object for the laboratory and modelling work had to be evaluated in a first step. For this, the current state of rock slope stability, the dominating mechanical processes, and the permafrost distribution at the field site were analysed by a combination of geotechnical, geophysical and remote sensing techniques (Sections 4 and 6, Publication 3). These were performed on the temporal scale of years (2013–2019) and on the spatial scale of a rock slope (Figure 1.1).

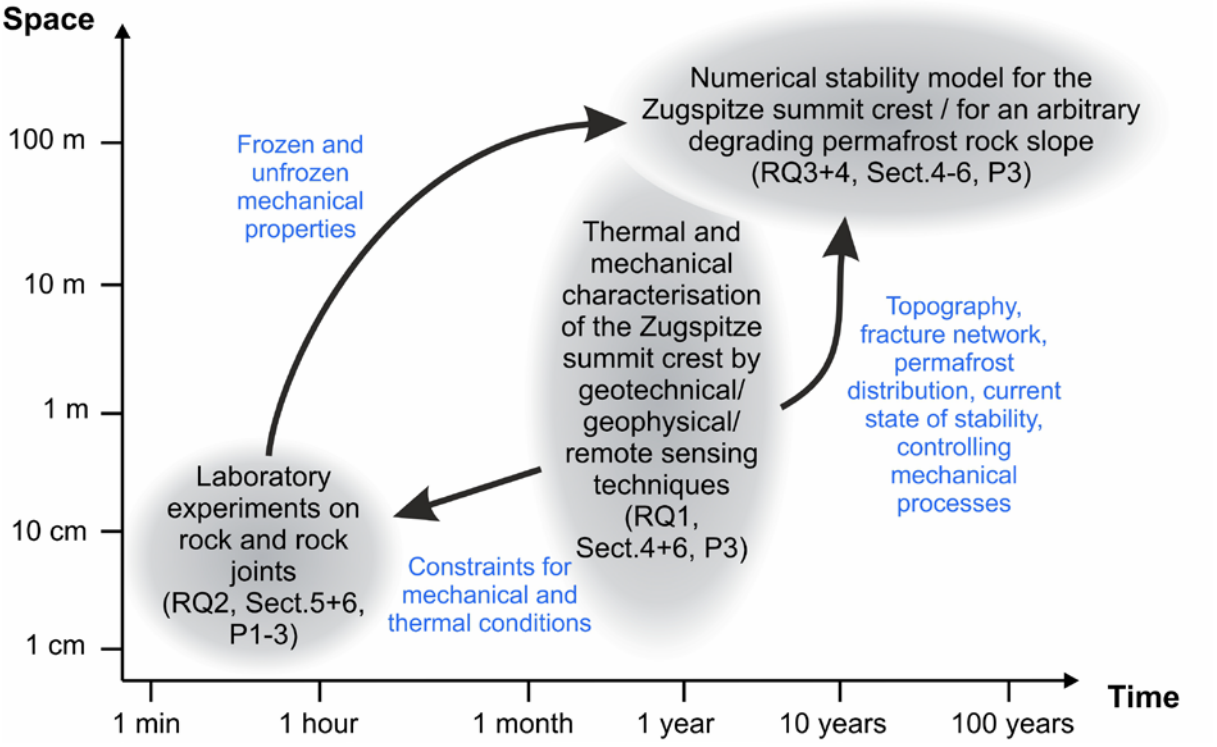

Figure 1.1: Temporal and spatial scales of the three key parts of this study, including respective research questions (RQ), publications (P) and sections within the main text.

2) What is the warming- and thawing-dependent mechanical response of frozen intact rock and ice-filled rock joints at the laboratory scale?

The mechanics of degrading Alpine permafrost rock slopes is a young research field. For instance, the brittle failure of ice-filled rock joints, which occurs during the advanced accelerating failure stage of rock slopes (Krautblatter et al., 2013), has been studied insufficiently to the present.

The following mechanical laboratory studies have been performed to gain a better process understanding for warming or thawing conditions, and to provide temperature-dependent rock-ice-mechanical input parameters for the numerical model: (i) The first shear tests with ice-filled joints constituted of natural rock (Section 5.2/Publication 1 and Section 5.3/Publication 2). (ii) A number of tests on a broad spectrum of frozen and unfrozen intact rock and rock joint properties, using specimens collected from or close by the study site (Sections 5.1, 5.4 and 6.3.1.3/Publication 3). The instability at the Zugspitze summit ridge was used as a benchmark analogue to constrain temperature and stress conditions for the shear tests. The laboratory experiments covered the smallest spatial and temporal scale of the applied methods: rock samples did not exceed 0.05 m^3 and experiments did not last longer than 2 h (Figure 1.1).

3 a) How can we join thermal and mechanical data from the field and the laboratory to develop a numerical stability model for a warming and thawing permafrost rock slope?

To date, the warming- and thawing-dependent strength reduction and deformability increase of a permafrost rock slope with ice-filled joints has been explained by theoretical concepts based on laboratory studies, or has been deduced indirectly from documented failures released from permafrost-affected rock walls. However, numerical modelling has not been applied so far. As a consequence, no common or standardised procedure exists how to (i) implement thermal, mechanical and geometrical data derived from laboratory and field work (and literature), (ii) convert properties of frozen/unfrozen intact rock to those of a frozen/unfrozen rock mass, and (iii) spatially assign temperature-dependent mechanical properties according to the thermal field of the numerical model.

These steps of the model set up were applied to the south-face of the Zugspitze summit crest (Sections 4–6/Publication 3). Laboratory testing and field surveying included a number of methods on (i) temporal scales ranging from a minute (laboratory experiments) to a period of six years (2013–2019, field work), and (ii) spatial scales ranging from the single joint (rock sample) to the whole slope (Figure 1.1).

3 b) How does the numerical stability model simulate the warming-dependent changes in stability observed at the laboratory scale?

Since numerical modelling of the stability of degrading permafrost rock slopes has not been performed yet (see above), a common or standardised numerical modelling procedure does not exist which describes how to (i) simulate a real-world destabilisation with successive stages each represented by process-specific material parameters and a spatial and temporal guideline according to which warming occurs, and (ii) represent the various stability-relevant processes by a comprehensive constitutive model.

A novel modelling procedure was proposed and applied to the Zugspitze summit crest (Section 6/Publication 3). The period of time, simulated by the numerical model, ranges between tens of years and millennia (Figure 1.1). This corresponds to (i) the timescale related to climate-induced deep permafrost degradation inside mountains (Nötzli et al., 2007), and the related response time of rock slides (Krautblatter et al., 2013; Wegmann, 1998), (ii) rock slope failure induced by progressive breaking of intact rock bridges along the main joint surface (Kemeny, 2003), and (iii) the projected loss of permafrost at the Zugspitze within the second half of the 21th century (Gallemann et al., 2017).

4) Which are the critical slope angles and fracture network orientations for the onset of a warming-dependent slope destabilisation? Can we apply these thresholds to other high-mountain permafrost sites?

As a future perspective, we need a modelling approach capable of supporting scientists and engineers in performing a mechanical stability analysis of any arbitrary warming permafrost rock slope. Critical stability thresholds will provide a preliminary, but easy and quick assessment of susceptibility to failure.

Therefore, a first attempt was made to apply the model to an arbitrary permafrost rock slope (Section 6/Publication 3). For this, the geometry and warming pattern of the Zugspitze model was generalised to study the numerical response of rising subzero temperature on rock slope stability for varying slope gradients and orientations of the fracture network.

1.3. Structure and contents

Section 1 presents the motivation for this thesis, the resulting main research questions and how they relate to each other. Section 2 provides a brief state of the art on the key topics of this thesis: mountain permafrost in steep rock slopes, the link between permafrost degradation and implications for the mechanical stability at different spatial and temporal scales, respective monitoring and field techniques, and approaches of numerical stability analyses. Each subsection is reduced to the contents that are relevant to understand and respond to the research questions of this thesis. The study site at the Zugspitze summit crest is introduced in Section 3.

This dissertation is divided into three key parts which are presented in Sections 4–6 (grey boxes in Figure 1.1): The geotechnical and geophysical surveys at the study site (Sections 4 and 6.3.1, Part I), the mechanical laboratory studies (Sections 5 and 6.3.1; Part II), as well as the set-up and analysis of the numerical stability model (Section 6, Part III).

The following research articles have been incorporated in this work:

1)	Mamot et al. (2018), The Cryosphere	Section 5.2
2)	Mamot et al. (2020), The Cryosphere	Section 5.3
3)	Mamot et al. (2021), Earth Surface Dynamics	Sections 4–6

Publication 3 is distributed over three sections: Section 6 contains the main manuscript and those supplements which refer to the numerical analysis. In contrast, the major part of Section 4 as well as Sections 5.1 and 5.4 constitute the remaining supplementary material to the third publication. Those contents in Section 4 which are not part of Mamot et al. (2021) refer to the refraction seismics, the synthesis of the geophysics or the conclusion. Sections 5.1 and 5.4 doc-

ument the set-ups and procedures of a series of laboratory experiments on frozen and unfrozen intact rock and clean unfilled rock joints. The results of these experiments are presented in Section 6.3.1.3.

Discussions are provided in the context of the three publications (Sections 5.2.5, 5.3.5 and 6.6); they aim at responding to the research questions of the respective study. In contrast, the synoptic discussion (Section 7) combines and discusses the overall outcome of this thesis by giving a review on the main research questions presented in Section 1.2. This thesis is closed by the conclusion (Section 8) and a short outlook (Section 9).

2. State of the art

2.1. Mountain permafrost in steep rock slopes

Permafrost is defined as ground material that remains at or below 0 °C for at least two consecutive years (Harris et al., 1988). Permafrost terrain is characterised by perennially frozen ground and a surface active layer, which freezes and thaws each year (Burn, 2013). In the Swiss Alps, the thickness of the active layer ranges from 1.4 to 10.4 m (between 2015 and 2018; Nötzli et al., 2019), and the thickness of permafrost ranges from a few metres up to several hundreds of metres below the highest peaks (Nötzli and Gruber, 2009). In mountain bedrock permafrost, fractures and fractured zones are likely to contain ice to depths of several tens of metres; in contrast, in the active layer, they are only ice-filled during winter (Deline et al., 2015; Gruber and Haeberli, 2007). Permafrost is sensitive to thermal perturbations such as atmospheric warming (Huggel, 2009). During the 20th century, European mountain permafrost warmed by 0.5 to 0.8 °C in the upper decametres (Harris et al., 2003).

Steep bedrock is characterised by terrain that (i) is not or only marginally affected by a snow cover during winter, (ii) does not contain large amounts of blocks and/or debris, and (iii) lacks a vegetation cover (Böckli et al., 2012a). These conditions refer to rock slopes with inclinations of between 35 and 55° (Böckli et al., 2012b). Steep bedrock can be found in mountain ridges, spurs or peaks, where warming signals penetrate from several sides being faster and deeper than in flat terrain. This may increase susceptibility to rock slope failures which are promoted by permafrost degradation. However, due to the slow penetration of thermal signals to the interior of mountains, permafrost can persist for decades, centuries or even millennia below surfaces that have warmed to positive mean annual temperatures (Nötzli et al., 2007).

The direction and density of subsurface heat flow in extreme topography are both controlled by spatially varying temperatures at the rock surface which depends on the radiation balance being a function of the slope´s aspect (Mittaz et al., 2000; Nötzli and Gruber, 2009). The subsurface thermal regime is also influenced by characteristics of the rock surface, such as ice or snow cover, the degree of fracturing and the availability of water. The snow cover insulates the ground surface from cold atmospheric conditions. This effect is usually reduced in steeper rock walls with a decreased snow cover thickness (Gruber and Haeberli, 2007). While in intact rock, subsurface heat can be transferred by conduction as the result of a temperature gradient, persistent fracture systems in rock slopes can transmit water or air to substantial depths leading to convective or advective heat transport (Dräbing et al., 2014; Moore et al., 2011). Advection presents the most rapid and efficient thawing process in bedrock permafrost, since it creates the deepest and largest thaw corridors due to water percolation along fractures (Hasler et al., 2011a). Water infiltration depends on the aperture and degree of fracturing, and on the availability of water; it reaches a maximum when snow and ice melting starts during early

summer (Dräbing et al., 2014). Convective heat flux works due to air ventilation along fractures (Moore et al., 2011) and can affect the ground thermal regime down to a depth of 100 m (Gischig et al., 2011b). During winter and at steep snow-free slope sections with large fractures it can reduce rock temperatures at depth by approximately 1.5 °C (Hasler et al., 2011b).

2.2. Thermal effects on the stability of a permafrost rock slope

Slope failure occurs as a response to various loading and triggering mechanisms. While geologic and geometric conditions are important preconditioning factors for rock slope failure in high mountains, the main trigger – which sometimes work in concurrence – are seismic activity, glacial debuttressing due to glacier retreat, alterations in groundwater and related pressures (e.g. due to extreme rainfall events), and permafrost degradation (McColl and Dräbing, 2019; Ravanel et al., 2017). Since permafrost is currently subject to fast change due to climatic warming (see earlier), its importance as triggering factor receives increasing attention among scientists. In the context of the thesis´ topic, this chapter will focus on warming and thawing bedrock permafrost as influencing factor on slope stability.

Originally, the effect of warming or thawing on the strength and deformability of rock-ice mechanical properties was investigated to estimate the influence of thermal alterations on the stability of tunnels or caverns used for liquefied natural gas storage (e.g. Inada and Yokota, 1984, or Mellor, 1973). The interest for Alpine rock faces emerged in the 1990s expressed in publications of e.g. Haeberli (1992), Haeberli (1999) or Wegmann and Gudmundsson (1999). The first related mechanical laboratory studies were published in the subsequent years. Hence, the mechanics of degrading Alpine permafrost rock slopes is a young research field, which has a great potential for progress.

The stability of rock slopes is often significantly influenced by the fracture network and the characteristics of the discontinuities which present planes of weakness in the much stronger intact rock. As such, a failing rock mass is usually destabilised along existing discontinuities (Wyllie, 2018), which are often ice-filled in bedrock permafrost (Gruber and Haeberli, 2007). Ice has been observed at a number of shear planes subsequent to failure in steep bedrock permafrost: for instance, after the 2012 Kitzsteinhorn block slide in Austria (0.0005 Mio m^3; Keuschnig et al., 2015) or after the 2003 Matterhorn block fall in Switzerland (0.002 Mio m^3; Weber et al., 2017). Further sightings are reported by Dramis et al. (1995), Guerin et al. (2020), Phillips et al. (2017) or Walter et al. (2020).

The overall shear resistance along discontinuities in a permafrost-affected rock slope is constituted by the following rock-ice-mechanical components/processes, which are altered when subzero-warming or thawing occurs (Figure 2.1):

1) Creep and fracture of ice fillings: The mechanical behaviour of ice-infillings in discontinuities is assumed to correspond to the stress-strain behaviour of polycrystalline ice. The creep of ice can be described by the flow relation for secondary creep which represents strain rates typical for mass movements (Krautblatter et al., 2013; Sanderson, 1988). It can be derived from the following formula:

Equation 2.1:

$$\tau = {}^{\varepsilon}/_{A_0}\ exp\left(\frac{-16700}{T}\right)$$

where τ is the shear stress, ε is the shear strain rate, T is the temperature, and A_0 is the Arhenius factor independent of the temperature (Krautblatter et al., 2013). It relates to $(3.2 + 5.8W) * 10^{-15}$, where W is the water content. Equation 2.1 is based on the law for secondary creep by Glen and Perutz (1955).

The transition from ductile creep to brittle fracture is observed at strain rates > 10^{-4} and 10^{-3} s^{-1} (Arenson and Springman, 2005a; Sanderson, 1988; Schulson and Duval, 2009) and with confining pressure > 25MPa in triaxial tests (Sanderson, 1988) or normal stress between 0.2–0.6 MPa in direct shear tests (Günzel, 2008). Numerous laboratory studies on the strength and deformability of polycrystalline ice or single ice crystals demonstrate a warming-dependent strength reduction and increase in deformability (Arakawa and Maeno, 1997; Barnes et al., 1971; Butkovich, 1954; Fish and Zaretzky, 1997; Gagnon and Gammon, 1995; Jones and Glen, 1968; Ladanyi, 2006; Sanderson, 1988; Schulson and Duval, 2009). The same dependency was shown for natural and artificial ice-rich soils under triaxial stress conditions (Arenson and Springman, 2005; Yamamoto and Springman, 2014) or for artificial ice-sand mixtures and rock-ice samples under direct shear (Günzel, 2008; Yasufuku et al., 2003).

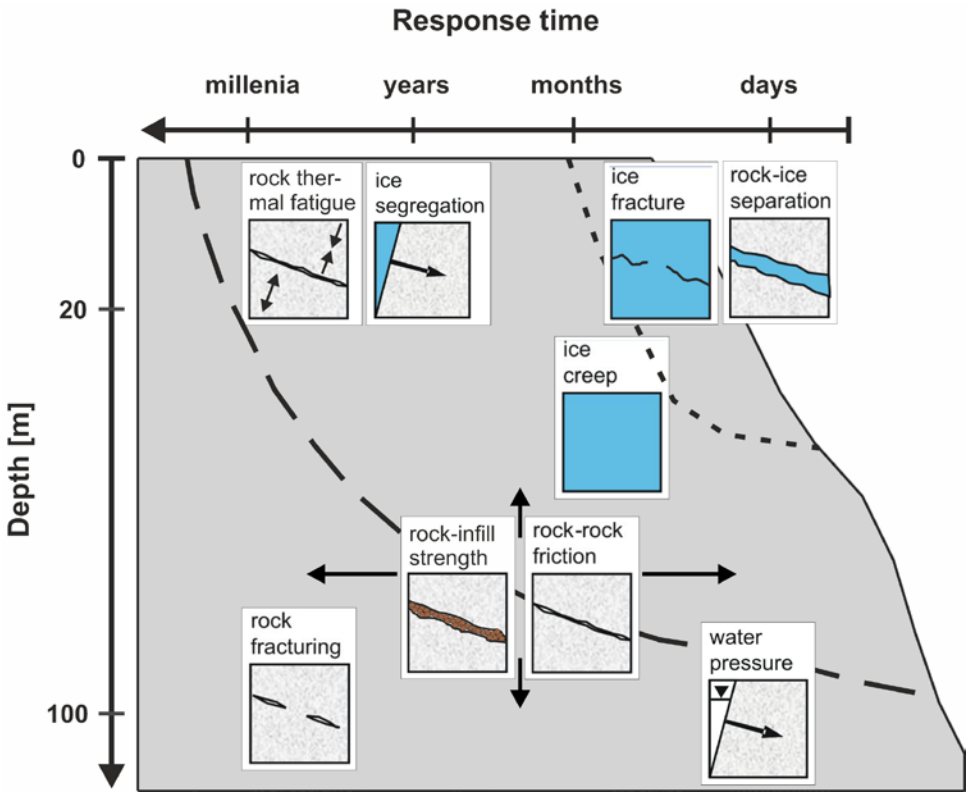

Figure 2.1: Spatial and temporal categorisation of the main components/processes of shear force and shear resistance influencing a jointed permafrost rock slope.

Dashed black lines represent potential failure planes. The sketch is based on Figures 1 and 2 in Krautblatter et al. (2013).

2) Brittle failure of rock-ice contacts: Ice fillings can contribute to a systematically higher shear strength of rock joints due to rock-ice-interlocking and adhesion (Ryzhkin and Petrenko, 1997), and thus increase rock slope stability especially when the ice is at a low temperature. The bonding at rock-ice-contacts is reduced or even lost when warming occurs (Davies et al., 2001; Gruber and Haeberli, 2007). This effect was demonstrated due to direct shear tests on synthetic concrete joints filled with ice (Davies et al., 2000; Günzel, 2008; Table 6.1). In 2013, Krautblatter et al. (2013) developed a general relation for the shear strength of a warming rock joint filled with ice which was based on the shear tests by Günzel (2008):

Equation 2.2:

$$\tau_f = 144 * T_C + (0.42 * \sigma' + 41.3)$$

where τ_f is the shear stress at failure, T_C is the temperature of the ice at failure and the term in brackets is the shear strength at 0° C.

A laboratory study by Günzel (2012) on the shear strength of rock joints filled with frozen sand showed that (i) these joints respond more sensitively to warming than

joints filled with pure ice and (ii) the shear strength of unfrozen sand-filled joints is lower when thawed, which is in contrast to the observations of ice-filled joints (Davies et al., 2001). Overall, the brittle failure of joints filled with ice or fine grains remains poorly understood as it is still based on a small number of experiments.

3) Friction along joint surfaces: Thawing reduces the friction of frozen rock-rock surfaces by 14–17 % at normal stresses > 500 kPa (Krautblatter et al., 2013; Table 6.1). A higher uniaxial compressive strength under frozen conditions (Inada and Yokota, 1984; Kodama et al., 2013; Mellor, 1973) prevents the shearing of asperities at the joint surface and leads to an increased shear strength. This effect is expected to be more pronounced for joint surfaces with a higher roughness and degree of pores or fissures which – under frozen conditions – are filled with "cementing" ice (Krautblatter et al., 2013).

   Krautblatter et al. (2013) propose the joint friction to be derived by the following empirical relation:

Equation 2.3:

$$\tau = \sigma' \tan\left(JRC \log_{10}\left(\frac{JCS}{\sigma'}\right) + \phi_r\right)$$

   where *JRC* is the roughness coefficient of the joint surface, *JCS* is the joint wall compressive strength, σ' is the effective normal stress and ϕ_r is the joint residual friction angle. Equation 2.3 was developed by Barton (1973) and modified by Barton et al. (1985).

4) Fracture toughness of intact rock bridges: Intact or unbroken segments along the joint surface are referred to as rock bridges which provide a joint cohesion against shear or tensile deformation. Subcritical crack growth leads to progressive shearing of rock bridges and a decrease in joint cohesion. The fracture toughness of rock bridges can be expressed by the following formula suggested by Kemeny (2003):

Equation 2.4:

$$C = \frac{K_{IIC}\sqrt{\pi a}}{2w}$$

   where *C* is the joint cohesion, *a* is the half width of the rock bridge, *2w* is the bridge-to-bridge spacing, and K_{IIC} (P m $^{0.5}$) is the fracture toughness under crack propagation mode II (in which the crack faces are mutually sheared in the direction of the crack plane; Chang et al., 2002). K_{CII} decreases with rising temperature close to the melting

point, since this dependency was observed in laboratory tests on the fracture toughness under mode I, K_{cI} (tensile opening; Dwivedi et al., 2000; Table 6.1), which correlates closely to K_{cII} (Chang et al., 2002).

5) Shear strength of infilled joints: Joints filled with fine material can considerably affect rock slope stability, since due to the low friction of the infill they provide very weak planes available for the initiation of sliding (Indraratna et al., 1999; Indraratna et al., 2005). The shear strength of an infilled joint is usually lower than a rough, clean joint. If the ratio of infill thickness to asperity height (t/a) is more than about 1.4–1.8, there will be little or no rock-to-rock contact, and the shear strength of the fracture will be solely controlled by the properties of the infill (Indraratna et al., 2005).

   The shear strength of in situ frozen and unfrozen fracture infill has been studied in the laboratory by Bledow and Krautblatter (2010). The authors could show a shear strength reduction by 50 % or more upon thaw. Barton et al. (1985) performed direct shear tests with frozen and unfrozen, artificially prepared joints constituted of concrete and sand. The study demonstrated that the friction angle decreased by 14–17° when the samples warmed from -4 °C to the unfrozen state. Similarly, shear tests with frozen sand or other sediment-ice-mixtures at different subzero-temperatures close to melting showed a warming-dependent reduction of the shear strength (Arenson and Springman, 2005a; Barton et al., 1985; Yamamoto and Springman, 2014; Yasufuku et al., 2003).

While rock-mechanical changes (3, 4 and 5) control the destabilisation of high-magnitude rock masses with failure planes in a depth below 20 m and with a reaction time of months to millennia, ice-mechanical processes (1 and 2) increasingly affect the failure of low-magnitude rock masses with detachment layers thinner than 20 m and with a reaction time of days to months (Krautblatter et al., 2013; Figure 2.1). However, the shear strength of infilled joints and clean rough joints (3 and 5) can also influence destabilisation closer below the rock surface and at timescales of days to months.

The shear resistance can vary seasonally: It keeps on a high level during winter and spring when the active layer is frozen, and it falls to the lowest level in summer and early autumn when bedrock permafrost and the active layer warm up and thaw (Dräbing et al., 2014). The exact timing may be altered in greater depth where thermal signals arrive with delay.

The overall shear strength of a permafrost rock slope is reduced by gravity, and the following permafrost induced shear forces (Figure 2.1):

- Local hydrostatic pressures are provided by high water columns in joints above aquicludes formed by ice fillings. Water pressure can be a controlling factor for shallow and deep-seated rock slope failures gaining importance at greater depths (Krautblatter et al., 2013). The hydraulic permeability of a frozen fractured rock mass is one to three

orders of magnitude lower than of the same unfrozen rock mass (Pogrebiskiy and Chernyshev, 1977); this can result in a build-up of high water pressure in the slope within days, which particularly occurs in early summer when snow melt provides a high amount of water infiltrating into fractures (Dräbing et al., 2014).

- Pressure by the formation of ice can develop by volumetric expansion of in situ cleft water or ice segregation (Krautblatter et al., 2013). The volume expansion of 9 %, which occurs when water freezes to ice, can theoretically lead to pressures up to 207 MPa. This stress exceeds the tensile strength of rock by one to two orders of magnitude causing rock fracturing (Matsuoka and Murton, 2008). Ice segregation refers to suction of unfrozen water through freezing or frozen ground towards lenses or layers of ice. This process requires a high temperature-gradient in a saturated porous or fractured rock (Murton et al., 2006), and it is capable of developing pressures up to 20 MPa (Radd and Oertel, 1973). Ice segregation is most effective down to 10–20 m depth and, hence, it predominantly controls rock slope failures with shallow shear planes (Krautblatter et al., 2013). Fracturing concentrates at the base of the active layer and at the top of the permafrost (Murton et al., 2006). Both volumetric expansion and ice segregation are effective from late autumn until early summer (Dräbing et al., 2014).

Diurnal or seasonal variations of warming and cooling can result in cyclic thermal expansion or contraction in the shallow bedrock (Figure 2.1). If these variations occur with high frequency and magnitude, they can cause thermal gradients in the rock which lead to alterations in the stress field. Thermal fatigue is induced over long timescales and reduces the shear resistance along weakened discontinuities (Dräbing et al., 2017a; Gischig et al., 2011c; Hall and Thorn, 2014; Jia et al., 2015; Weber et al., 2017).

Regarding the effect of warming or thawing on the mechanical properties of frozen intact rock, a number of laboratory studies were able to show a warming- or thawing-dependent strength reduction and increase in deformability for the investigated parameters (Glamheden and Lindblom, 2002; Inada and Yokota, 1984; Jia et al., 2015; Kodama et al., 2013; Mellor, 1973; Table 6.1).

2.3. Investigation and monitoring techniques

For the analysis and monitoring of the influence of warming and thawing on the stability of a permafrost rock slope, both the thermal regime and the kinematics (i.e. movements) of the study site have to be considered. A brief review of current methods is given in the subsequent Sections 2.3.1 and 2.3.2.

2.3.1. Bedrock permafrost

To this date, a broad variety of methods has been proposed and applied at specific mountain permafrost sites to monitor the spatial distribution and temporal evolution of permafrost and to study potential influencing factors:

- Temperature sensors in boreholes of various depth are used as a common tool to monitor bedrock permafrost and study the influence of slope aspect and gradient, elevation, fractures, lithology and snow pack on the thermal regime of permafrost rock walls. Thermistors are mostly inserted to borehole depths of 10 to 80 cm (Gruber et al., 2004b; Hasler et al., 2011b; Hipp et al., 2014; Keuschnig, 2016; Magnin et al., 2015); however, drilling boreholes with heavy machines allows to record rock temperatures in depths of several decametres (Gallemann et al., 2017; Harris et al., 2003; Moore et al., 2011; Nötzli et al., 2019; Phillips et al., 2016).
- Principal and widely accepted geophysical methods used in permafrost research are electrical resistivity (ERT) and seismic refraction tomography (SRT), electromagnetic induction (EM) and ground-penetrating radar (GPR). These methods are non-invasive and provide subsurface geophysical data several tens of metres below the surface. The obtained data can be correlated with specific properties of the underground, for instance, frozen or unfrozen bedrock or sediments. Hence, inversion models of 2D or 3D electrical resistivity distributions in mountain terrain allow the indirect localisation and monitoring of permafrost (Hauck and Kneisel, 2008; Hauck, 2013). Laboratory calibration of characteristic frozen and unfrozen P-wave velocity or electrical resistivity of the rock at the study site will facilitate the interpretation of tomographies performed in the field (Krautblatter et al., 2010; Krautblatter and Dräbing, 2014).

The acquisition rate of geophysical data is usually lower than of thermistors: due to the longer time required for acquisition and processing of the bigger datasets in 2D or 3D, the highest published frequencies for ERT surveys are daily and 4 h-intervals (Keuschnig et al., 2017; Supper et al., 2014). In contrast, thermistors are commonly used to record data on hour or even minute intervals (Haberkorn et al., 2015; Hasler et al., 2011b; Magnin et al., 2015; Weber et al., 2017).

While geophysical methods provide indirect and spatially interpolated data, a direct and accurate temperature measurement can be achieved by thermistors. Their limitation is the fact that they provide point data and therefore lack an intensive spatial coverage. However, when several sensors are distributed over the rock slope, they can be used for inter-/extrapolation to 1D, 2D or 3D and the development of a heat flow model for the rock slope (Hipp et al., 2014; Moore et al., 2011; Myhra et al., 2017; Nötzli et al., 2007). In order to increase the reliability of

the data interpretation, geophysics are frequently complemented by borehole rock temperatures (Keuschnig et al., 2017; Krautblatter et al., 2010; Krautblatter and Dräbing, 2014; Nötzli et al., 2008) or datasets of various geophysical methods are combined (Pellet et al., 2016; Pogliotti et al., 2015; Schrott and Sass, 2008).

2.3.2. Slope stability

Common techniques for kinematic and stability analyses of Alpine permafrost-affected rock slopes can be subdivided into remote sensing and in situ measurements (e.g. crackmeters/extensometers, differential global positioning systems (GPS), inclinometers):

- Near-surface fracture displacements can be recorded by a portable digital tape extensometer. For data acquisition, the device is screwed into two plugs which are firmly installed in the rock (Osasan and Afeni, 2010). However, permanent mounting of extensometers or crackmeters to the rock surface will increase the temporal resolution of the acquired data due to continuous recordings. This allows to study potential links between movements and influencing factors (McColl and Dräbing, 2019), or to detect an acceleration in rock movements. Sensors can be incorporated in an early warning system for rock slope failure being activated when a specified displacement threshold is exceeded. The distribution of sensors over the active part of the moving rock slope can provide information on critical slope sections in terms of deformations (Osasan and Afeni, 2010; Sättele et al., 2016). Wireless sensor networks permit a real-time data transfer from the site and reduce the susceptibility to lightning, rock or ice falls due to the absence of cable instrumentation (Hasler et al., 2012). Recordings are typically performed at time intervals of minutes to hours and with an accuracy of ± 0.01 to ± 0.003 mm (Dräbing et al., 2017b; Hasler et al., 2012; Sättele et al., 2016; Weber et al., 2017).
- Remote sensing methods allow for rapid mapping or monitoring of landslides in inaccessible or remote high-mountain areas (Casagli et al., 2017; Müller et al., 2014b). Multitemporal measurements permit detection of slope processes and movements over the time and determination of failure volumes (Wyllie, 2018). The various sensor systems are used to generate high resolution digital elevation models (DEM) with a large spatial coverage. Satellite-based tools include, for instance, synthetic aperture radar (SAR) or optical Very High Resolution (VHR) imagery; applications in Alpine permafrost terrain are presented by Barboux et al. (2014) or Necsoiu et al. (2016). Both methods work without accessing the field site as a ground-based instrumentation of reference points is redundant. Terrestrial technologies encompass digital photogrammetry (DP) or light detection and ranging (LiDAR) (Casagli et al., 2017); applications at mountain permafrost sites are, for instance, presented by Kenner et al. (2014), Müller et al. (2014a) or

Ravanel and Deline (2008). DP or LiDAR scans can be conducted from the ground (TLS) or from the air (DAP or ALS). In the latter case, data acquisition is performed by a camera or scanner mounted on a drone (unmanned aerial vehicle, UAV) or aircraft. The data are used to generate a 3D point cloud which is processed to a DEM with high spatial accuracy (Wyllie, 2018).

While in situ measurements have a lower coverage in spatial information than remote sensing techniques, they can be more precise and usually they have a higher temporal resolution (McColl and Dräbing, 2019). Among the remote sensing methods, the spaceborne tools provide data with a spatial resolution in the range of metres, while terrestrial methods obtain an accuracy of cm to mm (Casagli et al., 2017).

Digital terrain models, derived from digital images (DP) or LiDAR, allow identification of major geological structures and characterisation of the fracture network (Sturzenegger and Stead, 2009; Wyllie, 2018). This enables to reconstruct pre-failure planes of rockfalls or rockslides in steep Alpine rock walls (Heckmann et al., 2012 or Ravanel and Deline, 2008). Further, the position, length and persistence of potential failure planes can be identified. Therefore, potential failure volumes can be estimated (Wyllie, 2018). The latter requires the extrapolation of strike lines of major sliding planes to 3D planes below the slope face and subsequent intersection with each other and the slope face. This procedure has been similarly applied by Jaboyedoff et al. (2009).

2.4. Numerical analysis of rock slope stability

Mechanical modelling has been evolved to a vital tool for the assessment of rock slope stability in the context of civil and mining engineering (Stead et al., 2006). Numerical models express the mechanical response of a rock slope to in situ stresses, water levels, specific boundary conditions or induced changes such as excavation (Wyllie, 2018). Conventional modelling approaches can be subdivided into continuum and discontinuum methods (Stead et al., 2006). Continuum models assume a continuous material throughout the slope, which is discretised by a number of smaller elements (zones) connected to each other. Discontinuities are absent, but they are represented as part of the rock mass domain as they reduce the strength and deformability of the intact rock to those of the rock mass. By contrast, discontinuities in discontinuum models are represented explicitly with a specific orientation and location, dividing the rock mass domain into smaller blocks (Figure 2.2). Separation or displacement is allowed along these explicit surfaces. A material model and corresponding properties are assigned to each zone or discontinuity. The material model is a set of stress-strain relations that describe the behaviour of the material as a result of initial conditions or changing stresses and material properties (Wyllie, 2018).

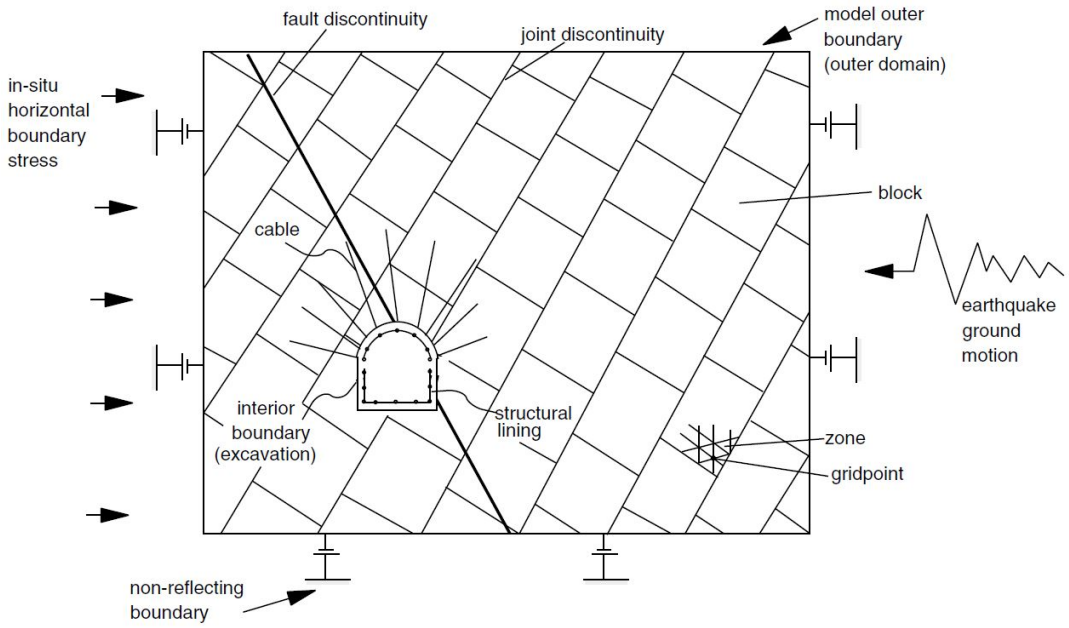

Figure 2.2: Basic elements in UDEC including special terminology for discontinuum model features (Itasca Consulting Group, 2019)

Among the discontinuum codes, the Universal Distinct Element Code (UDEC; Itasca Consulting Group, 2019) and its 3D equivalent 3DEC (Itasca Consulting Group, 2016) are the most common and are widely used by researchers and practitioners. Here, numerical models can be set up with hundreds to thousands of discontinuities (Figure 2.2). If model blocks are deformable, they are represented by continuum behaviour. UDEC and 3DEC are finite-difference programs in which equations are solved by a time-marching scheme (Wyllie, 2018). The factor of safety is analysed by the strength reduction method and corresponds to the global minimum stability state (Itasca Consulting Group, 2019).

Several numerical models have been developed of the subsurface thermal field and its evolution in a permafrost-affected mountain rock slope, most of them considering the effect of climatic changes or the current global warming (Haberkorn et al., 2017; Lebrouc et al., 2013; Magnin et al., 2017; Moore et al., 2011; Myhra et al., 2017; Myhra et al., 2019; Nötzli et al., 2007; Nötzli and Gruber, 2009). However, no numerical model has been presented yet which calculates how a change in the thermal field (e.g. induced by climatic warming) can affect the mechanical stability of a permafrost-affected mountain rock slope.

3. Study site

The studied rock slope is located at the German-Austrian border, 60 m below the Zugspitze peak (2962 m a.s.l.), Germany´s highest mountain (47°25'21, 10°59'13; Figure 3.1). The Zugspitze is the top of the Wetterstein massif which is situated in the Northern Calcareous Alps close to the city of Garmisch-Partenkirchen. The Zugspitze peak is an important tourist destination during summer and winter time and can be reached by three cable cars all year round. Half a million visitors per year ascend to the summit by use of the Bavarian cable car (Bayerische Zugspitzbahn Bergbahn AG, 2019).

The summit ridge consists of Triassic Wetterstein limestone which has a thickness of up to 1000 m and belongs to the Lechtal nappe of the East Alpine nappe system. The rock at the summit crest is stratified in tens of metres thick beds, however, it is highly weathered and fractured, sometimes with brecciated zones of 1 m thickness. The limestone shows typical characteristics of formation in lagoons or reefs, incorporating big oolites. In some places it occurs as dolomised limestone (Gallemann et al., 2017; Körner and Ulrich, 1965; Krautblatter et al., 2010; Lauber and Goldscheider, 2014; Miller, 1962; Vidal, 1953). The limestone is fine-grained and has a porosity of approximately 4.4 %. It shows little heterogeneity in terms of lithological properties (Krautblatter et al., 2010). Karst dissolution phenomena are present at the summit crest and, especially, at the lower cirque (Zugspitzplatt) in terms of caves, dolines and karren (Lauber and Goldscheider, 2014).

The Zugspitze summit ridge was chosen as real-world exemplification of an unstable permafrost-affected rock slope to perform numerical stability analyses (Section 6). Furthermore, it acts as a benchmark analogue to constrain simulated temperature- and stress-conditions for direct laboratory shear tests along ice-filled rock joints (Sections 5.2–5.3). The following set of conditions (Sections 3.1–3.4) gives a first, literature-based review on the applicability of the Zugspitze as field site for this study.

3.1. Rock slope instability

Recent rockfall activity in the area is evident due to four events with volumes between 10^3 and 10^4 m^3 which occurred between 2000 and 2005 (Gude and Barsch, 2005; Nötzli et al., 2010). A much bigger rock mass of $0.2–0.4 * 10^6$ m^3 detached from the north-face of the Zugspitze after the Holocene climatic optimum (3700 years B.P.) presumably supported by permafrost degradation (Gallemann et al., 2017; Gude and Barsch, 2005; Jerz and Poschinger, 1995).

At the Zugspitze summit ridge, close by the antenna of the Telekom Austria and the hiking path to the peak, a rock slope instability is observed since the 1990s. This instability is characterised by dolines of several metres depth and discontinuities or shear zones with a centimetre to decimetre thick infill of fine-grained material (Bledow and Krautblatter, 2010; Krautblatter

et al., 2010). Maximum displacements along one of the main shear zones (SZ1 in Figure 3.1b) lie in the range of decimetres, while the dolines are subject to continuous erosion to the present day.

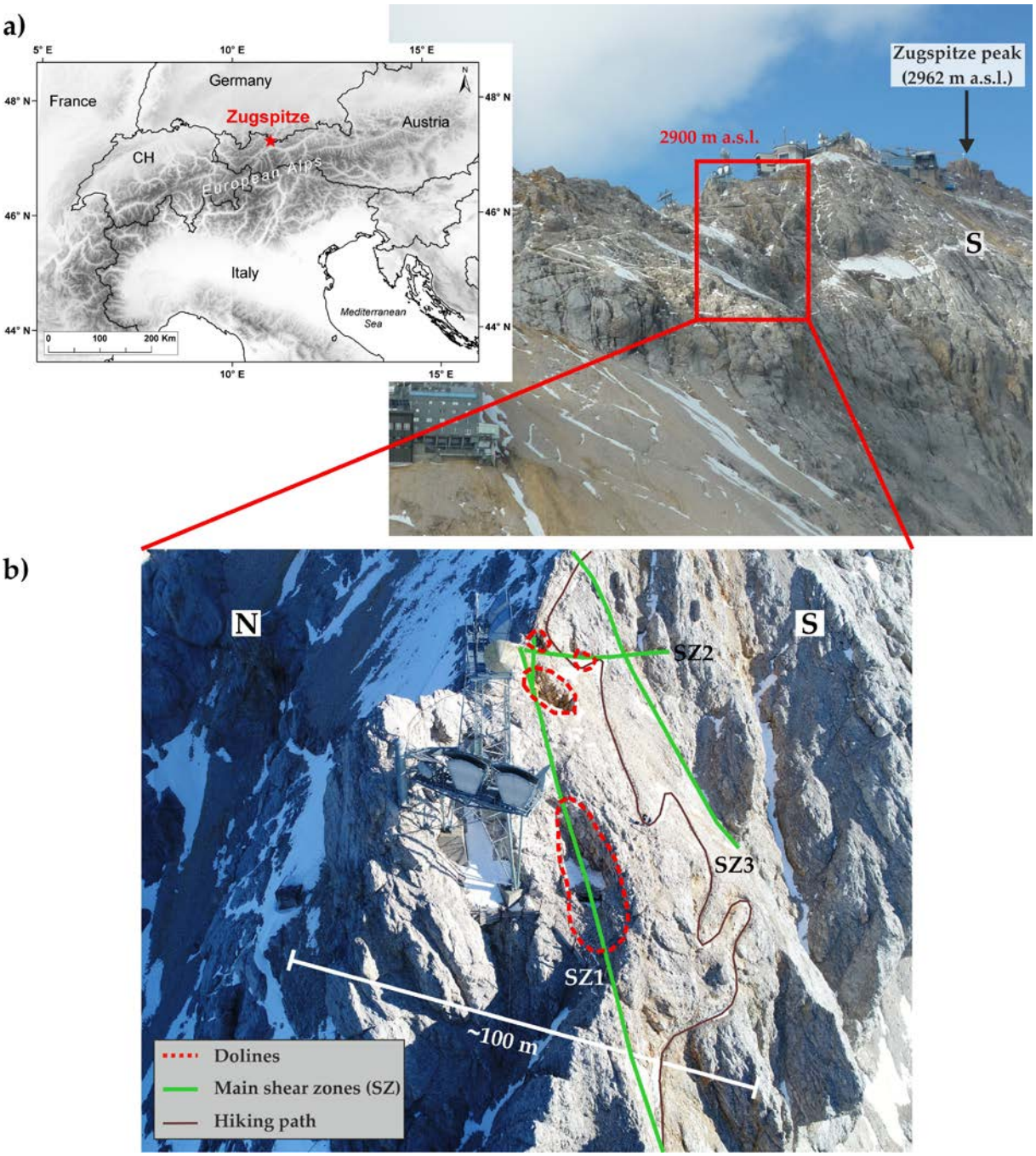

Figure 3.1: Location of the study site at the Zugspitze summit area including principal structural features.

(a) View on the south-slope of the Zugspitze, the summit crest and the summit stations of the three cable cars. The top of the study site is located 60 m below the peak (2960 m a.s.l.), highlighted by the red box. The map at the left side shows the location of the Zugspitze in the context of the European Alps. The digital elevation model was developed with SRTM data from CGIAR CSI and has a cell size of 90 m (Jarvis et al., 2008). (b) Structural features of the study site involving dolines and main shear zones of the upper part of the rockslide.

3.2. Permafrost occurrence

The Alpine Permafrost Index Map (APIM) by Böckli et al. (2012b) and the Bavarian Permafrost Map (Bayerisches Landesamt für Umwelt, 2019) demonstrate that the Zugspitze summit area is one of the few permafrost sites in Germany; it is probably even the most important site (Nötzli et al., 2010).

During the construction of the cable cars in the 1960s and the 1990s the occurrence of permafrost was confirmed by permanently ice-filled deep fractures with a thickness of 0.1 m and down to a depth of 3 m (Körner and Ulrich, 1965; Ulrich and King, 1993). During the construction of the railway tunnel to the Zugspitzplatt in the 1980s, a massive ice body was found in a karst sink hole (Ulrich and King, 1993).

Between 2012 and 2015, daily borehole temperatures at the Zugspitze peak average -1.1 °C within the permafrost core area (approximately 24 m away from the south face and 21 m away from the north face) and approach minima of -6 °C at the margins (ca. 5 m away from the north face) (Gallemann et al., 2017). 2D and 3D thermal models of the Zugspitze summit area demonstrate that permafrost can exist at the north-face above 2300 m a.s.l. and sporadically at the south-face which depends on the slope aspect and altitude (Figure 3.2) (Böckli et al., 2011; Gallemann et al., 2017).

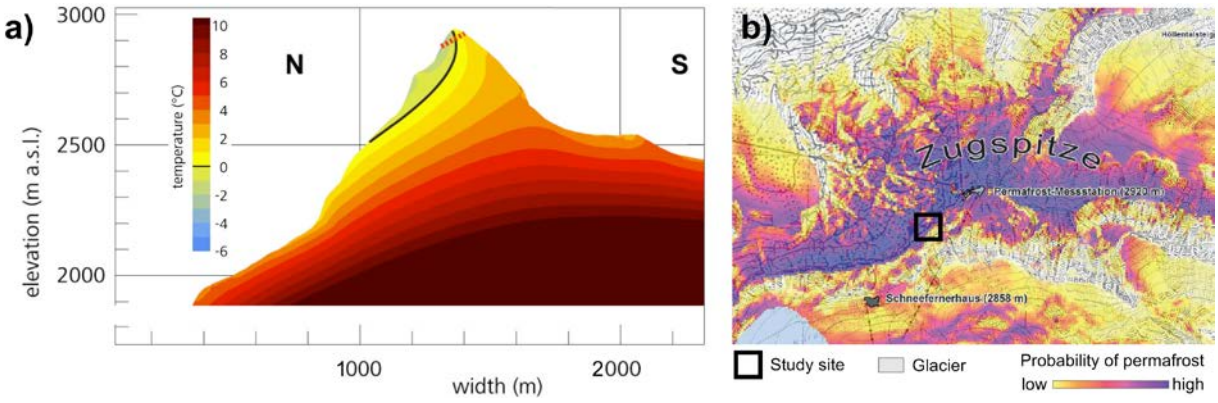

Figure 3.2: Modelled permafrost distribution in the Zugspitze summit area.

(a) Cross section of the modelled thermal field of the Zugspitze at the location of the borehole (indicated with the red dashed line), modified from Nötzli (2008). The permafrost boundary corresponds to the 0 °C isotherm and is marked by the black solid line. (b) Permafrost map of the Zugspitze summit area delivered by the Bavarian State Office for the Environment (Gallemann et al., 2017). The legend was enlarged for better readability. The black box shows the location of the study site. Source: Bavarian Agency for Digitisation, High-Speed Internet and Surveying.

The Zugspitze peak is 1–3 °C (mean rock temperature in a depth of 20 m) colder than Swiss Alpine permafrost sites located at a similar altitude and crest-like topography (Nötzli et al., 2019). Among the Swiss sites, the boreholes at the Gemsstock (Borehole altitude: 2940 m a.s.l.) and the Tsaté (B.a.: 3050 m a.s.l.) are installed in bedrock (such as the one at the Zugspitze), while the borehole at the Schilthorn (B.a.: 2910 m a.s.l.) is drilled in debris. In addition, the

active layer at the Zugspitze is 5–6 m thinner than at the other sites (within the time period 2010–2015). The colder conditions at the Zugspitze peak may be caused by the steep north-face leading to reduced solar radiation and an absent accumulation of a thick snow cover which can prevent an effective ground heat loss due to cold air temperatures in winter (Böckli et al., 2011).

3.3. Climatic warming and related permafrost evolution

A climatic warming in the last century and an even stronger temperature increase since the late 1980s can be observed at the Zugspitze (Gallemann et al., 2017; Krautblatter et al., 2010). The mean annual air temperature (MAAT) between 1991 and 2018 was 0.8–1.0 °C warmer than in the three prior 30-year reference periods between 1901 and 1990. A model of the permafrost evolution in the Zugspitze peak shows that between 1915 and 2015 the permafrost body lost a thickness of 2 m at the north-face and thickness of 7 m at the south-face. The permafrost temperature increased by approximately 1 °C (Gallemann et al., 2017). Between 1892 and 2009, the area of the northern and the southern Schneeferner glacier at the Zugspitzplatt decreased by 73 and 94 %, respectively (Hagg et al., 2012).

Within the current 30-year reference period (1991–2020) of air temperature measurements at the Zugspitze meteorological station, the mean of the aestival air temperature (June to August) was exceeded by more than 1 °C in four years, and by more than 2 °C in three years (Figure 3.3). The highest positive anomaly (+2.6 °C) corresponds to the unusually hot summer of 2003, in which an exceptionally high number of rockfall events from permafrost areas was reported (Gruber et al., 2004a; Ravanel et al., 2017). Four of the seven anomalous summers mentioned above occurred within the time period of field measurements for this thesis (2014–2019). Further, the six summers of field studies were 2.0–2.9 °C warmer than the summers of the previous three reference periods from 1901 to 1990, and even 1.1 °C warmer than the current reference period from 1991 to 2019.

The following conditions make the Zugspitze summit area susceptible towards a progression of permafrost degradation and a potentially resulting decrease in rock slope stability (Nötzli et al., 2007; Nötzli et al., 2010): (i) the summit area is located at the lower permafrost extension limit, (ii) the steep rock walls and ridges may respond quickly to climatic changes, and (iii) it is an important tourist destination with intensely used infrastructure. A future anomalously warm summer at the Zugspitze summit area can potentially initiate rock slope destabilisation, or trigger failure (mostly smaller events), as reported from many other alpine sites in the hot summer of 2003 (see above). Until the end of the 21st century the mean air temperature is projected to increase by 3.2 °C. This would result in a total loss of permafrost at the Zugspitze summit within the second half of this century (Gallemann et al., 2017), which will support rock

slope destabilisation and increase rock fall activity (Gude and Barsch, 2005), possibly including an elevated occurrence of high-magnitude failure events.

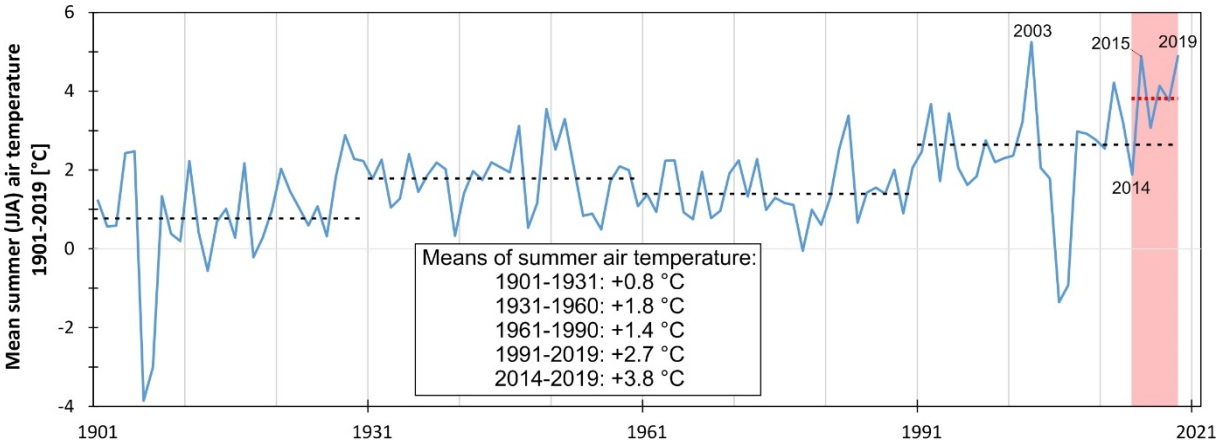

Figure 3.3: Mean summer (June to August) air temperatures between 1901 and 2019 measured at the Zugspitze meteorological station.

The black dashed lines represent the corresponding means of the 30-year reference periods since 1901. The red box marks the period of study for this dissertation (2014–2019). The red dashed line represents the mean summer air temperature for the period of field studies. Data source: German Meteorological Service.

3.4. Permafrost research activity

As a result of the sensitivity towards permafrost degradation and the easy accessibility of the Zugspitze summit area, it is one of the best equipped permafrost monitoring sites in the European Alps. It hosts the only two German borehole sites with temperature sensors included in the database of the Global Terrestrial Network for Permafrost (GNT-P) (Biskaborn et al., 2015; GTN-P database, 2019). The boreholes are located at the summit (44 m long, pierces the crest) and in a lower gallery within the summit crest (2.5–20 m away from the north face and each of them 0.4 m away from the tunnel wall) (Gallemann et al., 2017; Krautblatter et al., 2010). Further numerous thermistors were installed at the summit crest and at the lower Zugspitzplatt to log subsurface rock temperatures (in depths of 0.1–1 m) and ground surface temperatures (Böckli et al., 2011; Gude and Barsch, 2005). The distribution and evolution of bedrock permafrost in the gallery mentioned above is monitored irregularly by ERT since 2007 (Krautblatter et al., 2010), and monthly since 2014.

4. Thermal and mechanical characterisation of an unstable, permafrost-affected rock slope: field surveys at the Zugspitze summit crest

The primary objective was to simulate specific mechanical processes of the destabilisation of a degrading permafrost rock slope in laboratory experiments (Section 5.2 and Section 5.3) and in a numerical model (Section 6). The thermo-mechanical setting of the permafrost-affected Zugspitze summit crest was chosen (i) to constrain geometrical, thermal and stress conditions for the simulations in the laboratory and in the numerical model, and (ii) to provide geometrical and thermal input parameters for the numerical analysis. This required to evaluate the suitability of the study site as benchmark analogue and test object for the laboratory and modelling work. For these steps, the current state of rock slope stability, the controlling mechanical processes, and the permafrost distribution at the field site were analysed by the following methods:

Mapping of discontinuities and major structural features (Section 4.1) and UAV-based photogrammetry (Section 4.2) provided data on the topography of the crest, large-scale shear zones, the geometrical properties of the fracture network, the dimensions of the unstable rock mass, and the potential failure mechanism. Measuring of fracture displacements via digital tape extensometer (Section 4.3), helped to estimate the current state of rock slope stability. Electrical resistivity and seismic refraction tomography (ERT and SRT; Section 4.4), and logging of near-surface rock temperatures (NSRT; Section 4.4) resulted in the estimation of the spatial permafrost distribution in the summit crest.

4.1. Characterisation of the fracture network

Discontinuities and major structural features were mapped (i) to estimate the failure type and the volume of the unstable rock mass, (ii) to select the route of the cross section for the 2D model, and (iii) to provide input data for the numerical calculations.

4.1.1. Methods

The fracture network was mapped systematically along five distinct scan lines distributed over the south-slope and at the top of the summit crest (Figure 4.1; Figure 4.7d) as working at the north-face requires rope safeguarding. The studied joint characteristics involved dip and dip direction, spacing, aperture, joint frequency and joint roughness. The entire data set contains 129 discontinuities.

The mean dip and dip direction of the joint sets were calculated with DIPS 7.0 (RocScience) defining main joint sets in pole density plots. Geometrical Terzaghi weighting was applied to

correct potential bias which is introduced in favour of discontinuities perpendicular to the direction of the scan line.

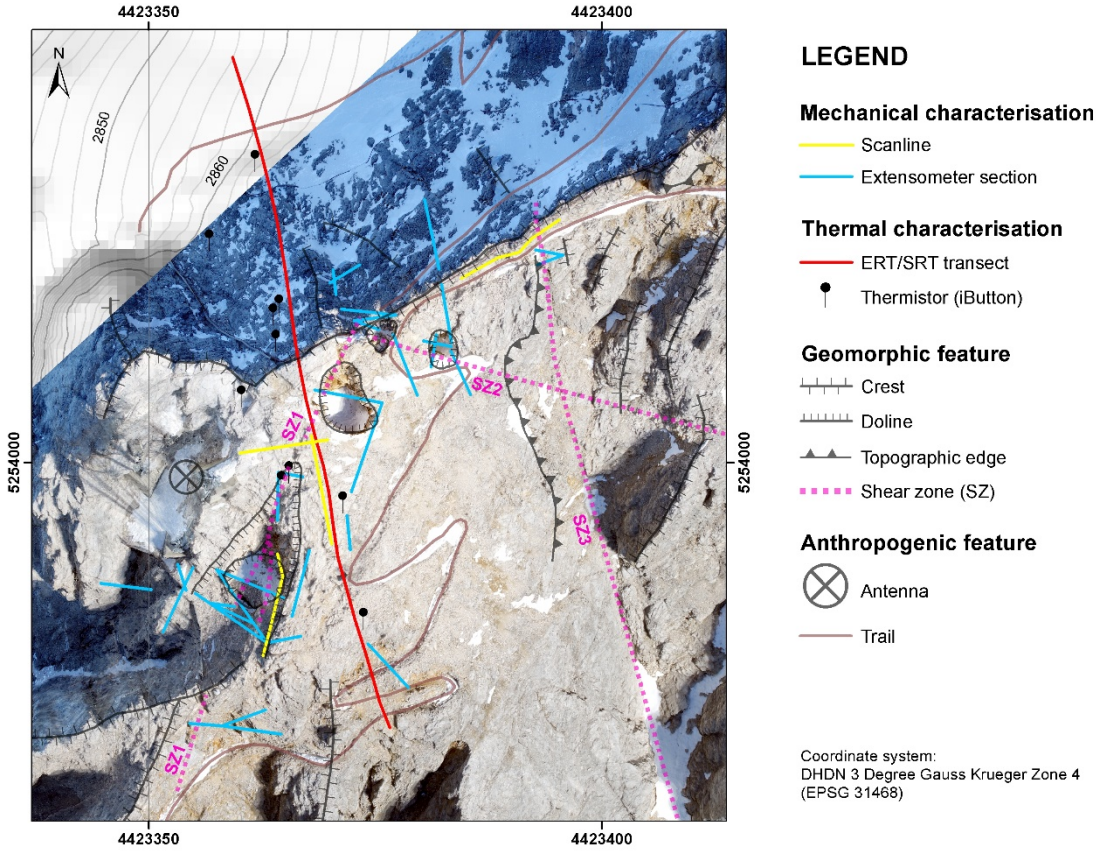

Figure 4.1: Network of geophysical and geotechnical measurements at the Zugspitze summit ridge including reference to geomorphologic and anthropogenic features.

The digital elevation model was obtained from the Bavarian Agency for Digitisation, High-Speed Internet and Surveying. The orthofoto was computed with Agisoft Photoscan v 1.4.5. derived by UAV-based photogrammetry. Coordinates are given in Gauss Krueger Zone 4 (EPSG 31468).

The joint roughness was recorded with a Barton comb/profilometer along 14 profiles not included in the five scan lines. Each profile consisted of between three and seven subsections of 26 cm. Data acquisition and analysis were performed according to Tse and Cruden (1979). The coefficient Z2 was determined by

Equation 4.1:

$$Z_2 = [\frac{1}{M(\Delta x)^2} \sum_{i=1}^{M} (yi + 1 - yi)^2]^{1/2}$$

where y_i is the distance between the rock surface and a fixed reference line, x is a specified equal record interval and M is the number of measured intervals along the profile. The applied sampling interval x at the field site was 5 mm. To calculate the JRC, the following formula proposed by Yang et al. (2001) was used:

Equation 4.2:

$$JRC = 32.69 + 32.98\, log_{10}\, Z_2$$

As Z_2 is only valid for the range of 0.1 to 0.42, values < 0.1 were assigned a zero JRC.

4.1.2. Results

A very prominent and persistent shear zone (SZ) was detected at the south-slope (SZ1 in Figure 3.1b and Figure 4.2d). According to geotechnical field mapping, SZ1 has a trace length of approximately 70 m and runs in a maximum depth of 10–15 m. Observed maximum displacements along the upper part of SZ1 lie in the range of decimetres and point to a high level of joint persistence. At some places it opens to a decimetre wide, highly fractured zone filled with fine material ranging from clay-size to gravel-size. This type of infilling is observed in most of the bigger shear zones at the summit region (Figure 4.2c). Four dolines develop along the major shear zones SZ1 and SZ2 (Figure 4.1): Two of them form along SZ1, while the third one develops along SZ2. The fourth doline is located at the point of intersection between SZ1 and SZ2 (Figure 4.2a and Figure 4.2b).

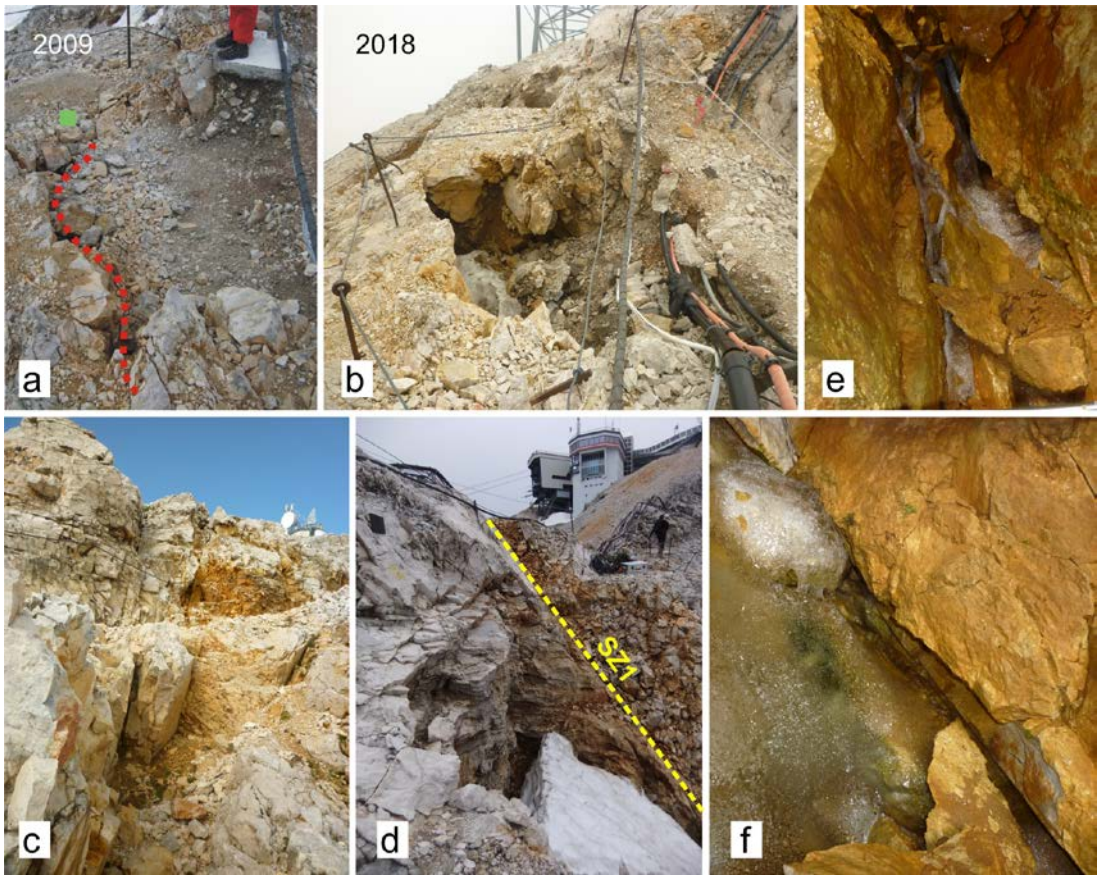

Figure 4.2: Growing doline (2009-2018) and prominent shear zones filled with fine material and ice at the crestline of the Zugspitze summit area.

(a)-(b) Doline at the intersection of SZ1 and SZ2 (Figure 4.1) in 2009 and in 2018. (c) Shear zone filled with fine material. (d) Shear zone SZ1, visible at the inner wall of a doline. (e)-(f) Ice fillings along SZ1.

A total of four joint sets – K1, K2, K3 and K4 – were mapped at the south-face of the crest (Table 4.1, Figure 4.3). Cuboids are formed when the joint sets K1, K2 and K3/K4 are mutually at right angles, otherwise parallelepipeds are formed.

Table 4.1: Mapped geometric discontinuity characteristics.

Standard deviations are given for measured parameters. The joint frequency is calculated by 1/spacing. K1-4 = Joint sets. SZ = Shear zone. This table is a slight modification of Table 6.2 and additionally includes data on joint set K4.

Geometric parameter	K1	K2	K3	K4	SZ1 (K4)
Dip / Dip direction [°]	24/175	63/033	69/293	66/125	63/130
Spacing [m]	0.3	0.8	0.5	0.6	--
Frequency [$J\,m^{-1}$]	3.7	1.3	1.9	1.6	--
Trace length [m]	5.1	2.4	2.5	3.0	50.0
Aperture [mm]	7.0	1.7	3.0	5.3	270.0
Joint roughness coefficient[a] (JRC)	5.5 ± 1.9	6.8 ± 0.9	8.6	--	4.4 ± 3.3
Number of mapped joints	15	21	37	19	1
Comment	Bedding planes				One of the main failure planes controlling the stability of the rock slope

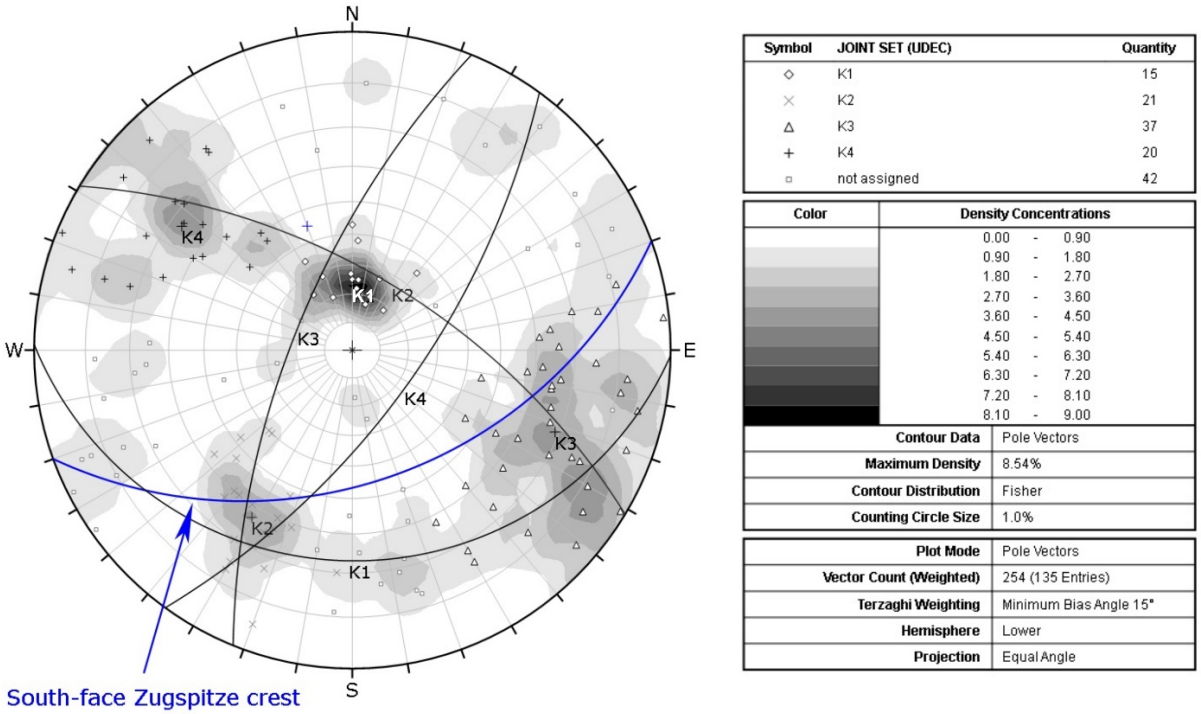

Figure 4.3: Orientations of field-measured joints and principal joint sets presented in a stereographic projection.

This figure is a slight modification of panel (a) in Figure 6.3. Presentation and calculation of the joints/joint sets was performed with DIPS 7.0 (Rocscience). The contours depict the Fisher concentrations (density) of the poles. Black great circles = Joint sets.

4.2. Kinematic analysis and estimation of the potential failure volume

A kinematic analysis and UAV-based photogrammetry (for the computation of a 3D point cloud) provided information on the possible (i) shear zones delimiting the unstable rock mass, (ii) type of failure and (iii) failure volume.

4.2.1. Methods

Digital images were acquired from the air with the drone Phantom 4 Pro (DJI). The included camera is equipped with a 1" CMOS sensor with 20 MP. Red, green and blue images are captured simultaneously and with different viewing angles. Agisoft Photoscan v.1.4.5 was used to generate an orthofoto with a resolution of 1.25 cm, and a 3D point cloud. The latter has a total number of 21 Mio points with a resolution of ca. 5 cm, and rgb information for identifying geological features. Analysis of the point cloud was performed with RISCAN PRO 2.7.1 64 bit.

A simple kinematic analysis of a potential plane and wedge failure was conducted with DIPS 7.0 including the southern slope-face (45/160) and the main shear zones, which were identified due to field mapping and the preceding analysis of the point cloud. The lateral limit for critical dip directions of the failure plane was set to the default of 20°. The friction angle was set to 30°, based on direct shear tests of frozen and unfrozen Wetterstein limestone by Krautblatter et al. (2013).

4.2.2. Results and interpretation

Shear zones SZ1, SZ2 and SZ3, which were identified as potential failure planes in the field (Figure 4.4), were recognised in the 3D point cloud by manually defining sections of points which lie on a common plane. These sections were extrapolated to mean failure planes and intersect with each other and the slope face. A fourth and fifth shear zone (SZ4 and SZ5) were determined to form the possible downslope boundary of the unstable rock mass (Figure 4.4). The approximate total volume of the potentially failing rock mass was estimated to be $2.9 * 10^4$ m³. This was done by calculating the difference between the intersected failure planes and the terrain surface, both related to a lower reference plane.

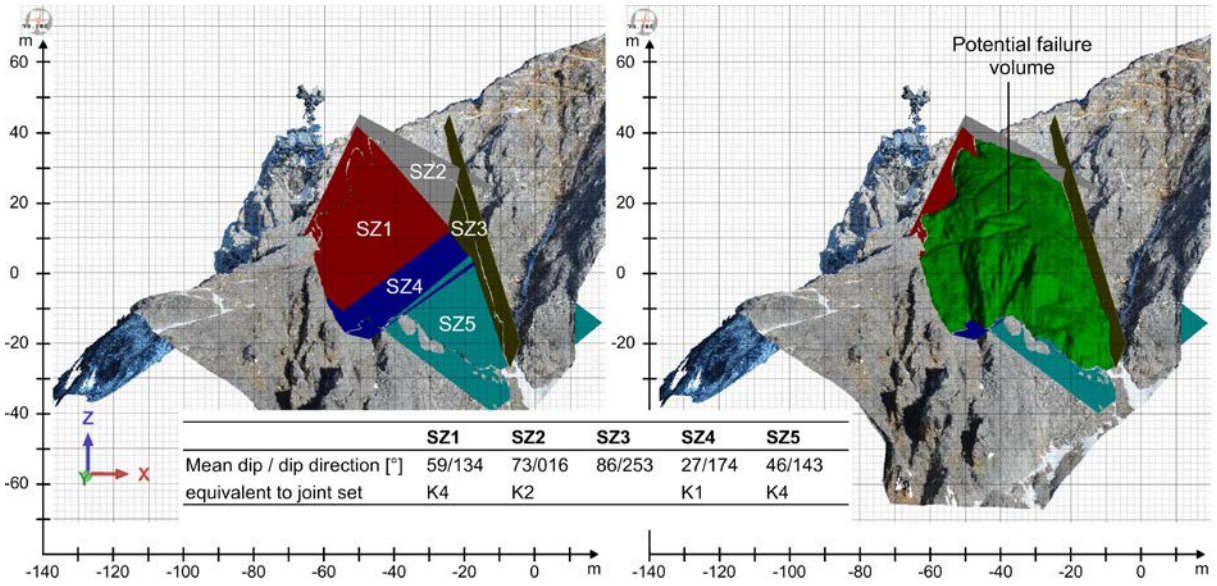

	SZ1	SZ2	SZ3	SZ4	SZ5
Mean dip / dip direction [°]	59/134	73/016	86/253	27/174	46/143
equivalent to joint set	K4	K2		K1	K4

Figure 4.4: Intersecting main shear zones (SZ) which delineate the unstable rock mass at the south face of the Zugspitze summit crest.

With (right) and without (left) the potential failure volume (green). This figure corresponds to panel (e) in Figure 6.1.

The results showed that pure plane failure can occur for those sections of SZ1, SZ4 or SZ5 for which the dip is lower than the inclination of the slope-face (45°) and higher than the friction angle of the rock joints (30°) (Figure 4.5a). Pure wedge failure is possible for intersections of SZ3/SZ5, and marginally for SZ3/SZ4 or SZ3/SZ1 (Figure 4.5b).

Though planar sliding is the dominant kinematic failure mode which affects the major left part of the unstable rock mass, we assume that the instability is driven by a complex combination of both a plane and a wedge failure (Figure 4.4, Figure 4.5). Neither pure planar sliding nor pure wedge sliding are likely to be the controlling failure mechanism. In the upper part of the rock slope, planar sliding may occur along SZ1, while wedge failure supports the displacement along SZ1/SZ3 including a tension crack SZ2. At lower slope sections, planar sliding can occur along SZ4 and SZ5, while wedge failure potentially enhances the failure process along SZ3 and a stepped plane constituted of SZ4 and SZ5.

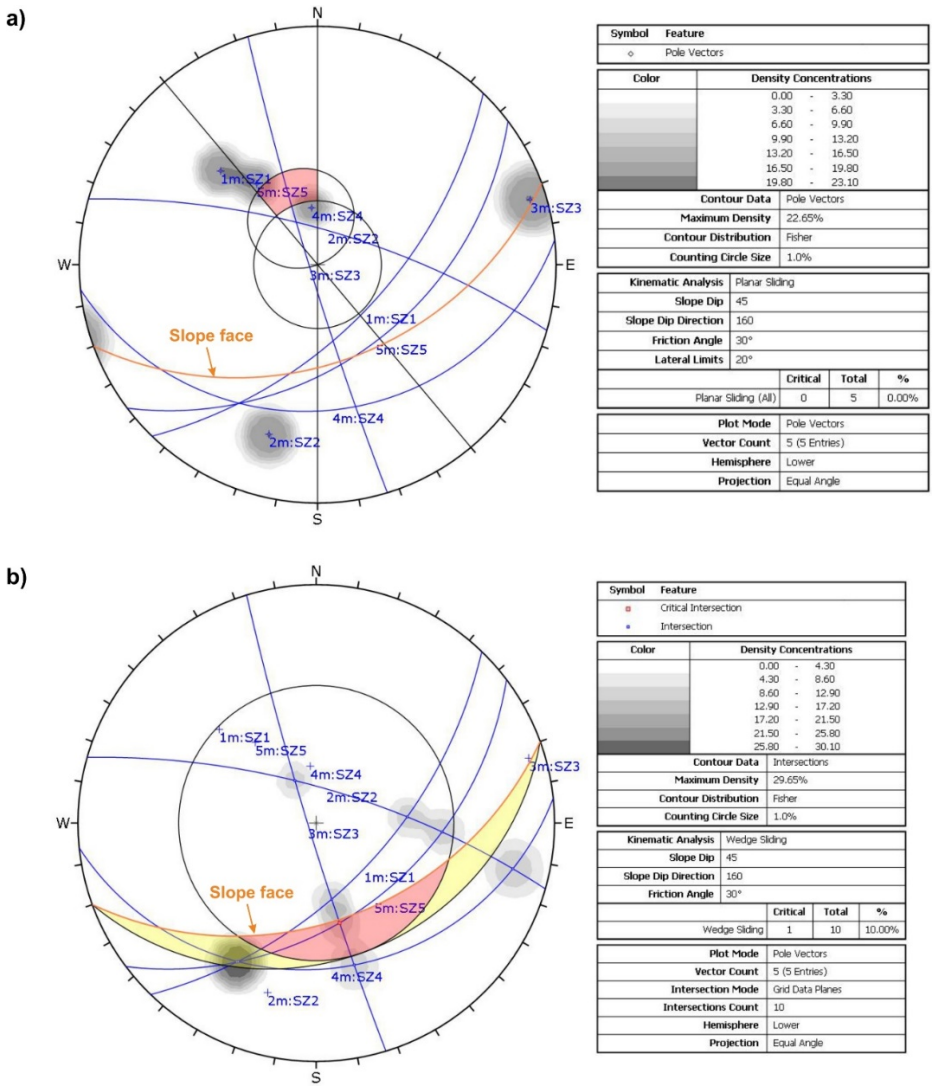

Figure 4.5: Kinematic analysis of the unstable south-face of the Zugspitze summit crest for a potential plane or wedge failure.

(a) Plane failure can occur for those shear zones whose poles lie within the critical red window. This is valid for SZ4 and SZ5, and marginally for SZ1. The friction cone in the centre has an angle of 30°. The lateral limit of the critical window is set to 20°. (b) Wedge failure is possible for intersections of planes which lie within the critical red window. This is the case for intersections of SZ3/SZ5, and marginally for SZ3/SZ4 or SZ3/SZ1. Sliding along SZ4 can occur for wedges constituted of SZ1/SZ4 or SZ5/SZ4 (yellow area). The friction cone at the margin has an angle of 30°.

4.3. Fracture displacements

Crack displacements were repeatedly recorded within the most active parts of the rockslide (i) to quantify mean displacement rates, (ii) to assess seasonal patterns of movement, and (iii) to analyse the evolution of rock displacements between 2013 and 2019.

4.3.1. Methods

The upper part of the south-face was equipped with 32 sections for displacement measurements. Each section is delimited by two plugs fixed in the rock crossing one or more important

joints or shear zones. Values were collected with a digital tape extensometer (Soil Instruments Ltd.) at the beginning (June/July) and at the end (September/October) of the accessible, snow-free summer season between 09/2013 and 07/2019. The tape extensometer measures with a maximum resolution of 0.01 mm. The locations of the sections are displayed in Figure 4.1.

4.3.2. Results

The annual mean absolute displacement for the period 09/2013–07/2019 measures 2.1 mm y^{-1} (Figure 4.6a). To study the evolution of displacements over time, absolute annual fracture displacement rates were calculated from early summer to early summer of the subsequent year. Here, the medians of annual displacements range between 0.3 and 4.8 mm y^{-1} and do not point to either an acceleration or a deceleration between 2013 and 2019. Recording crack displacements twice a year, at the beginning and at the end of the summer season, allowed us to compare summer displacement rates with those of the remaining year (Figure 4.6b): The monthly mean displacement rate reduces by a factor of 6.4 when changing from summer to the remaining seasons (summer: 0.63 mm mo^{-1}; remaining year: 0.10 mm mo^{-1}). This corresponds to a decrease by 84.4 %.

a)

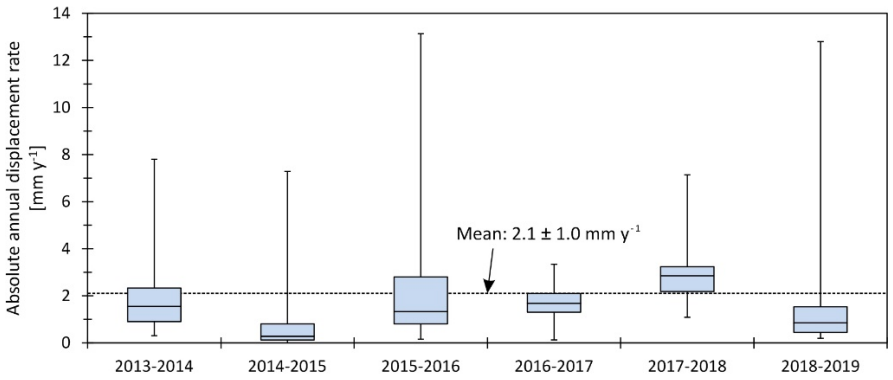

b)

Fracture displacement in summer [mm mo^{-1}]	2015	2016	2017	2018	Total
Mean	1,22	0,21	0,85	0,25	0,63
Standard deviation	1,45	0,15	0,39	0,50	
Number of measured sections	30	30	31	30	

in the remaining year [mm mo^{-1}]	2015/16	2016/17	2017/18	2018/19	Total
Mean	0,05	0,13	0,04	0,09	0,10
Standard deviation	0,04	0,07	0,04	0,15	
Number of measured sections	31	31	30	31	

Figure 4.6: Near-surface fracture displacements at the south-face of the Zugspitze summit crest between 09/2013 and 07/2019.

(a) Boxplot of annual absolute displacement rates for the time period 2013-2019. (b) Monthly rates for summer (June to September) and the remaining year (October to May) between 2015 and 2019.

4.4. Spatial distribution of permafrost

Geophysical techniques (ERT and SRT) were applied to localise permafrost in the surroundings of the unstable rock mass at the Zugspitze crest. By doing this, the temperature-dependent numerical stability model could be divided in frozen and unfrozen sections, and a spatial warming pattern could be derived for the simulation of permafrost degradation in the future. Near-surface rock temperatures (NSRT) were monitored to gain a general insight into their spatial and temporal pattern at the crest, and to validate the geophysics within the shallow rock layer.

4.4.1. Methods

4.4.1.1. Near-surface rock temperature

Rock temperature sensors (Maxim Integrated, iButton model DS1922L-F5) were instrumented in the direct surroundings of the geophysical survey lines in depths of 10 and 80 cm (locations are displayed in Figure 4.1 and Figure 4.7c). So far, iButtons have been applied successfully to measure ground surface or bedrock temperatures in alpine terrain (Gubler et al., 2011; Keuschnig, 2016). The preparation of the sensors and the installation technique in solid rock were taken from Keuschnig (2016). The sensors measured the rock temperature every two hours between August of 2015 to August of 2019 with an accuracy of ± 0.5 °C. Five iButtons were installed at the north-face and five iButtons at the south-face, whilst two of them were located within the shear zone SZ1 (Table 4.2).

Table 4.2: Metadata on the instrumented temperature sensors at the Zugspitze summit ridge.

iButton	Aspect [°]	Slope [°]	Depth [cm]	Characteristics
1	210 (S)	24	10	thick snow cover in winter/spring, intense solar radiation in summer
2	320 (N)	70	10	thin snow cover in winter/spring, shaded or little radiation in summer
3	320 (N)	70	10	
4	320 (N)	60	10	
5	320 (N)	52	10	
6	320 (N)	70	80	
7	160 (S)	32	10	thick snow cover in winter/spring, intense solar radiation in summer (iButtons 8 and 10 located at shear zone SZ1)
8	140 (S)	55	10	
9	160 (S)	58	10	
10	140 (S)	55	75	

4.4.1.2. Electrical resistivity tomography

Laboratory-calibrated ERT is capable of characterising and monitoring the spatial variability and evolution of mountain bedrock permafrost in steep rock walls (Keuschnig et al., 2017; Krautblatter et al., 2010; Magnin et al., 2015; Murton et al., 2016; Scandroglio et al., 2021). The

outlined procedure of the measuring set-up in the field was similarly applied to the Zugspitze summit crest to accurately assess the distribution of permafrost along the profile of the numerical model (Figure 6.1a). Two surveys were conducted at the end of August 2014 and 2015, which corresponds to the time that the active layer at the Zugspitze peak usually reaches its maximum extent (Gallemann et al., 2017).

ERT was applied along a transect of approximately 100 m, crossing the ridge and covering its north- and south-face (Figure 4.1, Figure 6.1). In this way, we could assess the effect of thermal differences induced by various expositions at the crest-topography. The transect for ERT consists of 41 electrodes (stainless steel nails) which were installed once and used for both surveys. The electrodes were separated from each other by a mean spacing of 2.5 m (Figure 4.7a). To enhance electrode coupling, the steel nails were greased with an electrically conductive fluid and water was added to the contact between nails and ground just before the survey. Acquisition of geoelectrical data was performed with two distinct devices: an ABEM Terrameter SAS 1000 and a Terrameter LS with maximum input/output voltages of ± 400 and ± 600 V, respectively, and corresponding injected currents of 1 and 0.1 mA, respectively. The applied input/output voltage and the current were standardised for all surveys and were 500 V and 1 mA, respectively. The applied electrode configurations for the ER surveys were Wenner (in 2014) and Wenner-Schlumberger (in 2015). 2D data processing and inversions were performed with the commercial software package Res2Dinv. Data inversions were performed using robust inversion and model refinement with half the unit electrode spacing (Loke, 2019).

To assign the measured ERT of the summit crest to frozen or unfrozen slope sections, we used the resistivity of saturated frozen and unfrozen Wetterstein limestone in the laboratory, defined (i) by Krautblatter et al. (2010) in the same lithology, and (ii) in the context of this study based on two rock blocks from the field site. For the laboratory tests, we followed the suggested procedure by Krautblatter et al. (2010), although it was limited to a single cooling and subsequent freezing trajectory of the samples from 10 °C down to -6 °C. The rock samples (both with a size of 0.02 m^3) were kept in a custom-built, temperature-controlled cooling box for the duration of the tests. Rock temperature was measured simultaneous to resistivity with two Pt100 sensors (Greisinger GMH 3750, with a 0.03 °C precision) inserted in the rock samples (Figure 4.10c). Measurements were performed along 3–4 different Wenner arrays installed parallel to each other.

4.4.1.3. Seismic refraction tomography

ERT was complemented with laboratory-calibrated SRT to increase the trustworthiness of the data interpretation (Schrott and Sass, 2008). The procedure for the data acquisition and analysis was performed in accordance to Krautblatter and Dräbing (2014). SRT was applied along the same transect as for the ERT (Figure 4.1). 24 geophones were inserted in holes drilled next

to the electrodes which have a mean spacing of 2.5 m. Seismic impulses were applied with a 5 kg sledgehammer (Figure 4.7b). 6–9 offset-shots were conducted on both ends of the SR profile to extend the tomography to a similar dimension as the one for the ER. Data were collected with a Geometrics Geode and processed and inverted with the commercial software package ReflexW 8.5. Two surveys were conducted at the same days as the ERT (end of August 2014 and 2015), while a third survey was performed at the end of August 2016.

To convert the SR-tomographies into profiles with sections of frozen and unfrozen bedrock, characteristic laboratory P-wave velocities of frozen and unfrozen saturated Zugspitze limestone were used: according to Dräbing and Krautblatter (2012; Figure 2), the P-wave velocity increases from 3.7 to 6.4 km s^{-1} upon freezing (when measured parallel to cleavage/bedding). The first shift occurs at -0.5 °C where the P-wave velocity jumps from 3.7 to 5.9 km s^{-1}. At freezing down to approximately -2 °C, the velocity of the rock sample rises to 6.4 km s^{-1} and remains invariable at this level. The described velocity increase upon freezing was similarly observed with numerous other rock types (Dräbing, 2016).

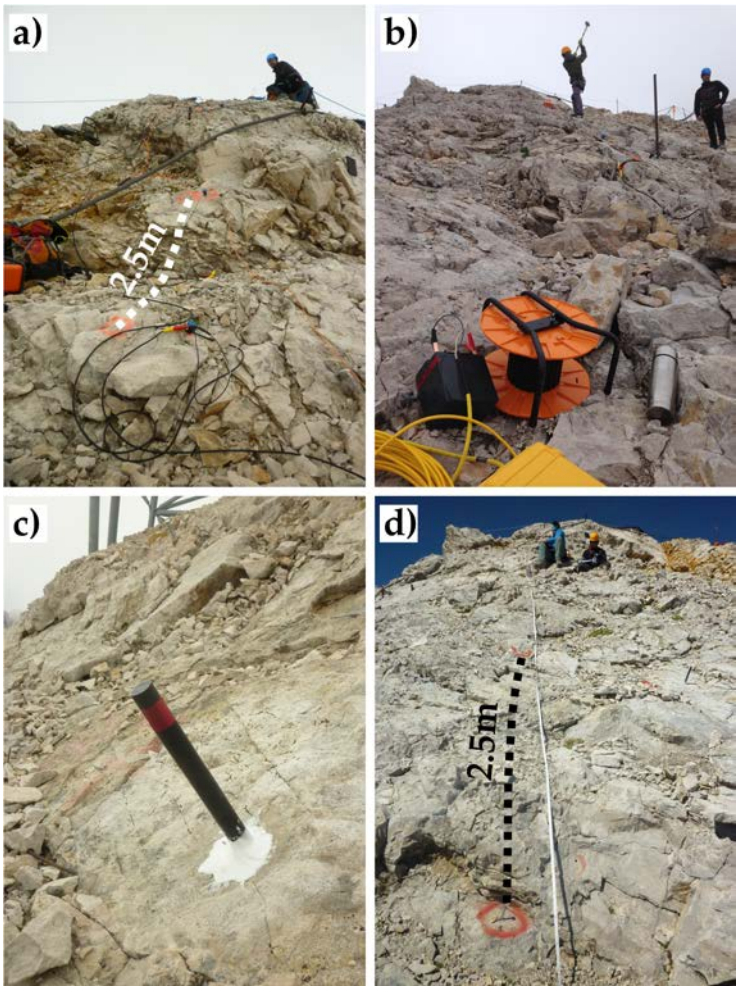

Figure 4.7: Geophysical/geotechnical surveys and instrumentations at the Zugspitze summit ridge.

(a)-(b) Measuring set-up and data acquisition for refraction seismics. (c) Installation of a rock temperature logger (iButton 7). (d) Scan line running parallel to the ERT/SRT transect (visible due to the locations of the electrodes marked with a red circle).

However, seismic refraction velocities in the field (V_F) are often below ultrasonic velocities measured in the laboratory (V_L). This is due to the higher degree of jointing of the rock mass in contrast to the intact rock cores used for laboratory tests (Budetta et al., 2001; Barton, 2007). P-wave velocity decreases with increasing rock joint frequency (J m^{-1}) which can be correlated to the ratio V_F/V_L (Sjøgren et al., 1979; Barton, 2007). The mean joint frequency at the study site, measured for all four joint sets, is 2.1 ± 1.1 m^{-1} (Table 4.1). The standard deviation accounts for the joint frequency variation of the various joint sets. The respective V_F/V_L ratio ranges between 0.85 and 0.90 dependent on the degree of joint frequency (Barton, 2007). Assignment of V_F values for frozen and unfrozen Wetterstein limestone was done using measured V_L and J m^{-1}. Hereby, maximum unfrozen P-wave velocities were corrected to 3.3 km s^{-1} (with V_F/V_L = 0.88, and V_L = 3.7 km s^{-1}) and minimum frozen P-wave velocities were adjusted to 5.2 km s^{-1} (with V_F/V_L = 0.88, and V_L = 5.9 km s^{-1}). A domain of possibly frozen rock with higher uncertainty was assigned to V_L between 3.3 and 5.2 km s^{-1}.

4.4.2. Results and interpretation

4.4.2.1. Near-surface rock temperature

The recordings of the thermistors demonstrate that the surficial rock layer (< 1 m) thaws during the summer months. This is valid for both slope-faces of the summit ridge (Figure 4.8).

During winter and spring, mean temperatures are negative, but in summer they are positive (Figure 4.9). In autumn mean temperatures are positive at the south-slope and negative at the north-slope. Thermistors B6 and B10 show a lower seasonal variation in temperatures. As they were installed 70 cm deeper in the rock, they presumably include the delay of thermal signals from the surface due to the low thermal conductivity of the rock mass.

Within the period of NSRT monitoring (2015–2019), seasonal means for the north-face are 2–3.3 °C lower than for the south-face (Figure 4.9); this difference is greatest in summer (3.3 °C) and smallest during winter (2.0 °C). As the slopes at the field site are snow-free during summer, the higher radiation input at the south-face leads to a greater NSRT difference between shaded and sunny expositions in summer. Annual data sets without gaps were recorded for 2016 and 2017 (Figure 4.9b): here, the difference in averaged annual rock temperatures between shaded (N) and sun-exposed (S) locations is 2.5 °C. This value is lower than the mean annual NSRT differences observed by Haberkorn et al. (2015), Hasler et al. (2011b) or Magnin et al. (2015), who measured a difference of approximately 4–6 °C between shaded and sun-exposed locations at the Matterhorn, Gemsstock and Jungfraujoch, Switzerland, or at the Aiguille du Midi, France. The lower difference at the Zugspitze crest may be explained by the accumulation of a thick snow cover on the south-slope and even on most parts of the steeper, but rough north-slope, which insulates the ground from cold air temperatures in winter.

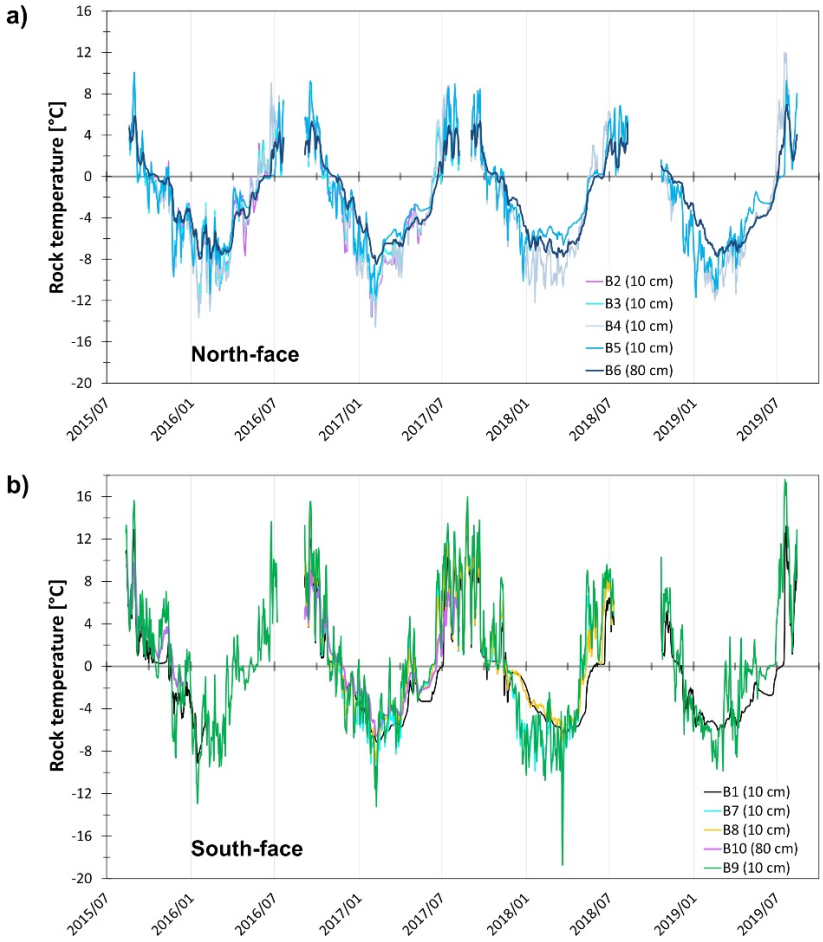

Figure 4.8: Near-surface rock temperatures measured in a depth of 10-80 cm at the Zugspitze summit crest between 08/2015 and 08/2019.

(a) North-face. (b) South-face.

4.4.2.2. Electrical resistivity tomography

The laboratory electrical resistivity (ER) clearly showed values lower than 19 kΩm for unfrozen rock and values higher than 28–29 kΩm for frozen rock (Figure 4.10). The equilibrium freezing point at -0.2 to -0.4 °C is indicated by a 21- to 37-fold increase in the frozen temperature–resistivity gradient. This pattern of ER versus rock temperature is similar to the one demonstrated by Krautblatter et al. (2010): here, the ER measures 30 ± 3 kΩm at the equilibrium freezing point (-0.5 °C). Overall, we defined ER values lower than 19 kΩm and higher than 33 kΩm as unfrozen or frozen respectively, and the range of values between the above-mentioned thresholds are defined as possibly frozen rock.

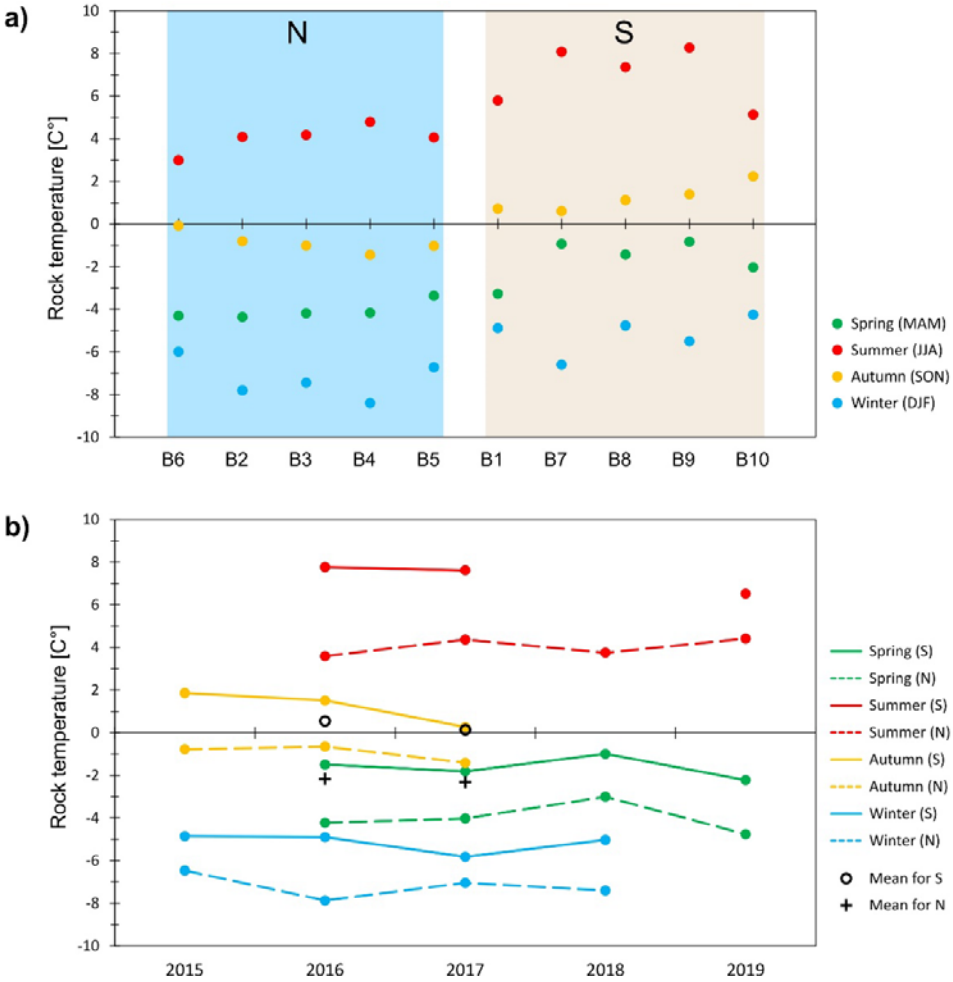

Figure 4.9: Rock temperatures versus slope aspect, season and time between 08/2015 and 08/2019.

(a) The blue box represents rock temperatures measured at the north-face (N) of the Zugspitze summit crest, while the red box refers to the south-face (S). Note that B6 and B10 are sensors installed in 80 cm depth, unlike the remaining sensors in a depth of 10-15 cm. (b) Evolution of seasonal means over the time. Annual means (black crosses and circles) are only displayed for 2016 and 2017, because data of the remaining years were incomplete.

The ERT results from 2014 and 2015 are interpreted as follows (Figure 4.11):

- The shallow rock layer is almost continuously unfrozen on both aspects of the crest. This assumption is confirmed by (i) borehole rock temperatures at the Zugspitze peak which show a 2–4 m thick active layer on the north face (Gallemann et al., 2017), and (ii) thermistor-based rock temperatures measured along the ERT transect at a depth of 10–80 cm below the ground surface. The corresponding thermistors (specially modified iButtons in rods) show that the rock temperatures do not remain below 0 °C throughout the year and are positive at the moment of the ERT surveys (Figure 4.1, Figure 4.8).
- Due to this evidence, the current boundary to permafrost on the north face and at the upper part of the south face was set to a continuous depth of approximately 5 m (black line in Figure 4.11).

- Most near-surface interstitial patches of resistivity > 33 kΩm relate to massive ice visible in the metre-deep karst doline close to the crest line and surficial drying of rock usually limited to the upper decimetre (Hauck and Kneisel, 2008; Sass, 2005).
- On the lower south slope, the unfrozen bedrock becomes thicker with decreasing altitude and can be found down to a depth of 10 m or more indicated by resistivity values < 19 kΩm.
- Other individual patches of low electrical resistivity (< 19 kΩm) refer to major shear zones or to the highly porous talus slope below the northern rock wall filled with air or with unfrozen, saturated and fine material (Hauck and Kneisel, 2008; Supper et al., 2014). Zones of high conductivity can be promoted by precipitation or water from snowmelt which easily infiltrates along unfrozen fine fillings or fractures (Keuschnig et al., 2017).
- The resulting spatial extent of permafrost relates to the core of the crest and rock layers below 5 m at the north face.

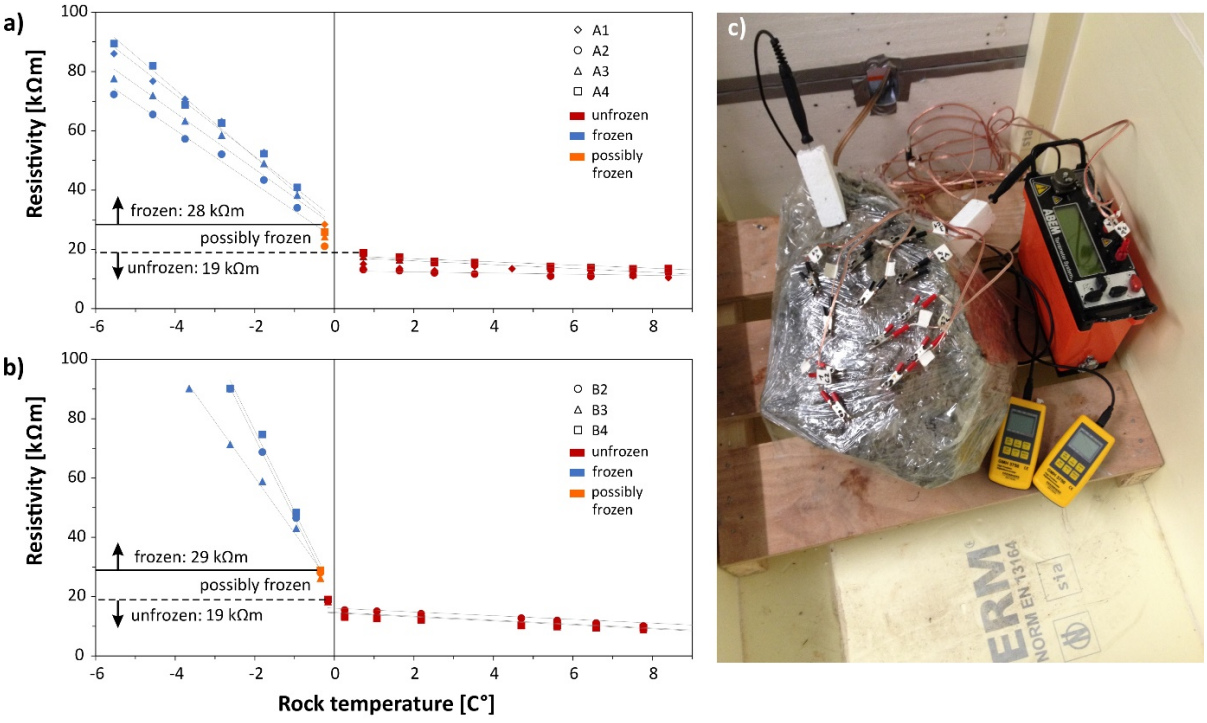

Figure 4.10: Laboratory-tested electrical resistivity of frozen and unfrozen Wetterstein limestone collected at the study site.

(a) and (b) Definition of frozen (blue symbols), unfrozen (red symbols) and possibly frozen (orange symbols) electrical resistivity based on the freezing-trajectories of two rock samples. Measurements were performed along 3 or 4 different Wenner arrays (i.e., A1-A4 or B2-B4) installed parallel to each other. (c) Test set-up in the laboratory cooling box.

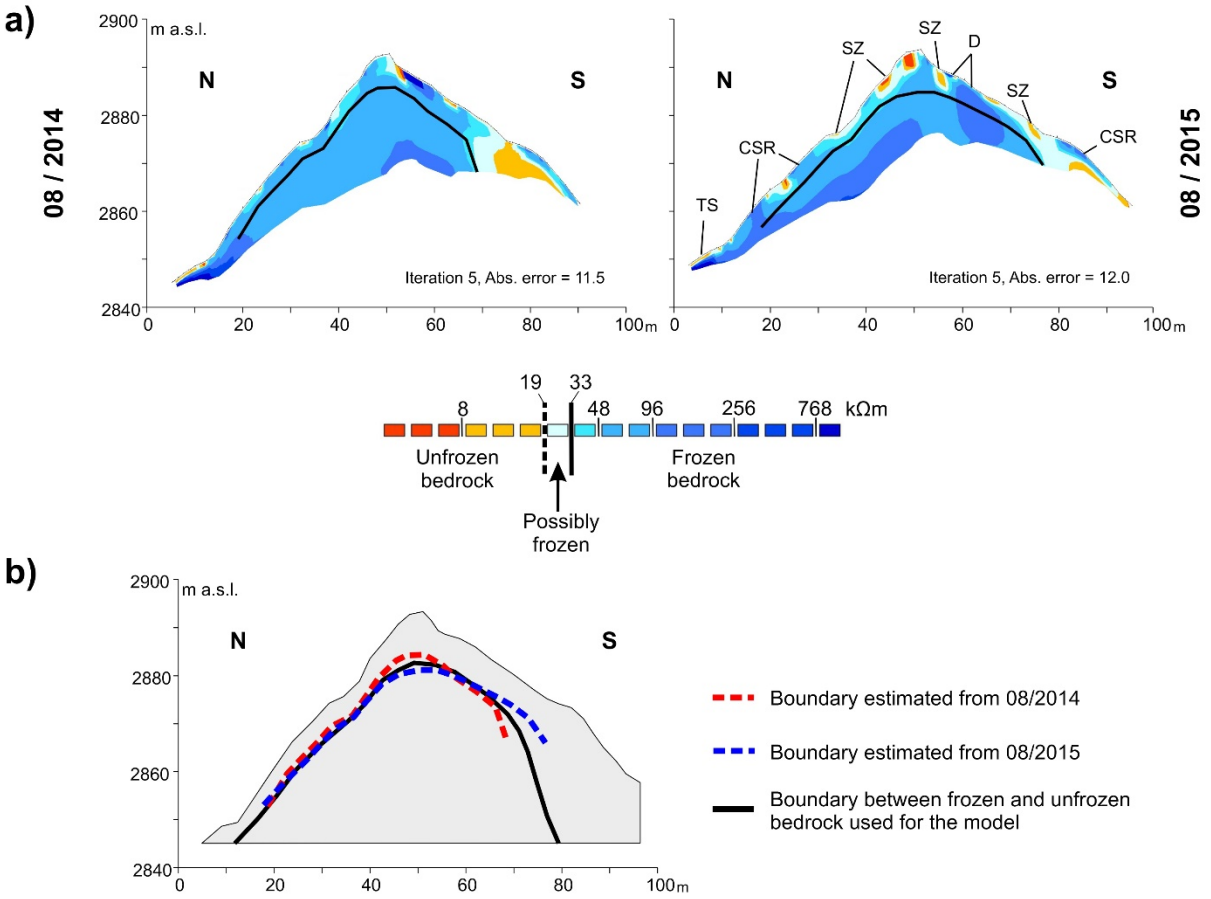

Figure 4.11: Distribution of frozen and unfrozen bedrock in the Zugspitze summit crest derived from two ERT surveys in August 2014 and August 2015.

(a) TS represents the talus slope; CSR stands for compact solid unfrozen rock; SZ corresponds to shear zone; D represents doline. The locations of these features are the same in the tomography of 2014. (b) displays the current spatial extent of bedrock permafrost, which was estimated from the ERT campaigns and used for the numerical model (Figure 6.4).

4.4.2.3. Seismic refraction tomography

The SR inversions of 2014, 2015 and 2016 demonstrate that the core and the lower north-face of the summit crest are affected by possibly frozen and frozen bedrock (blue areas in Figure 4.12, with a P-wave velocity > 3.3 km s^{-1} and > 5.2 km s^{-1} respectively). For the same reason as for the ER (thermistor-based rock temperatures measured at the moment of the surveys are positive, see Section 4.4.2.1), the patches of high P-wave velocity in the near-surface rock layer at the north-slope are attributed to unfrozen bedrock instead of frozen bedrock. The patches of high P-wave velocity are explained by a combination of lower joint frequency (Barton, 2007; Krautblatter and Dräbing, 2014), higher proportion of solid compact rock and a lower amount of porous debris cover (Dräbing, 2016), which were all observed in the field. As a consequence, the boundary to possibly frozen bedrock at the north-face and the crest line was set to a uniform depth of approximately 5 m (dashed lines in Figure 4.12). The low P-wave velocities at

the northern talus slope may be caused by the high porosity of the unfrozen debris cover including air-filled pores (Dräbing, 2016; Hauck and Kneisel, 2008).

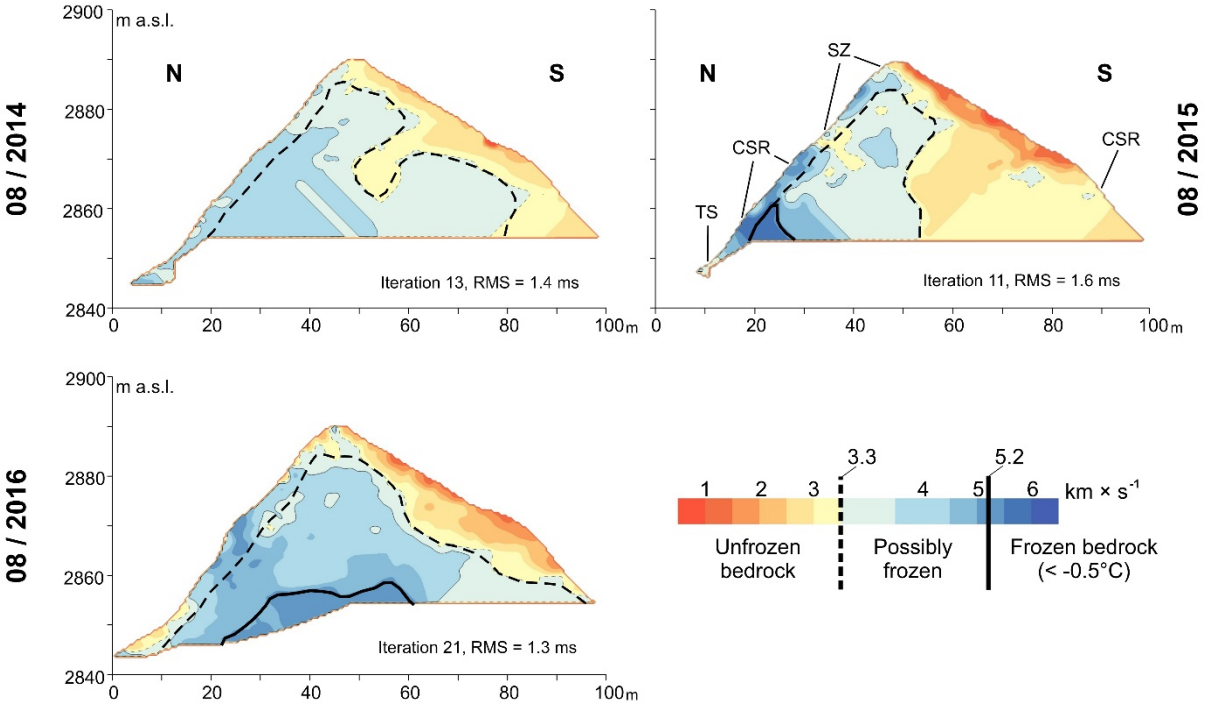

Figure 4.12: Spatial distribution of bedrock permafrost in the Zugspitze summit ridge based on three SRT surveys in August 2014, 2015 and 2016.

The distinction between unfrozen, possibly frozen and frozen bedrock is highlighted by dashed and solid lines. TS = Talus slope. CSR = Compact solid unfrozen rock. SZ = Shear zone. Locations of these features are the same for all tomographies.

4.4.2.4. Synthesis of geophysics

The SRT-derived distribution of possibly frozen rock and frozen rock in the summit crest (Figure 4.12) coincides with the one deduced from the ERT (Figure 4.11). Both techniques indicate (i) a frozen section in the core of the crest and in the rock layers below 5 m at the north-face, and (ii) an unfrozen section at the south-slope becoming thicker with decreasing altitude (down to a depth of 10 m and more). This pattern fits well to the corresponding section in the modelled thermal field of the Zugspitze peak by Nötzli (2008) (Figure 3.2a).

Comparison of the two surveys in 08/2014 and in 08/2015 reveals a variable section of ER-values in the near-surface rock layers, while the ER-values in the deeper rock layers or the core of the crest do not change significantly. This observation may be explained as follows: In 2014, the surficial rock layer and the shear zones were not fully saturated since precipitation was scarce in advance of the survey (5 mm, two days before the survey; Table 4.3). In contrast, a day before the survey in 2015, a high amount of precipitation (12 mm) was measured at the nearby weather station at the Zugspitze peak, probably leading to the saturation of shear zone

fillings which locally lowered the resistivity. Higher air temperatures during the summer months (June to August) of 2015 may have enhanced the effect of lower ER-values in the surficial rock layer. The observed field of differently varying ER-values indicates that the inversions for this specific site are mainly a function of two process regimes acting at different temporal scales: the variable near-surface ER-values are influenced by the evolution of the precipitation some days ahead of the survey, and the seasonal air temperature and evaporation, while the constant ER-values of the core of the crest depend on the long-term evolution of permafrost. This pattern has also been observed at other sites by Krautblatter et al. (2010) or Keuschnig et al. (2017).

The variation in the P-wave velocities over the three surveys is presumably the result of a different short-term rock mass saturation and/or a long-term rock mass temperature (similar to the ERT): Lower mean air temperatures in the summer months of 2014 and 2016 induced higher P-wave velocities than in 2015, while high precipitation in advance of the survey in 2015 may have reduced the corresponding velocities additionally. While for most rock types, a higher saturation leads to higher P-wave velocities, it seems to be the opposite for carbonate rocks (Dräbing, 2016).

Table 4.3: Meteorological data for the summer months (JJA) of 2014, 2015 and 2016 ahead of the ER- and SR-surveys.

The parameters were measured at the nearby weather station "Zugspitze" operated by the German Meteorological Service.

Long-term meteorological influence			Short-term meteorological influence		
Date	Mean of air temperature (C°)	Sum of precipitation (mm)	Date	Mean of air temperature (C°)	Sum of precipitation (mm)
2014			2014		
June	1,1	128,3	Aug 19	1,2	2,1
July	3,2	381,4	Aug 20	-0,4	5,0
August	1,4	173,6	Aug 21	-2,1	0,0
Mean/Sum	1,9	683,3	Mean/Sum	-0,4	7,1
2015			2015		
June	2,1	167,2	Aug 22	2,5	0,0
July	6,5	105,9	Aug 23	3,5	0,0
August	6,0	146,2	Aug 24	4,2	12,0
Mean/Sum	4,9	419,3	Mean/Sum	3,4	12,0
2016			2016		
June	1,4	207,2	Aug 15	5,2	2,0
July	3,9	183,2	Aug 16	4,5	0,6
August	4,0	163,8	Aug 17	3,2	2,1
Mean/Sum	3,1	554,2	Mean/Sum	4,3	4,7

4.5. Conclusion

Investigation of the mechanical, geometrical and thermal characteristics of the Zugspitze summit ridge revealed the following main findings:

- The current extent of permafrost was investigated down to a maximum depth of 20–30 m. Both ERT and SRT show a similar thermal pattern: (i) a frozen section in the core of the crest and in the rock layers below 5 m at the north-face, and (ii) an unfrozen section at the south-slope becoming thicker with decreasing altitude (down to a depth of 10 m and more). NSRT was used to exclude permafrost in the shallow rock layers.
- Fractures and fractured zones in mountain bedrock permafrost usually contain ice to depths of several tens of metres (Deline et al., 2015; Gruber and Haeberli, 2007). Observations of ice-filled dolines and fractures at the study site (Figure 4.2), as well as the identified permafrost body in the deeper rock layers, indicate that fractures at the study site are mostly ice-filled. Annual mean borehole temperatures of the permafrost body at the Zugspitze peak are close below the melting point (Gallemann et al., 2017). Since the measured NSRT at the field site coincide well with the borehole temperatures in a similar depth, the temperatures of the permafrost body at the study site are expected to be in a similar range (i.e., around -1 °C in the centre, not lower than -6 °C at the northern margin).
- The mean absolute crack displacement rate is 2.1 mm y^{-1} between 09/2013–07/2019, without any indication to an acceleration or deceleration. Between October and May, monthly mean deformation rates are 84 % lower than in the remaining summer months.
- Four joint sets and five main shear zones could be identified and characterised. The slope instability was found to be characterised by two main kinematic modes: plane and wedge failure. Though, planar sliding is clearly the dominant failure mechanism. The potentially failing rock mass was estimated to a volume of $2.9 * 10^4$ m^3.
- The rock mass is characterised by a high degree of fracturing. Observed maximum displacements along the upper part of shear zone SZ1 lie in the range of decimetres and point to a high joint persistence. The shear zones SZ1–3 have trace lengths in the range of several decametres. The shear plane SZ1 is assessed to run in a maximum depth of 10–15 m, and reveals ice-filled fractures at one location (Figure 4.2e, Figure 4.2f).

These findings caused us to assume that the rock slope can be close to or at the advanced stage of destabilisation, in which most of the cohesive intact rock bridges have supposedly been destroyed (Krautblatter et al., 2013). The remaining shear resistance is controlled by the friction along rock-rock-contacts, the creep of ice fillings, and the shear strength of rock-ice-interfaces and ice fillings. The latter becomes relevant, since SZ1 runs in depths not greater than 20 m

(Section 2.2, Figure 2.1). A high joint surface roughness and filling with fine cohesive material in some places along the main shear planes may additionally enhance the shear resistance.

All in all, the rock instability at the Zugspitze summit ridge acts as a real-world exemplification of the simulated fracturing along rock-ice interfaces in the laboratory, and the simulation of permafrost rock slope destabilisation in a numerical discontinuum model. Thus, it is a benchmark analogue to constrain mechanical and thermal conditions for the laboratory and modelling work:

The study site is characterised by bedrock permafrost close to thawing. The rock mass is possibly close to the accelerated stage of rock slope destabilisation. This stage is controlled by (rock-)ice-mechanics along ice-filled joints in frozen sections, and by rock-mechanics along rough clean joints in unfrozen sections. It is certainly interesting and relevant, how far the filling of joints could affect the overall rock slope stability in the given setting, but this was beyond the scope of this thesis.

5. Laboratory strength and deformability of frozen/unfrozen intact rock/rock joints

Laboratory testing was performed on a broad spectrum of frozen and unfrozen intact rock and rock joint properties. This should result in a better understanding of the warming or thawing effect on the mechanical strength and deformability at the sample scale, and provide temperature-dependent rock-ice-mechanical input parameters for the numerical model (Section 6). A focus was on the analysis of the shear strength of ice fillings and rock-ice-contacts along ice-filled joints (Sections 5.2–5.3), which has been hardly studied so far. More experiments on rock joint properties were conducted in terms of tilting and Schmidt hammer tests (Section 5.4), while uniaxial compressive strength, indirect tensile strength and ultrasonic tests were performed on the intact rock (Section 5.1).

5.1. Intact rock

The following frozen and unfrozen intact rock properties of the field site material were tested in the laboratory: the intact rock uniaxial compressive and tensile strength (σ_c, σ_t), the rock mass density ρ and porosity ϕ, the Poisson ratio υ and the dilatational wave velocity V_D. The parameters ρ, υ and V_D were measured for calculating the elastic moduli of the intact rock E (Young's modulus), the bulk modulus K and the shear modulus G (Section 6.3.1.3). These were later used to determine the joint stiffness parameters k_n and k_s. The lab results of υ, and additional lab tests on σ_c were used to quantify elastic moduli and σ_{tm} of the rock mass. V_D and υ of the intact rock were derived by ultrasonic tests.

5.1.1. Preparation of the rock samples

The rock samples for the laboratory tests were cored from Wetterstein limestone blocks with a mean side length of 0.4 ± 0.1 m that were picked from the study site and the lower Zugspitzplatt (2590 m a.s.l.; Figure 6.1). Uniaxial compression and Brazil tests were conducted in accordance with the recommendations of the Commission on Rock Testing of the German Geotechnical Society (Lepique, 2008; Mutschler, 2004). Ultrasonic tests were performed in accordance with the norm on Non-destructive testing of the European Committee for Standardization (DIN EN ISO 16810, 2014). The rock cores of 51 ± 0.1 mm diameter were cut with a diamond saw into 103 ± 1 mm thick cylinders for the uniaxial compression and ultrasonic tests and into 25 ± 1 mm thick discs for the Brazil tests (Figure 5.1a, Figure 5.1d). The high structural isotropy of the Wetterstein limestone allowed us to ignore any specific drilling orientation dependent on bedding or foliation.

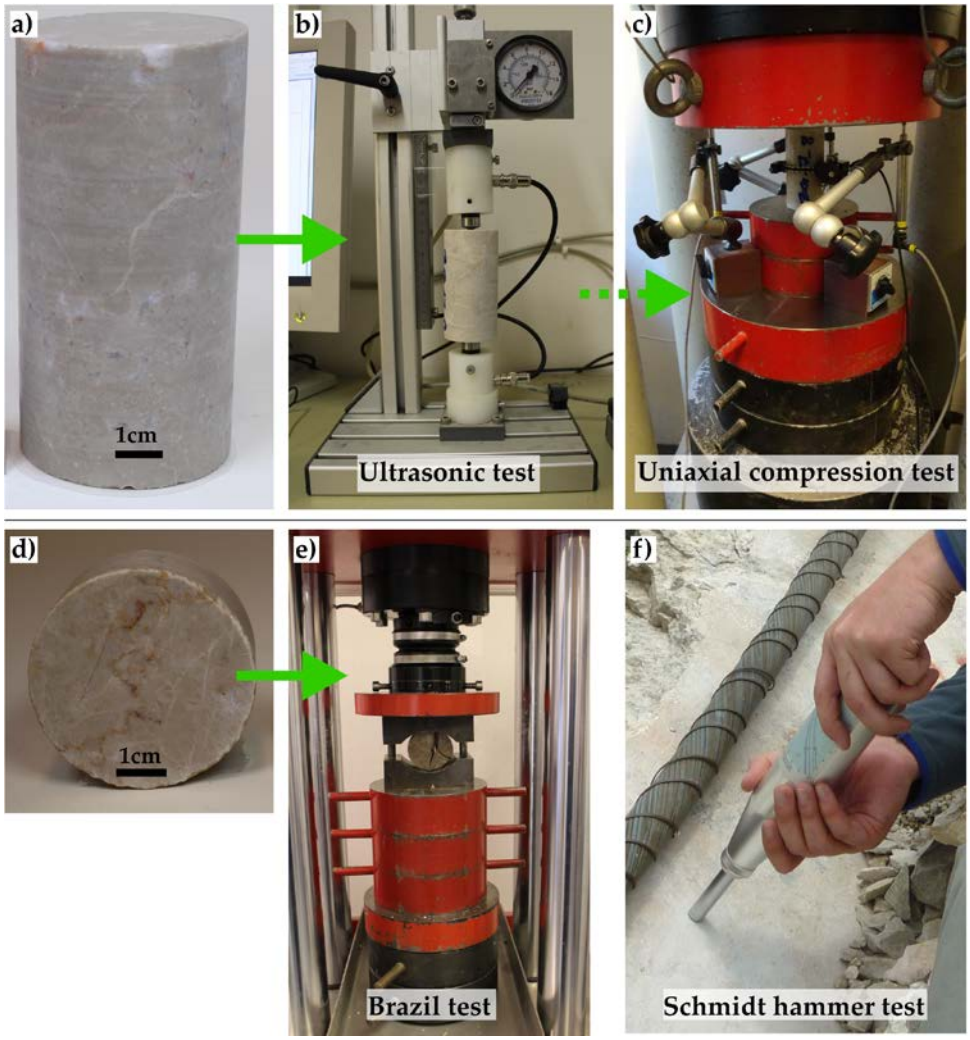

Figure 5.1: Rock samples and typical set ups of the laboratory experiments.

(a) and (d) Cored and prepared rock cylinder and disc for the mechanical experiments. Typical set-ups with unfrozen samples are given for (b) ultrasonic tests, (c) uniaxial compression tests, and (e) Brazil tests. The green arrows show which type of rock sample was used for the various tests. Photos (a–e) were taken and provided by Saskia Eppinger. (f) Typical Schmidt hammer test in the field. The same measuring device and testing procedure was applied for the laboratory experiments on single rock samples which are presented in this thesis.

We assume the rock mass of a real-world rock slope to be close to a saturated state. Therefore, we tested the rock samples in a frozen saturated and unfrozen saturated condition. For this, they were kept in a water bath for at least 48 h (DIN EN ISO 13755, 2002). The samples were regarded as nearly saturated when successive mass determinations yielded values varying less than 0.1 %. Frozen conditions were achieved by freezing saturated rock cores at -28 °C in a cooling box for at least 48 h.

A natural rock slope is expected to be nearly water-saturated for the following reasons: (i) While near surface rock saturation fluctuates highly due to meteorological influences like precipitation, wind or insulation, the rock moisture in depths greater than 15 cm remains unchanged; here, it ranges between approximately 75 and 90 % dependent on the rock type and its porosity (Rode et al., 2016; Sass, 2005). (ii) The successful application of ER surveying in permafrost bedrock in the presented study (Section 4.4.2.2) and in many others confirm that

the investigated rock slopes are saturated, since this technique only works well in saturated rock: (a) In rocks with a high degree of water saturation, electric current can be propagated due to electrolytic conduction. The DC conductivity of porous or fractured subsurface matter highly depends on saturation of the pore space and conductivity of the pore fluid (Supper et al., 2014; Telford et al., 1990). (b) The detected large ranges in electrical resistivity indicate a high degree of water saturation, since only water-saturated rocks can show a significant difference in conductivity/electrical resistivity when switching from the unfrozen to the frozen state, or vice versa (e.g. Mellor, 1973). Accordingly, water-saturated rock samples are recommended to be used for the laboratory calibration of the electrical resistivity of frozen and unfrozen rock for ERT in rock walls (Krautblatter et al., 2010).

5.1.2. Test set-ups

As the testing instruments were not located in a cooled room, the frozen rock samples warmed during the tests. However, for determination of frozen mechanical properties, the rock specimens had to remain frozen during the whole experiments. Thus, the rock discs during Brazil tests were isolated with a polystyrene box which did not affect the progress of the tests (Figure 5.2d). Isolation of the rock cylinders could not be realised as the box would prevent the measurement of axial and diametric strain during uniaxial compression and the measurement of dilatational waves during ultrasonic testing.

Hence, we additionally simulated a series of pretests to carefully observe the warming behaviour of dummy rock samples during typical uniaxial compression and Brazilian tests. The warming of rock cylinders during ultrasonic testing was assumed to behave in the same way as in uniaxial compression. As a result, the pretests of the latter were taken as representative for warming during ultrasonic tests. Warming was monitored by Pt100 temperature sensors (Greisinger GMH3750, with a 0.03 °C precision) inserted in the centre and close to the end of the rock sample (Figure 5.2b and Figure 5.2d). A pretest consisted in fitting the dummy sample into the apparatus and monitor the progress of warming inside the rock specimens until they were thawed. A negligible load was applied to the samples to prevent the destruction of the thermistors or a potential weakening of the sample due to the drilled holes.

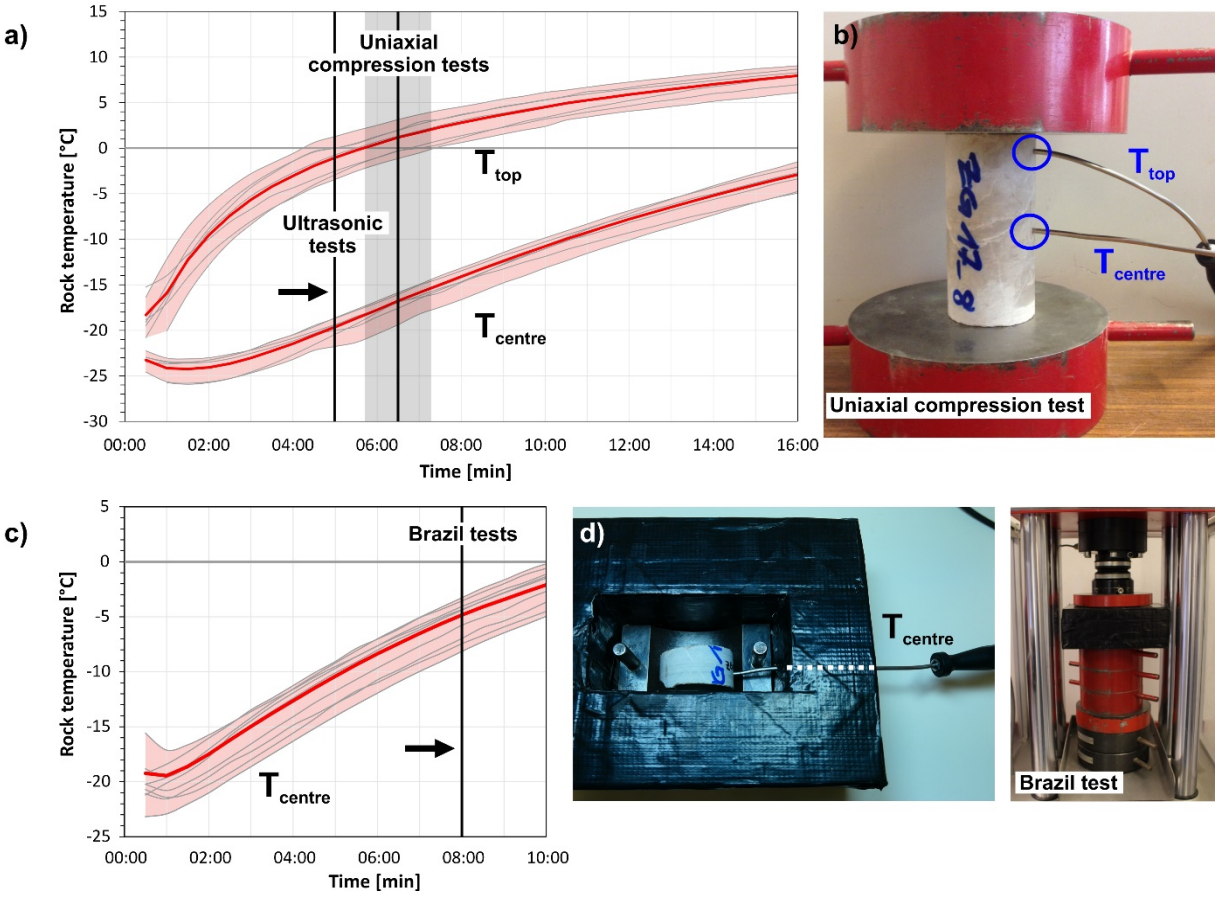

Figure 5.2: Warming pattern for frozen dummy rock samples during simulated uniaxial compression and Brazil pretests.

(a) For rock cylinders with two thermistors during simulated uniaxial compression testing. (b) Rock cylinder mounted between loading plates that are used in a typical uniaxial compression test. (c) Warming curves for frozen dummy rock discs with one central thermistor during simulated Brazil tests. (d) Isolation of a rock disc during pretests with temperature logging (left) and a typical Brazil test (right). Black lines = Maximum duration of mechanical tests. Black line with grey area = Mean duration of compression tests with standard deviation. Red thick line = Mean rock temperature during pretests. Red area = Range of variation of warming curves during pretests.

5.1.3. Testing conditions

Overall, we performed 28 uniaxial compression tests (14 unfrozen, 14 frozen), 60 Brazil tests (30 unfrozen, 30 frozen), 60 ultrasonic tests (30 unfrozen, 30 frozen) and 90 density tests (60 with the discs and 30 with the cylinders):

- Uniaxial compression tests were performed to provide data on the uniaxial compressive stress at failure. Tests were run with a ToniNorm compression testing machine (DIN EN ISO 7500-1, 2018; Figure 5.1c). A constant strain of 0.6 mm / (m ∗ min) was applied to the samples provoking failure within 8 min.
- Brazil tests were conducted to collect data on the indirect tensile stress at failure which is the tensile stress normal to the uniaxially loaded areas of the specimen. A ToniNorm

tension testing machine according to the DIN EN ISO 7500-1 (2018) was used to apply a load at a constant rate of 70 N/s, leading to failure within 6 min (Figure 5.1e).

- Ultrasonic tests were run to determine the velocity of the dilatational wave propagating through the specimen (DIN EN ISO 16810, 2014). The apparatus consisted of a signal generator USG40, a transmitter type UPG 250, a receiver type UPE and a preamplifier VV41 by Geotron Electronics. The rock samples were fixed between the piezoelectric transducer pair at the centres of the flat contact surfaces (Figure 5.1b). Any water film at the contact surfaces of the rock cylinders was removed before testing with an absorbent cloth. Measurements were run with a frequency of 20 kHz.
- The rock density ρ was defined due to weighing in an immersion bath following the standard procedure of the DIN EN ISO 1097-6 (2005).

The test durations, provided by the black lines in Figure 5.2a and Figure 5.2c, also include the mounting of the samples into the apparatus: uniaxial compression tests had a mean duration of 6.5 ± 0.8 min, while Brazil tests and ultrasonic tests did not exceed 8 and 5 min, respectively. Hereafter, rock temperatures in the centre of the samples lay below -5 °C during Brazil tests, below -15 °C during uniaxial compression tests and below -20 °C during ultrasonic tests. As such, we could guarantee frozen conditions for the Brazil and the ultrasonic tests, while the major central part of the cylinders in the uniaxial compression tests were frozen, too. Unfrozen mechanical properties were studied at room temperature.

5.2. A temperature- and stress-controlled failure criterion for ice-filled permafrost rock joints

The following section constitutes the accepted version of the research article "Mamot, P., Weber, S., Schröder, T. and Krautblatter, M.: A temperature- and stress-controlled failure criterion for ice-filled permafrost rock joints, The Cryosphere, 12, 3333–3353, 2018". The final version of Publication 1 can be downloaded from https://doi.org/10.5194/tc-12-3333-2018. For inclusion in this dissertation, captions and numbers of sections, figures, tables and equations had to be modified.

5.2.1. Abstract

Instability and failure of high mountain rock slopes have significantly increased since the 1990s coincident with climatic warming and are expected to rise further. Most of the observed failures in permafrost-affected rock walls are likely triggered by the mechanical destabilisation of warming bedrock permafrost including ice-filled joints. The failure of ice-filled rock joints has only been observed in a small number of experiments, often using concrete as a rock analogue. Here, we present a systematic study of the brittle shear failure of ice and rock-ice interfaces, simulating the accelerating phase of rock slope failure. For this, we performed 141 shearing experiments with rock-ice-rock "sandwich" samples at constant strain rates (10^{-3} s^{-1}) provoking ice fracturing, under normal stress conditions ranging from 100 to 800 kPa, representing 4–30 m of rock overburden, and at temperatures from -10 to -0.5 °C, typical for recent observed rock slope failures in alpine permafrost. To create close to natural but reproducible conditions, limestone sample surfaces were ground to international rock mechanical standard roughness.

Acoustic emission (AE) was successfully applied to describe the fracturing behaviour, anticipating rock-ice failure as all failures are predated by an AE hit increase with peaks immediately prior to failure. We demonstrate that both, the warming and unloading (i.e. reduced overburden) of ice-filled rock joints lead to a significant drop in shear resistance. With a temperature increase from -10 °C to -0.5 °C, the shear stress at failure reduces by 64–78 % for normal stresses of 100–400 kPa. At a given temperature, the shear resistance of rock-ice interfaces decreases with decreasing normal stress. This can lead to a self-enforced rock slope failure propagation: as soon as a first slab has detached, further slabs become unstable through progressive thermal propagation and possibly even faster by unloading. Here, we introduce a new Mohr-Coulomb failure criterion for ice-filled rock joints that is valid for joint surfaces, which we assume similar for all rock types, and which applies to temperatures from -8 to -0.5 °C and normal stresses from 100 to 400 kPa. It contains temperature-dependent friction and

cohesion, which decrease by 12 % °C^{-1} and 10 % °C^{-1} respectively due to warming and it applies to temperature and stress conditions of more than 90 % of the recently documented accelerating failure phases in permafrost rock walls.

5.2.2. Introduction

Rock slope failures in high mountain areas potentially endanger human lives, settlements and alpine infrastructure. The impact of the climate-induced degradation of mountain permafrost on rock slope destabilisation has been inferred from numerous studies in the last 2 decades (Fischer et al., 2006; Gruber et al., 2004a; Gruber and Haeberli, 2007; Ravanel and Deline, 2015). The number of failure events has increased since the 1990s coincident with climatic warming; failures influenced by permafrost degradation are expected to respond to a warming climate by more frequent events (Gobiet et al., 2014; Huggel et al., 2012a; Ravanel and Deline, 2011). The majority of failures in permafrost-affected rock frequently expose ice-filled joints as potential shear and detachment planes (Dramis et al., 1995; Gruber and Haeberli, 2007; Ravanel et al., 2010), as for example, the recent 3–4 $*$ 10^6 m^3 rock slope failure at Pizzo Cengalo, Graubünden, Switzerland, on 23 August 2017 (Baer et al., 2017; Beniston et al., 2018; Marcia Phillips, personal communication, 2018). Fractures and fractured zones in mountain bedrock permafrost usually contain ice to depths of several tens of metres (Deline et al., 2015; Gruber and Haeberli, 2007). Ice fillings can contribute to systematically higher shear strengths due to rock-ice-interlocking and adhesion and thus increase rock slope stability, especially when the ice is at a low temperature. This bonding of ice-filled joints is reduced or even lost as the temperature increases (Davies et al., 2001; Gruber and Haeberli, 2007).

Rock joints that are located within bedrock permafrost (ground that remains permanently frozen for at least 2 consecutive years; Harris et al., 1988) are referred to as "permafrost rock joints" in this paper. Permafrost conditions are below the maximum thaw depth, which typically ranges between 2 and 8 m in alpine environments (Böckli et al., 2011; Delaloye et al., 2016), and apply to ice-filled rock fractures, rock pores and microfractures (Gruber and Haeberli, 2007). In this paper, both "joints" and "fractures" substitute the more general term "rock discontinuities".

To anticipate failure in a warming climate, we need to improve the understanding of how rock-ice mechanical components control rock slope destabilisation and failure between -10 and 0 °C. Generally, warming of permafrost in rock slopes affects the shear stress along sliding planes in terms of (i) fracture toughness of rock bridges, (ii) friction of rock-rock contacts, (iii) ductile creep behaviour of ice and (iv) brittle failure of ice infillings (Krautblatter et al., 2013). Whereas the mechanics of frozen rock (Glamheden and Lindblom, 2002; Kodama et al., 2013; Mellor, 1973), the mechanics of frozen rock joints without fillings (Dwivedi et al., 2000; Krautblatter et al., 2013), and the ductile temperature- and stress-dependent creep of ice and ice-rich

soils (Arenson and Springman, 2005a; Sanderson, 1988; Yamamoto and Springman, 2014) have been investigated in a number of studies, the brittle failure of ice infillings is still poorly understood. We hypothesise that the brittle failure of ice infillings (i.e. either along rock-ice interfaces or inside the ice) is a common final failure mechanism, which is documented by numerous exposed ice-filled joint surfaces subsequent to failure. It is mechanically dependent on fast deformations (i.e. strain rates) and thus is likely to control the final failure of many recent events. This study aims at developing the first comprehensive temperature- and stress-dependent brittle failure criterion for ice-filled joints based on shear tests on rock-ice-rock samples.

Fracturing of ice and rock-ice contacts mainly occur below a rock overburden ≤ 20 m and become less important at greater depths, where rock mechanical components take over at greater stresses (Krautblatter et al., 2013). Here, higher confinement suppresses brittle failure and may favour creep deformation of ice (Renshaw and Schulson, 2001; Sanderson, 1988). Shear tests on concrete-ice and concrete-ice-concrete "sandwich" samples under constant stress show that fracturing along rock-ice interfaces is the dominant failure process that occurs at a simulated rock overburden of 5–25 m, i.e. 135–630 kPa; constant strain experiments show that with rising normal stress levels (from 207 to 562 kPa, i.e. approximately 8–21 m of rock overburden), fracturing along rock-ice interfaces is replaced by creep deformation of the ice (Günzel, 2008; Krautblatter et al., 2013). In addition, higher normal stresses increasingly cause ice fillings to be squeezed away from "abutments" and preferentially lead to stress concentrations along rock-rock contacts (Krautblatter et al., 2013). Various inventories of rock slope failures in the Mont Blanc Massif show that virtually all of the failures displayed a plate-like shape with an area ranging from 25 m^2 to 33.800 m^2 (average of 1.570 m^2) and scar depths of 1–20 m (average of 4 m) (Ravanel et al., 2010; Ravanel and Deline, 2008; Ravanel and Deline, 2011). Most of the events have been linked to the degradation of bedrock permafrost and ice-filled joints. A total of 97 % of them had volumes ≤ $3 * 10^4$ m^3, which correspond to the relevant size of dominantly ice-fracturing-controlled rock slope failures (considering the approximately ≤ 20 m of rock overburden and the average area of the reported failure planes). A total of 94 % of the failures had volumes ≤ $2.3 * 10^4$ m^3, which also refer to mainly ice-fracturing-controlled rock slope failures (considering the tested 15 m of rock overburden in this study and the average area of the documented failures), as will be shown in this paper. However, even larger volumes will be partially influenced by rock-ice fracturing phenomena.

Warming of permafrost in rock slopes reduces the shear resistance along rock joints in a chronological order by (i) reducing the fracture toughness of cohesive rock bridges, (ii) by lowering friction along rock-rock contacts, (iii) by altering the creep of ice infillings and (iv) finally by reducing the fracture toughness of the ice itself and of rock-ice contacts (Krautblatter et al.,

2013). Cyclic thermal expansion or contraction in the shallow bedrock occurs due to warming or cooling as a result of daily or seasonal variations in temperature. Variations in high frequency and magnitude can cause thermal gradients in the rock, which leads to alterations in the stress field. This can induce thermal fatigue, which, over long timescales, reduces the shear resistance along weakened discontinuities (Dräbing et al., 2017a; Gischig et al., 2011c; Hall and Thorn, 2014; Jia et al., 2015; Weber et al., 2017).

When ice becomes mechanically stressed, it can deform by (i) elastic or ductile creep without fracture or by (ii) brittle or ductile-brittle fracture including crack formation and propagation (Sanderson, 1988). The deformation and failure behaviour of ice changes from ductile creep to brittle fracture with strain rates > 10^{-4} and 10^{-3} s^{-1} (Arenson and Springman, 2005a; Fellin, 2013; Sanderson, 1988; Schulson and Duval, 2009). Thus, the accelerating final failure along predefined slip surfaces is increasingly likely to be governed by the brittle failure of ice (Krautblatter et al., 2013). When the ice ceases to be able to bear a certain applied load, it fails and then brittle fracture occurs. In this case, the applied load at fracture can be described as "strength" (Sanderson, 1988), an analogue to the strength at fracture in rock mechanics. In this paper, we use the term strength when talking about ice-mechanical behaviour as we simulate accelerating final rock slope failure conditions with strain rates that provoke ice fracturing (10^{-3} s^{-1}).

The temperature dependence of mechanical properties of ice has been studied in numerous publications up to now (Arakawa and Maeno, 1997; Barnes et al., 1971; Fish and Zaretzky, 1997; Gagnon and Gammon, 1995; Jones and Glen, 1968; Sanderson, 1988; Schulson and Duval, 2009). The unconfined compressive strength of polycrystalline ice decreases by 82 % (from approximately 17 to approximately 3 MPa) with increasing temperature from -50 to 0 °C (at strain rates of 10^{-3} and 10^{-1} s^{-1}; Schulson and Duval, 2009). A warming of artificial ice from -10 to 0 °C results in a decrease in the unconfined compressive strength by 50 % (from ca. 4 to ca. 2 MPa) and in tensile strength by 13.3 % (from 1.5 to 1.3 MPa) (Butkovich, 1954b). The behaviour of sediment-ice mixtures has been investigated in detail by Arenson and Springman (2005a). According to them, the strain rates of frozen soil increase with rising temperature and higher volumetric ice content. The peak shear strength of ice-rich soil (ice content > 60 %) decreases with increasing temperature from -5 to -1 °C.

Laboratory tests on the shear strength of ice-filled rock joints reveal a decreasing shear stress at failure with decreasing normal stress and increasing temperature towards 0 °C (Davies et al., 2000; Davies et al., 2001; Günzel, 2008; Krautblatter et al., 2013). These studies rely on approximately 40 constant stress and 50 constant strain shear experiments at temperatures from -5 to 0 °C, in which the joints were composed of concrete and ice (Davies et al., 2000; Günzel, 2008). However, the applied strain rates in constant strain tests were too low to enforce fracturing of ice. Constant stress tests delivered significantly higher strain rates (Günzel, 2008;

Krautblatter et al., 2013), but they are difficult to interpret in terms of fracturing initiation due to the rapidly changing strain rate conditions. In these tests, the shear strength of laboratory ice-filled rock joints consisting of concrete and ice decreases by 144 kPa $°C^{-1}$ between -0.5 and -5 °C (Krautblatter et al., 2013). Experiments by Davies et al. (2000) demonstrate a reduction in shear strength by 16 or 18 % $°C^{-1}$ (i.e. 124 or 69 kPa $°C^{-1}$ respectively depending on the normal stress level) due to warming from -5 to -0.5 °C. A similar relation is shown for sandwich samples composed of ice and polished steel plates whose shear strength decreases by 10 % $°C^{-1}$ (i.e. 113 kPa $°C^{-1}$) with increasing temperature from -10 to -2 °C (Jellinek, 1959).

We measured acoustic emission (AE) in this study to monitor the strength reduction due to creep or brittle failure of ice and rock-ice contacts and to document the progressive evolution of damage. AE refers to the generation of transient elastic waves generated by a sudden release of energy in a material (Hardy, 2003). AE events can indicate damage increase, i.e. microcrack generation and coalescence, initiation and propagation of fractures or shearing and failure along fractures (Cox and Meredith, 1993; Scholz, 1968). AE technology has been used extensively on rock samples in the laboratory (Lockner, 1993; Nechad et al., 2005; Yamamoto and Springman, 2014). Scaling properties of fracturing dynamics in the domains of size, space and time have usually been observed during mechanical loading (Alava et al., 2006). In the time domain, the seismic events induced by damage processes display a power-law distribution

Equation 5.1:

$$N(s) \sim s^{-b}$$

where N is the probability distribution function of the event size estimation s (e.g. the maximum amplitude of the AE signal or its energy) and b is a constant (Amitrano et al., 2012). The exponent b, originally defined in seismology, describes the slope of the magnitude distribution and provides information on the states of fractures (Scholz, 1968). Larger b exponents indicate the more predominant occurrence of microscopic fractures, while smaller b exponents indicate the occurrence of macro-fractures. An improved b exponent approach, defining the number of AEs by either accumulation from the starting data or per time unit, enables application in the acoustic (Shiotani et al., 1994) with an appropriate number of AE data between 50 and 100 (Shiotani et al., 2001).

In this study, we performed 141 shear tests, using limestone-ice-limestone samples with realistic ISRM (International Society for Rock Mechanics and Rock Engineering) rock surface roughness and predefined strain rates provoking fracturing. The onset of fracturing was controlled using the AE technique. To simulate the real-world fracturing of ice and rock-ice con-

tacts along discontinuities in alpine permafrost rock slopes, our tests were performed in a temperature-controlled, cooled laboratory shear box with samples collected in the field. Our experiments focus on the impact of temperature and normal stress on the fracturing behaviour. Temperatures between -10 and -0.5 °C were tested to represent recently observed daily and annual mean temperatures of mountain bedrock permafrost (Böckli et al., 2011; Delaloye et al., 2016). Normal stresses of 100, 200 and 400 kPa (corresponding to rock overburdens of approximately 4, 8 and 15 m or more) were chosen to reconstruct relevant stress conditions for ice- and rock-ice fracturing processes in permafrost rock joints mostly below the annual maximum thaw depth. Additional tests at 800 kPa (i.e. 30 m rock overburden) were performed to study a potential stress-dependent transition from brittle fracture to creep at stress levels above 400 kPa.

This paper addresses the following questions:

1) How does the shear strength of ice-filled rock joints respond to permafrost warming (-10° C to -0.5° C) and sudden changes in rock/ice overburden (i.e. normal stress)?
2) Can we derive a comprehensive stress- and temperature-dependent failure criterion for ice-filled rock joints?
3) Which real-world conditions of permafrost rock slope destabilisation can be simulated by the new failure criterion?
4) Can AE be applied to decipher precursors of breaking ice and rock-ice interfaces within fractures?

5.2.3. Methodology

5.2.3.1. Real-world setting to constrain laboratory tests

The design of the presented laboratory test set-up is inspired by a benchmark example of shallow, ice-supported rock instability prior to failure exemplified by an approximately 10^4 m^3 large rockslide at the summit crest line (2885 m a.s.l.) of Germany´s highest peak, the Zugspitze (2962 m a.s.l.; Figure 5.3). Since 2007, the rock mass creeps slowly at an average of 3.75 mm yr^{-1}. From July to October it moves more than 5 times faster than in the remaining months.

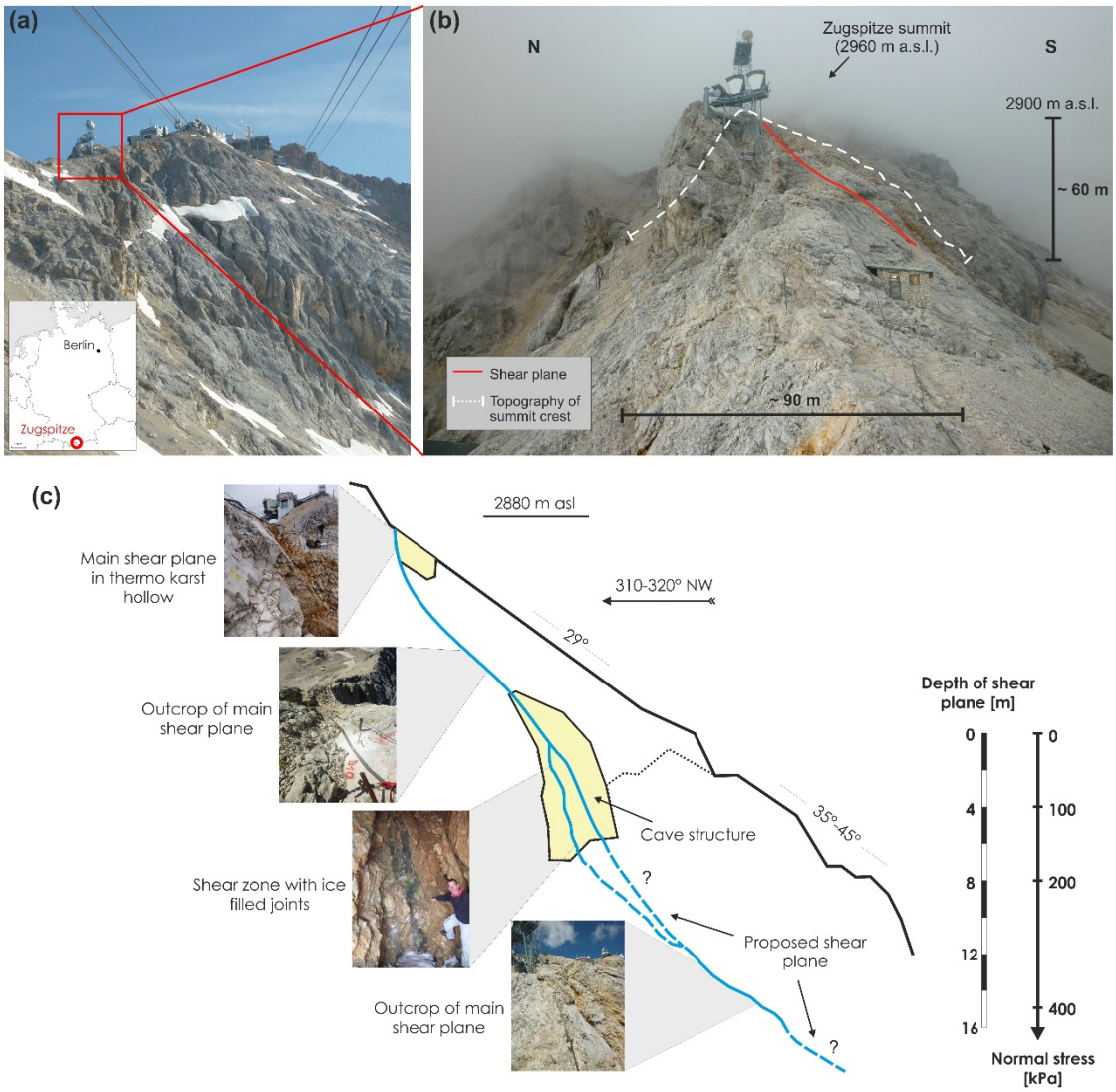

Figure 5.3: Location of the rockslide and characteristics of the main shear plane.

(a) The Zugspitze summit area with Germany's highest peak (2962 m a.s.l.). (b) Profile view of the Zugspitze summit crest with dimensions of the rockslide. The supposed shear plane is indicated by the red line. (c) Mechanical situation and geometry of the ice-supported rockslide that is used as a real-world exemplification of the simulated temperature and stress-controlled fracturing along rock-ice interfaces in the laboratory.

The ice-supported rockslide acts as a real-world exemplification of the simulated temperature and stress-controlled fracturing along rock-ice interfaces in our laboratory, and as such, it is a benchmark analogue to constrain temperature and stress conditions for the performed tests.

(i) The depth of the main shear plane is assessed to a maximum of 10–15 m due to field mapping. The corresponding normal stresses on this shear plane (mostly ≤ 400 kPa) lie within the range of the tested stress levels (Figure 5.3c).

(ii) The occurrence of permafrost is confirmed by permanent ice-filled caves and fractures along the main shear zone (Figure 5.3c).

(iii) The Zugspitze summit area is located at the lower permafrost extension limit. Current borehole temperatures at the peak of the Zugspitze average -1.3 °C within the permafrost core area (approximately 24 m away from the south face and 21 m away from

the north face) and approach minima of -6 °C at the margins (ca. 5 m away from the north face) (Böckli et al., 2011; Gallemann et al., 2017; Krautblatter et al., 2010; Nötzli et al., 2010). These temperatures lie well within the range of the tested temperature levels in this study.

(iv) A climatic warming in the last century and an even stronger temperature increase since the late 1980s can be observed at the Zugspitze, i.e. the mean annual air temperature (MAAT) in 1991–2007 was 0.8–1.1 °C warmer than in the three prior 30-year reference periods between 1901 and 1990 (Gallemann et al., 2017; Krautblatter et al., 2010). An ongoing warming may potentially cause the degradation of permafrost in the summit crest, leading to an accelerated movement in the future and thus to the fracturing of ice and rock-ice contacts, among other processes.

5.2.3.2. Sample preparation

The tested rock samples were collected at the Zugspitze summit crest (Figure 5.3). The rock samples consist of Triassic Wetterstein limestone, which builds up the upper part of the Zugspitze (Jerz and Poschinger, 1995). The limestone is finely grained, dolomised, has a porosity of approximately 4.4 % and shows little heterogeneity in terms of its lithological properties (Krautblatter et al., 2010). Seven pairs of rock cylinders with a diameter of 148 ± 1 mm and a height of 82 ± 3 mm were prepared. Following the ISRM recommendations for standardised tests (Coulson, 1970; Ulusay, 2015), the roughness of the specimen's surfaces was produced using abrasive grinding powder with a grit of 80 grains per inch (FEPA, Federation of European Producers of Abrasives Standard) leading to a roughness amplitude equivalent to the mean diameter of the abrasive grains of 0.185 mm. Consequently, the rock surfaces are reproducible and close to the conditions of fractures in the field. The uniform joint surface roughness prohibits any potential effect on the shear strength results. Rock cylinders were saturated in a water bath under atmospheric pressure for at least 72 h.

The rock-ice-rock sandwich samples were produced by freezing two cylinders of Wetterstein limestone with a gap filled with tap water, using matchsticks as spacers. The samples were subjected to a number of pretests to guarantee uniform conditions. Pretests showed that simultaneous freezing of the interlocking rock surface and the ice surface is necessary to generate a firm contact. The gap was wrapped with tape and transparent film to prevent water draining (Figure 5.4). The 3 ± 1 mm thin ice layer resembles the thin nature of most encountered infillings and provokes fracturing, as thicker ice infill produces more creep camouflaging the fracturing behaviour. Our experiments (including the pretests) have shown that unavoidable thickness variations of ± 1 mm yield no significant differences in fracture toughness (Figure 5.14a). In other shear tests with constant stress, the shear strength of sandwich samples with a

1 mm thick ice layer also did not differ significantly from the results of concrete-ice specimens representing a 25 mm thick ice infilling (Günzel, 2008). All samples were frozen for at least 14 h at -14 °C to ensure that the ice layer was entirely frozen and firmly attached to the rock surfaces. During the freezing process, the shear planes and the gap for the ice layer were oriented vertically to make sure that no air bubbles could form in the ice. A hole was drilled into the lower rock cylinder (Figure 5.4b) to monitor the rock temperature during the shear test with a 0.03 °C precision Pt100 sensor (Greisinger GMH 3750).

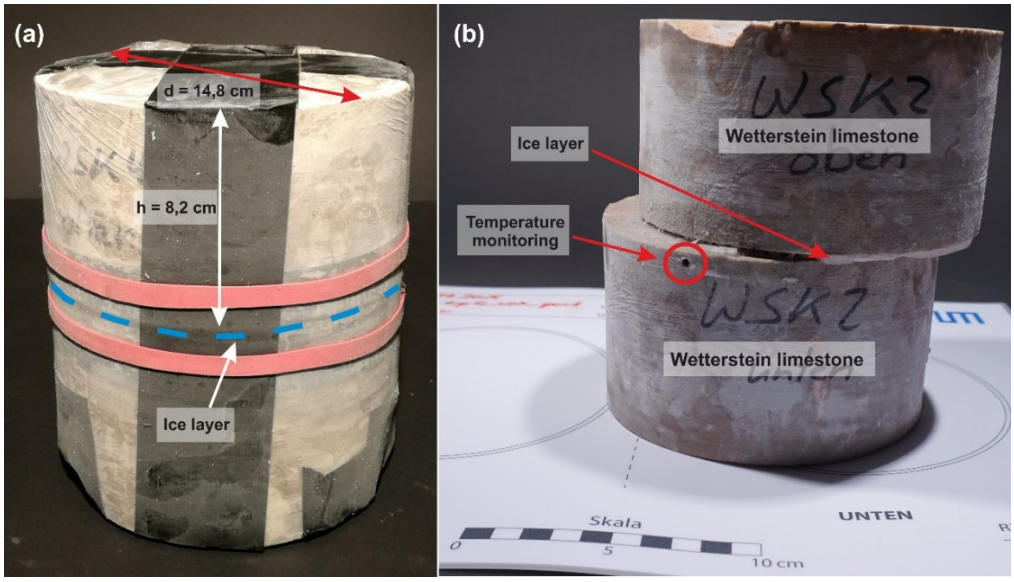

Figure 5.4: Sandwich sample before (a) and after (b) shearing.

5.2.3.3. Experimental set-up

After freezing, the sandwich specimens were fixed within the upper and lower ring of the RDS-100 direct rock shear machine from GCTS (Geotechnical Consulting & Testing Systems; Figure 5.5a). The ice layer position then corresponded to the open gap between the upper and the lower shear ring (Figure 5.5b). Consequently, failure within the ice layer or along the ice-rock interface is provoked. During the whole test series, we did not change the constellation of specimen pairs and always placed them identically oriented into the shear frame to prevent effects of variations in the surfaces of the shear planes.

The machine is embedded in an isolated box in which temperature can be held constantly at a specified level between -10 °C and -0.5 °C by a custom-designed FRYKA cooling device. The cooling operation is controlled by a Pt100 sensor placed inside the rock sample (Figure 5.5b). The experiments were performed at temperatures of -0.5, -1, -2, -3, -4, -5, -6, -8 and -10 °C. Ventilation prevented thermal layering inside the cooling box. An AE monitoring system with two sensors was fixed at the top of the upper specimen ring (Figure 5.5b) to record the elastic

waves generated during fracturing events. Due to the external hydraulic control, AE can be better recorded than in servo-controlled devices.

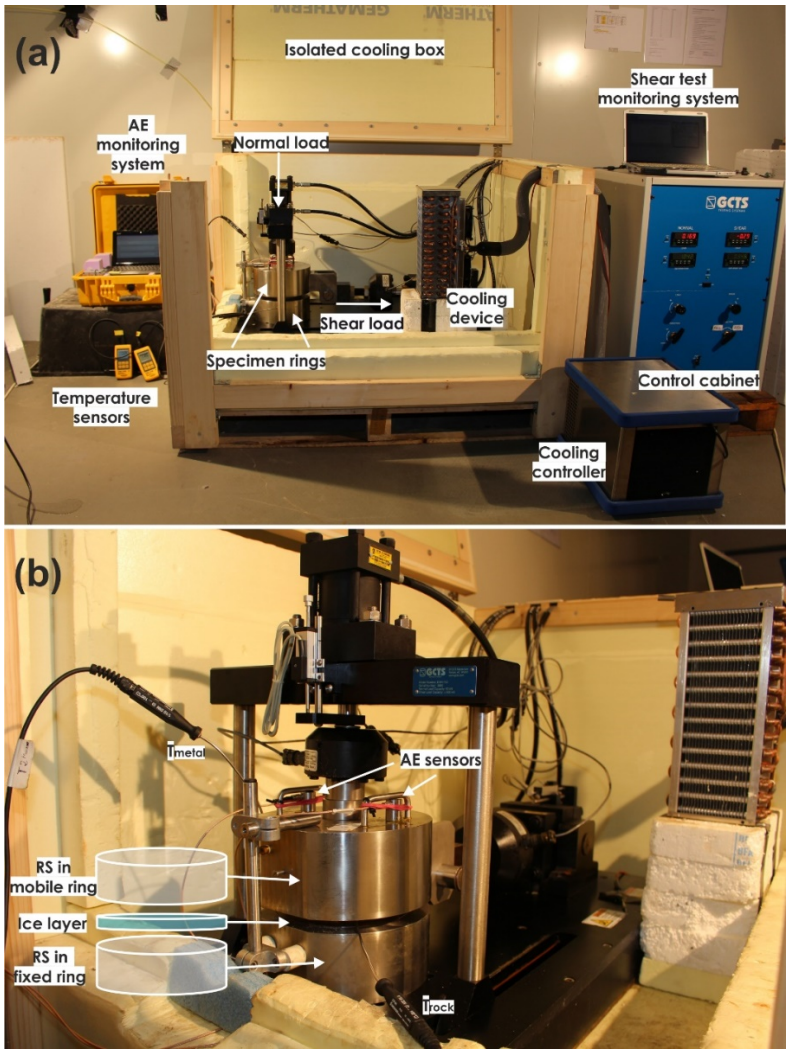

Figure 5.5: Experimental set-up showing the laboratory shear machine, acoustic emission monitoring system, the cooling device and the cooling box.

RS: rock sample. T: Rock temperature sensor.

The hydraulically driven normal load and shear velocity were adjusted by the rock shear machine and were held at constant levels during the shear tests. Normal stress levels of 100, 200 and 400 kPa were applied for the whole temperature range. Tests at 800 kPa were performed to study a potential gradual stress-dependent transition from brittle fracture to creep. This transition is observed with increasing confining pressure in triaxial tests (Sanderson, 1988) and with increasing normal stress in uniaxial shear tests (Günzel, 2008) and is expected under the similarly tested normal stress conditions above 400 kPa. High rock overburden (i.e. 800 kPa) was simulated for temperatures from -4 to -0.5 °C, representing most of the recently measured annual mean temperatures of alpine and Arctic bedrock permafrost (Delaloye et al., 2016; Gallemann et al., 2017; Harris et al., 2003). In steep rock faces shear planes are inclined rather than horizontal. With increasing inclination of a shear plane at a certain depth, the normal stress

acting on it will decrease and downhill forces will increase. Correspondingly, a shear plane with a normal stress of 200 kPa but a dip > 0 ° will also exist in depths greater than 4 m. The mean horizontal displacement rate was 0.7 ± 0.1 mm min^{-1}, corresponding to a mean strain rate of 4.8 ± 1.4 ∗ 10^{-3} s^{-1}. The minimum test strain rate was 1.58 ∗ 10^{-3} s^{-1}, which combines the minimum accounted deformation speed (0.005 mm s^{-1}) and the maximum ice layer thickness of 4 mm. The shear rate was hereby calculated as the shear velocity (mm s^{-1}) divided by the height of the ice layer (mm). This strain rate guaranteed the dominant deformation mode to be ice fracturing instead of creep, as 10^{-3} s^{-1} is the strain rate threshold for ice fracturing (Arenson and Springman, 2005a; Sanderson, 1988). As the shear and compressive strength of pure and dirty ice increases with the strain rate (Arenson et al., 2007; Sanderson, 1988; Schulson and Duval, 2009; Yasufuku et al., 2003), variations in the shear rate were kept as low as possible (with ± 0.1 mm min^{-1}) and had no measurable influence on the shear strength at failure (Figure 5.14b). These conditions were applied to all tested stress and temperature conditions.

During the shear tests, normal load, shear load, normal deformation and shear deformation were recorded and used to calculate normal and shear stress considering the changing area of contact $A_{contact}$ (Figure 5.15):

Equation 5.2:

$$A_{contact} = 2\left(r^2\cos^{-1}\left(\frac{\Delta x}{2r}\right) - \frac{\Delta x}{4}(4r^2 - \Delta x^2)^{1/2}\right)$$

with specimen radius *r* (mm) and shear displacement Δx (mm).

Between one and six experiments were performed for each test condition characterised by a specific temperature and normal stress level (Table 5.3). The total number of tests was 141, significantly more than the cumulative number of the tests in all previously published studies on rock-ice failure.

5.2.3.4. Developing a temperature-dependent failure criterion for ice-filled rock joints

To develop a shear strength description of ice-filled permafrost rock joints we used the linear and stress-dependent Mohr-Coulomb failure criterion (a combination of Coulomb, 1776, and Mohr, 1900; a discussion of its limitations is given in Jaeger et al., 2007):

Equation 5.3:

$$\tau = \sigma * \tan(\phi) + c$$

which represents the shear stress at failure τ as a function of the normal stress σ, the cohesion c and the friction angle ϕ. The Mohr-Coulomb failure criterion has not only been suggested for rock mechanics but also for ice mechanics (Arenson and Springman, 2005b; Sanderson, 1988). Using this failure criterion is essential to include ice mechanics and rock mechanics in the same model.

The linear envelopes for the friction and the cohesion (as functions of the temperature) were quantified based on the shear stress at failure dependent on normal stress. The cohesion values were derived by taking the shear stress values at the intercepts of the regression lines with the abscissas for each tested temperature level. The friction values were determined by taking the slope values from the linear regression functions which correspond to the coefficient of friction μ. Values for the friction angle were derived by calculating the respective arc tangents of μ. The cohesion and the friction of ice-filled rock joints as a function of temperature were calculated by linear fitting, which is estimated by a linear regression model using the LinearModel class of MATLAB (Version R2017a). The predictor and response variables are arithmetic means, while only the predictor variable is weighted with the reciprocal value of its variance. In addition to the correlation coefficient (r) and the coefficient of determination (R^2), the MATLAB function returns the regression parameters "intercept" and "slope" with its standard error (MathWorks, 2017).

The equations for the cohesion and the friction were combined to a new shear strength description for ice-filled rock joints based on Mohr-Coulomb. A validation test was performed at the end comparing the measured peak shear stresses with the model and its uncertainties at each tested temperature level.

5.2.3.5. AE monitoring

For measuring the acoustic activity, a two-channel high-frequency acquisition system composed of two USB AE nodes (Mistras, Physical Acoustics) employing a single-channel AE digital signal processor with 16-bit resolution and 10 V maximum amplitude was used. The AE sensors were coupled to the specimen holder using silicone-free lubricating grease (Glisseal HV, Borer Chemie). The AE piezoelectrical sensors (PK6I) provided an operating frequency range of 40–70 kHz with a resonant frequency of 55 kHz. They included a preamplifier of 26 dB and were connected to the USB AE node with coaxial cables.

The system was controlled by AEwin (Mistras, Physical Acoustics), a real-time data acquisition software. The system sampled continuously with 1 MSPS (mega samples per second), while events over a fixed threshold of 70 dB were recorded. The signal characteristics (timestamp, rise time, amplitude, pulse count, energy and length) were parameterised according to Girard et al. (2012, Figure 1).

5.2.4. Results

5.2.4.1. Typical behaviour of shear stress, shear deformation and acoustic signals

A representative time series for shear stress, shear deformation and AE activity is shown in Figure 5.6. A selection of additional time series is displayed in Figure 5.16.

In Stage I, the experiment starts with a consolidation of approximately 5–6 minutes applying the specified normal load. After initial AE activity during initial consolidation (starting after 2–3 minutes, Figure 5.6), the AE hit rate decreases again to almost zero (after five minutes, Figure 5.6) before entering Stage II. Shearing starts, and the shear rings gain a tight fit to the sample and then start to apply the stress. In Stage III, shear stress increases without significant changes in AE hit rate corresponding to elastic and ductile ice deformation. In Stage IV, a pronounced peak shear stress is observed in all experiments after a few minutes coinciding to a pronounced rise in the AE hit rate that indicates brittle failure. Correspondingly, the ice infill between the rock cylinders fails and shear deformation reaches one of its maximum values. The moment of failure can also be identified by a clearly audible cracking. In Stage V, just after failure, the shear stress suddenly drops to a minimum, then rises again and quickly reaches a plateau of residual shear stress. In a few experiments (such as in Figure 5.6), the post-failure shear stress exhibits several small peaks, which are often accompanied by a minor increase in AE hits, audible cracking and a pronounced rise in shear strain. The peaks in shear stress may refer to healed ice that breaks when stresses exceed a certain threshold. Further, more than 90 % of the samples with observed post-failure peaks also failed within the ice or both in the ice and along the rock-ice interface. Hence, these peaks may also be caused by ice-ice interlocking leading to the observed decrease in shear strain (Figure 5.6). Subsequent failure occurs when the shear stresses overcome the ice strength.

The number of AE hits usually increases very suddenly and sharply just before failure (Figure 5.7a and Figure 5.7c). The average offset between the onset of AE hit increase and fracturing (i.e. Stage IV) is 107 ± 98 sec (Figure 5.7b). In all the experiments, the onset of AE hit increase occurs when 65 ± 31 % (mean value with standard deviation) of the time between shear start and failure has passed (Figure 5.7d). However, in some experiments at temperatures between -4 and -0.5 °C, the AE hit increase starts even earlier than within the standard deviation of 31 % (outliers < 34 %). The lag in absolute and relative time shows a weak correlation to temperature, though it is not dependent on normal stress.

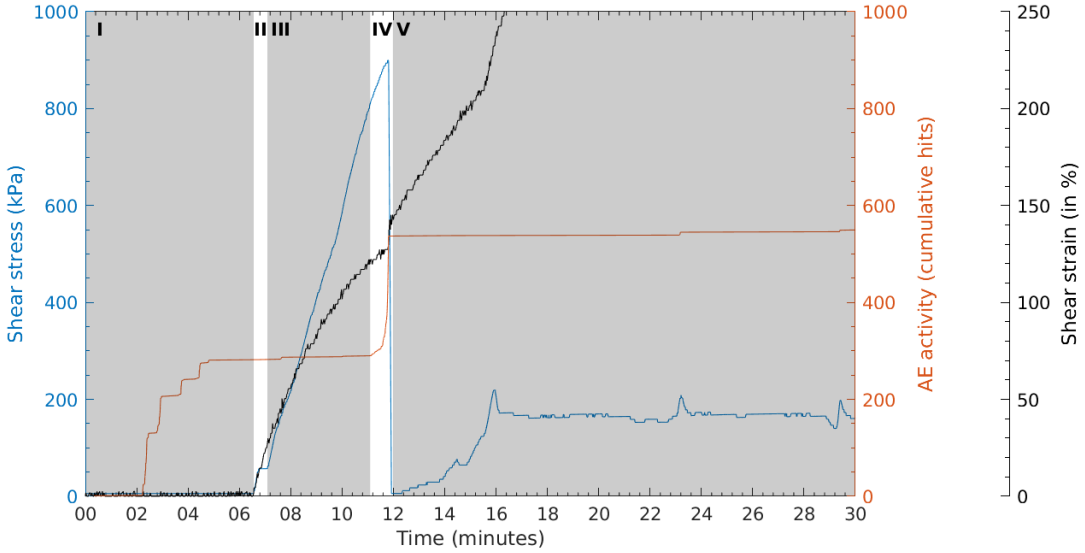

Figure 5.6: Typical curves of shear stress, shear strain and acoustic activity for a shear test at T = -3 °C and normal stress σ = 200 kPa.

Stages (I)-(V) represent the typical stages of each experiment: consolidation (I), sample fitting to shear rings (II), pre-peak shear deformation (III), shear failure (IV) and post-peak shear strength (V). Rupture is clearly detectable by the strong decrease in shear stress. An increase in the evolution of the cumulative AE hits can be observed before rupture. This figure (i.e., the shear strain curves) has been slightly modified from the original version in Mamot et al. (2018).

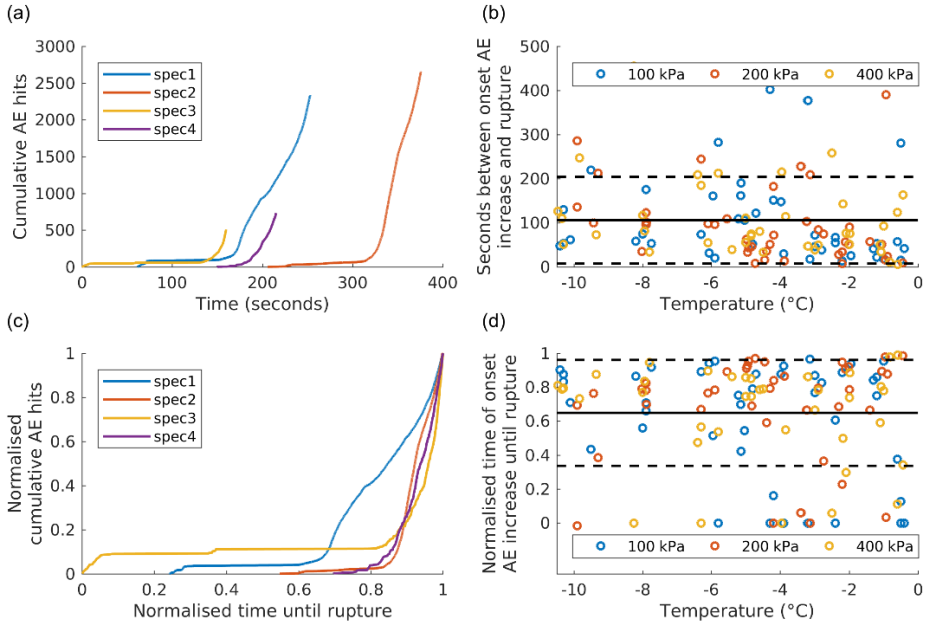

Figure 5.7: Cumulative AE hits versus time and temporal gap between onset of AE increase and failure versus rock temperature.

Time series of (a) cumulative AE hits and (c) normalised cumulative AE hits with 400 kPa normal stress and at -4° C. Time zero corresponds to the shear start of the experiments (spec1-4). Curves starting at x > 0 represent tests in which the first AE signals were recorded a certain time after shear start. The temperature-dependent time between onset of AE increase and rupture is displayed in seconds (b) and normalised (d). The black lines indicate the overall mean while the dashed lines indicate the standard deviation range. Tests at 800 kPa were not considered in (b) and (d) because they were only conducted at temperatures between -0.5 and -4 °C.

To analyse the scaling properties of the AE energy, we calculated the distribution for each experiment condition, combining the data of all experiments with the same condition to enlarge the number of events. The probability density functions (PDFs) of event energy show a power-law behaviour spanning 3–5 orders of magnitude (Figure 5.17). The exponent *b* is between 1.6 and 1.9 for the different conditions, but it does not show any relation to temperature or normal load. As a result, it does not indicate any stress or temperature dependence of the size of fracturing events.

5.2.4.2. Shear stress at failure and its temperature dependence

The shear stress at failure decreases with increasing temperature at all tested normal stress levels (Figure 5.18). Table 5.1 shows the decrease in shear stress at failure with increasing temperature for each tested normal stress condition. The calculated total decrease at stresses 100–400 kPa ranges between 63.5 and 78.1 % and refers to a warming from -10 to -0.5 °C. The maximum decrease at 800 kPa measures 60.1 % and refers to temperatures from -4 to -0.5 °C.

Table 5.1: Calculated decrease in shear stress at failure with increasing temperature.

Normal stress class [kPa]	Temperature range used for calculation [°C]	Calculated percentage decrease due to warming [%]		R^2	p-value
		total	per increase of 1 °C		
100	-10 to -0.5	70.2	7.4	0.47	< 0.01
200	-10 to -0.5	78.1	8.2	0.58	< 0.01
400	-10 to -0.5	63.5	6.7	0.44	< 0.01
800	-4 to -0.5	60.1	17.2	0.75	< 0.01

5.2.4.3. Developing a temperature-controlled brittle failure criterion for ice-filled permafrost rock joints

Shear stress at failure versus normal stress was plotted for all temperature levels and normal stresses from 100 to 400 kPa (blue regression lines; Figure 5.8) and additionally for temperatures from -4 to -0.5 °C and normal stresses from 100 to 800 kPa (orange regression lines; Figure 5.8). Here, the peak shear stresses generally increase with increasing normal stresses at all tested temperatures.

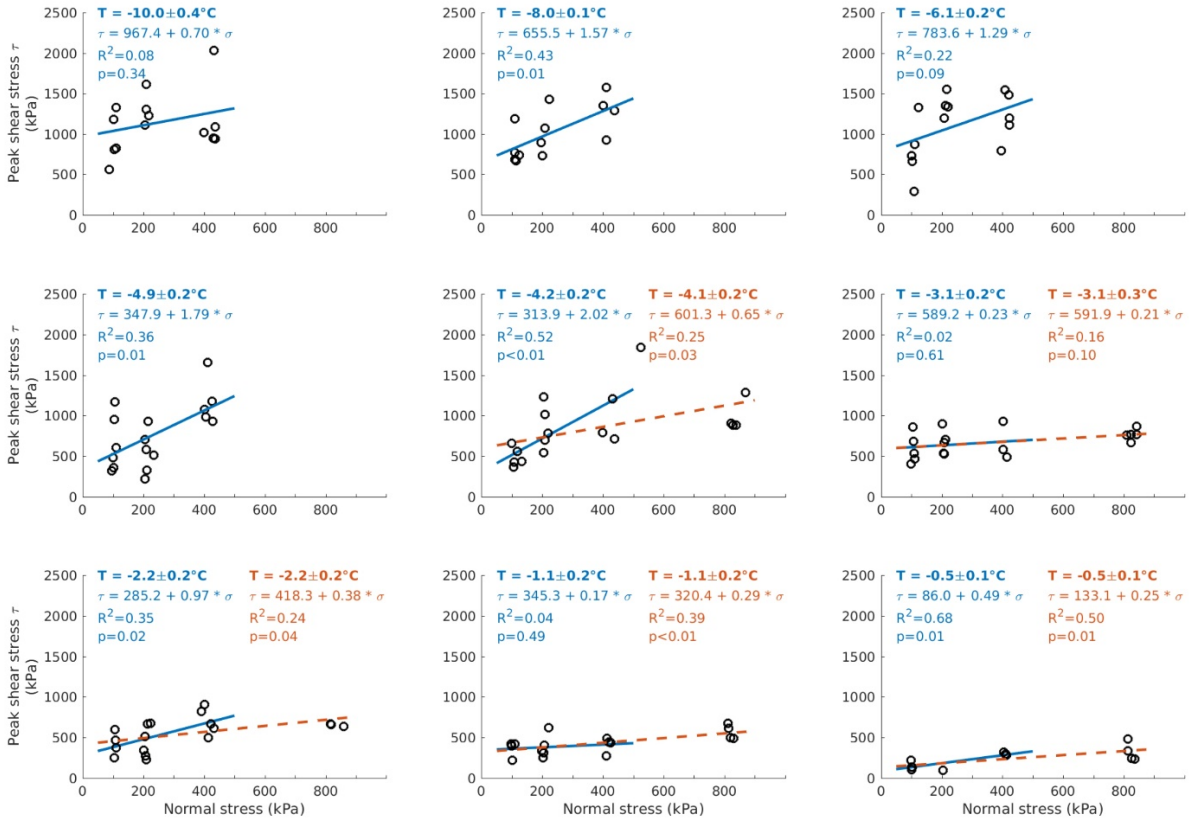

Figure 5.8: Measured shear stress at failure as a function of normal stress for temperatures between -10 and -0.5 °C.

The temperature values are the means (including standard deviation) of the measured rock sample temperatures (close to the moment of failure) of all experiments belonging to a specific temperature level. Normal stress levels of 100, 200 and 400 kPa were applied for the whole temperature range. The level of 800 kPa was additionally tested between -4 and -0.5 °C. Blue solid lines: calculated regression lines for normal stresses at 100-400 kPa. Orange dashed lines: calculated regression lines for 100-800 kPa. p: probability of rejecting the null hypothesis (H_0) although it is true.

We utilised Figure 5.8 to calculate the linear envelopes of cohesion and friction as functions of the temperature (Sect. 5.2.3.4). A temperature-dependent cohesion and friction for all test temperatures is displayed in Figure 5.19. Here, R^2 values range between 0.61 and 0.92 for the cohesion and between 0.12–0.40 for the coefficient of friction. *P* values measure < 12 % for the cohesion and 7–57 % for the coefficient of friction. The ranges depend on the included stress levels and the temperature range tested. Due to these high uncertainties, we used only specific temperature levels with a statistical significance level of $p \leq 5$ % for the elaboration of the Mohr-Coulomb failure criterion. The *p* values had been calculated earlier for the relation between peak shear stress and normal stress at the tested temperature levels (Figure 5.8). The temperature levels with *p* values > 5 % were excluded from further steps of the model development, as the corresponding peak shear stresses are considered to be not significantly dependent on the normal stress. Further, only the shear experiments from 100 to 400 kPa were utilised for the development of the failure criterion, as they cover the whole range of tested

temperatures. This leads to a greater valid temperature range for the model and to a more robust correlation between cohesion or friction and temperature.

Figure 5.9 shows the temperature-dependent cohesion and friction of ice-filled rock joints for temperature levels with p ≤ 5 % (Figure 5.8). Here, the temperature-dependent loss of cohesion of ice-filled rock joints is described by

Equation 5.4:

$$c\,[\mathrm{kPa}] = 53.3 - 73.5 * T$$

where *T* (°C) is the temperature of the ice-filled joint at failure, valid for temperatures from -8 ± 0.1 °C to -0.5 ± 0.1 °C and normal stresses from 100 to 400 kPa (Figure 5.9a).

When approaching the melting point, the cohesion decreases by 86 % from -8 °C to -0.5 °C (Table 5.2). Equation 5.4 exhibits a decrease in cohesion of 74 kPa $°C^{-1}$ due to warming, which refers to a reduction by 12 % $°C^{-1}$. The temperature-dependent friction coefficient can be expressed by

Equation 5.5:

$$\mu = 0.42 - 0.21 * T$$

where *T* (°C) is the temperature of the ice-filled fracture at failure, valid for temperatures between -8 ± 0.1 °C and -0.5 ± 0.1 °C and normal stresses from 100 to 400 kPa (Figure 5.9a). The coefficient of friction falls by 75 % with increasing temperature from -8 °C to -0.5 °C (Table 5.2). The corresponding friction angle decreases by 60 % (64.5–27.7°). This equation shows a warming-dependent loss of friction of 0.21 $°C^{-1}$ corresponding to a reduction by 10 % $°C^{-1}$.

We did not perform tests at temperatures warmer than -0.5 °C because we assume the ice to melt or be squeezed out of the rock cylinders, which leads to shearing along rock-rock contacts. Cohesion will be absent at the melting point and shear strength values will rise. This is shown by the tests of Davies et al. (2001) in which the shear strengths of ice-concrete samples closely approach the concrete-concrete sample line.

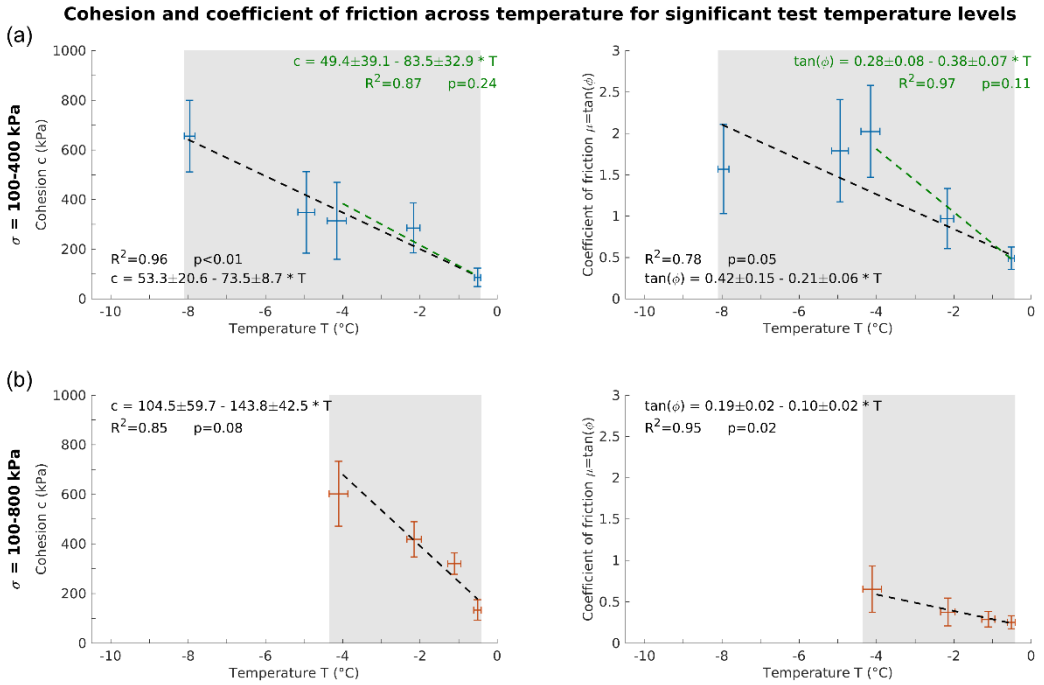

Figure 5.9: Cohesion and friction of ice-filled rock joints as a function of temperature for significant temperature levels with a statistical significance level of p ≤ 5 %.

The crosses display the means and standard deviations of rock temperature and cohesion or friction, grouped by the tested temperature classes. (a) Tests at normal stresses at 100–400 kPa and temperatures at -8 to -0.5 °C (blue crosses). (b) Tests at normal stresses at 100–800 kPa and temperatures at-4 to -0.5 °C (orange crosses). The dashed lines represent the linear regression functions, which were inversely weighted with the squared standard errors. The green regression lines in (a) refer to a temperature range from -4 to -0.5 °C. The grey areas represent the valid temperature range for the respective parameter.

Table 5.2: Calculated absolute and percentage decrease in cohesion and friction due to warming for various normal stress and temperature ranges.

Valid normal stress range [kPa]	Valid temperature range [°C]	Mechanical parameter	Decrease due to warming				R²	p-value
			total		per increase of 1 °C			
			absolute	%	absolute	%		
100 to 400	-8 to -0.5	c [kPa]	551.3	86.0	73.5	11.5	0.96	0.00
		μ	1.58	75.0	0.21	10.0	0.78	0.05
	-4 to -0.5	c [kPa]	257.3	74.1	83.5	21.2	0.87	0.24
		μ	0.74	58.3	0.38	16.7	0.97	0.11
100 to 800	-4 to -0.5	c [kPa]	503.3	74.1	143.8	21.2	0.85	0.08
		μ	0.35	59.3	0.10	17.0	0.95	0.02

Combining Equation 5.4 and Equation 5.5 in a Mohr-Coulomb failure criterion (Equation 5.3), we can describe a temperature-dependent and normal stress-dependent shear stress at failure τ (kPa) for ice-filled rock joints

Equation 5.6:

$$\tau\,[\mathrm{kPa}] = \sigma * (0.42 \pm 0.15 - 0.21 \pm 0.06 * \mathrm{T}) + (53.3 \pm 20.6 - 73.5 \pm 8.8 * \mathrm{T})$$

where the friction angle is the arc tangent of μ while both friction and cohesion respond to a temperature increase. This formula is valid for normal stresses between 100 and 400 kPa and temperatures between -8 ± 0.1 °C and -0.5 ± 0.1 °C.

5.2.4.4. Cohesion and friction for normal stresses between 100 and 800 kPa

When comparing the loss of friction and cohesion for normal stresses 100–400 kPa with the loss for 100–800 kPa, both in the same temperature range of -4 and -0.5 °C, the following can be observed (Figure 5.9, Table 5.2): (i) the absolute reduction in cohesion is more pronounced for tests including all normal stress levels; (ii) the absolute decrease in friction is stronger for tests excluding 800 kPa and (iii) percentage decreases are nearly the same for both groups of tests.

5.2.4.5. Failure type and its dependence on temperature and normal stress

Three types of failure could be observed during the shearing tests: i) fracture along the rock-ice interfaces (Figure 5.20a), ii) fracture within the ice layer and iii) a composite fracture type of i) and ii) (Figure 5.20b). In the first type, the entire ice infill stuck to either the upper or the lower rock cylinder, whereas in the second case the rock surfaces were unaffected by failure. The last fracture type refers to specimens whose ice layer broke transversely and was separated so that the rear portion remained at the lower cylinder and the front part stuck to the upper one.

With temperatures rising from -8 to -0.5 °C, the percentage of tests with fracture along the rock-ice interface increase from 8 to 100 % (Figure 5.10). At -0.5 °C it constitutes the only failure type. However, the lower number of tests at this temperature level has to be considered. Vice versa, the proportion of fracturing within the ice infillings increases with decreasing temperature from 6 % at -1 °C to 79 % at -10 °C. At -8 and -10 °C, it is the dominating failure type. The composite failure type shows no clear trend, with either decreasing or with increasing temperature.

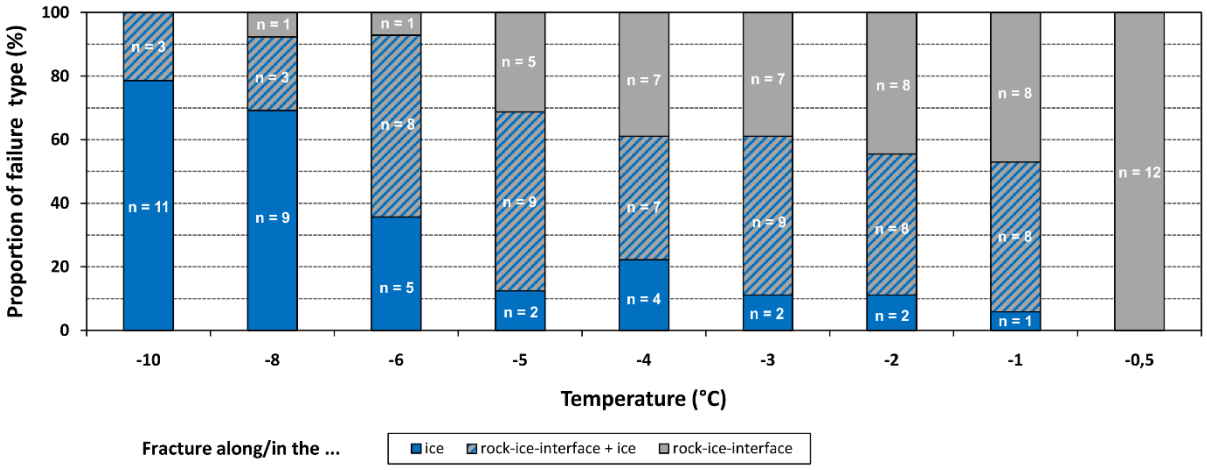

Figure 5.10: Proportions and absolute numbers of fracture types as a function of temperature (for tests at 100–800 kPa).

Failures inside the ice dominate at low temperatures whereas failure along rock-ice interfaces become more important close to 0 °C.

5.2.5. Discussion

Our experimental results generally show decreasing shear strength of ice-filled rock joints with increasing temperature and decreasing normal stress. We used these data to develop a new brittle failure criterion for ice-filled permafrost rock joints (Equation 5.6), which is based on Mohr-Coulomb and shows that both the cohesion and the friction, are temperature dependent and decrease with increasing temperature ($R^2 = 0.96$ for the cohesion and $R^2 = 0.78$ for the friction). Similar tendencies have been indicated by previous studies of the shear strength of ice-filled rock joints (Davies et al., 2000; Davies et al., 2001; Günzel, 2008; Krautblatter et al., 2013). However, all of these studies were performed with a much smaller number of experiments and with concrete as a rock analogue; further, their results have not yet been combined into a comprehensive failure criterion.

5.2.5.1. Real-world conditions of permafrost rock slope destabilisation simulated by the new failure criterion

The experiments presented apply to real-world rock-ice fracturing in rock slope failures (i) with ice-filled failure planes in a depth of 4 to 15 m, i.e. mainly below the active layer and shallower than the ice fracturing suppression in favour of creep deformation of ice, (ii) with virtually all realistic alpine and Arctic permafrost bedrock temperatures between -0.5 °C and -10 °C, and (iii) with fast displacements (0.7 ± 0.1 mm min^{-1}) coinciding with the final accelerating failure stage. Rock-ice fracturing certainly dominates rock failure volumes of $\leq 2.3 * 10^4$ m^3 in which all ice-filled failure planes are ≤ 15 m deep (Section 5.2.2), but it might

also play an important role for larger failures, for which just a certain proportion of ice-filled failure planes are ≤ 15 m deep.

If we leave the range of considered boundary conditions in terms of (i) higher normal stresses, (ii) lower temperatures or (iii) lower strain rates, fracturing along ice-filled permafrost rock joints will presumably not occur. (i) A potential gradual stress-dependent transition from brittle fracture to creep is expected at the tested normal stresses above 400 kPa. In our experiments, all sandwich shear samples, including those at 800 kPa normal stress, only failed by fracturing, presumably due to the elevated strain rate of 10^{-3} s^{-1}, leading to fracture. It appears that the transition from shear fracturing to creep is not only stress dependent but also strain rate dependent within a certain transition level of normal stress (Sanderson, 1988). Other reasons for the unexceptional fracture-dominated failures are that the simulated rock overburden of 30 m may still be within the transition depth and seems to favour fracturing at elevated strain rates. (ii) Tests at temperatures below -10 °C were not performed because measured daily and annual mean temperatures at various alpine and Arctic permafrost bedrock sites do not drop below -10 °C at depth (Böckli et al., 2011; Delaloye et al., 2016; Harris et al., 2003). (iii) The samples were sheared with high strain rates of 10^{-3} s^{-1} to provoke brittle failure of ice and rock-ice contacts. At lower strain rates, stress concentrations along the shear zone can be relaxed and the mechanical behaviour changes to ductile creep deformation without fracturing (Arenson and Springman, 2005a; Arenson et al., 2007; Krautblatter et al., 2013; Renshaw and Schulson, 2001; Sanderson, 1988).

Our experiments simulate the final accelerating stage of rock slope failure in which the structure of the ice infillings is deformed by intense shear displacement. The ice infill at the start of the shear tests reproduces an ice-filled joint that has already been loaded and deformed by uniaxial compression. This is somehow similar to polycrystalline ice in natural fractures as ice has a high capacity to perform self-healing and thus deletes previous deformation-induced imperfections. At strain relaxation, the ice bonding heals itself within hours and days due to refreezing and causes a strengthening of the sample (Arenson and Springman, 2005a; Sanderson, 1988); thus a sample with a preset normal stress is similar to an ice-filled fracture under similar conditions irrespective of the deformation history. In this study, the bonding of the rock-ice interface is mostly established by adhesion, whereas rock-ice interlocking is less important due to the small surface roughness of the rock samples.

So far the failure of ice-filled permafrost rock joints has been studied using concrete as a rock analogue (Davies et al., 2000; Günzel, 2008). For the first time, we use rock to closely reproduce real conditions along rock joints. Synthetic materials possibly deviate from shear strength values representative for rock joints in the field. For instance, ice sliding on granite shows a friction coefficient μ approximately 3–4 times higher than ice sliding on glass or metals, all having

a similar surface asperity roughness. The higher friction of the granite-ice interfaces is due to a higher effective adhesion (Barnes et al., 1971). We assume that the shear strength of rock-ice interfaces is mostly affected by temperature, normal stress, strain rate and joint surface roughness. However, the applied constant strain rate as well as the standardised preparation of a uniform joint surface roughness prohibit any potential effects on the shear strength. We postulate that the influence of the rock type on the shear strength is less important for the following reasons:

(i) The thermal conductivity of the rock may affect the shear strength by facilitated melting along heat-insulating surfaces, causing a decrease in friction (Barnes et al., 1971). The thermal conductivity of rocks varies in a range of 0.3–5.4 W m^{-1} K^{-1} (Clauser and Huenges, 1993; Schön, 2015). A metal like brass, with a much higher thermal conductivity of 100 W m^{-1} K^{-1}, would lead to a warming at the interface 14.5 °C lower than granite (Barnes et al., 1971). Due to the relatively small range of thermal conductivities for different rock types, we do not expect a rock-type-dependent effect on the shear strength.

(ii) The porosity of the rock and the type of constitutive minerals may play a role in the growth of ice crystals along the rock-ice interface which in turn affects the shear strength. The strain rate and the compressive strength of ice crystals are significantly higher for those oriented parallel to the applied stress than for those oriented randomly (Hobbs, 1974; Paterson, 1994). However, we assume any potential rock-type-dependent orientations of ice crystals to be deleted before shearing starts due to the applied uniaxial compression during initial consolidation.

(iii) The strength of the constitutive minerals of the rock surfaces may control the friction of the rock-ice contact. However, we assume the strength of minerals to play a minor role in the shear strength because at the rock-ice interface the ice will fail before the rock material and ice strength will control the failure process. In our tests we could not observe particles breaking off the rock surfaces. Elastic moduli of most rock minerals (bulk modulus k: 17–176 GPa; shear modulus μ: 9–95 GPa) are 2–20 times higher than those of ice (k: 8.9 GPa; μ: 3.5 GPa) (Schulson and Duval, 2009; Schön, 2015). The small applied roughness of the shear surfaces additionally prevented any relevant impact of differing mineral strengths.

(iv) Rock minerals heat up differently and can generate thermal stresses (Gómez-Heras et al., 2006) in the intact rock and along discontinuities, causing thermal fatigue and a reduction in the shear resistance (Dräbing et al., 2017a). However, we do not expect an impact on the shear strength as repetitive temperature cycles with high magnitude and frequency are required for thermal stress fatigue (Hall and Thorn, 2014). During our tests, temperatures were kept constant.

Thus, the tests using limestone represent rock-ice fracturing along joints of all rock types. To use rock instead of other materials probably has a greater effect on the shear strength than different rock types. Still, a potential shear strength dependence on different rock types has to be proven in additional experiments. Further, it is certainly interesting to systematically analyse the strain-rate-dependent brittle fracture-creep transition beyond 800 kPa normal stress or the influence of the joint surface roughness on the shear strength and the failure behaviour in other studies, but this is beyond the scope of this study.

5.2.5.2. Validation of the new failure criterion

The new derived failure criterion (Equation 5.6) describes the shear strength of ice-filled fractures in all types of rock and combines a temperature-dependent cohesion and friction angle. A temperature dependence of both the cohesion and friction angle has not been demonstrated yet, but for pure ice (Fish and Zaretzky, 1997). However, other publications have postulated either a temperature dependence of the cohesion of ice-rich soils (Arenson and Springman, 2005b; Arenson et al., 2007) or a temperature dependence of the friction coefficient of granite-ice interfaces (Barnes et al., 1971). Here, we have developed a failure criterion for rock-ice interfaces that contains both a temperature-dependent coefficient of friction and an even stronger temperature-dependent cohesion.

Figure 5.11 depicts the new Mohr-Coulomb failure criterion (Equation 5.6) with the range of uncertainty for the different temperature levels tested and corrected by their true means (including standard deviation). The means of the measured peak shear stress values, represented by the intersections of the error bars of normal stress and peak shear stress, mostly correlate well with the calculated failure criterion and the respective error ranges. Statistical dispersion measures of the measured peak shear stress values around the failure criterion are shown in Table 5.4. Best accordance is achieved for the shear stress means used for model calibration (correspond to significant temperature levels with p values ≤ 5 %). The mean absolute deviation (MAD) and coefficient of variation (CV) range between 40 and 146 kPa and between 8.8 and 24.6 % respectively. The experiments at temperatures -1, -3, -6 and -10 °C (with p values > 5 %), which had been excluded from the elaboration of the failure criterion, were used for validation. Their shear stress means show higher deviations from the failure criterion, i.e. the MAD and the CV range from 98 to 252 kPa and from 15 to 43.5 % respectively. For normal stresses at 100–400 kPa, the model seems to show a robust fit even with values not included in the initial model development data set. The means of peak shear stress at 800 kPa mostly lie within the calculated error margins, but at their lower boundaries. This demonstrates the mechanical parameters controlling the failure behaviour start to change at higher normal stresses (800 kPa) and temperatures close to the melting point.

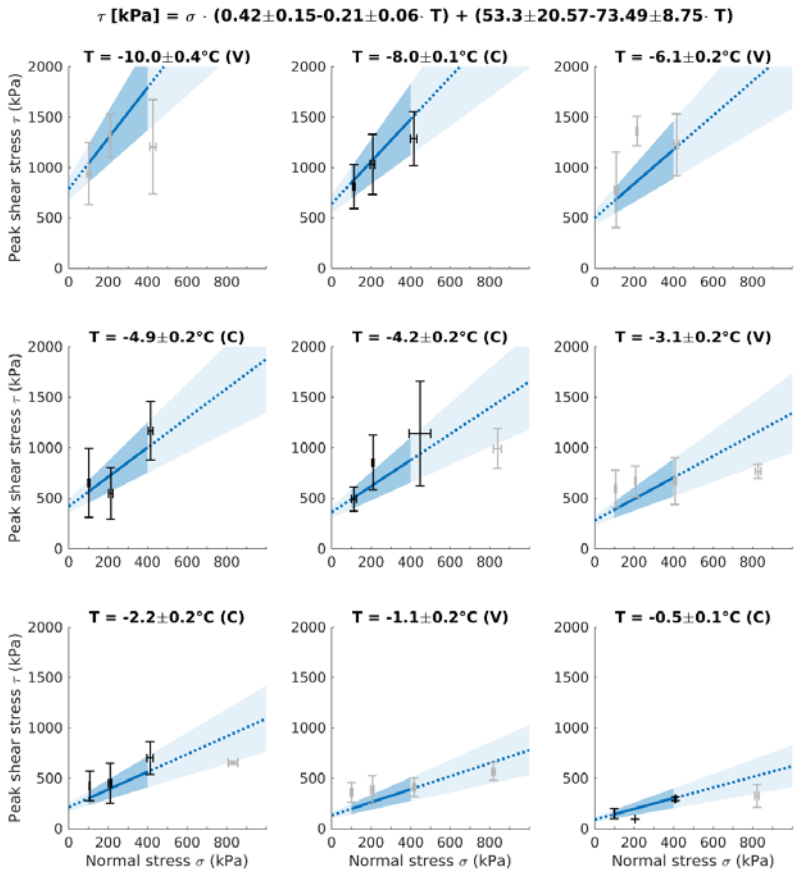

Figure 5.11: Validation test for the new Mohr-Coulomb failure criterion for ice-filled rock joints (Equation 5.6).

The black and grey crosses represent means and standard deviations of normal stress and peak shear stress, grouped by the tested normal stress classes 100, 200, 400 and 800 kPa. C: calibration temperature level that was used for the model as $p \leq 5$ % (black crosses). V: validation temperature level that was excluded from the elaboration of the failure criterion because $p > 5$ % (grey crosses). As tests at 800 kPa were excluded from the development of the failure criterion, they also serve as validation (grey crosses). Solid blue lines and dark blue areas represent the calculated failure criterion and respective error ranges within the valid normal stress range. Dotted blue lines and light blue areas are extrapolations of the failure criterion and error margins beyond the valid normal stress range.

This study shows that both warming and unloading of ice-filled rock joints lead to a significant drop in shear resistance, which may cause a self-enforced rock slope failure propagation. The progressive degradation of bedrock permafrost and ice in rock joints may control the cohesion and friction angle of the joints. However, as soon as a first slab has detached from the rock slope (A in Figure 5.12), further slabs below can become unstable and finally detach as the shear strength along the ice-filled failure plane is affected by progressive warming (i.e. permafrost degradation, B2 in Figure 5.12), but even faster by sudden unloading (B1 in Figure 5.12). The latter is represented by a significant drop in normal stress in the Mohr-Coulomb failure criterion (Figure 5.13).

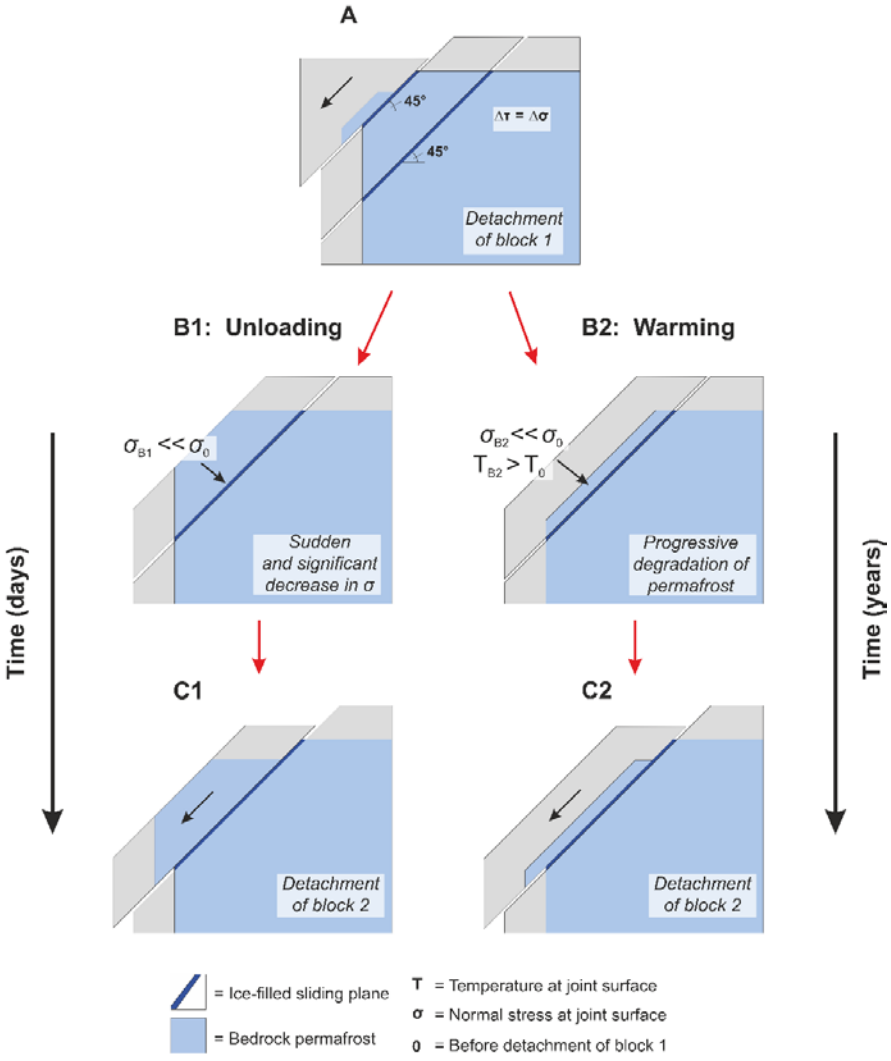

Figure 5.12: Progressive failure in a warming permafrost rock slope displaying thermal and normal stress conditions before and after detachment of a first slab.

Both can initiate failure: (B2) progressive thermal warming (i.e. permafrost degradation) occurs within years, but (B1) sudden unloading develops even faster within days.

We consider three scenarios of rock slope stability depending on the reduction in normal stress and its relationship to cohesion along a specific shear plane with an inclination of 45 °. Correspondingly, all changes in shear forces equal the changes in the shear resistance $\Delta\tau = \Delta\sigma$. However, instability may increase when the loss in friction surpasses the loss of applied shear forces: $\Delta\sigma * tan\,\varphi > \Delta\tau$. This may happen in an underlying frozen rock mass upon unloading when μ or $(0.42 - 0.21 * T) > 1$. The cohesion may possibly compensate for the decrease in friction when $c > \Delta\sigma * tan\,\varphi$. In this case the shear plane could become more unstable without complete failure. This is valid for temperatures between -10 and -3 °C and normal stresses between 100 and 200 kPa (yellow boxes in Figure 5.13). When the loss of friction in an underlying frozen rock mass upon unloading is much bigger than the reduction in the shear forces $\Delta\sigma * tan\,\varphi \gg \Delta\tau$ and even exceeds the ice cohesion $c < \Delta\sigma * tan\,\varphi$, then failure along the shear plane is strongly promoted. This is valid for temperatures between -10 and -0.5 °C and

normal stresses of 400–800 kPa (red boxes in Figure 5.13). Rock slope stability in an underlying frozen rock mass upon unloading is only weakly affected if the reduction in friction is smaller than the reduction in the shear force: $\Delta\sigma * tan\,\varphi + c < \Delta\tau$. This is valid for temperatures between -2 and -0.5 °C and normal stresses of 100–200 kPa (blue boxes in Figure 5.13). In summary, the red scenario in Figure 5.13 indicates a high likelihood of subsequent failures by unloading the underlying frozen rock mass, the yellow scenario exposes a moderate likelihood and the blue scenario shows a small likelihood. Unloading may lead to instability or even failure when the shear planes (i) are affected by a high reduction in normal stress exceeding the ice cohesion and/or (ii) are below -2 °C due to a friction coefficient higher than 1.

Temperature class [°C]	Coefficient of friction [μ]	Cohesion [kPa]	Normal stress-dependent friction at σ_1 =			
			100 kPa	200 kPa	400 kPa	800 kPa
$\|\tau\| = \sigma * (0.42 - 0.21 * T) + (53.3 - 73.5 * T)$						
			Unloading reduces stability of underlying frozen rock mass		Critical stability loss of underlying frozen rock mass	
-10	2.52	788	252	504	1008	2016
-8	2.10	641	210	420	840	1680
-6	1.68	494	168	336	672	1344
-5	1.47	421	147	294	588	1176
-4	1.26	347	126	252	504	1008
-3	1.05	274	105	210	420	840
			Unloading increases stability of underlying frozen rock mass			
-2	0.84	200	84	168	336	672
-1	0.63	127	63	126	252	504
-0.5	0.53	90	53	105	210	420

Figure 5.13: Three scenarios of rock slope stability after the sudden unloading of an underlying frozen rock mass with 45 ° fractures.

Blue boxes: increasing stability of underlying frozen rock mass. Unloading increases shear resistance relative to shear forces in 45 ° fractures. Yellow boxes: reducing stability. Unloading reduces shear resistance (friction) relative to shear stress in 45 ° fractures. Red boxes: critical stability loss. Friction loss along underlying 45 ° fractures even exceeds ice cohesion.

5.2.5.3. Cohesion and friction for normal stresses including 800 kPa

Combining the 100–400 kPa with the 800 kPa tests results in a higher (absolute) reduction of cohesion and a lower (absolute) loss in friction with increasing temperature (Figure 5.9). The relatively low peak shear stress values at 800 kPa normal stress flatten the linear regression curves and raise their intercepts with the abscissas (Figure 5.8). This behaviour can presumably be explained due to an enhanced pressure melting effect at higher normal stresses and

temperatures close to 0 °C, leading to liquid formation along the rock-ice interface and decreasing the friction (see also Sect. 5.2.5.5; Arenson and Springman, 2005a; Barnes and Tabor, 1966; Hobbs, 1974). This hypothesis is supported by two findings. (i) Failures along the rock-ice contact dominate at higher temperatures between -0.5 and -5 °C (Figure 5.10). (ii) The proportion of rock-ice failures to all failure types is 42 % for normal stresses at 100–400 kPa and temperatures from -0.5 to -4 °C. The corresponding proportion for the same temperature range and normal stresses at 100–800 kPa is 51 %. When tests at 800 kPa are added, the rock-ice failures in particular increase in number, whereas failures within the ice are not affected. At normal stresses of 800 kPa and temperatures below -4 °C, the enhanced pressure melting effect may reduce and shear stresses are expected to rise significantly.

5.2.5.4. AE activity as an indication of correlated damage, potentially preconditioning failure

AE is generally very capable of anticipating rock-ice failure as (i) all failures are predated by an AE hit increase, (ii) the hit rate increases well before brittle failure starts and (iii) AE peaks immediately prior to failure. This AE pattern coincides with observations in triaxial constant strain rate tests on frozen soil (Yamamoto and Springman, 2014). The experiments conducted clearly show that precursors before failure can be observed by the AE technique, providing complementary information to the displacement measurements. To exceed the AE trigger level, AE events have to be emitted from significantly large evolving microcracks and thus document microcrack generation and coalescence. It is interesting to consider that in ice, even secondary and tertiary creep are constituted by the generation and healing rate of microfractures (Paterson, 1994; Sanderson, 1988). The measured pre-failure increase in AE activity (Figure 5.16) is thus an indication for damage increase, i.e. microcrack generation and coalescence typical for cryospheric damage propagation (Murton et al., 2016; Yamamoto and Springman, 2014). The culmination of progressive damage involves complex interaction between multiple defects and growing microcracks (Eberhardt et al., 1999; Senfaute et al., 2009; Sornette, 2006). An increase in the AE hit rate prior to failure accompanies the evolution of the internal damage and can therefore be used as a precursor signal.

The power-law distribution of the AE event energy, which shows only small variations for all different temperature and loading conditions, indicates that strength heterogeneity, a main factor influencing this parameter (Amitrano et al., 2012), is similar for all tests at different conditions. Hence, neither a stress nor a temperature dependence of the size of fracturing events is expected in the tested conditions. A main challenge with AE monitoring is the absolute comparison of the event number and energy. The measured signal is strongly influenced by the coupling of the sensor with the medium. Additionally, the event triggering depends on the selection of an amplitude threshold. However, relative comparison (e.g. evolution of the hit

rate) and statistical means (e.g. exponent *b*) are not very sensitive to the above-mentioned challenges, as long as enough events are detected.

At temperatures above -4 °C, a higher number of samples displayed an earlier start in fracturing before failure occurred. This trend is visible in the higher number of outliers below the standard deviation range and at temperatures above -4 °C (Figure 5.7d). It may be explained by the lower shear strength of samples at warmer temperatures. Accordingly, at colder temperatures failure is increasingly characterised by a later onset of AE events because of higher shear strengths. Challenges remaining for field application of the recorded offset between the onset of AE hit increase and shear failure are the positioning of the sensors and their density, the strength of the signal and the missing signal emission history prior to instrumentation.

5.2.5.5. Failure types

Three types of failure were identified: fracture along the rock-ice interfaces, fracture within the ice layer and a composite type. From a practical point of view, Equation 5.6 has to include all types of failure due to five main reasons:

(i) We cannot observe what types occur in natural systems.
(ii) A specific stress, strain or temperature condition could not be assigned explicitly to one of the failure types.
(iii) Along spatially extensive rock joints, all these failure types coexist and coincide.
(iv) All three types together fit in a failure criterion, showing that they converge to a range of values under given temperature and stress conditions.
(v) It is physically impossible to constrain the exact fracturing plane in a sub-millimetre range away from the rock-ice interface.

In this study we observe a tendency of temperature dependence of the distinct failure types: when comparing fractures in the ice with fractures along the rock-ice contact, tests with the first failure type dominate at cold temperatures between -10 and -6 °C, while the proportion of tests with fracture along the rock-ice interface dominate at higher temperatures between -5 and -0.5 °C. This behaviour is similar to the pattern observed by Jellinek (1959), albeit at lower temperatures, showing “cohesive breaks” (comparable with fracture within the ice infilling) of ice-steel interfaces at temperatures colder than -13 °C and “adhesive breaks” (equal to fracture of rock-ice interfaces) at temperatures warmer than -13 °C. Previous publications highlight three potential reasons for this pattern that explain the formation of liquids, which may support the failure of rock-ice contacts at warmer conditions:

(i) Above -3 °C the deformation of ice is increasingly influenced by pressure melting (Hobbs, 1974), which can be pronounced in regions of stress concentration along the shear plane (Arenson and Springman, 2005a; Arenson et al., 2007).

(ii) In porous media, curvature-induced and interfacial pre-melting (caused by long-range intermolecular forces between different materials and phases) leads to a depressed equilibrium freezing temperature. An unfrozen liquid melt film, several nanometres thick, forms at the ice-solid interface at -1 °C, increasing its thickness when approaching 0 °C (Rempel et al., 2004).

(iii) Grain boundary sliding occurs at temperatures above approximately -10 °C, which generates heat by friction (Hobbs, 1974) and may additionally support the formation of this liquid-like layer along the rock-ice interface.

5.2.6. Conclusions

Most of the documented failures in permafrost rock walls are likely triggered by the mechanical destabilisation of warming bedrock, discontinuities with rock bridges and joints with or without ice fillings. The latter may evolve into shear planes, supporting destabilisation on a larger spatial scale and leading to failure. To anticipate failure in a warming climate, we need to better understand how rock-ice mechanical processes affect rock slope destabilisation with temperatures increasing close to 0 °C.

This paper presents a systematic series of constant strain rate shear tests on sandwich-like limestone-ice-limestone samples (i) to simulate the brittle failure of ice infillings and rock-ice interfaces along ice-filled shear planes of rockslides, (ii) to study its dependence on temperature and normal stress and (iii) to develop a new brittle failure criterion for ice-filled permafrost rock joints. The set-up and boundary conditions of our experiments are inspired by a 10^4 m^3, ice-supported rockslide at the Zugspitze summit crest. Our tests apply to failures of permafrost rock slopes (i) with volumes of $\leq 2.3 * 10^4$ m^3, (ii) with ice-filled shear planes in a depth of 4–15 m, (iii) with bedrock temperatures between -0.5 °C and -10 °C and (iv) with high strain rates ($4.8 \pm 1.4 * 10^{-3}$ s^{-1}) coinciding with the accelerating final failure stage. Tests at a rock overburden of 30 m and temperatures from -4 to -0.5 °C were performed to study a potential stress-dependent transition from brittle fracture to creep. Of all the previous laboratory studies on the shear strength of ice-filled joints, the data set presented is the most extensive, containing 141 tests at nine temperature and four normal stress levels. For the first time, preconditioned rock from a permafrost-affected rock slope was used.

Monitoring of AE activity during the shear tests was successfully used to describe the fracturing behaviour of rock-ice contacts focusing on the precursors of failure. The onset of AE hit increase occurred when 65 % of the time between shear start and failure had passed (107 ± 98 s before failure). The shear strength clearly declines with decreasing normal stress and increasing temperature. At rock overburdens of 4 to 15 m, warming from -10 to -0.5 °C causes a decrease in shear strength by 64 to 78 %. At a rock overburden of 30 m and warming from -4 to -

0.5 °C, shear strength decreases by 60 %. Warming drastically reduces the shear resistance of ice-filled rock joints and is thus a key process contributing to permafrost rock slope failure. Progressive failure is initiated when a first slab has detached from a rock slope. The underlying frozen rock mass is subsequently destabilised by progressive thermal warming and even more quickly by sudden unloading. The latter may lead to instability or even failure when the shear planes (i) are affected by a high reduction in normal stress exceeding the ice cohesion and/or (ii) are below -2 °C due to a friction coefficient higher than 1.

For the first time, we have introduced a failure criterion for ice-filled permafrost rock joints that includes the fracturing of ice infillings, rock-ice interfaces and a combination of both. It is based on a Mohr-Coulomb failure criterion, it refers to joint surfaces which we assume similar for all rock types and it is valid for normal stresses at 100–400 kPa and temperatures from -8 to -0.5 °C. The failure criterion contains a temperature-dependent cohesion and coefficient of friction decreasing by 12 % $°C^{-1}$ and by 10 % $°C^{-1}$ respectively with increasing sub-zero temperatures. The model fits well to the measured calibration means and even to the values excluded from the model development which mostly lie within or close to the calculated error margin. Further, we show that the failure type depends on the temperature and is also affected by higher normal stresses (i.e. 800 kPa) above -4 °C, which can presumably be explained by an enhanced pressure melting effect along the rock-ice interface.

The new failure criterion can be applied in numerical modelling and enables scientists and engineers to anticipate more accurately the destabilisation of degrading permafrost rock slopes, as it reproduces better real shear strength conditions along sliding planes.

5.2.7. Supplement

Variations in the shear rate (0.3–1.0 mm/min) and in the ice layer´s thickness (1.5–4 mm) were kept low and have no influence on the shear stress at failure (Figure 5.14). This is valid for all tested stress and temperature conditions.

Normal and shear load as well as normal and shear deformation were recorded during the shear tests and used to calculate normal stress and shear stress considering the changing area of contact $A_{contact}$ which is schematically shown in Figure 5.15.

The number of experiments for each test condition (characterised by a specific temperature and normal stress level) ranged between 1 and 6 (Table 5.3).

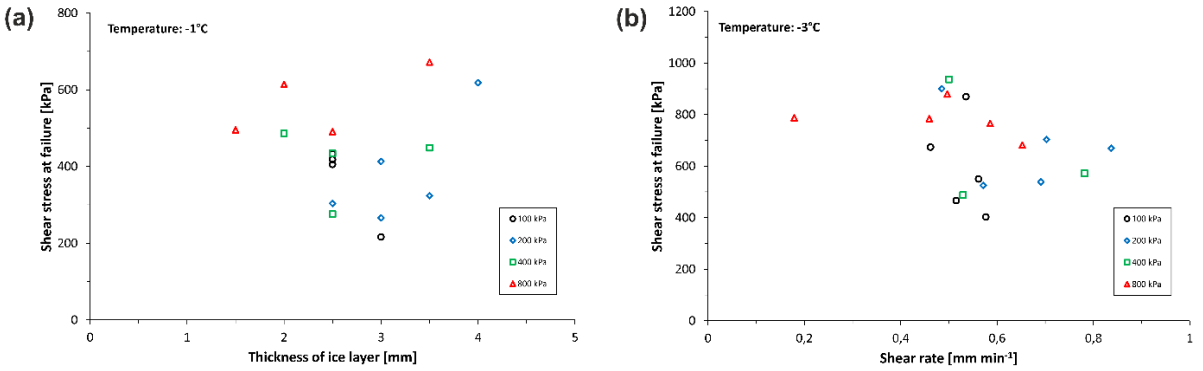

Figure 5.14: Typical variations in (a) ice layer thickness and (b) shear rate versus shear stress at failure.

The data refer to normal stress levels of 100, 200, 400 and 800 kPa and are each plotted for one single temperature level.

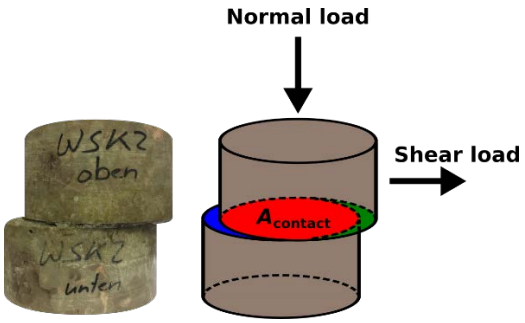

Figure 5.15: Schematic visualisation of decreasing area of contact $A_{contact}$ between upper and lower rock cylinder during shear experiments.

Table 5.3: Number of experiments per temperature and normal stress condition.

Normal stress class [kPa]	Temperature level [°C]								
	-10	-8	-6	-5	-4	-3	-2	-1	-0.5
100	5	5	5	6	5	5	4	4	4
200	4	4	4	6	5	5	6	5	1
400	5	4	5	5	4	3	5	4	3
800	-	-	-	-	4	5	3	4	4

Figure 5.16 displays a selection of additional representative time series of shear stress, shear deformation and AE activity. Failure is clearly detectable at all presented temperature levels by the peaks in shear stress and their following strong decrease. Furthermore, an increase in cumulative AE hits can be observed just before rupture, pointing to growing microcracks that coalesce and lead to progressive damage. In most of the experiments, the shear deformation reaches one of its maxima at failure. The character of the presented curves corresponds to the demonstrated stages in Figure 5.6.

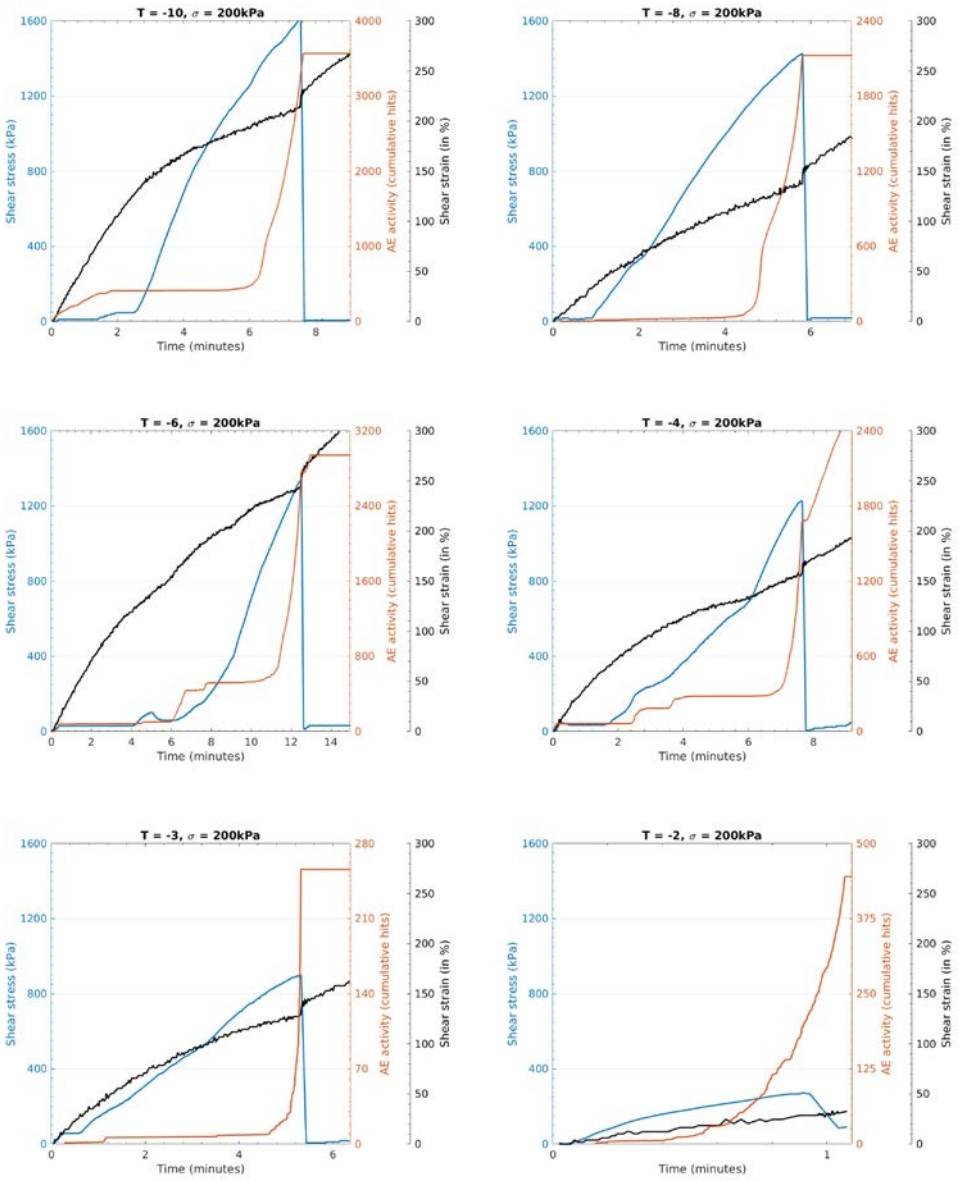

Figure 5.16: Typical curves of shear stress, shear deformation and acoustic activity for tests applying a normal stress of 200 kPa and various temperatures.

All stages of the shearing process are depicted excluding the main part of stage V (post-failure). This figure (i.e., the shear strain curves and the lower two graphs) has been slightly modified from the original version in Mamot et al. (2018).

The probability density functions (PDFs) of event energy show a power-law behavior spanning 3–5 orders of magnitudes (Figure 5.17). The exponent *b* ranges between 1.6 and 1.9 for the different conditions, but it does not show a relation to temperature or normal load.

At all tested normal stress levels (100, 200, 400 and 800 kPa) the shear stress at failure decreases with increasing temperature (Figure 5.18). The calculated total decrease at stresses 100–400 kPa ranges between 63.5 and 78.1 % and refers to a warming from -10 to -0.5 °C. The maximum decrease at 800 kPa measures 60.1 % and refers to temperatures from -4 to -0.5 °C. The measured normal stress means and errors of the tests assigned to a certain normal stress class differ little from the respective class values (maximum 28 ± 16 kPa).

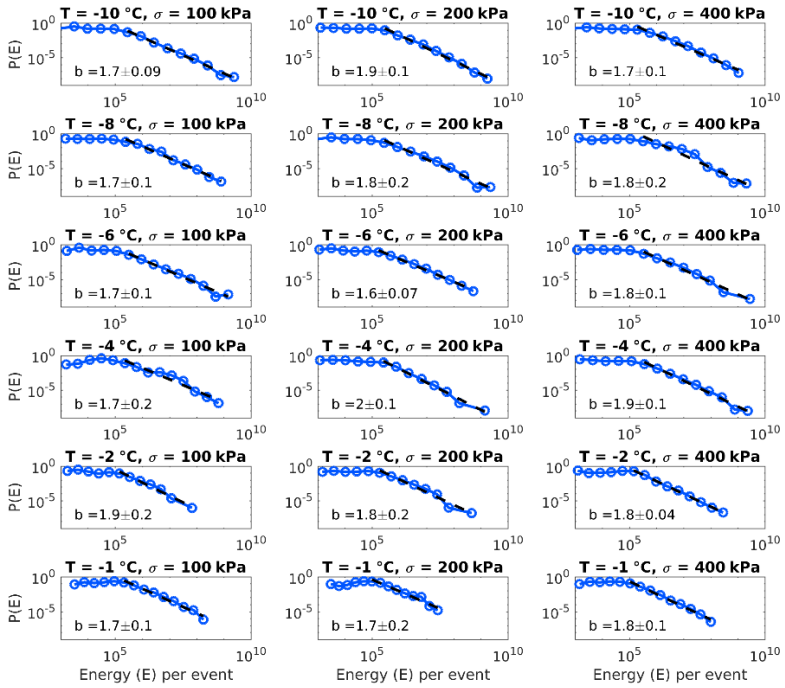

Figure 5.17: Probability distribution of the event energy for different conditions (temperature and stress level).

The power-law function is marked with a dashed black line and its exponent b is given with an error estimation.

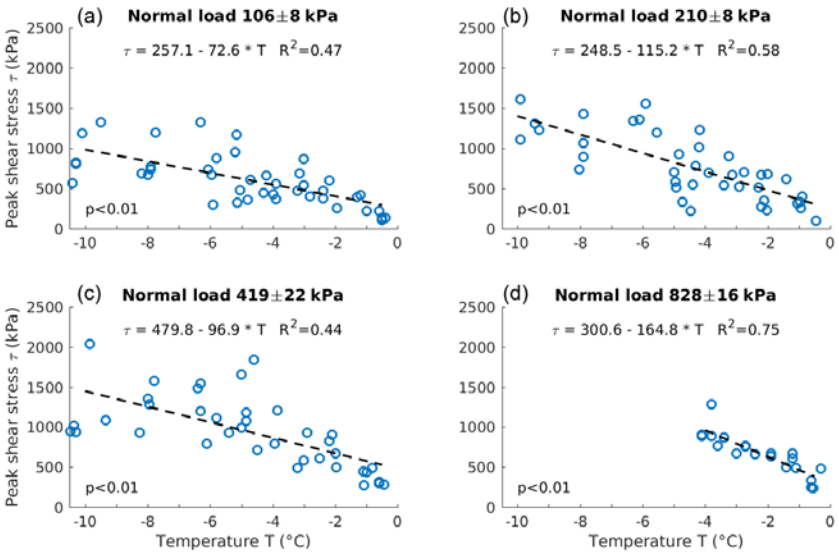

Figure 5.18: Shear stress at failure as a function of temperature for normal stress levels of 100, 200, 400 and 800 kPa.

The measured normal stress means and errors of the tests assigned to a certain normal stress class differ little from the respective class values (maximum 28 ± 16 kPa).

Figure 5.19 displays the development of formulas for a temperature-dependent cohesion and friction at all tested temperatures. The values of the regression lines correspond roughly to the

ones taken for the Mohr-Coulomb failure criterion, which only considers temperature levels with a statistical significance level of $p \leq 5$ % (Figure 5.8). In Figure 5.19, R^2-values range between 0.61–0.92 for the cohesion and between 0.12–0.40 for the coefficient of friction. P-values measure 0–12 % for the cohesion and 7–57 % for the coefficient of friction. The ranges depend on the included stress levels and the temperature range tested. The uncertainties (R^2 and p) presented in Section 5.2.4.3 are higher than the errors of the functions used for the failure criterion (Figure 5.9). This justifies the exclusion of tests at certain temperature levels for the development of a robust model.

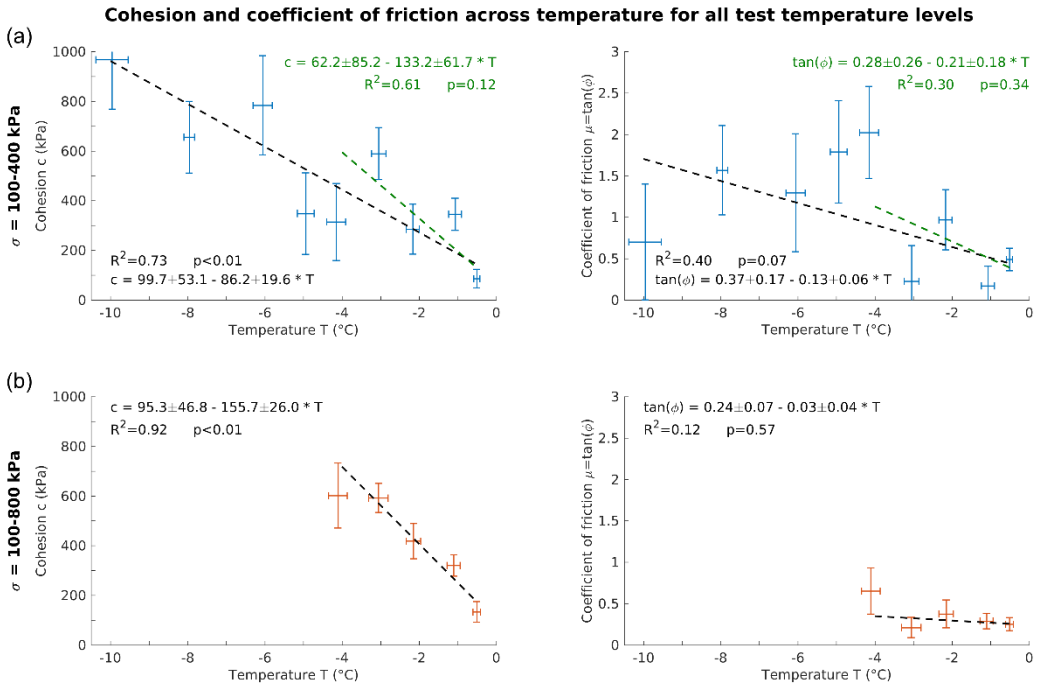

Figure 5.19: Cohesion and coefficient of friction of ice-filled rock joints as a function of temperature for all tested temperature levels.

The crosses display the means and standard deviations of rock temperature and cohesion or friction for the different test temperature classes. (a) Tests at normal stresses 100–400 kPa and temperatures -10 to -0.5 °C (blue crosses). (b) Tests at normal stresses 100–800 kPa and temperatures -4 to -0.5 °C (orange crosses). The dashed lines represent the linear regression functions, which were inversely weighted with the squared standard errors. The green regression lines in (a) refer to a temperature range from -4 to -0.5 °C.

Three different types of failure could be identified: (i) Fracture along the rock-ice interface, where the entire ice infill sticks to the upper rock cylinder (Figure 5.20a). (ii) Fracture within the ice layer. (iii) A composite fracture type of (i) and (ii), where the ice layer broke transversely and was separated so that the rear portion remains at the lower cylinder and the front part sticks to the upper one (Figure 5.20b).

A clear relationship between failure type and normal stress could not be identified for stress levels 100–400 kPa (Figure 5.21). However, at normal stresses of 800 kPa fracturing in the ice

did not occur whereas fracturing of rock-ice contacts dominated with 75 %. This overrepresentation of failures along the rock-ice interface may be caused due to the absence of tests at temperatures below -4 °C, where much higher proportions of failures in the ice were observed for tests at ≤ 400 kPa (Figure 5.10).

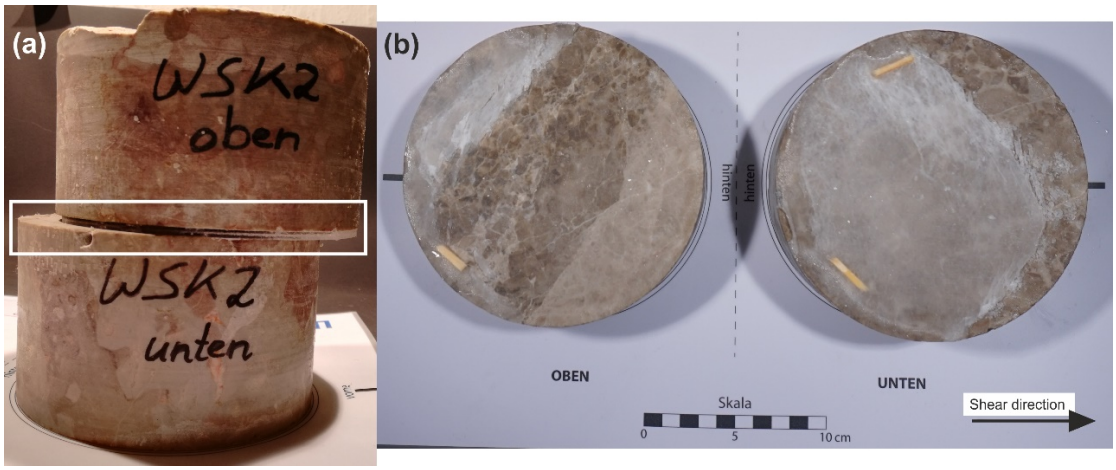

Figure 5.20: Sheared sandwich samples revealing different types of fracture along the shear planes.
(a) Fracture occurred along the rock-ice contact. (b) The composite failure type.

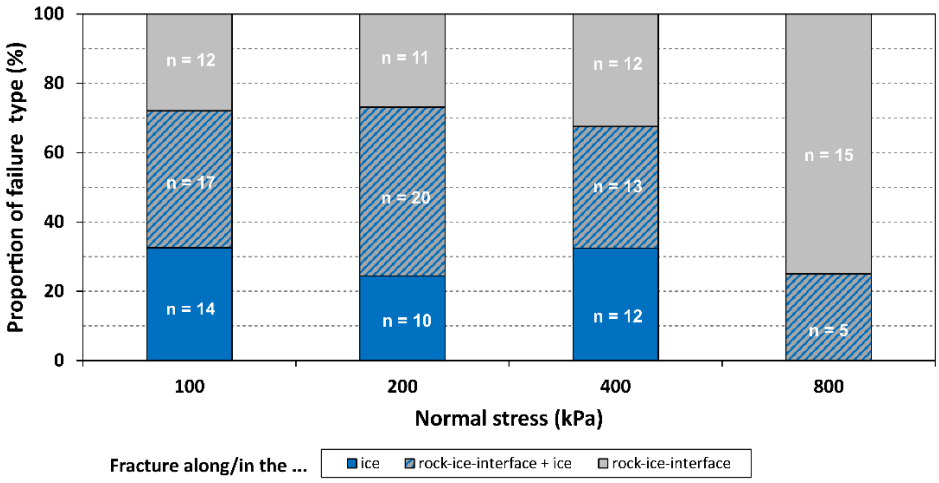

Figure 5.21: Proportions and absolute numbers of failure types for normal stresses 100–800 kPa and temperatures from -10 to -0.5 °C.

Statistical dispersion measures of the measured peak shear stress values around the failure criterion (Figure 5.11) are shown in Table 5.4. Best accordance is achieved for the shear stress means used for model calibration (correspond to significant temperature levels with *p*-values ≤ 5 %). The mean absolute deviation (MAD) and coefficient of variation (CV) range between 40–146 kPa and 8.8–24.6 % respectively. The experiments at temperatures -1, -3, -6 and -10 °C (with *p*-values > 5 %), which had been excluded from the elaboration of the failure criterion, were used for validation. Their shear stress means show higher deviations from the failure criterion, i.e. the MAD and the CV range from 98 to 252 kPa and from 15 to 43.5 % respectively.

Table 5.4: Statistical dispersion measures of the measured peak shear stress values around the new derived failure criterion.

Mean temperature [°C]	σ = 100-400 kPa		Used for model development [C]	Used as validation data for error measurement [V]
	MAD [kPa]	CV [%]		
-0.5 ± 0.1	40.0	19.9	x	
-1.1 ± 0.2	97.5	43.5		x
-2.2 ± 0.2	99.3	24.6	x	
-3.1 ± 0.2	137.8	30.5		x
-4.2 ± 0.2	145.7	19.8	x	
-4.9 ± 0.2	136.4	17.9	x	
-6.1 ± 0.2	206.6	24.6		x
-8.0 ± 0.1	110.4	8.8	x	
-10.0 ± 0.4	252.3	15.0		x

Note: Errors calculated for normal stresses 100–400 kPa refer to the valid stress range of the failure criterion. MAD = Mean absolute deviation. CV = Coefficient of variation. Validation data (V) correspond to temperatures not utilised for the elaboration of the failure criterion.

5.3. Brief communication: The influence of mica-rich rocks on the shear strength of ice-filled discontinuities

The following section constitutes the accepted version of the research article "Mamot, P., Weber, S., Lanz, M. and Krautblatter, M.: Brief communication: The influence of mica-rich rocks on the shear strength of ice-filled discontinuities, The Cryosphere, 14, 1849–1855, 2020". The final version of Publication 2 can be downloaded from https://doi.org/10.5194/tc-14-1849-2020. For inclusion in this dissertation, captions and numbers of sections, figures, tables and equations had to be modified.

5.3.1. Abstract

A temperature- and stress-dependent failure criterion for ice-filled rock (limestone) joints was proposed in 2018 as an essential tool to assess and model the stability of degrading permafrost rock slopes. To test the applicability to other rock types, we conducted laboratory tests with mica schist and gneiss, which provide the maximum expected deviation of lithological effects on the shear strength due to strong negative surface charges affecting the rock-ice interface. Retesting 120 samples at temperatures from -10 to -0.5 °C and normal stress of 100 to 400 kPa, we show that even for controversial rocks the failure criterion stays unaltered, suggesting that the failure criterion is transferable to mostly all rock types.

5.3.2. Introduction

Climate-related changes in the thermal conditions in steep bedrock permafrost can lead to rock slope destabilization or failure (e.g. Gruber and Haeberli, 2007), potentially triggering large-scale hazards via process chains (Huggel et al., 2012b). A number of failures in bedrock permafrost have exposed residual ice at their shear and detachment planes (Keuschnig et al., 2015; Phillips et al., 2017; Ravanel et al., 2017; Weber et al., 2018; Walter et al., 2020). These observations indicate the occurrence of ice-filled rock discontinuities and their importance as a controlling factor for the stability of degrading permafrost rock slopes. While the shear strength of rock joints can be increased by ice fillings due to adhesion and rock-ice interlocking (Gruber and Haeberli, 2007), warming can reduce the strength of ice-filled joints (Krautblatter et al., 2013). To improve attempts to accurately assess the stability of rock slopes with degrading permafrost due to climate change, we will have to better understand the effect of warming on the shear strength of ice-filled joints.

So far, the shear failure of ice-filled rock joints has been studied in a number of direct shear tests using samples of concrete and ice (Davies et al., 2000; Günzel, 2008). Mamot et al. (2018) added a series of constant strain shear tests with real rock samples. The ice-filled rock joints were represented by "sandwich"-like limestone-ice-limestone samples. Normal stresses of

100, 200 and 400 kPa were applied to the ice-filled discontinuities, which simulated rock overburdens of 4, 8 and 15 m, respectively. A brittle failure criterion was developed for these overburdens and validated for rock temperatures from -8 to -0.5 °C. The failure criterion is based on Mohr-Coulomb (a combination of Coulomb, 1776, and Mohr, 1900) and contains temperature- and stress-dependent cohesion and friction which decrease upon warming. When warming from -1 or -0.5 °C leads to thawing and a subsequent loss of the ice infill, the shear strength of unfrozen joints reduces slightly by approximately 100 kPa (Krautblatter et al., 2013; Mamot et al., 2018). However, the unfrozen shear strength is 400–1000 kPa lower when compared with the one of ice-filled joints at temperatures between -2 and -10 °C.

Mamot et al. (2018) postulate that their failure criterion can be applied to shear planes in all rock types, even though they solely used limestone in their laboratory experiments. The authors discussed potential influences of the rock type on the shear strength, and they emphasized the need to study a potential rock type dependency with additional laboratory tests. An inventory of rock slope failures in the central European Alps by Fischer et al. (2012) shows that the rock types, in which failure occurred and which potentially include the fracturing of ice-filled rock joints, are not only limestone but also gneiss and granite. Most of the detachment zones are likely affected by permafrost and roughly follow the assumed lower altitudinal boundary of permafrost for the respective area. Rock slopes within this boundary are expected to respond sensitively to warming and a related reduction in stability (Nötzli et al., 2010) and predominantly consist of gneiss, limestone or schist at altitudes from 2000 to 3000 m a.s.l. and mostly of gneiss or granite at altitudes >3000 m a.s.l. (Fischer et al., 2012).

Among the rock types observed to be involved in permafrost rock slope failures, gneiss and schist are metamorphic rocks with a pronounced foliation and typically show bands with a concentrated abundance of aligned, platy mica. These bands can form weak zones where shear planes develop more easily (Shea and Kronenberg, 1993). Furthermore, basal cleavage surfaces of mica carry a strong negative surface charge compared to other minerals like quartz, feldspar or calcite. When in contact with water, this leads to the formation of a common but specifically strong electrical double layer (Fenter et al., 2000; Bourg and Sposito, 2011). Such an electrical double layer causes a homogenous alignment of at first water molecules, and, with freezing, structural integrity in ensuing ice crystals (Dosch et al., 1996). As a result, adhesion at the interface is increased and the process of phase change upon warming is delayed. While the mean equilibrium freezing point in permafrost rocks is depressed to -0.7 ± 0.4 °C (Krautblatter, 2009), mica-rich rocks with strongly attractive surfaces are observed to increase the freezing temperature (Alba-Simionesco et al., 2006). Close below the melting point, this results in a crystalline contact layer on mica-rich surfaces while inner layers remain fluid. In contrast, a liquid layer forms along the rock-ice interface on weakly attractive silica-rich surfaces while

the absorbed water in the mineral is crystalline (Alba-Simionesco et al., 2006). Consequently, one would theoretically expect a stronger adhesion at the rock-ice interface for mica-rich rocks, presumably leading to a higher shear strength close below 0 °C.

Therefore, this study aims to verify if the failure criterion by Mamot et al. (2018) accounts for (i) the relevance of gneiss for permafrost rock slope failures, (ii) the abundance of gneiss and schist within the lower permafrost boundary, and (iii) the potentially significant effects of foliated metamorphic rocks with high mica content on the shear strength of ice-filled joints. For this, we performed 120 shear tests on ice-filled joints in gneiss and mica schist, rerunning the sample preparation, test set-up and procedure of Mamot et al. (2018). In the present article we address the following question: is the failure criterion for ice-filled rock joints by Mamot et al. (2018) valid for rocks with different mineral composition, specifically containing mica?

5.3.3. Methods

Two different rock types with a considerable mica content were selected for this study: gneiss that originates from the Matterhorn (45°58'52'' N, 07°40'14'' E, 3218 m a.s.l.), Switzerland, and mica schist that was involved in the Ramnanosi landslide, close to the village of Flåm (60°49'41'' N, 07°08'59'' E, 750 m a.s.l.), Norway (Figure 5.22a). The limestone samples used for the precedent laboratory tests by Mamot et al. (2018), to which this study refers, were picked from the Zugspitze (47°25'21'' N, 10°59'13'' E, 2900 m a.s.l.), Germany.

A thin section analysis was added to the direct shear tests to determine the mineral composition and the amount of mica in the rock samples. The thin sections were taken from the same rock blocks from which the cylinders for the shear tests were cored. Two thin sections were prepared of each, the gneiss and the mica schist; the results were averaged per rock type. One thin section was produced of the limestone. To account for the anisotropic nature of both gneiss and mica schist, all samples (Sect. 5.3.3.1 and 5.3.3.2) were prepared from cuts parallel to the foliation of the rocks. As such, we assume a similar mica content for both the thin sections and the sample surfaces in the shear tests.

5.3.3.1. Petrographical analysis

The thin section analysis was conducted through cross polarized light microscopy with an Olympus DP26 microscope which is standardized according to the DIN ISO 8576 (2002). The proportionate mineral compositions were recorded in a PELCON automatic point counter for a point-counter analysis as recommended by Chayes (1949). Two point-counter tracks of at least 100 points were indexed on each thin section. We estimated the mica content on sample surfaces via image histogram analysis.

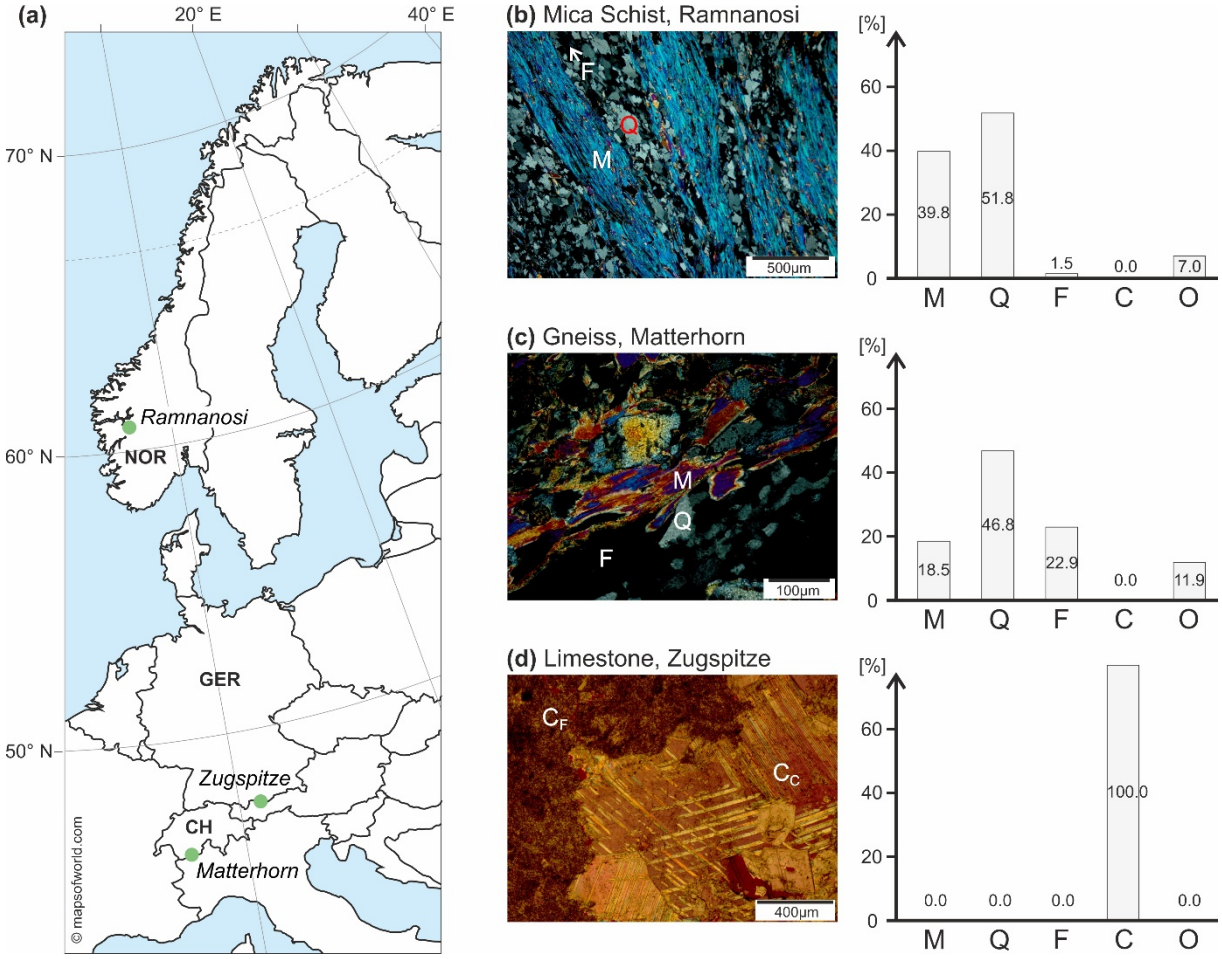

Figure 5.22: (a) Map showing the locations where samples for this study and the previous one by Mamot et al. (2018) were collected. Panels (b), (c) and (d) show associated results of thin section analyses.

M refers to mica, Q to quartz, F to feldspar, C to calcite (C_F: fine grains; C_C: coarse grains) and O to others.

5.3.3.2. Shear experiments

The sample preparation, set-up and procedure of the tests were conducted according to Mamot et al. (2018) to guarantee comparability: (i) each rock-ice-rock sandwich sample consisted of two pieces of rock with a surface roughness of 80 grains per inch and its gap is filled with a 3.5 ± 0.5 mm thin ice layer. (ii) We used the same custom-built shear apparatus installed in a temperature-controlled cooling box. (iii) We applied a constant strain rate of $5 * 10^{-3}$ s^{-1}, provoking brittle fracture of ice and thereby representing the well-advanced stage of rock slope failure.

Tests were performed at temperatures of -10, -6, -2, -1 and -0.5 °C and at normal stress levels of 100, 200 and 400 kPa. Four tests were conducted per rock type and per combination of temperature and normal stress, leading to a total of 120 tests. As in the tests by Mamot et al. (2018),

the type of failure was identified qualitatively by visual inspection of the failure surfaces immediately after removing them from the shear apparatus. Samples which did not allow a definite failure type classification were assigned to the mixed failure.

5.3.4. Results and interpretation

5.3.4.1. Mineral composition relevant for rock-ice interfaces

The mica schist is a fine-grained rock with well-developed foliation. Layers of dark mica, predominantly biotite, and light quartz and plagioclase alternate in the rock. In the thin section analysis (Figure 5.22b) the mica schist shows very distinct bands of mica (39.8 %) in a ground mass mostly comprised of quartz (51.8 %). Other minerals identified in the sample are feldspar and chlorite as well as possibly sillimanite and amphibole. An average porosity of 1.3 % was determined in the thin section analysis. The gneiss is clearly laminated and shows bands of mica (18.5 %), yet it is less distinctly layered than the mica schist (Figure 5.22c). The main components are quartz (46.8 %) and feldspar (22.9 %); other minerals identified in the sample are chloritoid and epidote as well as traces of chlorite, amphibole and rutile. Furthermore, the porosity of the gneiss is considerably low (0.9 %, Dräbing and Krautblatter, 2012) compared to the mica schist. Both rock types show a high abundance of mica minerals at the sample surfaces, presumably leading to a higher concentration of negative surface charges than at limestone surfaces. The latter is only constituted of calcite without any occurrence of mica (Figure 5.22d).

5.3.4.2. Shear tests of rock-ice interfaces with mica-rich rocks

Mamot et al. (2018) subdivided the paths of shear stress and shear strain into five distinct stages including (i) consolidation, (ii) adjustment to the sample holder, (iii) build-up of the shear stress, (iv) failure and (v) post-failure behaviour. The same pattern can be identified by the presented laboratory tests with mica-rich rocks. We also observe a general decrease in peak shear stress with increasing temperature from -10 to -0.5 °C at all tested normal stress levels, without any systematic difference between the samples of mica schist and gneiss (Figure 5.23). Overall, the measured peak shear stresses of this study lie well within, or close to, the range of the failure criterion (dark blue area in Figure 5.23). Even the laboratory tests conducted at -10 °C fit mostly within the expected values of the same failure criterion, although they are outside the valid temperature range proposed. Nevertheless, the measured peak shear stresses tend to fall below the failure criterion for the same temperature and at a normal stress of 400 kPa. This pattern is also noted in the previous tests with limestone (grey triangles in Figure 5.23) and in the concrete-ice shear experiments by Günzel (2008), possibly due to the beginning transition from brittle to ductile failure with higher rock overburden leading to a lower shear strength (Renshaw and Schulson, 2001). When approaching the melting point of the ice, above

-2 °C, the measured peak shear stresses slightly exceed the calculated range of the failure criterion.

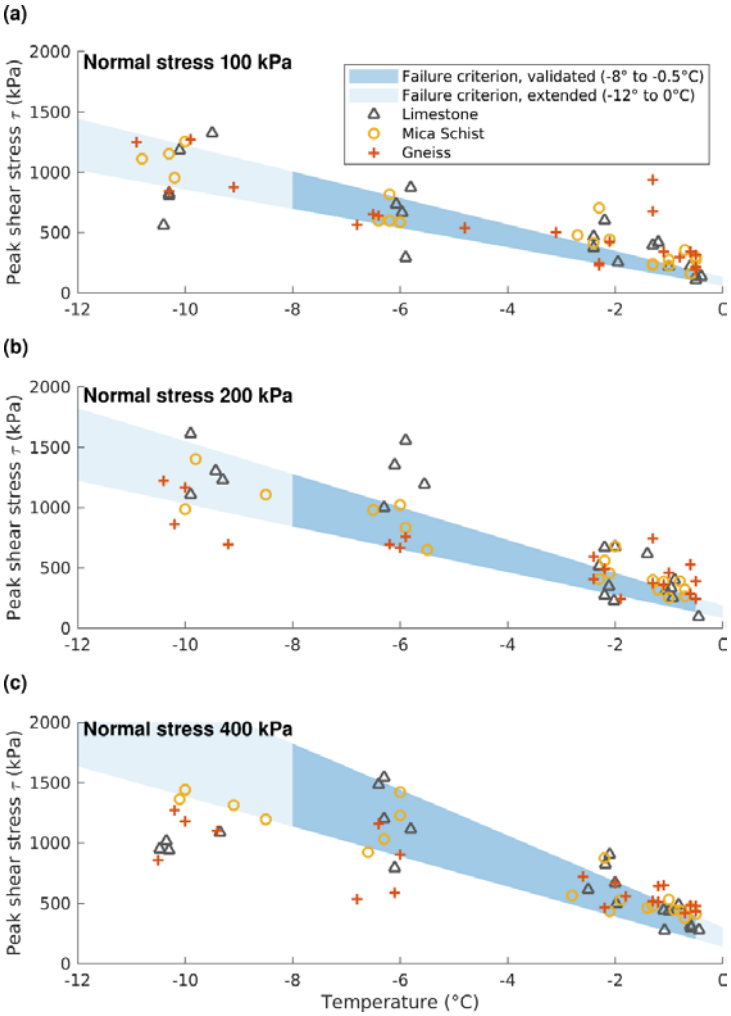

Figure 5.23: Peak shear strength across sub-zero temperature of ice-filled rock joints constituted of gneiss (red crosses), mica schist (orange circles) and limestone (grey triangles).

The relationships are plotted for normal stresses of (a) 100, (b) 200 and (c) 400 kPa. The limestone data are added from previous tests by Mamot et al. (2018). The validated range of the failure criterion by Mamot et al. (2018) is marked in dark blue while an extended section to -12 and to 0 °C is displayed in light blue.

Figure 5.24 illustrates the temperature-dependent ratio of failure types that were observed in the shear tests for distinguishing rocks with and without mica content. Failure within the ice is very dominant for mica-rich rocks in the temperature range from -10 to -1 °C, but absent at -0.5 °C. In contrast, rock without mica (limestone) shows a gradual decrease in the ratio of failure within the ice and a gradual increase in the ratio of failure along the rock-ice interface with warming. Overall, it is remarkable that the fracture along the rock-ice interface and mixed fracture are the only failure types at -0.5 °C for limestone and mica-rich rocks.

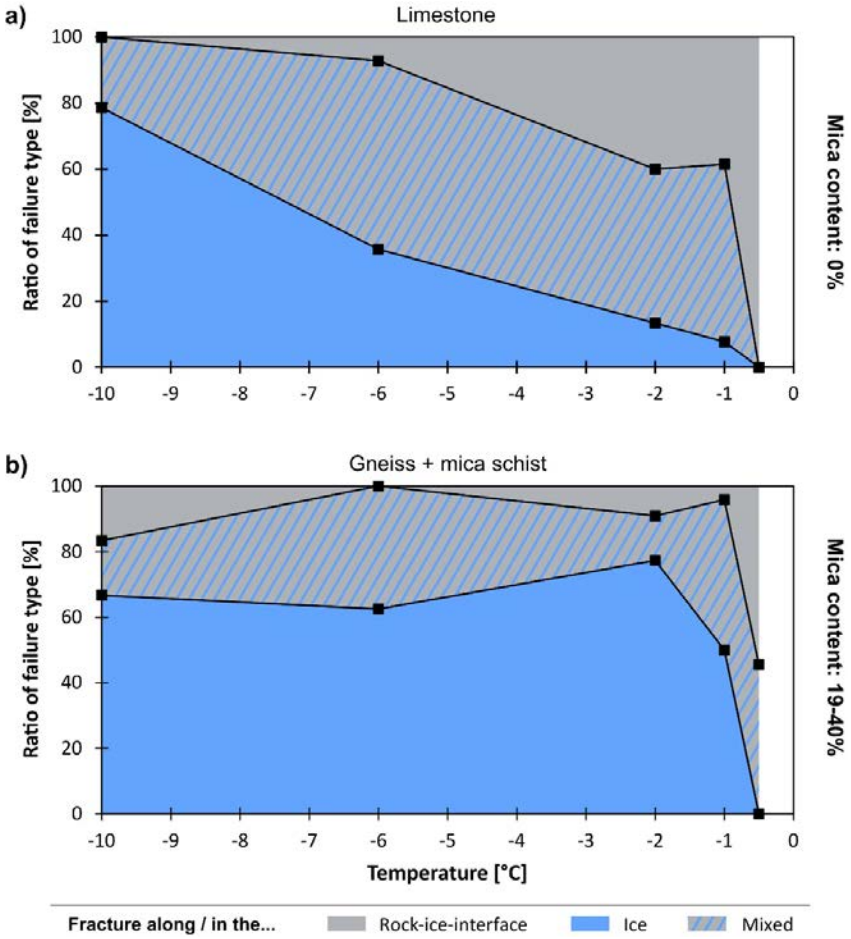

Figure 5.24: Ratios of failure types versus temperature for (a) mica-free (0 %) and (b) mica-rich (19–40 %) surfaces in ice-filled rock joints.

Failure in mica-rich joints is dominated by fracturing inside the ice layer, whereas at temperatures warmer than -1 °C failure is controlled by fracturing along the rock-ice interface and the mixed type. However, in mica-free joints the proportion of ice fracturing decreases gradually when approaching the melting point of ice while rock-ice fracturing gains importance, especially at temperatures warmer than -1 °C.

5.3.5. Discussion

In Mamot et al. (2018) the question remained open if the failure criterion for ice-filled rock joints was transferable to rock types other than limestone. As Fischer et al. (2012) demonstrated that gneiss and schist are among the most relevant rock types involved in rock slope failures within the Alpine mountain permafrost belt, this study aims at testing the applicability of the failure criterion for those rock types. Furthermore, gneiss and schist were selected since they are characterized by foliation with high mica content, which may potentially affect the shear strength of ice-filled joints close to 0 °C.

We quantified the shear strength of ice-filled discontinuities in mica-rich rocks, which fits well to the temperature- and normal stress-dependent failure criterion (Figure 5.23), thereby indicating its validity for mica-rich rocks. It is remarkable that the failure criterion seems to be conservative for conditions close to 0 °C compared to the shear tests with mica-rich rocks.

However, this underestimation of shear strength does not state a problem for any purpose of rock slope stability assessment and, hence, does not diminish the applicability of the failure criterion. The higher shear strength close to 0 °C for mica-rich rocks has been expected by the authors and may be explained by the higher adhesion at the rock-ice interface, the delayed phase change upon warming and the absence of a liquid layer along mica-rich joint surfaces close to the melting point of ice. The strengthening effect of the rock-ice contact by mica also becomes evident when looking at the temperature-dependent distribution of failure types (Figure 5.24): while in mica-rich rocks failures along the rock-ice interface only dominate at temperatures warmer than -1 °C, in limestone (without mica) the same failure type gradually gains in importance at temperatures warmer than -6 °C.

Previous publications on the shear strength of ice-filled rock joints relate to a small number of tests on samples with ice and concrete, generally not below -5 °C (Günzel, 2008; Davies et al., 2000). Krautblatter et al. (2013) developed a first failure criterion which was based on the experiments by Günzel (2008). About 5 years later, Mamot et al. (2018) proposed an improved failure criterion which refers to rock-ice-rock samples and covers a broader range of bedrock temperatures. This study demonstrates that the failure criterion by Mamot et al. (2018) is surprisingly resilient as it can be applied to (i) different failure types including the fracture in ice and along the rock-ice contact, (ii) a wide range of temperatures relevant for bedrock permafrost (-0.5 to -8 °C), (iii) a wide range of relevant stress conditions (100-400 kPa) and (iv) mostly all rock types relevant for permafrost rock slope failures in the Alps, as the metamorphic mica-rich rocks tested in this study represent the expected maximum deviation of potential lithological effects on the shear strength of ice-filled rock joints. This strong deviation is established due to three characteristics of the tested rock types:

(i) They are foliated and typically have a high amount of mica aligned subparallel within major shear planes. This property and the resulting effect of the surface charge are expected to be more emphasized along natural joints than along the tested surfaces, as these were cut within intact rock samples.

(ii) The platy and subparallelly aligned mica grains lead to a very low surface roughness, potentially reducing the shear strength. This effect will become more relevant at temperatures close to 0 °C where we observe a higher proportion of fractures along the rock-ice interface. As it is hard to define a representative surface roughness for typically diverse natural fractures, and to guarantee reproducibility of the laboratory rock surfaces, we standardized the joint surface roughness in our tests. Therefore, we assume the effect of varying surface roughness and its dependence on the rock type to be visible in natural fractures, but not in our tests.

(iii) The strong negative surface charge results in an elevated adhesion and equilibrium freezing point which likely leads to a higher peak shear strength.

Due to the uniform surface roughness in the presented tests, we are not able to determine the extent to which the reduction in shear strength by a lower surface roughness (see ii) may offset the increase in shear strength by a strong negative surface charge (see iii). But, overall, we expect the observed mica-dependent higher shear strength close to 0 °C to be suppressed slightly.

5.3.6. Conclusions

In this study, we carried out 120 constant strain rate shear tests on ice-filled joints in gneiss and mica schist to investigate a potential influence of metamorphic foliated rocks with a high amount of mica on the shear resistance of ice-filled discontinuities. Based on the laboratory tests, we could demonstrate a slight increase in peak shear strength at temperatures close to 0 °C, which is most likely caused by the presence of mica. However, overall our data correspond well with the failure criterion for ice-filled rock joints introduced by Mamot et al. (2018). As the tested mica-rich rocks represent the expected maximum deviation of potential lithological effects on the shear strength, we conclude that the failure criterion is transferable to a wide variety of rock types relevant for permafrost rock slope failures in the Alps.

5.4. Unfilled rock joints

Laboratory experiments were performed on the basic friction angle φ_b and the Schmidt hammer rebound hardness (R for unweathered sawn surfaces, and r for weathered surfaces) of frozen and unfrozen rock joints of the field site material. Both parameters were later used to estimate the residual friction angle φ_r according to Barton and Choubey (1977; Section 6.3.1.3). The experiments were conducted to extend the knowledge of the thawing influence on the mechanical strength and deformability of clean rock joints, and to determine the required material parameters for the discontinuities in the numerical discontinuum model.

5.4.1. Preparation of the rock samples

For the basic friction angle of the rock joints, we performed 110 tilt tests with unweathered sawn rock surfaces of frozen and unfrozen Wetterstein limestone following the procedure suggested by Barton and Choubey (1977) and Barton (2013). For the Schmidt hammer rebound hardnesses R and r, we conducted a series of Schmidt hammer tests in the laboratory with four dry unweathered sawn and three wet weathered rock surfaces of frozen and unfrozen Wetterstein limestone. The tests were prepared and realised following the proposed procedure of the International Society for Rock Mechanics (ISRM; Ulusay, 2015) and Aydin et al. (2005).

The rock samples were cored from Wetterstein limestone blocks with a mean side length of 0.4 ± 0.1 m that were picked from the study site or the lower Zugspitzplatt (2590 m a.s.l.; Figure 6.1). The rock cores were cut with a diamond saw into 10 cylinders for the tilt tests, while two of them were taken for testing the Schmidt hammer rebound hardness R (Figure 5.4). The samples for the tilt tests had a mean height of 83.1 ± 2.6 mm and the samples for the Schmidt hammer tests on unweathered joint surfaces had a mean height of 84.1 mm. The corresponding mean diameters ranged between 148.5 ± 0.2 and 148.6 mm, respectively. The wet weathered joint surfaces (for determining r) were tested at a single Wetterstein limestone block with a volume of 0.02 m³, collected from the Zugspitze summit ridge.

5.4.2. Test set-ups and procedures

Unfrozen conditions corresponded to ambient room temperature. Frozen conditions for the tilt tests and the Schmidt hammer tests on unweathered joint surfaces were achieved by storing the rock specimens in a cooling box at -28 °C for 48 h. The bigger block for the Schmidt hammer tests on wet weathered joint surfaces were stored for 48 h in a bigger, self-constructed and isolated cooling box at -10 °C. The samples were tested directly after taking them out of the cooling box. As the experiments did not exceed 2-4 min, we could guarantee the rock samples to be frozen during the tests. Isolation of the specimens during the tests was technically

not feasible. Any ice layer that could have developed at the rock surfaces during freezing was carefully removed before testing to prevent a potential influence on the results.

According to the ISRM (Ulusay, 2015), samples for Schmidt hammer tests have to be firmly fixed to a heavy steel base or a firm and flat ground to avoid a potential loss of impact energy. The big rock block was too heavy to move during the tests. However, the smaller and lighter rock cylinders (for determining *R*) were mounted with their flat ends between two load platens of a ToniNorm uniaxial compression machine (with a maximum applicable load of 250 kN). After that, the samples were firmly fixed by applying an axial load of 60 N.

A Schmidt hammer of the N-type was used for testing the rebound hardness (Figure 5.1f). For the unweathered surfaces, the impacts by the plunger tip of the hammer were applied to the rounded smooth sides of the cylinders. The impacts were distributed along the cylinder sides by rotating it on the flat ends in steps of 90°. The weathered surface of the bigger rock block was sampled on two faces of the specimen. We collected at least 20 impact readings per specimen and averaged the upper 50 %. Rebound values collected in down- or upward direction were normalised in accordance with the ISRM standard (Ulusay, 2015).

The weathered surface of the rock block was characterised by a higher roughness and small asperities which got partly destroyed by the hammer impacts. This led to a higher variation in the data.

6. A temperature-dependent mechanical model to assess the stability of degrading permafrost rock slopes

The following section is the accepted version of the research article "Mamot, P., Weber, S. Eppinger, S. and Krautblatter, M.: A temperature-dependent mechanical model to assess the stability of degrading permafrost rock slopes", Earth Surface Dynamics, 9, 1125-1151, 2021. The final version of Publication 3 can be accessed at https://doi.org/10.5194/esurf-2020-70. For inclusion in this dissertation, the numeration of sections, figures, tables and equations had to be adjusted.

6.1. Abstract

Over the last 2 decades, permafrost degradation has been observed to be a major driver of enhanced rock slope instability and associated hazards in high mountains. While the thermal regime of permafrost degradation in high mountains has been addressed in several modelling approaches, no mechanical models that thoroughly explain rock slope destabilisation controls in degrading permafrost have been developed. Meanwhile, recent laboratory studies have shown that degrading permafrost affects both, rock and ice mechanical strength parameters as well as the strength of rock–ice interfaces.

This study presents a first general approach for a temperature-dependent numerical stability model that simulates the mechanical response of a warming and thawing permafrost rock slope. The proposed procedure is exemplified using a rockslide at the permafrost-affected Zugspitze summit crest. Laboratory tests on frozen and unfrozen rock joint and intact rock properties provide material parameters for discontinuum models developed with the Universal Distinct Element Code (UDEC). Geophysical and geotechnical field surveys reveal information on permafrost distribution and the fracture network.

This model can demonstrate how warming decreases rock slope stability to a critical level and why thawing initiates failure. A generalised sensitivity analysis of the model with a simplified geometry and warming trajectory below 0 °C shows that progressive warming close to the melting point initiates instability above a critical slope angle of 50–62°, depending on the orientation of the fracture network. The increase in displacements intensifies for warming steps closer to 0 °C.

The simplified and generalised model can be applied to permafrost rock slopes (i) which warm above -4 °C, (ii) with ice-filled joints, (iii) with fractured limestone or probably most of the rock types relevant for permafrost rock slope failure, and (iv) with a wide range of slope angles (30–70°) and orientations of the fracture network (consisting of three joint sets). Here, we present a benchmark model capable of assessing the future destabilisation of degrading permafrost rock slopes.

6.2. Introduction

Rock slope failures in high-mountain areas endanger human lives, settlements and infrastructure. The stability of alpine rock slopes can be considerably affected by the climate-induced degradation of bedrock permafrost (Fischer et al., 2006; Gruber et al., 2004; Gruber and Haeberli, 2007; Ravanel and Deline, 2015). The best empirical trends are provided by the well-monitored rock slope failures in the Mont Blanc Massif that have been linked to the degradation of bedrock permafrost and ice-filled joints (Ravanel et al., 2010; Ravanel and Deline, 2008, 2011).

Mountain permafrost warmed globally by 0.19 °C between 2007 and 2016 (Biskaborn et al., 2019). Simulations of long-term permafrost evolution in Swiss, German or Norwegian mountain ranges show an overall warming of permafrost and thaw layer deepening up to the end of the century (Gallemann et al., 2017; Hipp et al., 2012; Marmy et al., 2016). Rock slope failures influenced by permafrost degradation are expected to become more frequent as a result of the warming climate (Gobiet et al., 2014; Huggel et al., 2012a).

Most rock slope failures develop along discontinuities, whose patterns predetermine potential critical paths of failures (Wyllie, 2018). Fractures and fractured zones in mountain bedrock permafrost contain massive ice to depths of several tens of metres or more (Deline et al., 2015; Gruber and Haeberli, 2007). The majority of failure events in permafrost-affected rock exposed ice-filled joints as potential shear and detachment planes at different volumetric scales all over the world. Some prominent examples are the 2003 Matterhorn block fall ($0.002 * 10^6$ m^3; Weber et al., 2019), the 2014 Piz Kesch rock slope failure ($0.15 * 10^6$ m^3; Phillips et al., 2017) and the 2017 Pizzo Cengalo failure with eight fatalities ($3–4 * 10^6$ m^3; Walter et al., 2020; Mergili et al., 2020) in Switzerland; the 1987 Val Pola debris avalanche in the Italian Alps ($33 * 10^6$ m^3; Dramis et al., 1995); the 2005 Mount Steller rock–ice avalanche in Alaska ($40–60 * 10^6$ m^3; Huggel et al., 2010); and the 2002 Kolka–Karmadon rock–ice avalanche with 140 fatalities in the Russian Caucasus ($100 * 10^6$ m^3; Huggel et al., 2005).

The warming of permafrost in rock slopes reduces the shear resistance along rock joints by (i) reducing the fracture toughness of cohesive rock bridges, (ii) lowering the friction along rock–rock contacts, (iii) altering the creep of ice infillings, and (iv) reducing the fracture toughness of ice fillings and of rock–ice contacts (Krautblatter et al., 2013). Ice fillings contribute to higher rock joint shear strengths in terms of interlocking and adhesion along the rock–ice interface and increase the stability of a rock slope. The strength of ice in fractures decreases when the temperature approaches the melting point (Davies et al., 2001; Gruber and Haeberli, 2007; Mamot et al., 2018). Several laboratory test series have demonstrated the influence of warming or thawing on the mechanical properties of rock and ice: the ductile temperature- and stress-dependent creep of ice and ice-rich soils has been investigated in studies such as Arenson and

Springman (2005), Bray (2013) and Sanderson (1988). Whilst the brittle failure and creep of ice-filled rock joints have been observed by Davies et al. (2000) and Günzel (2008), Mamot et al. (2018) proposed a new failure criterion that demonstrates the loss of ice friction and cohesion in rock fractures dependent on normal stress and temperature. The mechanics of frozen and unfrozen intact rock have been studied in works such as Dwivedi et al. (2000), Inada and Yokota (1984), Kodama et al. (2013), Mellor (1973), Pläsken et al. (2020) and Voigtländer et al. (2014). The friction along frozen and unfrozen rock joints was measured by Krautblatter et al. (2013). Table 6.1 summarises the temperature-dependent strength reduction for all of these investigated mechanical parameters.

The necessity to better link permafrost degradation and rock slope stability has been stated several times (Etzelmüller, 2013; Harris et al., 2009; Krautblatter et al., 2012). However, the attempt to study the effect of warming or thawing on the mechanical response of a rock slope has been realised only once: Davies et al. (2001) simulated the warming of a simplified, full rock slope in a laboratory centrifuge model and estimated factors of safety for unfrozen and ice-filled joints at temperatures close to the melting point using mechanical properties from prior laboratory shear tests by Davies et al. (2000).

Numerical modelling is an established method to (i) mechanically assess rock slope stability and characterise failure, deformation and influencing factors (Stead et al., 2006), and (ii) thermally analyse the spatial distribution and evolution of permafrost in a mountain or rock slope (Haberkorn et al., 2017; Moore et al., 2011; Myhra et al., 2017; Nötzli and Gruber, 2009). However, no temperature-dependent mechanical numerical model has been developed yet that implements the deformation and strength reduction of permafrost bedrock and ice-filled discontinuities upon warming or thawing. To anticipate failure in a warming climate, we need to understand how the mechanical components of rock and ice control rock slope destabilisation and how failure in warming permafrost rocks can be mechanically expressed in models.

Discontinuum discrete element codes simulate the deformation behaviour of fractured rock masses and consider the influence of jointing (Stead et al., 2006). Among these codes, UDEC (Universal Distinct Element Code) is one of the most commonly used modelling tools for distinct element modelling of jointed and blocky material in 2D and has been applied in numerous published stability analyses on unfrozen rock slopes (Bhasin and Kaynia, 2004; Fischer et al., 2010; Gischig et al., 2011a, b, c; Glamheden and Lindblom, 2002; Kveldsvik et al., 2008; Welkner et al., 2010).

Table 6.1: A systematic survey of previous laboratory studies on the thaw-dependent strength reduction of mechanical properties of rock, rock joints and ice.

The original version of this table in Mamot et al. (2021) was slightly modified by adding two further properties.

Mechanical parameter	Decrease due to warming		Temperature range tested [°C]	Type of rock / Normal stress	Reference
	% °C^{-1}	absolute			
Uniaxial compressive strength [MPa]					
rock	1.5	200 to 170	-10 to 0	granite	Mellor (1973)
	4.7	95 to 50		sandstone	
	5	70 to 35		limestone	
	2	45 to 30	-20 to -5	tuff and andesite	Kodama et al. (2013)
	0.6	220 to 165	-40 to 0	granite	Inada and Yokota (1984)
	0.9	200 to 130	-40 to 0	andesite	
polycrystalline ice	1.5	6 to 1.5	-50 to 0	--	Inada and Yokota (1984)
	1.7	17 to 3	-50 to 0	--	Schulson and Duval (2009)
	5	4 to 2	-10 to 0	--	Butkovitch (1954)
Uniaxial tensile strength [MPa]					
rock	1.7	12 to 10	-10 to 0	granite	Mellor (1973)
	6.7	12 to 4		sandstone	
	6.7	12 to 4		limestone	
	4	5.5 to 2.5	-20 to -5	tuff and andesite	Kodama et al. (2013)
	1.1	14 to 10	-20 to 0	granodiorite	Glamheden (2001)
	0.6	12 to 9	-40 to 0	granite	Inada and Yokota (1984)
	1.1	20 to 11.5	-40 to 0	andesite	
polycrystalline ice	0.9	2.5 to 1.4	-50 to 0	--	Inada and Yokota (1984)
	1.3	1.5 to 1.3	-10 to 0	--	Butkovitch (1954)
Young's modulus [GPa]					
rock	0.5	42 to 39	-15 to 0	granodiorite	Glamheden (2001)
polycrystalline ice	0.1	--	-50 to 0		Schulson and Duval (2009)
Poisson's ratio					
rock	0.7	0.27 to 0.24	-15 to 0	granodiorite	Glamheden (2001)
Fracture toughness [MPa m$^{-0.5}$]					
rock bridges	0.8	1.2 to 0.8	-10 to 30	limestone	Dwivedi et al. (2000)
	0.9	0.4 to 0.2		sandstone	
	0.02	1.5 to 1.5		basalt	
	0.2	1.6 to 1.4		dolerite	
polycrystalline ice	0.6	0.1 to 0.08	-50 to -2	--	Schulson and Duval (2009)
P-wave velocity [km s^{-1}][a]					
rock	2.8	6.4 to 3.7	-15 to 0	limestone[b]	Draebing and Krautblatter (2012)
	0.8	6.1 to 5.4		gneiss[b]	
	1	6.1 to 5.2		granodiorit[b]	
Joint shear strength [MPa]					
concrete-ice	18.1	0.4 to 0.1	-5 to -0.5	100 kPa	Davies et al. (2000)
	16	0.8 to 0.2		1400 kPa	
	31	0.5 to 0.2	-2.5 to 0	140 kPa	Krautblatter et al. (2013)
	24	0.6 to 0.3		500 kPa	
ice-steel-ice	10.2	1.1 to 0.2	-10 to -2	--	Jellinek (1959)

Table 6.1: Continued.

rock-ice-rock	7.4	1 to 0.3	-10 to -0.5	limestone, 100 kPa	Mamot et al. (2018)
	8.2	1.4 to 0.3		limestone, 200 kPa	
	6.7	1.4 to 0.5		limestone, 400 kPa	
	17.2	1 to 0.4	-4 to -0.5	limestone, 800 kPa	
rock-rock	21	0.63 to 0.5	-4.5 to 22	dolomite, 800 kPa	Krautblatter et al.
	9	0.55 to 0.5		limestone, 800 kPa	(2013)
Joint friction angle [°]					
rock-rock	0.4	43.1 to 38.7	-4.5 to 22	dolomite	Krautblatter et al.
	0.6	35.5 to 30		limestone	(2013)
rock-ice-rock	10	64.5 to 27.7	-8 to -0.5	limestone, 100-400 kPa	Mamot et al. (2018)
	17	30.5 to 13.5	-4 to -0.5	limestone, 100-800 kPa	
	4	47.7 to 13.5	-18.5 to -0.5	granite	Barnes et al. (1971)
Joint cohesion [MPa]					
rock-ice-rock	11.5	0.6 to 0.1	-8 to -0.5	limestone, 100-400 kPa	Mamot et al. (2018)
	21.2	0.7 to 0.2	-4 to -0.5	limestone, 100-800 kPa	

Note: [a]The P-wave velocity of rock correlates highly to Mode I fracture toughness which relates closely to Mode II fracture toughness (Chang et al., 2002). [b]P-wave velocities are parallel to cleavage/bedding.

In this paper, we present the first numerical model that calculates the influence of warming and thawing of frozen rock and rock joints on the mechanical strength and deformation behaviour of a rock slope. The proposed model is applied to a rockslide at the permafrost-affected Zugspitze summit which is one of the highest peaks of the Northern Calcareous Alps, located in the Eastern Alps. In this context, we address the following research questions:

1) How can mechanical and thermal data from the field and from the laboratory be combined to develop a numerical stability model for a warming and thawing permafrost rock slope?
2) Is the numerical stability model of the Zugspitze summit crest capable of simulating the warming-dependent changes in stability observed at the laboratory scale?
3) How is the generic stability of a warming permafrost rock slope dependent on the slope angle and the orientation of the fracture network?

6.3. A general approach applied to the Zugspitze summit crest

A slowly moving rockslide at the Zugspitze summit crest (2900 m a.s.l.), Germany, with extensive monitoring data on kinematics and degrading permafrost bedrock was chosen to develop a close-to-nature rock slope instability model for degrading permafrost rock slopes (Figure 6.1; see also Mamot et al., 2018). Homogeneous lithology, well-known permafrost degradation history for the Zugspitze summit area and the accessibility to an ice-filled rock sliding surface (Figure 6.1c) made it an ideal benchmark for the mechanical model development. The model profile and the characteristics of the fracture network for the numerical model were

taken from the study site. Rock specimens collected in close proximity to the rockslide were used for a unique set of mechanical laboratory tests on a broad spectrum of frozen and unfrozen intact rock and rock joint properties. Intact rock properties were converted to rock mass characteristics using internationally standardised mathematical equations. Electrical resistivity tomography (ERT) was applied to identify current frozen and unfrozen slope sections. These were implemented in the numerical model to spatially assign frozen or unfrozen rock mass and joint parameters to the corresponding model sections and to derive a rough spatial warming pattern. Considering the numerous laboratory-based observations of the strength reduction of the mechanical properties of rock and ice at warming/thawing (Table 6.1), we expect to model a significant effect on the slope stability. For this, we set up a discontinuum model in 2D with UDEC 7. In a first step, we modelled the numerical impact of warming and thawing on the stability of the Zugspitze summit crest with ice-filled joints. In a second step, we applied the same model to a frozen rock slope with simplified geometry to study the numerical impact of rising sub-zero temperature on the rock slope stability for varying slope angles and orientations of the joint set configuration.

Figure 6.2 demonstrates a general procedure to develop a numerical discontinuum model to calculate the influence of warming and thawing on the mechanical strength and deformation behaviour of a (partially) frozen rock slope. Here, we present one exemplary way of applying the set-up of the model and the modelling procedure to a real-world example of alpine rock slope instability potentially affected by permafrost degradation. For instance, the detection of bedrock permafrost can also be performed using other techniques like seismic refraction tomography; similarly, the conversion of the intact rock properties to those of the rock mass can also be done using the Q-value (and not by the geological strength index (GSI) scheme, as presented in this article).

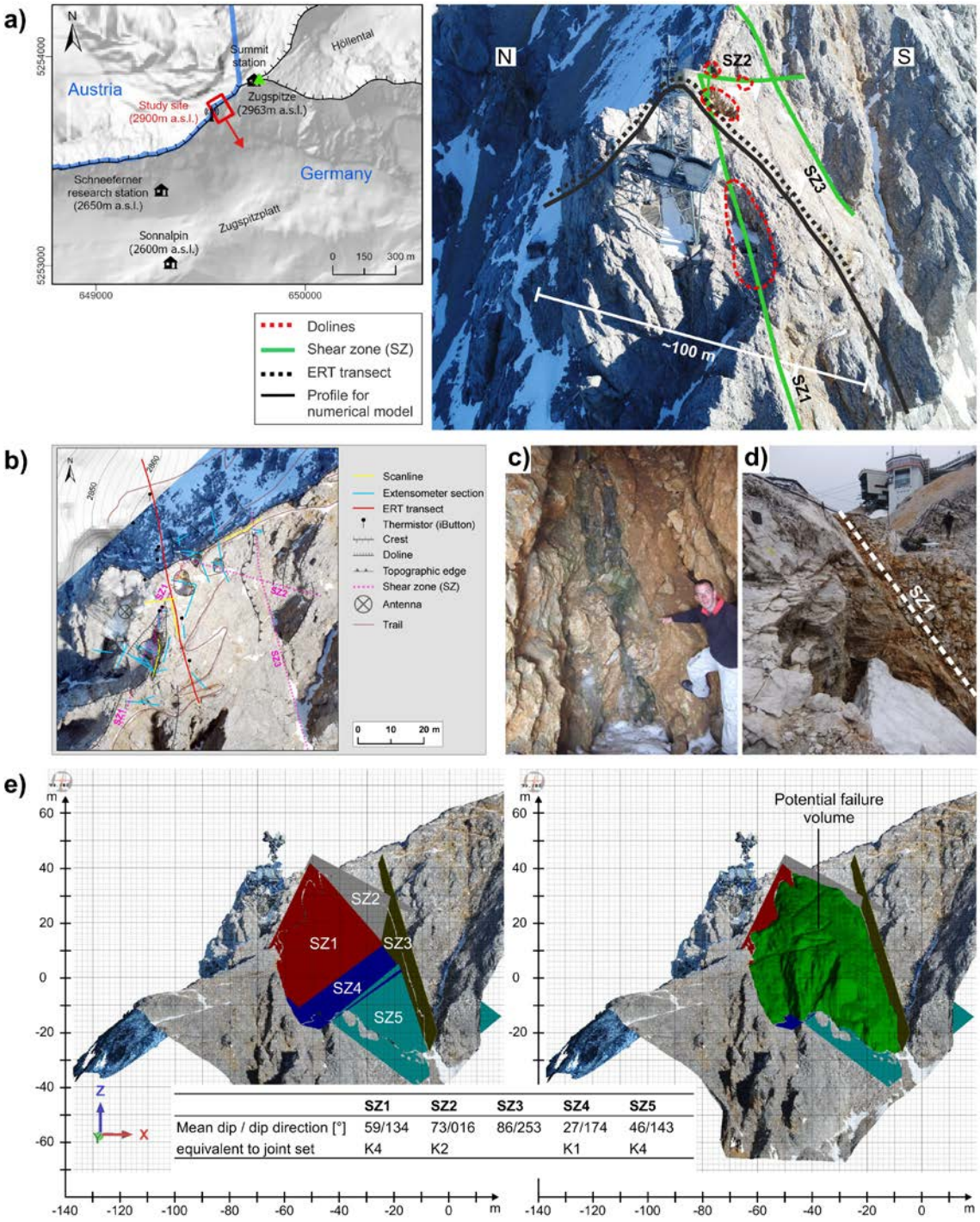

Figure 6.1: Location of the study site at the Zugspitze peak, network of field measurements and geological, structural features of the rock slope instability.

The left side of panel (a) shows the location of the study site (red box) in the Zugspitze summit area, ca. 60 m below the peak (2963 m a.s.l.). The red arrow points in the sliding direction of the unstable rock mass. The hillshade is calculated from a digital elevation model with a cell size of 10 m for Austria and 5 m for Germany (Bavarian Agency for Digitisation, High-Speed Internet and Surveying, 2006). Coordinates are given in ETRS 1989 UTM Zone 32N. The right side of panel (a) is the view from above down on the study site, including dolines, the assumed main shear zones of the upper part of the rockslide, the profile used for the numerical model and the transect for the electrical resistivity survey. Panel (b) displays the network of geophysical and geotechnical measurements at the study site, including reference to geomorphologic and anthropogenic features. The orthophoto is derived from UAV-based photogrammetry. Panels (c) and (d) display the shear zone SZ1 filled with ice or with fine material, exposed at the inner wall of dolines. Panel (e) outlines the intersecting main shear zones which delineate the unstable rock mass at the south face of the Zugspitze summit crest both with (right) and without (left) the potential failure volume.

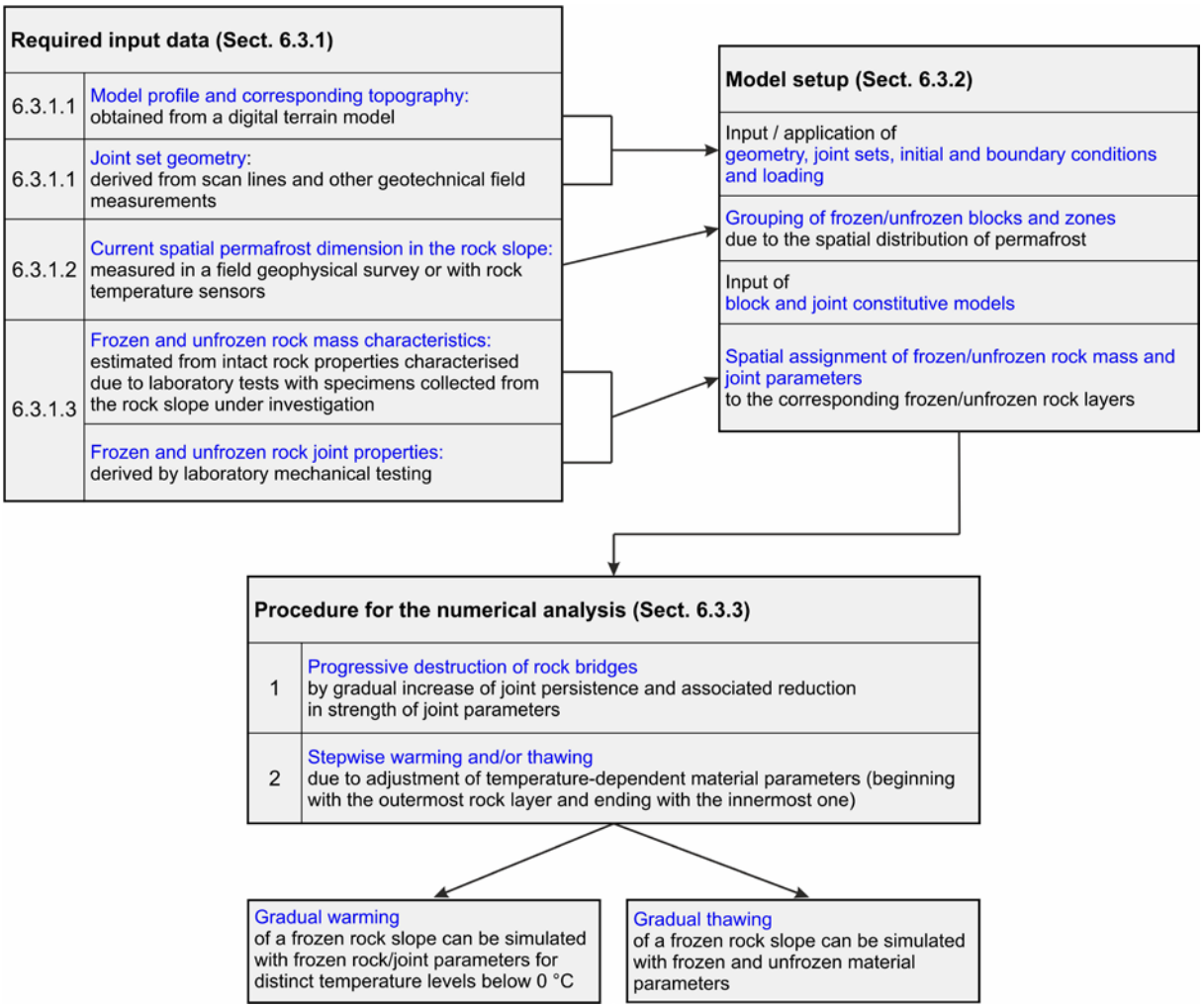

Figure 6.2: General procedure for a temperature-dependent mechanical discontinuum model for the stability of a warming or thawing permafrost rock slope.

The procedure is embedded as a methodological approach in this paper and, hence, is linked to specific sections. Their numbers have been modified from the original version.

6.3.1. Characterisation of the mechanical and thermal setting

6.3.1.1. Model profile, rock joint geometry and kinematic analysis

The numerical model was set up in 2D and, thus, required a cross section of the summit crest. This profile covers a distance of 100 m; it runs from the north face, across the crest line, to the south face; and it crosses one of the main shear zones of the rockslide (Figure 6.1a, Figure 6.1b). Four discontinuity sets (K1–K4) were identified in scan lines and field mapping (Figure 6.3a). The profile for the mechanical model strikes at 146°, which is in the direction of the assumed movement and follows the dip of the southern slope face (45/160). K2 (33/063) was excluded from the numerical analysis, as the dip direction deviated by 66.5° from the model profile. The remaining joint sets deviating by 20–33° were implemented in the model, as the standard deviations of their dip directions ranged between 5 and 20°, falling within the tolerable range of

30° deviation (Table 6.2). Joint set K1 represents the bedding planes and daylights in the south face at an angle of 24° (Figure 6.3b).

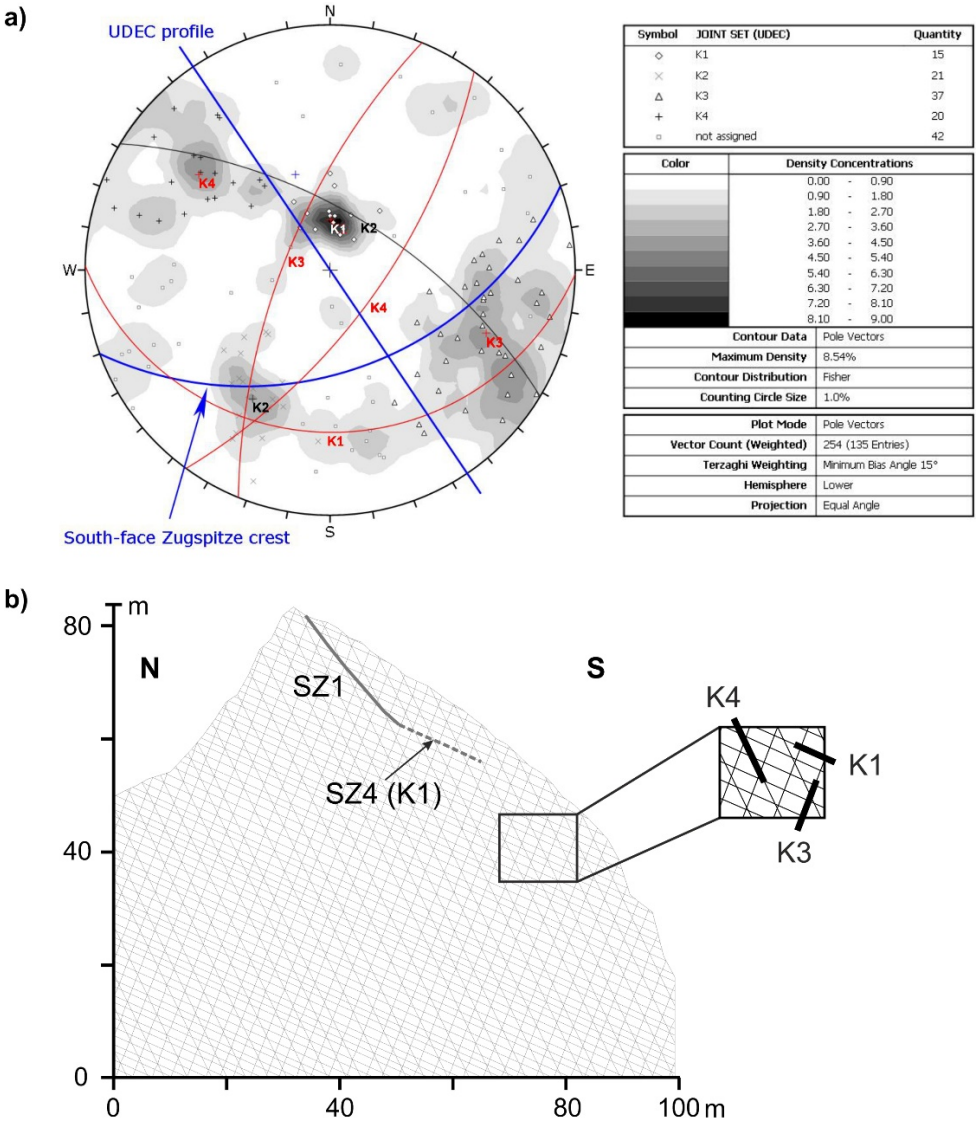

Figure 6.3: Joint sets and shear zones included in the numerical model.

(a) Orientations of field-measured discontinuities in a stereographic projection, calculated with Dips 7.0 (Rocscience). Great circles with red labels represent the joint sets (K) implemented in the numerical model. Contours depict the Fisher concentrations (density) of the poles. (b) Fracture network, extent and topography of the 2D numerical model. Shear zones (SZs) included in the model are marked with thick grey lines. The dashed line represents the assumed prolongation of the potential failure plane in the lower slope sections.

Table 6.2: Geotechnical characteristics of the joint sets.

Standard deviations are only given for measured parameters. K1 to K4 are joint sets. SZ denotes shear zone. J denotes joints.

Geometric parameters	K1	K3	K4	SZ1 (K4)	Input for numerical model
Dip/dip direction [°]	24/175	69/293	66/126	63/130	✓
Deviation of dip direction from trend of model profile [°]	29	33	20	16	✓ (as below 30°, considering the standard deviation)
Standard deviation of dip direction [°]	20	13	5	–	✓
Standard deviation of dip [°]	3	4	8	–	
Spacing [m]	0.27 ± 0.3	0.54 ± 0.6	0.59 ± 0.7	–	✓
Aperture [mm]	7.0 ± 17.1	2.9 ± 6.8	5.3 ± 8.1	270.0	
Joint frequency [$J\,m^{-1}$]	3.7	1.9	1.6	–	✓ (simplified representation)
Joint roughness coefficient JRC*	5.5 ± 1.8	8.6	–	4.4 ± 3.3	
Number of mapped joints	15	37	19	1	

Note: [a]The JRC was measured along joints not included in the scan lines.

The possible failure mechanism and shear zones which delimit the currently observed unstable rock mass were assessed manually with a 3D point cloud of the Zugspitze summit crest line derived by UAV-based (UAV – unmanned aerial vehicle) photogrammetry (Figure 6.1e) and with a kinematic analysis of a potential plane and wedge failure (Figure 4.5 in the Supplement). The latter was conducted with Dips 7.0 (Rocscience) for the southern slope face and along the main shear zones identified due to field mapping and the preceding analysis of the point cloud. The instability is driven by a complex combination of a plane and a wedge failure, although planar sliding is the dominant kinematic failure mode that affects the major left part of the unstable rock mass (Figure 4.5, Figure 6.1a and Figure 6.1e). Planar sliding mainly occurs along shear zone SZ1, while wedge failure supports the displacement along SZ1 and SZ3 including a tension crack SZ2 in the upper part of the slope instability. Two further shear zones (SZ4 and SZ5) form the assumed downslope boundary of the unstable rock mass in the lower slope sections. Planar sliding can occur along SZ4 and SZ5, while wedge failure potentially enhances the failure process along SZ3 and the planes SZ4 and SZ5.

The geophysical transect and the numerical model profile run along the stepped planar failure part of the unstable rock mass (shear zones SZ1, SZ4 and SZ5; left part in Figure 6.1e). Shear zone SZ1 (equivalent to K4) and shear zone SZ4 (corresponding to K1) were included in the numerical model (Figure 6.3b) to allow simplification and a representation in 2D. We assume the slope instability to be significantly dominated by shear zone SZ1. Observed maximum displacements along the upper part of SZ1 lie in the range of decimetres and point to a high level of joint persistence. Further, three karst dolines with a depth of several metres were mapped along SZ1 and at the intersection of shear zone SZ1 with SZ2 (Figure 4.2, Figure 6.1a). SZ1 has a trace length of approximately 70 m, runs in a maximum depth of 10–15 m and dips to the

southeast. It is highly fractured and displays joint opening of several decimetres filled with fine material which ranges from clay to gravel in size (Figure 6.1d).

The 3D point cloud analysis was used to assess the unstable rock mass at the south face of the summit crest to a volume of approximately $2.9 * 10^4$ m^3 (Figure 6.1e). Measured fracture displacements between 2013 and 2019 show that the rock mass creeps slowly at an average of 2.1 mm yr^{-1} (Figure 4.6). Between October and May, deformation rates are 84 % lower than in the remaining summer months. Details on the volume estimation and the measurement of the crack displacements are given in the Supplement (Section 4.2).

6.3.1.2. Spatial permafrost distribution

In the 1960s and 1990s, permafrost at the Zugspitze summit was found in deep and permanently ice-filled fractures with a maximum aperture of 0.1 m (Körner and Ulrich, 1965; Ulrich and King, 1993). Current borehole temperatures at the peak of the Zugspitze average -1.1 °C within the permafrost core area (20–25 m away from the rock walls). At the margin to the active layer (ca. 5 m away from the north face), the temperatures approach a minimum of -6 °C during winter (Böckli et al., 2011; Gallemann et al., 2017; Krautblatter et al., 2010; Nötzli et al., 2010). A model for the permafrost evolution at the Zugspitze peak by Gallemann et al. (2017) shows that the permafrost decreased by 2 m at the north face and by 7 m at the south face between 1915 and 2015, with an increase in the permafrost temperature of approximately 1 °C.

Information on (i) the calibration of electrical resistivity in the laboratory and (ii) the measuring set-up, data acquisition and analysis of the ERT surveys at the study site have been shifted to Sections 4.4.1.2 and 4.4.2.2. This results in a modification of the original manuscript, but it ensures a clear and easy-to-follow structure of this thesis.

6.3.1.3. Mechanical properties

The Zugspitze summit crest consists of Triassic Wetterstein limestone which has a thickness of 1000 m and constitutes the majority of the Zugspitze Massif and the Wetterstein mountains (Gallemann et al., 2017; Miller, 1962). The limestone is massy, fine-grained and dolomised and shows little heterogeneity in terms of lithological properties (Krautblatter et al., 2010). Its porosity ranges between 1.9 % (Dräbing and Krautblatter, 2012) and 4.4 % (Krautblatter et al., 2010).

The distinct element method in UDEC enables one to simulate the mechanical behaviour of a discontinuous medium: the assemblage of discrete rock blocks separated from each other by discontinuities. We extensively investigated frozen and unfrozen rock and joint properties in the laboratory to assess the effect of thawing on the mechanical strength and deformability, and to determine the required material parameters for the model. All tests were performed

with fully water-saturated Wetterstein limestone samples collected at the study site. Frozen rock samples had a mean temperature of -5 °C, whereas unfrozen rock specimens were tested at room temperature (~22 °C). Detailed information on the preparation of the rock samples, the test set-ups and the conditions can be found in the Supplement (see Sections 5.1 and 5.4).

The strength and deformability of the model blocks and zones within the blocks were represented by the Mohr–Coulomb plasticity constitutive model with a tension cut-off. At the slope scale, material properties of the rock mass instead of intact rock are needed, as discontinuities reduce rock mass strength and induce non-linearities and anisotropy in the stress–strain behaviour (Hoek et al., 2002; Wyllie, 2018). Hence, blocks and zones were allocated rock mass properties. The intact rock data were transferred to rock mass characteristics and switched to field-scale properties following the GSI (geological strength index) rock mass classification system by Hoek and Brown (1997). The GSI system is directly linked to Mohr–Coulomb or Hoek–Brown strength parameters and rock mass deformation moduli (Cai et al., 2004). The deformation modulus of the rock mass E_m can be described based on a field survey of the rock mass including description and measurement of block volumes and joint characteristics (Hoek et al., 2002):

Equation 6.1:

$$E_m\ [\mathrm{GPa}] = \left(1 - \frac{\mathrm{D}}{2}\right)\sqrt{\sigma_c}/100\ * 10^{((GSI-10)/40)}$$

where *GSI* is the geological strength index for the rock mass, *D* is the disturbance factor and σ_c is the uniaxial compressive strength of the intact rock. The latter was tested in the laboratory and is a function of temperature (Table 6.3). Following Cai et al. (2004), a *GSI* value of 65 was derived which relates to an interlocked, mostly blocky to very blocky rock mass formed by four joint sets with a mean spacing of 56 cm (Table 6.2) and to rough slightly weathered surfaces. The disturbance factor *D* was set to 0 as the near surroundings of the profile are not affected by significant blast damage or excavating actions.

Values for the elastic rock mass shear and bulk moduli G_m and K_m respectively were derived according to the equations presented by Tipler and Mosca (2015) for intact rock:

Equation 6.2:

$$G\ [\mathrm{GPa}] = \frac{E_{dyn}}{2\ *(1+\ \upsilon)}$$

and

Equation 6.3:

$$K\ [\mathrm{GPa}] = \frac{E_{dyn}}{3 * (1 - 2 * \upsilon)}$$

where the Poisson's ratio υ, measured in this study (Table 6.3), describes the ratio of the transverse strain to the longitudinal strain under conditions of uniaxial stress (Jaeger et al., 2007). For G_m and K_m, the dynamic Young's modulus E_{dyn} was substituted by E_m (see Equation 6.1). The mass density ρ (g cm^{-3}) and dilatational wave velocity V_D (m s^{-1}) were measured in additional tests (Table 6.3) and utilised to calculate the dynamic Young's modulus E_{dyn} for intact rock (Rentsch and Krompholz, 1961):

Equation 6.4:

$$E_{dyn}\ [\mathrm{GPa}] = \rho * V_D^2$$

E_{dyn} and G were later used to determine the joint stiffness parameters. The rock mass internal friction angle ϕ_m and cohesion c_m were estimated with the *GSI* and the Hoek–Brown constant m_i according to Cai et al. (2004). It should be noted that while rock mass cohesion could be determined for both thermal conditions (as it is based on the temperature dependent uniaxial compressive strength), the unfrozen friction angle value was used for all thermal conditions (as the respective relation is not temperature dependent). The uniaxial tensile strength σ_{tm} was calculated using the following relation:

Equation 6.5:

$$\sigma_{tm} = \frac{\sigma_c}{2}\left(m_b - \sqrt{m_b^2 + 4s}\right)$$

where m_b and s are constants for the rock mass (Hoek and Brown, 1997).

All mechanical properties of the intact rock and the rock mass, either tested in the laboratory or calculated, decrease in a temperature-dependent fashion with 0.3 % °C^{-1} to 0.8 % °C^{-1} (absolutely 8 %–22 %) upon thawing (see Table 6.3 and Table 6.4); this pattern corresponds to other mechanical studies (see Table 6.1). While the increase in deformability is more pronounced for intact rock (0.8 % °C^{-1}; 20.4 %–20.5 %) than for rock mass (0.3 % °C^{-1}; 8.3 %–8.9 %), the tensile strength decreases by a similar amount when comparing intact rock with rock mass. This difference can be explained by the small variation in frozen and unfrozen E_m values caused by the similar frozen and unfrozen intact rock uniaxial compressive strength (see Equation 6.1).

Table 6.3: Laboratory-tested strength reduction of intact dolomised Wetterstein limestone due to thawing.

Standard deviations (indicated with ±) are given for measured parameters, and they were used for the determination of minimum and maximum values (given in parentheses) of the calculated parameters. RMC refers to parameters that are used for rock mass characterisation.

Mechanical parameter	Saturated frozen (−5 °C)	Saturated unfrozen (+22 °C)	Decrease due to thawing %	Decrease due to thawing % °C^{-1}	Test/equation applied	RMC
Density ρ [g cm^3]	–	2.7 ± 0.01	–	–	Weighing tests in water bath	✓
Porosity n [%]	–	0.9 ± 0.4	–	–	Weighing tests in water bath	
Shear modulus G [GPa]	32.4 (31.7/32.6)	25.8 (21.9/29.2)	20.4	0.8	Eq. **6.1**, after Tipler and Mosca (2015)	
Bulk modulus K [GPa]	70.3 (64.8/74.8)	55.9 (40.4/76.0)	20.5	0.8	Eq. **6.2**, after Tipler and Mosca (2015)	
Young's modulus E [GPa]	84.3 (81.7/85.3)	67.1 (55.7/77.6)	20.4	0.8	Eq. **6.3**, after Tipler and Mosca (2015)	
Poisson's ratio υ	0.3 ± 0.01	0.3 ± 0.03	0	0	Ultrasonic tests	✓
Dilatational wave velocity V_D [m s^{-1}]	5560 ± 50	4950 ± 400	11.0	0.4	Ultrasonic tests	
Uniaxial tensile strength σ_t [MPa]	9.0 ± 1.4	7.2 ± 1.9	20.0	0.7	Brazilian tests	
Uniaxial compressive strength σ_c [MPa]	109 ± 25	91 ± 27	16.5	0.6	Uniaxial compressive strength tests	✓

Table 6.4: Estimated and calculated strength reduction of Wetterstein limestone rock mass due to thawing, derived from the GSI scheme after Hoek and Brown (1997).

Minimum and maximum values of calculated parameters are given in parentheses. These were determined with the standard deviations of the measured parameters (Table 6.3). IP denotes that the parameter was used as an input parameter for the numerical model.

Mechanical parameter	Saturated frozen (−5 °C)	Saturated unfrozen (+22 °C)	Decrease due to thawing %	Decrease due to thawing % °C^{-1}	Test/equation applied	IP
Young's modulus E_m [GPa]	24.8 (21.7/27.5)	22.6 (19.0/25.8)	8.9	0.3	Eq. **6.1** after Hoek et al. (2002)	
Shear modulus G_m [GPa]	9.5 (8.4/10.5)	8.7 (7.5/9.7)	8.4	0.3	Eq. **6.2** after Tipler and Mosca (2015)	✓
Bulk modulus K_m [GPa]	20.6 (17.2/24.1)	18.9 (13.7/25.3)	8.3	0.3	Eq. **6.3** after Tipler and Mosca (2015)	✓
Uniaxial tensile strength σ_{t_m} [MPa]	−0.9 (0.7/ − 1.1)	−0.7 (−0.5/ − 0.9)	22.2	0.8	Eq. **6.5** after Hoek et al. (2002)	✓
Friction angle φ_m [°]	44*	44	0	0	Estimated after Cai et al. (2004)	✓
Cohesion c_m [MPa]	3.9	3.3	15.4	0.6	Estimated after Cai et al. (2004)	✓
Parameter of the Hoek–Brown strength criterion						
GSI value	–	65	–	–	Estimated after Marinos and Hoek (2000)	
m_i	–	9	–	–	Estimated after Marinos and Hoek (2000)	
m_b	–	2.6	–	–	Calculated after Hoek et al. (2002)	
s	–	0.02	–	–	Calculated after Hoek et al. (2002)	
Disturbance factor D	–	0	–	–	Estimated after Hoek et al. (2002)	

Note: [a]The frozen rock mass friction angle was given the same value as for the unfrozen friction angle, resulting in a decrease in thawing of zero.

In UDEC, the deformability and strength of rock discontinuities were simulated by the Mohr–Coulomb area contact constitutive model. Rock joint parameters for ice-free and ice-filled joints were considered in the presented stability analyses. The deformability of the joints is described by the joint normal stiffness k_n,

Equation 6.6:

$$k_n\ [\mathrm{MPa\ m^{-1}}] = \frac{E_m * E}{\mathrm{s} * (E - E_m)}$$

and the joint shear stiffness k_s,

Equation 6.7:

$$k_s\ [\mathrm{MPa\ m^{-1}}] = \frac{G_m * G}{\mathrm{s} * (G - G_m)}$$

where s is the joint spacing (m), E_m and E are the Young's moduli (GPa) for rock mass and intact rock respectively (Barton, 1972), and G_m and G are the shear moduli (GPa) for rock mass and intact rock respectively (Glamheden and Lindblom, 2002; Itasca Consulting Group, 2019). Finally, temperature (T) dependent cohesion c,

Equation 6.8:

$$c\ [\mathrm{kPa}] = 104.5 - 143.8 * T$$

and friction ϕ,

Equation 6.9:

$$\tan\ [\varphi] = 0.19 - 0.1 * T$$

of frozen ice-filled rock joints are determined based on the failure criterion presented by Mamot et al. (2018), which is valid for temperatures ranging from -4 to -0.5 °C and normal stresses between 100 and 800 kPa. Therefore, the cohesion and friction angle were calculated for temperatures of -4, -3, -2, -1 and -0.5 °C, which are currently measured in the frozen sections of the Zugspitze summit (Gallemann et al., 2017). The stress range of 100–800 kPa corresponds to the rock overburden represented by the model of the Zugspitze summit crest (Figure 6.3).

Values for the cohesion of frozen and unfrozen, ice-free rock joints were roughly estimated from Krautblatter et al. (2013). As initial displacements lead to the destruction of asperities and smoothing of joint surfaces, the frictional strength of rock–rock contacts was represented by the residual friction angle ϕ_r, estimated following Barton and Choubey (1977):

Equation 6.10:

$$\varphi_r = (\varphi_b - 20°) + 20 * (\frac{r}{R})$$

where ϕ_b is the basic friction angle; r is the Schmidt hammer rebound value of weathered surfaces; and R is the Schmidt hammer rebound value of unweathered, sawn surfaces. Rebound hardness values of weathered frozen and unfrozen Wetterstein limestone surfaces were collected with the Schmidt hammer (N-type) following the proposed method of Aydin and Basu (2005) and Ulusay (2015). In contrast, the basic friction angle was determined by tilt tests of frozen and unfrozen joint surfaces as recommended by Barton (2013).

The investigated and calculated joint deformation and mechanical strength properties decrease absolutely by 2 % to 22 % upon thawing (0.1 % °C^{-1} to 0.8 % °C^{-1}; Table 6.5). The small variation between frozen and unfrozen E_m values results in a small difference between frozen and unfrozen k_n and k_s (0.1% °C^{-1}; 2.6 %–2.8 %). In contrast, the stiffness values vary more strongly between the various joint sets which are also dependent on the joint spacing. In general, the estimated unfrozen k_n and k_s lie well within the range of values proposed by the UDEC database (Itasca Consulting Group, 2019) and Kulatilake et al. (1992), or measured by Barton (1972) and Bandis et al. (1983). Similarly, the measured unfrozen ϕ_b corresponds well to the values listed in studies such as Barton and Choubey (1977) or Ulusay and Karakul (2016).

6.3.2. Model set-up

The topography of the rock slope used in the model was derived from a digital terrain model of the Zugspitze summit area. Three fully persistent joint sets (K1, K3 and K4) and the dominant shear zone were included (Figure 6.3). For simplification and shorter computation time, the joint spacing was scaled up in the model by a factor of 5. The presence of intact rock bridges was accounted for according to the approach by Jennings (1970). After this, the joint cohesion and friction angle were proportionately increased by the respective rock mass cohesion and friction angle depending on the estimated percentages of the surface areas of rock bridges and joints within the rock slope.

The blocks in the model are supposed to be deformable and were subdivided into a mesh of finite difference elements with a size of 1.5 m. The stress field was initialised according to the varying density of overburden which depends on the topography of the slopes. We assumed a horizontal to vertical stress ratio of 0.5. Roller boundary conditions were implemented at the sides of the model (i.e. vertical movements were allowed), whereas vertical and horizontal displacements were suppressed along the base.

Table 6.5: Laboratory-tested and calculated strength reduction of saturated Wetterstein limestone discontinuities due to warming or thawing.

Standard deviations (indicated with ±) are given for measured parameters, and they were used for the determination of minimum and maximum values (given in parentheses) of the calculated parameters. IP denotes that the parameter was used as input parameter for the model.

Joint mechanical parameter	Type of joint filling	Sub-zero temperature [°C]	Frozen			Unfrozen (+22 °C)			Decrease due to thawing/warming		Reference/equation applied	IP
			Joint set						%	% °C^{-1}		
			K1	K3	K4/shear zone	K1	K3	K4/shear zone				
Normal stiffness [MPa m^{-1}]	Ice-free/ice-filled	−5	26 000 (21 900/30 000)	11 100 (9400/12 900)	13 000 (11 000/15 000)	25 300 (21 300/28 600)	10 800 (9100/12 200)	12 600 (10 700/14 300)	2.8	0.1	Eq. **6.6** calculated after Barton (1972)	✓
Shear stiffness [MPa m^{-1}]	Ice-free/ice-filled	−5	10 000 (8500/11 400)	4300 (3600/4900)	5000 (4300/5700)	9700 (8400/10 700)	4200 (3600/4600)	4900 (4200/5400)	2.6	0.1	Eq. **6.7** calculated after Kulatilake et al. (1992)	✓
Cohesion [MPa]	Ice-filled	−4	0.68 (0.45/0.91)			–			74.1	21.2.	Eq.**6.8**, calculated after Mamot et al. (2018)	✓
		−3	0.54 (0.35/0.72)			–						
		−2	0.41 (0.25/0.54)			–						
		−1	0.26 (0.15/0.35)			–						
		−0.5	0.18 (0.10/0.26)			–						
	Ice-free	−4.5	0.00			0.00			0	0	Estimated after Krautblatter et al. (2013)	✓
Peak friction angle [°]	Ice-filled	−4	30.5 (26.1/34.6)			–			59.3	17.0	Eq.**6.9**, calculated after Mamot et al. (2018)	✓
		−3	26.4 (22.3/29.7)			–						
		−2	22.0 (18.3/24.2)			–						
		−1	16.8 (14.0/18.3)			–						
		−0.5	13.5 (11.9/15.1)			–						
Rebound value for dry unweathered, sawn surfaces	Ice-free	−5	55.0 ± 1.0			51.9 ± 1.0			1.6	0.1	Schmidt hammer tests	
Rebound value for wet weathered surfaces	Ice-free	−5	53.0 ± 2.1			52.1 ± 0.8			1.7	0.1	Schmidt hammer tests	
Basic friction angle [°]	Ice-free	−5	38.3 ± 4.4			30.0 ± 4.7			21.7	0.8	Tilt tests	
Residual friction angle [°]	Ice-free	−4.5	37.6 (32.8/42.4)			30.1 (25.5/34.7)			22.1	0.8	Eq.**6.10**, calculated after Barton and Choubey (1977)	✓

The combined boundary of bedrock permafrost within the summit ridge, derived from ERT measurements from 2014 and 2015 (Figure 4.11), was used to define the current frozen and unfrozen sections of the numerical model. We then introduced six subsurface layers to simulate a stepwise warming or thawing from the slope surface to the core of the crest by adjusting the temperature-dependent material parameters for a specific temperature level and subsequent numeric cycling. The layers are oriented parallel to the derived permafrost boundary and account for a stronger warming signal directed from the south slope (Figure 6.4). The defined current permafrost boundary and the estimated spatial pattern of layers for warming are both in accordance with modelled current and future thermal fields of arbitrary mountain ridge geometries (Nötzli et al., 2007) and, in particular, of the Zugspitze (Böckli et al., 2011; Nötzli, 2008).

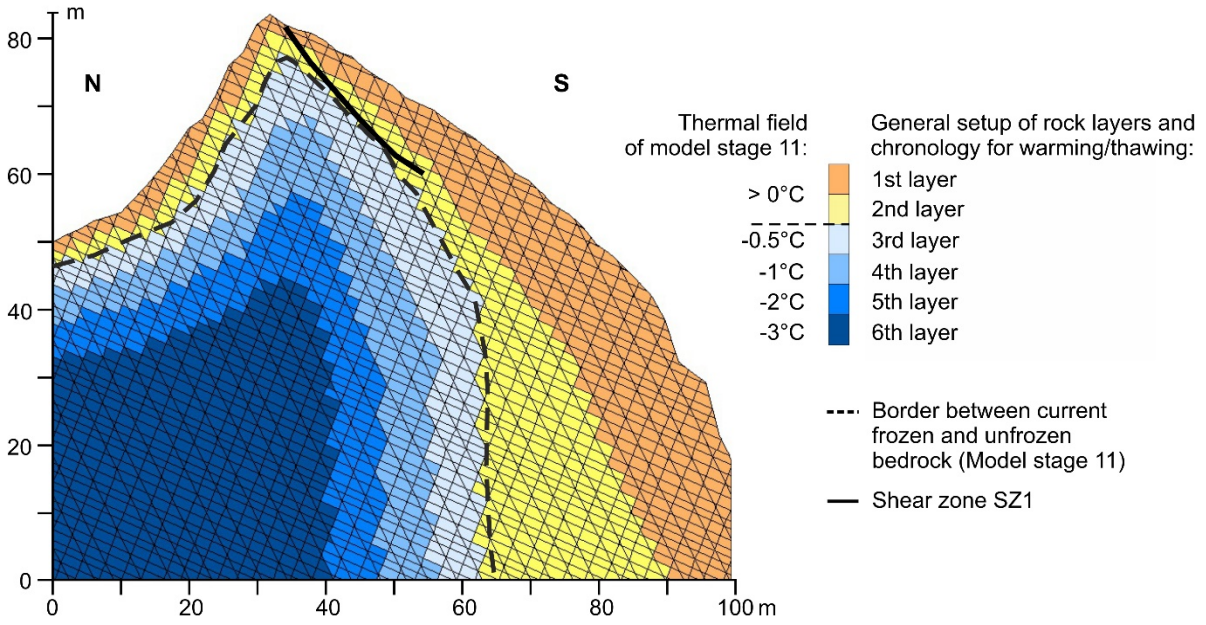

Figure 6.4: Spatial warming/thawing pattern for the numerical model of the Zugspitze summit crest.

For each warming/thawing step, the six rock layers (coloured areas) are assigned an individual temperature with a characteristic set of mechanical parameters. Warming or thawing proceeds from the outside to the inside of the crest. The dashed black line marks the current boundary between frozen and unfrozen rock, derived in Section 6.3.1.2. The presented thermal field is estimated and refers to model stage 11 in Table 6.6 (current state of permafrost distribution in the crest).

6.3.3. Procedure for the numerical analysis

The general modelling procedure consists of four steps – the calculation of an initial equilibrium and three successive steps of potential destabilisation which include the progressive destruction of intact rock bridges, the warming and the thawing of a permafrost rock slope:

1) Initial state – the numerical analysis was started by developing an initial equilibrium with a low joint persistence of 30 % (Model stage 1 in Table 6.6). The summit crest is assumed to be fully frozen representing an undefined moment in the past.
2) The progressive loss of rock bridges – the destabilisation of a permafrost-affected rock slope is initiated by the progressive destruction of cohesive intact rock bridges which prepare new shear planes along which displacement can take place (Krautblatter et al., 2013). The current overall joint persistence was assessed to be 90 %–100 %, as we observed a high trace length of the discontinuities and a displacement of several decimetres along the main shear zone, indicating that most of the rock bridges are lost. The past destruction of rock bridges was simulated by a reduction in the apparent joint cohesion and friction angle in three steps which represents a progressive increase in the joint persistence from 30 % to 90 % (stages 1–4 in Table 6.6 and Table 6.7; for more details, see Section 6.8).

   Joints may be partly filled with ice during the loss of rock bridges. However, joints were assigned properties of ice-free joints as, according to Krautblatter et al. (2013), deformation and shear strength are mainly controlled by rock mechanical processes at this early stage of destabilisation. As long as a certain part of intact rock bridges and asperities along joint surfaces are present, stresses are supposed to concentrate at these locations while the softer ice fillings may be squeezed away (in particular, at greater depths).

   Following Krautblatter et al. (2013), the advanced stage of accelerated displacements in a permafrost-affected rock slope begins as soon as most of the rock bridges are broken. Ice mechanics (fracturing of rock–ice contacts and ice, as well as the creep of ice) will then increasingly replace rock mechanics (friction of rock–rock contacts and fracture of rock bridges) in controlling displacements along discontinuities and their potential acceleration. To introduce this stage of destabilisation, the joint persistence was further increased to 100 % and rock joints were simulated to be ice-filled (Stage 5 in Table 6.6). For simplification and due to data availability, the joint shear resistance was solely given by the fracture of ice or rock–ice contacts, whereas the creep of ice was neglected.
3) Warming permafrost – the frozen crest was gradually warmed from the slope surface to the core from -4 to -0.5 °C (stages 6–9 in Table 6.6). This was applied to the six rock layers defined in Figure 6.4. Firstly, the outermost (orange) section was warmed to -3 °C, while the inner sections remained at -4 °C (Stage 6). After that, the outermost section was warmed to -2 °C and the adjacent inner section (yellow layer in Figure 6.4)

was warmed to -3 °C, while the inner sections remained unchanged (Stage 7). This procedure was continued until the outermost layer was at -0.5 °C (Stage 9). Each warming step was characterised by adjusting the temperature-dependent material parameters to the warmer temperature and by subsequent numeric cycling. The simulated temperature range of the rock mass is consistent with currently monitored borehole temperatures in permafrost rock walls across the European Alps (Gallemann et al., 2017; Nötzli et al., 2019).

4) Thawing from the slope surface to the core was implemented in the same way as warming (Stages 10–15 in Table 6.6), until all subsurface layers of the summit ridge were unfrozen. The spatial pattern of thawing is illustrated in Figure 6.4.

To assess the level of a potential slope stability loss due to warming or thawing, we calculated the factor of safety (FS) by using the common strength reduction technique (Wyllie, 2018). Using this approach, the cohesion and frictional strength of the rock mass and the joints are reduced simultaneously and gradually by increasing trial factors in a series of numerical simulations until failure occurs. A bracketing solution approach was applied to progressively reduce the bracket between stable and unstable solutions until it falls below a specified threshold (Itasca Consulting Group, 2019). The resulting FS is a single indicator of minimum stability which globally refers to the entire slope.

Table 6.6: Modelling strategy for the Zugspitze summit crest.

The model was run with varying rock mass temperature, joint persistency and filling. The temperature levels for gradual warming were as follows: -4, -3, -2, -1 and -0.5 °C.

Model stage	Thermal state of the rock slope	Joint persistence [%]	Type of joint filling	Principal steps of the numerical analysis
1	All frozen (−4 to −5 °C)	30	No ice	Initial equilibrium
2		50		Progressive destruction of rock bridges
3		70		
4		90		
5	All frozen (−4 °C)	100	Ice-filled	
6	First layer at −3 °C	100	Ice-filled	Stepwise warming from rock surface to core in four steps
7	First layer at −2 °C			
8	First layer at −1 °C			
9	First layer at −0.5 °C			
10	First layer unfrozen	100	Thawed layers: no ice/ Frozen layers: ice-filled	Stepwise thawing from rock surface to core in six steps
11	Second layer unfrozen			
12	Third layer unfrozen			
13	Fourth layer unfrozen			
14	Fifth layer unfrozen			
15	All unfrozen		No ice	

Table 6.7: Implemented strength properties for ice-filled and frozen ice-free joints during the initial stage of rock bridge destruction, represented by a joint persistence of 30 % to 90 %.

The different cohesion and friction values are calculated after Jennings (1970) and depend on the estimated relative percentage of rock bridges and joints. The corresponding values at a joint persistence of 100 % are shown in Table 6.5. The numbers of the sections have been modified from the original version in Mamot et al. (2021) to fit to the numbering of the sections in this thesis.

Joint mechanical parameter	Type of model	Type of joint filling	Joint persistence [%]			
			30	50	70	90
Apparent cohesion [MPa]	Zugspitze summit crest (Sect. 6.5.1)	Ice-free	2.8	2.00	1.2	0.4
	Simplified rock slope (Sect. 6.5.2)	Ice-filled	–	–	–	1.0
Apparent residual friction angle [°]	Zugspitze summit crest (Sect. 6.5.1)	Ice-free	42.1	40.8	39.5	38.2
Apparent peak friction angle [°]	Simplified rock slope (Sect. 6.5.2)	Ice-filled	–	–	–	31.9

6.4. Sensitivity analysis for a simplified, warming permafrost rock slope

The relation between the dip of the joint sets, especially the bedding, and the slope face is a crucial factor for rock slope stability (Cruden, 2003; Wyllie, 2018). Thus, we performed a sensitivity analysis on the numerical impact of varying (i) slope angles and (ii) orientations of the fracture network on rock slope stability. For this, we transferred the Zugspitze model to a rock slope with a simplified topography, and warming steps were applied to the entire model domain without spatial differentiation. The topography of the Zugspitze south face was modified to a straight line. In accordance with the dimensions of the crest geometry, the height of the slope and the width of the upper face were standardised to 84 and 32 m respectively (Figure 6.6).

Modelling was applied to 12 different slope angles between 30 and 69°. For inclinations of 70° and higher, no initial equilibriums could be calculated as cycling exceeded the maximum computation time. The joint set orientations were kept constant. In a first step, an initial equilibrium was calculated for a frozen rock slope with ice-filled joints and a joint persistence of 90 %. In a second step, the joint persistence was increased to 100 %, and the rock slope was then warmed in four steps from -4 to -0.5 °C (by reducing the rock joint strength equivalent to the Zugspitze model). However, each warming step to the next degree centigrade was applied to the entire rock slope and not just to a single rock layer. Reducing the complexity of the model facilitates the transferability to other frozen rock slopes.

We also remodelled the stability for 12 different dip angles of the fracture network with reference to the slope. The positioning of the three model joint sets to each other was held constant while rotating them counterclockwise in steps of 15° for each of the 12 slope angles used for the first sensitivity test. The analysed orientations of the fracture network represented anaclinal and cataclinal slopes after Cruden (2003; Figure 3). Hereafter, cataclinal slopes have a slope

face and bedding with the same dip direction, whereas for anaclinal slopes, the dips of both planes have the opposite direction. The orientation and dip of the fracture network was represented by the bedding and then applied to the scheme after Cruden (2003). The simulated temperature of the rock mass was constantly at -4 °C as a stepwise warming was not applied.

6.5. Numerical model results

6.5.1. Stability of the warming/thawing Zugspitze crest

Figure 6.5 shows the cross section of the Zugspitze summit crest with a factor of safety for different model states. While an increase in joint persistence or warming hardly lead to a rising block displacement magnitude (indicated by colours – note that panels a–c and d–f use different scales), thawing causes a drastic increase in displacements. As soon as thawing starts, the south face becomes unstable and maximum displacements increase to 0.14 m (Stage 10, Figure 6.5d). Rock deformations rise to 0.42 m when the dimension of thawed bedrock reaches the current state (Stage 11, Figure 6.5e) and measure 0.78 m for the whole rock slope thawed (Stage 15, Figure 6.5f). The highest deformations (> 0.4 m) concentrate on the upper 5–7 m of rock in the most inclined lower part of the slope (with a mean angle of 49°). While warming brings the factor of safety close to unity, it lies below 1 for stages 10–15, which all refer to thawing.

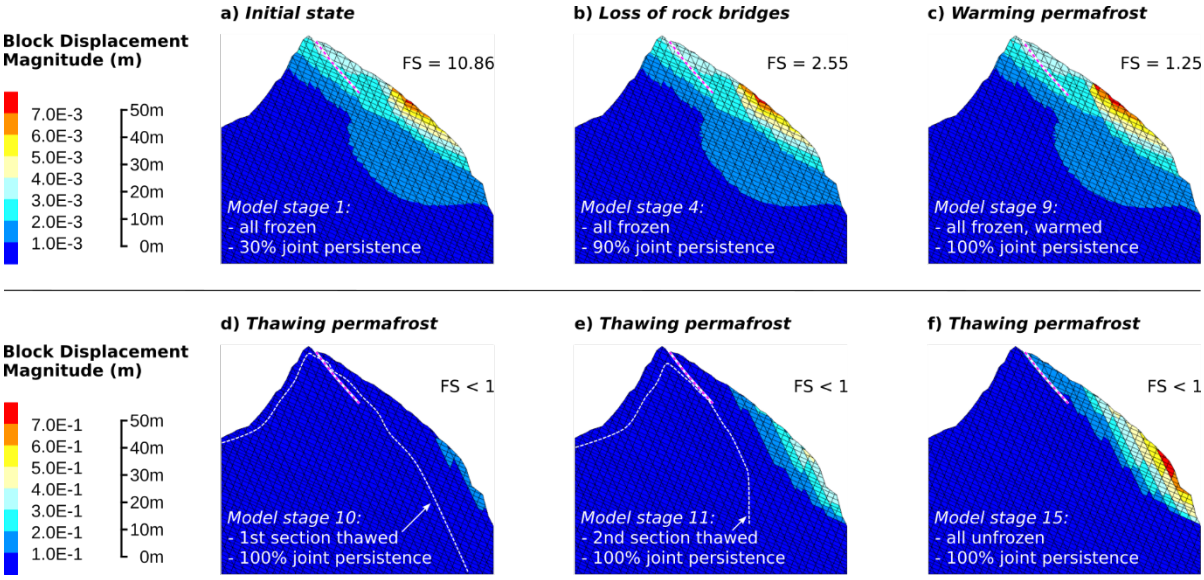

Figure 6.5: Calculated spatial distribution and magnitude of displacements for the Zugspitze summit ridge.

(a)–(c) Factors of safety (FS) are given for Stages 1, 4 and 9, which refer to the loss of rock bridges and warming. (d)–(f) Stages 10, 11 and 15 correspond to thawing with FS below 1. The prominent shear zone is marked by a white and red dashed line. The permafrost boundary in panels (d) and (e) is highlighted by a white dashed line.

6.5.2. Stability of a simplified permafrost rock slope with rising temperature

6.5.2.1. Sensitivity to the slope angle

The model results for exemplary slope inclinations between 60 and 64° are shown in Figure 6.6. The block displacements increase and the related factors of safety decrease with higher slope angles and temperatures below the melting point. The factor of safety falls below unity at temperatures above -1 °C when a rock slope with a slope angle of 62° or more is warmed up. A 60° steep rock slope becomes unstable at temperatures above -0.5 °C.

The interaction between slope gradient, maximum displacements and temperature can be separated into three domains (Figure 6.7a):

1) Domain 1 (30–50°) – "Stable slope" – the maximum displacements increase slightly by 0.4 mm per degree of slope angle. The correlations for all temperatures are significant with p values ≤ 0.04.
2) Domain 2 (55–62°) – "First onset of instability" – slope destabilisation sets in for rock slopes at -0.5 °C and above an inclination of 50°. This becomes obvious due to the abrupt increase in displacements, and the p value > 0.05. For rock slopes at -1 °C and below, the onset of instability is visible above an inclination of 55°. Note that all displacements are 1 order of magnitude higher than in Domain 1.
3) Domain 3 (64–69°) – "Accelerating slope destabilisation" – the displacements increase suddenly with a further increase in the *p* value and a corresponding decrease in the R^2 value for a slope angle of 64° and for all rock temperatures. This points to a second stage of accelerating slope destabilisation. The displacements are 1 order of magnitude higher than in Domain 2.

The displacements are sensitive to the sub-zero temperatures at all slope gradients. However, the intensity of rock slope destabilisation is increased by higher rock temperatures close to the melting point (Figure 6.7b): a warming from -4 to -2 °C leads to an increase in absolute displacements, which are low in Domain 1 (0.2 mm C^{-1}) but high in Domain 3 (7 mm C^{-1}). A respective warming from -2 to -0.5 °C also shows an increasing trend with higher slope gradients but is more pronounced with a massive increase from Domain 1 (0.6 mm C^{-1}) to Domain 3 (45 mm C^{-1}). Nevertheless, the highest temperature-dependent relative increase in displacements is observed in Domain 2 (Figure 6.7b): values increase from 9.2 % C^{-1} (Domain 1) to 38.5 % C^{-1} (Domain 2) and fall to 25 % C^{-1} for slopes steeper than 62° (Domain 3), which is valid for a warming from -2 to -0.5 °C. Again, the same pattern is less pronounced for a warming from -4 to -2 °C.

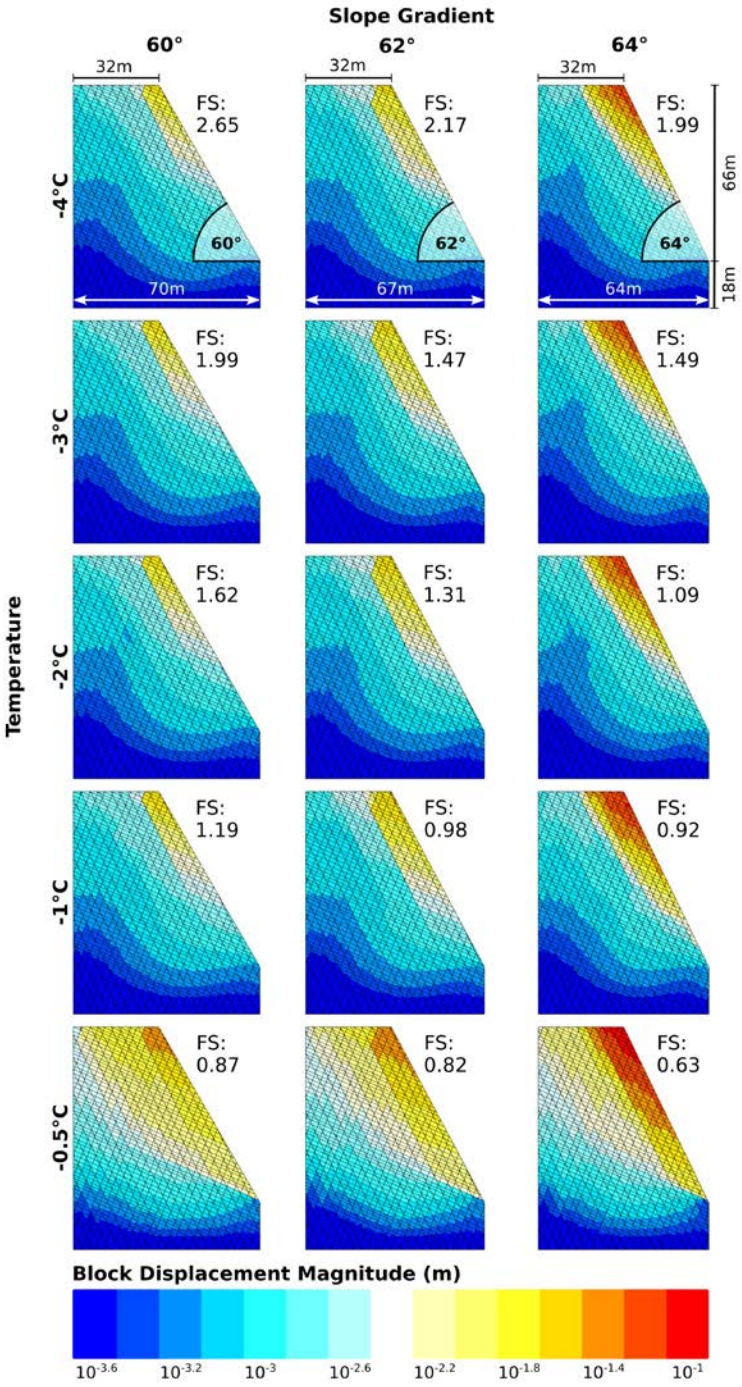

Figure 6.6: Numerically calculated block displacements (on a log scale) for a simplified rock slope geometry with exemplary inclinations of 60, 62 and 64°, and five temperatures between -4 and -0.5 °C.

In contrast to the displacements, the factor of safety also depends on the slope angle and the temperature (Figure 6.7c): for a rising steepness from 30 to 69°, the calculated FS decreases inversely and is always lower for higher temperatures. Warming from -4 to -0.5 °C reduces the FS of a permafrost rock slope by a mean factor of 3.3. The pattern of the domains in Figure 6.7a can be easily applied to the relation between FS, temperature and slope angle (Figure 6.7c): the mean relative reduction of the FS per degree of the slope angle is low in Domain 1 (-1.8 % ± 0.4) and becomes higher over Domain 2 (-4.5 % ± 3.3), until it reaches a maximum in Domain 3 (-

9.8 % ± 8.3). Correspondingly, rock slopes are stable for all modelled temperatures in Domain 1. When shifting to Domain 2, the FS falls below unity at -0.5 and -1 °C which coincides with an abrupt increase in displacements. Rock slopes at -4 °C remain stable over the whole range of slope gradients.

As we did for the maximum block displacements, we tested if warming closer to the melting point led to a distinct diminishing pattern of the FS (Figure 6.7d): the absolute decrease is very similar for both warming steps from -4 to -2 °C and from -2 to -0.5 °C. However, the relative decrease from -4 to -2 °C is always lower than the one at higher temperatures.

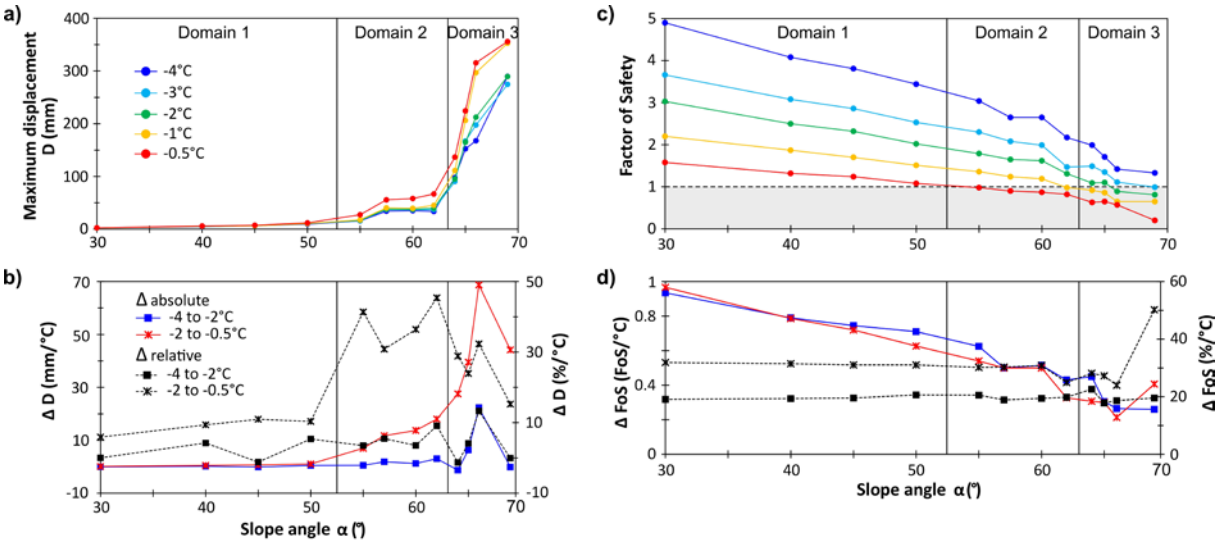

Domain	Relative change (% °C⁻¹)		Absolute change (mm °C⁻¹)	
	-2 to -0.5°C	-4 to -2°C	-2 to -0.5°C	-4 to -2°C
1	9.2	2.1	0.6	0.2
2	38.5	5.4	12.6	1.7
3	25.1	4.0	45.0	6.8

Domain	Relative change (% °C⁻¹)		Absolute change (FoS °C⁻¹)	
	-2 to -0.5°C	-4 to -2°C	-2 to -0.5°C	-4 to -2°C
1	31.4	19.7	0.7	0.8
2	29.1	19.7	0.5	0.5
3	32.4	19.7	0.3	0.3

Figure 6.7: The above figure provides critical slope angles and rock temperatures beyond which instability is introduced.

(a) Calculated maximum displacements against slope angle for temperatures between -4 and -0.5 °C. The curves are assigned to three distinct domains depending on the slope gradient, with domain divisions above 50° and above 62° respectively, where the curves point to a sudden onset of instability. (b) Absolute and relative increase in displacements versus slope angle for a warming from -4 to -2 °C and from -2 to -0.5 °C. (c) Calculated factor of safety (FS) against slope angle for different sub-zero temperatures. (d) Absolute and relative decrease in FS versus slope angle for a warming from -4 to -2 °C and from -2 to -0.5 °C.

6.5.2.2. Sensitivity to the fracture network orientation

Modelling resulted in 8 out of 12 orientations of the fracture network that show a significant displacement acceleration and initiating slope instability above a critical slope inclination (Figure 6.8a): for anaclinal slopes, the critical angles range between 50 and 62°, and for cataclinal slopes, they range between 55 and 62°. Cataclinal rock slopes with a bedding dip of 84 and 69°

do not indicate a significant knick point in the displacement curves. As such, the corresponding critical slope angles were set to the maximum of the investigated values (69°). Fracture networks rotated counterclockwise by 30 and 75° from the joint set of the Zugspitze summit crest showed very noisy model data and were not used for the analysis.

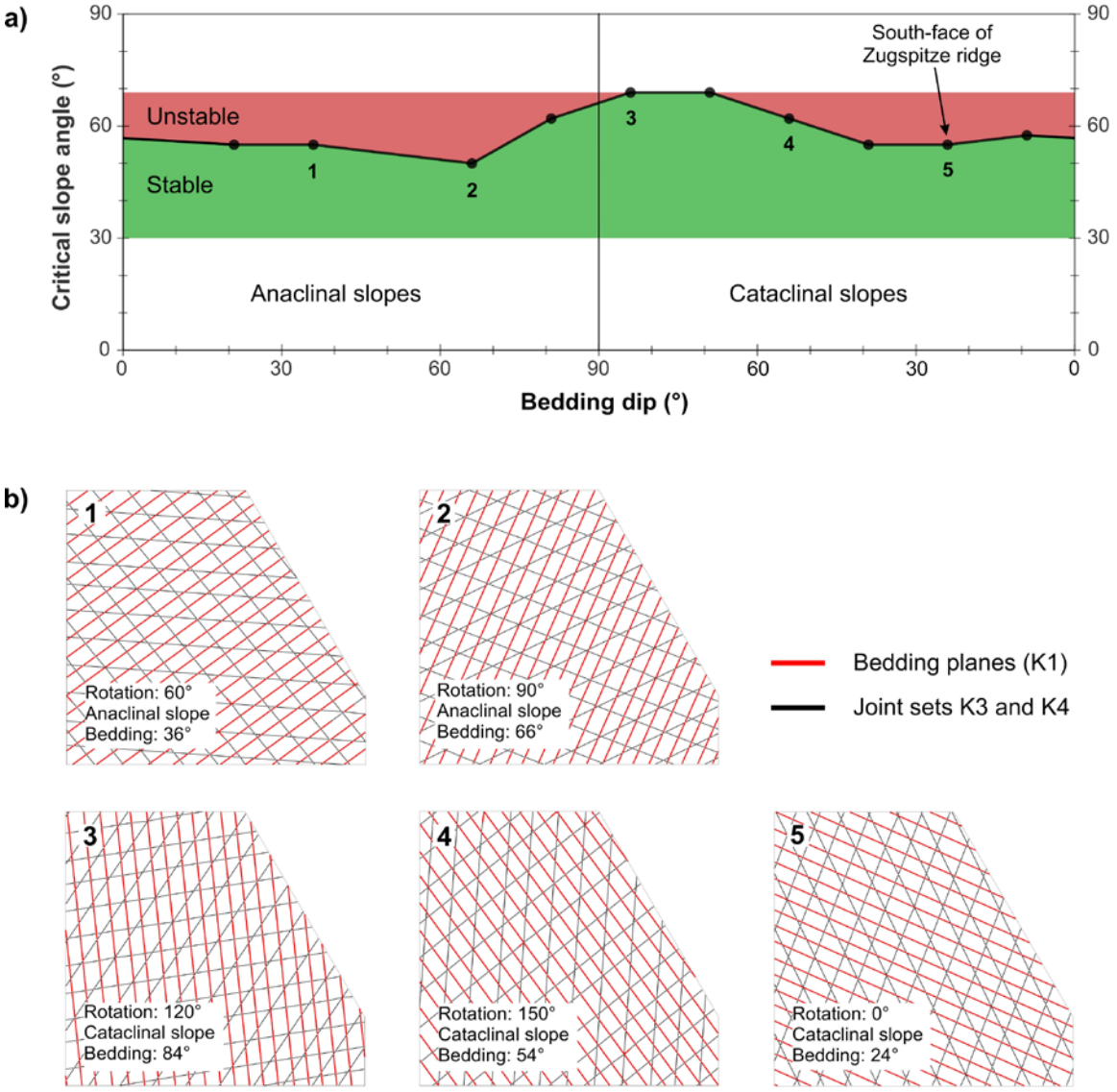

Figure 6.8: A rule of thumb for critical slope gradients and fracture network orientations of anaclinal and cataclinal permafrost rock slopes.

For cataclinal slopes, both the slope face and the bedding have the same dip direction, but for anaclinal slopes, the dips of both are oriented oppositely (Cruden, 2003). (a) The green area refers to stable rock slopes, whereas the red area refers to unstable ones. For simplification, the fracture network is represented by the bedding dip. The coloured areas indicate the studied range of slope angles. (b) Five exemplary joint set constellations for cataclinal and anaclinal slopes with an inclination of 60°. The numbers of the rock slopes correspond to the numbers in panel (a). The joint spacing is 10 times bigger than in reality and is only applied for illustration. Example 5 refers to the Zugspitze summit crest.

6.6. Discussion

This study successfully simulated the mechanical response of a warming and thawing permafrost rock slope using a temperature-dependent numerical model. The following sections show the general limitations of the presented models and critically discuss the site-specific model, the model of the generalised permafrost rock slope and its transferability to other high-mountain conditions.

6.6.1. Limitations

Mechanical models are sensitive to material parameters. However, the availability of these parameters and the technical opportunities to establish them are limited. Therefore, the presented mechanical model of the Zugspitze summit crest is based on a few simplifications. First, the knowledge of the subsurface structure (i.e. joint spacing and joint persistence) is limited and has to be estimated by inspection of the rock surface. Second, mechanical parameters were not determined for the specific joint sets. Only the joint normal and shear stiffness varied between the joint sets due to their different joint spacing. Third, a standardised recommendation for the disturbance factor D for an unstable rock slope (without blast damage) does not exist; such a recommendation should be validated numerically and include a classification of various degrees of instability. Therefore, D was set to 0, but the potential influence of a higher D on the slope stability was analysed by additional model runs with the geometry of the Zugspitze crest (Figure 6.9); a modified D approaching 1 leads to higher displacements, but the factor of safety remains unchanged. Fourth, it is crucial to consider the temperature dependency of the material parameters, as freezing can increase rock mass strength. However, the influence of freezing effects is mostly ignored in the GSI rock mass classification system (see also Gambino and Harrison, 2017). In our model, the friction angle after Cai et al. (2004; Figure 5) applies the temperature-independent Hoek–Brown constant m_i and the GSI value, defined for the unfrozen rock mass. To our knowledge, the friction angle of a frozen rock mass and its change due to thawing have hardly been investigated and are not yet described by a general law. Model test runs with very low to unrealistically high values of the mechanical rock mass properties demonstrated that the displacements in the rock slope mostly remained within the same order of magnitude (Figure 6.12). Therefore, the rock mass internal friction angle was derived by the GSI scheme, and its unfrozen value was assigned to both the frozen and the unfrozen rock mass.

Furthermore, the implementation of the numerical model implies a few limitations which are addressed with the following approaches:

- When implementing non-persistent joints, UDEC discards those that do not split a block. An irregular joint and block pattern may be formed that does not correspond to

reality. Therefore, discontinuities were constructed as fully persistent, but joint strength parameters were increased according to Jennings (1970) in order to omit the potential result of favoured higher displacements and velocities along persistent joints.

- The size of the Zugspitze model domain was constrained to a local section of the rock slope ending in a steep part at the south face. The model domain fully incorporates the unstable rock mass under investigation, thereby perfectly accounting for the simulated spatial conditions of the mechanical processes of rock and ice. To investigate the slope angle at the domain boundary, we rerun the model with a bigger domain size ending in a flatter section of the south slope (Figure 6.9): the results demonstrated that a change in the size of the model domain does not significantly change the overall stability of the slope.
- The initial temperature of the frozen rock slope does not affect the displacement magnitudes and the general pattern of dependency between maximum displacements and slope inclination. The potential effect of a lower strength on the calculation of the initial equilibrium and on the resulting maximum displacement values was proven by reiterating the generalised model with an initial temperature at -2 °C and comparing it with the original -4 °C (Figure 6.10).
- Warming to the next degree centigrade was, by default, calculated with 3000 cycles, which was a compromise between a representative number of cycles for potentially reaching a numerical equilibrium (for stable rock slopes) and a reasonable, not overly time-consuming, calculation. Computations for low/intermediate slope angles and temperatures reached an equilibrium prior to 3000 cycles, whereas calculations for higher slope angles and temperatures mostly failed to reach an equilibrium (for unstable rock slopes) or scarcely required > 3000 cycles. Hence, the numerical calculation was repeated with warming steps with 6000 cycles to test a potential cut-off effect of cycles required for the rock slope to react to a change in stress–strain due to a modification of material parameters. However, the results coincide well with the model runs with 3000 cycles, as displacements significantly accelerate above slope angles of 50 and 62°, and they are higher for temperatures closer to melting (Figure 6.11).

We are at the beginning of developing numerical models for the mechanical response of a rock mass to warming/thawing. Therefore, there is a huge potential for improvements. For instance, more mechanical laboratory tests are necessary to improve process understanding and to extend the number of frozen and unfrozen material parameters for modelling. Future numerical models should be based on further sensitivity analyses or should include water pressure or the creep of ice at lower displacement rates within the advanced stage of rock slope destabilisation. Time-dependent cycling is not yet implemented in most of the numerical models nor in the presented ones. Hence, they are not suited to forecast a precise time of rock slope failure.

Further, the spatial warming pattern for the Zugspitze model is simplified and is based on a static temperature field derived from ERT, rock thermistors and published thermal models. For a more accurate characterisation of the warming pattern, future mechanical models should include a subsurface temperature field based on a combination of geophysics and a heat flow model for different time steps.

6.6.2. Stability assessment of the warming/thawing Zugspitze summit crest based on the factor of safety

The numerical model for the Zugspitze summit ridge simulates the strength reduction at warming and thawing based on laboratory tests of this and of previous studies (Table 6.1). Warming of ice-filled joints takes the slope close to a critical level of stability (FS = 1.3), but it does not initiate instability. As soon as thawing sets in and the ice is lost, the south face becomes massively destabilised as displacements increase by 2 orders of magnitude and the factor of safety falls below unity. The reduction in joint stability is significantly influenced by a loss of the joint cohesion from 0.18 MPa (at -0.5 °C) to 0 MPa (Table 6.5), even though the joint friction angle is increased from 13.5 to 29.3°. In contrast to our numerical analysis, Davies et al. (2001) postulate that the FS of a permafrost-affected rock slope is higher for unfrozen joints than for ice-filled joints between approximately -1.5 °C and 0 °C. The differing observations on the stability upon thaw may be explained as follows: (i) our model assumes a lower joint roughness and uses the residual friction angle which is lower than the peak friction angle taken for the centrifuge model. We suppose that the simulated rock slope has already been moving for a long time and joint surfaces are flattened due to the progressive destruction of asperities along joints. In contrast, the sliding surface in the centrifuge model is not affected by any previous displacements. (ii) The calculated FS by Davies et al. (2001) corresponds to an independent moment in time, whereas the FS in the Zugspitze model is path-dependent and affected by the history of the previous numerical calculations.

The permafrost evolution model by Gallemann et al. (2017) predicts permafrost at the Zugspitze peak to be lost within the second half of the 21st century which may result in an elevated occurrence of rock slope instability. This scenario is related to a projected increase in the mean air temperature by 3.2 °C until the end of the century. Stages 11 to 15 of the mechanical model represent the same time period (current state until second half of the century) and simulate progressive thawing of the summit crest that leads to the continuation of increasing displacements and the preparation of final slope failure (Figure 6.5).

The factors of safety for all stages with one or more thawed rock layers, including the current extent of permafrost (Stage 11, Figure 6.5e), lie below unity, which indicates slope instability. This is consistent with the observations of the current displacements and characteristics of the main shear zone at the field site. However, the high values calculated by the model are not

comparable with the measured displacement rates at the field site (2.1 mm yr^{-1}) for the following reasons: (i) the numerically calculated displacements are maximum values and refer to local sections in the model. (ii) Cycling in UDEC was not linked to specific time steps. As such, we could not assign specific periods of time to the distinct, non-linear steps of warming or thawing. This did not permit us to estimate the approximate time period required for the calculated displacements to occur. (iii) Absolute displacements are path-dependent and affected by the history of calculations, including input and alteration of parameters as well as the stress–strain behaviour in the system.

Based on the 3D kinematic analysis (Section 6.3.1.1), we postulate that the most likely mechanism controlling the slope instability is a combination of a plane and a wedge failure. However, for the 2D numerical model and at the scale of the failure plane, we consider various possible complex mechanisms: (i) sliding of several rock blocks along a polygonal shear zone SZ1 and SZ4 that is constituted by joint sets K1, K3 and K4. This complex type of failure is provided by antithetic fractures which enable shear displacements between the moving blocks (Eberhardt et al., 2004; Poisel and Preh, 2004). (ii) Shear or tensile failure along joint sets K3 or K4 may favour shear displacements along K1 by supplying additional stress onto the blocks and inducing "step-path" failure (Huang et al., 2015; Mejía Camones et al., 2013). (iii) Failure at the scale of single blocks can be induced by forward block toppling with K1 and K3 or backward block toppling with K1 and K4 (Itasca Consulting Group, 2019). Both options will only work for higher columns subdivided by surfaces of K1 which stick together due to locally higher frictional or cohesive strength. (iv) The two joint sets K1 and K4 favour the displacements to concentrate on the south face. The highest deformations concentrate on the lower slope section with a mean gradient of 49°, but they are not coupled to the prominent shear zone. This can be the result of (i) the dominating influence of the slope angle on the stability of the system and (ii) the lack of variation in the joint properties of the shear zone and the remaining joint sets (Table 6.5).

6.6.3. The stability of a simplified permafrost rock slope with rising temperature

A permafrost rock slope with ice-filled joints as well as a fracture network and rock/joint properties similar to the Zugspitze south face can become unstable at a slope gradient > 50 or 55° (transition from Domain 1 to Domain 2 in Figure 6.7). This range of inclinations seems to be the most critical in terms of slope destabilisation, as it is characterised by the highest relative increase in displacements per degree of the slope angle. Interestingly, this could be confirmed by the study of the critical slope angle for varying orientations of the fracture network (Figure 6.8): 50 % of the studied orientations have a critical slope angle of 50 or 55°, which corresponds to the transition from Domain 1 to Domain 2; 30 % of the orientations lead to instability with

angles of between 57.5 and 62°; and 20 % remain stable within the studied range of slope gradients. The relevance of slope angles at the described transition from Domain 1 to Domain 2, identified by the numerical model, is in accordance with documented rock slope failures in the Swiss Alps, adjacent areas in France and Italy (Fischer et al., 2012), and in the Mont Blanc Massif (Ravanel et al., 2010), which are mostly attributed to the degradation of bedrock permafrost: the mean slope gradient of the detachment zones in the Mont Blanc Massif was 54°, whereas the highest percentage of detachment zones in the Swiss Alps and adjacent areas had slope angles of between 40 and 60°, leading to a postulated lower slope gradient threshold of between 40 and 45° for rock slope failures.

We further demonstrate that the factor of safety falls below 1 when a rock slope with a gradient ≥ 50° is warmed from -4 °C to a temperature of between -3 and -0.5 °C. This sensitive temperature range corresponds well to (i) the temperatures currently monitored in boreholes in permafrost rock walls in the European Alps (Gallemann et al., 2017; Nötzli et al., 2019) and (ii) the temperatures which are characteristic for warm permafrost areas or the lower permafrost boundary (-5 to 0 °C). The latter posed the release zones for most of the rock slope failure events documented by Fischer et al. (2012) and Ravanel et al. (2010).

The model results also demonstrate that the increase in displacements becomes more pronounced when approaching the melting point which indicates a non-linear relation (Figure 6.7b): the relative and the absolute increase are always higher for a warming from -2 to -0.5 °C than for a warming from -4 to -2 °C. The relation between rising sub-zero temperature and reduced stability was also observed by Davies et al. (2000, 2001). However, on the basis of our model results, we propose complementing the conclusions of Davies et al. (2001) in the following way: (i) the temperature of critical stability is highly dependent on the inclination of the main fractures versus the slope angle; (ii) it is of crucial importance to consider the stress conditions in a rock slope when extrapolating the results from the laboratory scale to the field scale; and (iii) the use of rock instead of concrete samples for the laboratory determination of joint parameters results in a closer reproduction of the real conditions along rock joints in the field.

6.6.4. Transferability and implications for other field sites

The general procedure for a temperature-dependent mechanical stability model (Figure 6.2) can be applied to any warming or thawing permafrost rock slope. However, the results of the sensitivity analysis with input data from the Zugspitze summit ridge (Section 6.5.2) are valid for rock slopes with increasing sub-zero temperatures, consisting of fractured limestone, with strength and deformability similar to the Wetterstein limestone tested in this study. A transfer to permafrost rock slopes with a different lithology is possible, but it requires more laboratory

calibration tests and modelling. A provisional transfer may be possible with the following justification:

Mamot et al. (2018, 2020) studied the shear strength of ice-filled permafrost rock joints and developed a resilient temperature- and stress-dependent failure criterion which is valid for the majority of the rocks that are relevant for observed permafrost rock slope failures in the Alps. As this failure criterion was used to calculate the cohesion and the friction of the ice-filled joints in the presented model, the numerical description of them may also be applied to other lithologies. However, the joint stiffness and the mechanical parameters of the rock mass still vary among different rock types and may lead to different model results. To get a first impression of this potential effect, we performed a couple of model test runs with varying values for the mechanical properties of the rock mass ranging from very low to unrealistically high. As the displacements remained within the same order of magnitude (Figure 6.12), we infer that the model results will not be significantly influenced by other rock types with distinct properties of strength and deformability. Nevertheless, we strongly recommend verifying the effect of different rock types by thorough modelling in the future.

The transferability of the numerical results is also limited to rock slopes with a similar joint set configuration as in this article because the rule of thumb for critical slope angles and fracture network orientations (Figure 6.8) is valid for a specific constellation of three joint sets and not only for the bedding, as presented by Cruden (2003). Considering the constraints above, the simplified model, developed by the sensitivity analysis (Section 6.5.2), can be transferred to warming permafrost rock slopes with ice-filled discontinuities and slope gradients smaller than 70°. In addition, these rock slopes consist of limestone (and probably mostly all rock types relevant for permafrost rock slope failures in the Alps), and they contain three joint sets separated from each other by an angle of 45°.

6.7. Conclusion

This study presents the first numerical model which is capable of performing comprehensive mechanical stability analyses of degrading permafrost rock slopes. In this context, we provide (i) a universal procedure for the input of thermal and mechanical data, the model set-up and the modelling strategy; (ii) a numerical benchmark application to a specific test site at the Zugspitze peak; and (iii) the first numerically derived critical stability thresholds related to the slope angle, rock mass temperature and orientation of the fracture network. The related main findings are summarised as follows:

(i) The proposed instruction for the temperature-dependent mechanical stability model can be used for any permafrost-affected rock slope across the globe that is subjected to climatic warming.

(ii) Laboratory tests and field reconnaissance of the benchmark site Zugspitze exemplify thermal, geometrical and mechanical input data for the numerical model. Frozen and unfrozen bedrock material properties were assigned to specific sections in the model and changed due to warming/thawing. The modelling procedure was divided into three stages: rock bridge destruction, warming with ice-filled joints and thawing. Process-specific and temperature-dependent input parameters were modified when switching from one stage to the next.

(iii) The Zugspitze model demonstrates a stability decrease towards a critical level as a result of (a) rock bridge destruction and (b) gradual warming of frozen rock and ice-filled joints from -4 to -0.5 °C. Surficial rock slope failure starts coincident to thawing of the outermost rock layer. Upon full thaw of the summit crest, expected within the next 5 decades, the model predicts an increase in displacements which potentially lead to final slope failure.

(iv) We developed a framework to generalise and upscale the Zugspitze model. A sensitivity analysis with simplified geometry and warming pattern was performed to calculate three critical stability thresholds. The first of these was the dependence between instability and the slope angle which can be classified into a stable first domain (≤ 50°), a second domain with a first onset of instability (55–62°) and a third domain characterised by an accelerated slope destabilisation (≥ 64°). The greatest relative increase in displacements is observed in the second domain. The second was the warming from -4 °C to a temperature between -3 and -0.5 °C which initiates instability for rock slopes ≥ 50°. Destabilisation is more pronounced for warming closer to the melting point (from -2 to -0.5 °C) than for warming from -4 to -2 °C. This difference becomes greatest in the second domain. Finally, for anaclinal slopes, the critical slope angles range between 50 and 62°, and for cataclinal slopes, they range between 55 and 62°.

(v) The calculated critical slope angles and rock mass temperatures correspond well to the characteristics of documented rock slope failures in permafrost areas in the European Alps, which often showed large amounts of residual ice in their scars.

(vi) The critical thresholds can be applied to warming permafrost rock slopes with (a) ice-filled joints; (b) limestone equivalent to Wetterstein limestone, or probably most of the rock types relevant for permafrost rock slope failure in the Alps; (c) slope angles smaller than 70°; and (d) various orientations of the fracture network consisting of three joint sets.

(vii) The critical thresholds can be used to detect rock slopes which are susceptible to fail in the future and potentially endanger human life and mountain infrastructure. For this, it is a prerequisite to have data on the fracture network, lithology, geometry and

the thermal field of the investigated rock slopes. In contrast, a detailed stability assessment of a single rock slope requires a number of further site-specific input data.

6.8. Supplements to the numerical analysis

6.8.1. Further assumptions for the procedure of the numerical analysis

The general modelling procedure consists of four steps: the calculation of an initial equilibrium and three successive steps of potential destabilisation which include the progressive destruction of intact rock bridges, the warming and the thawing of a permafrost rock slope. The past destruction of cohesive intact rock bridges was simulated by a reduction of the apparent joint cohesion and friction angle in three steps which represents a progressive increase of the joint persistence from 30 to 90 % (Stages 1–4 in Table 6.6 and Table 6.7). This procedure simulates "step-path" failure on the slope scale in a simplified way which is characterised by the interconnection of pre-existing, adjacent discontinuities through intact rock bridges (Eberhardt et al., 2004; Huang et al., 2015; Mejía Camones et al., 2013). The reduction in the shear strength involves processes of stress concentration, crack initiation, crack propagation and coalescence, slip weakening and the formation of a continuous failure plane or zone (Zhang et al., 2015), which were not numerically modelled as this would be beyond the scope of this study. The presented model of the Zugspitze ridge considers crack coalescence to occur by shear and tensile mode or a tensile-shear combination, which has been observed on the micro-scale by Zhang and Wong (2013). The resulting new connections can form coplanar or oblique to the pre-existing joints (Huang et al., 2015). At the scale of the Zugspitze ridge, we assume the joint sets K1, K3 and K4 to link in both coplanar and oblique form, leading to the formation of straight or stepped failure planes.

6.8.2. Additional sensitivity analyses of the numerical models

To analyse the influence of a higher disturbance factor D on the stability of the Zugspitze summit crest, D was changed to a maximum of 1. Accordingly, the mechanical parameters G, K, σ_{tm}, k_n and k_s reduced by a mean of 56 %. While the model results showed higher displacements, the factor of safety remained unchanged (Figure 6.9). Further, we extended the model domain by 20 m to the right/south and by 20 m downward to test if the model results are affected by a bigger model domain which ends in a flatter slope (Domain B in Figure 6.9). Again, the model results demonstrated that the overall stability of the slope does not change, although the displacements are higher by a factor of 1 to 3.

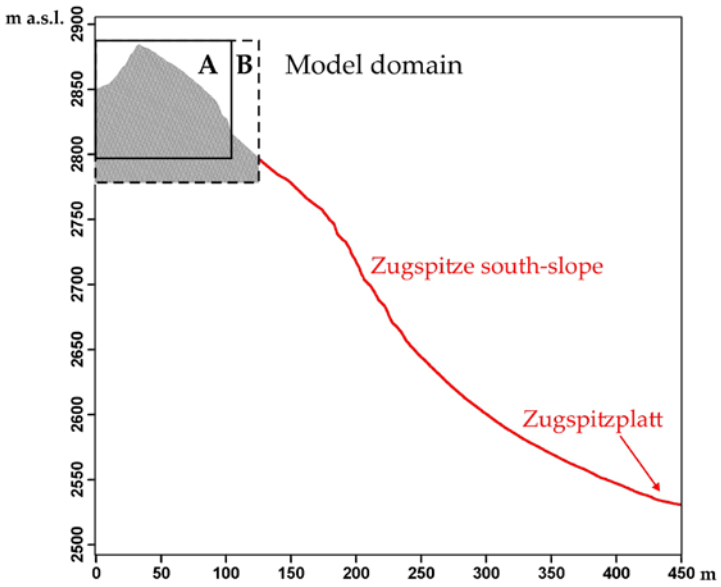

		Principal modelling steps	Initial state	Progressive destruction of rock bridges			Stepwise warming from surface to core				
		Model stage number	1	2	3	4	5	6	7	8	9
Max displ. [mm]	Model domain size Disturbance factor	A (D = 0)	7,6	7,8	7,8	7,7	7,7	7,7	7,8	7,9	8,2
		B	23,8	24,0	24,0	26,1	26,2	26,2	26,1	26,2	27,3
		D = 1	18,2	19,5	19,5	19,4	19,4	19,5	17,9	18,9	19,1
FoS	Model domain size Disturbance factor	A (D = 0)	10,9			2,6	3,4				1,3
		B	9,1		4,6	2,2	2,8				1,1
		D = 1	10,7			2,6	3,4				1,3

		Principal modelling steps	Stepwise thawing from surface to core					All unfrozen
		Model stage number	10	11	12	13	14	15
Max displ. [mm]	Model domain size Disturbance factor	A (D = 0)	141,1	419,5	520,4	616,8	689,7	776,3
		B	107,3	316,7	671,0	1066,4	1192,0	1226,4
		D = 1	273,2	782,3	1085,0	1232,7	1327,0	1407,7
FoS	Model domain size Disturbance factor	A (D = 0)	0,6	0,6				0,6
		B	0,5	0,6				0,7
		D = 1	0,6	0,7				0,7

Figure 6.9: Influence of a bigger model domain and a higher disturbance factor D on the slope stability.

Model domain A and D = 0 were used for the original Zugspitze model (Section 6.3). The topography of the Zugspitze (red line) was extracted from a digital elevation model in ArcGIS.

All numerical stability analyses for progressive warming were started with a frozen rock slope at a temperature of -4 °C. The stability calculations of the universal model were additionally run with a start temperature of -2 °C to be able to estimate the effect of a higher start temperature on the model results as material parameters with a lower strength have been assigned for the calculation of the initial equilibrium. However, the additional model runs led to similar displacement magnitudes as for a modelling start at -4 °C (Figure 6.10): the slope-dependent pattern is generally the same with two onsets of initiating instability at slope gradients of above 50 or 55° (transition to Domain 2) and a slope gradient above 62° (transition to Domain 3).

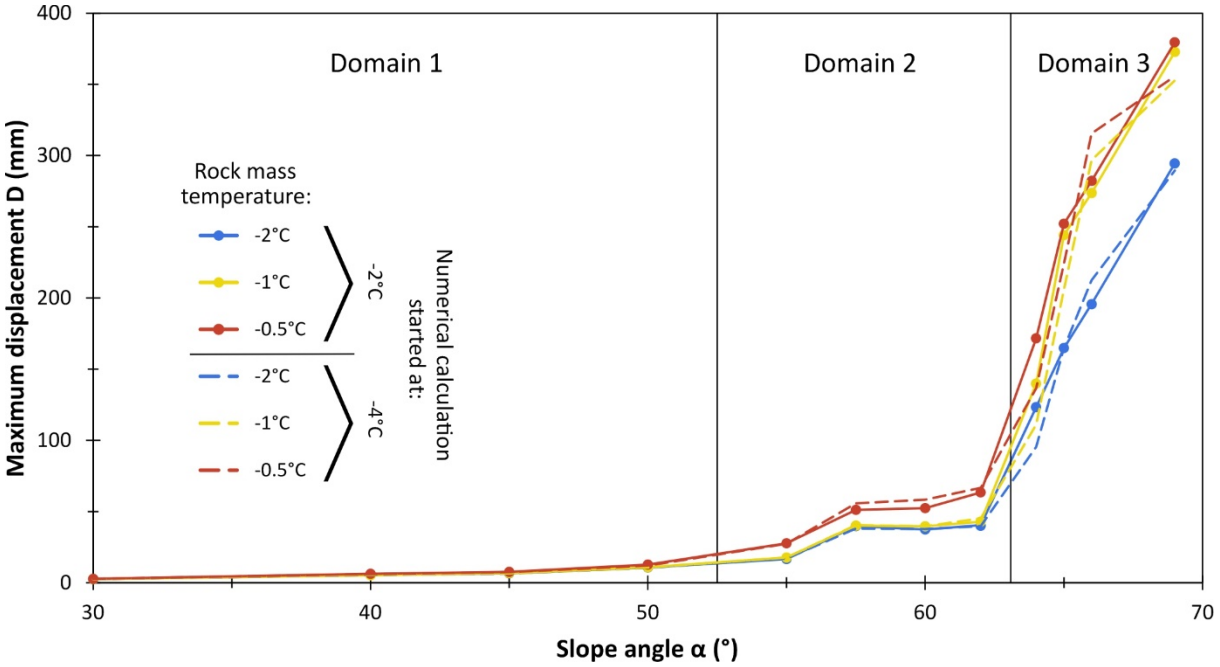

Figure 6.10: Maximum block and zone model displacements versus slope gradient for a permafrost rock slope at -2, -1 and -0.5 °C.

Solid lines with circles represent numerical results of calculations started at -2 °C, while dashed lines represent numerical results of calculations started at -4 °C (according to Figure 6.7). The three domains relate to a distinct displacement behaviour and are in accordance with the domains presented in Figure 6.7a.

The progressive warming steps for the universal rock slope were remodelled with twice the amount of cycles to assess the effect of longer numerical computation on the mechanical response of the system. Overall, the slope-dependent pattern remains generally the same with two onsets of initiating slope instability at 50 and at 62° (Figure 6.11). For warming steps between -4 and -2 °C the rock slope responded similar to the previous calculations with 3000 cycles (dashed lines). However, a warming to -1 or -0.5 °C in rock slopes with an inclination of higher than 60° resulted in displacements 10–111 % higher than in the model runs with 3000 cycles. However, the displacements remained within the same order of magnitude.

The results of the sensitivity analysis with input data from the Zugspitze summit ridge (Section 6.5.1) are valid for warming permafrost rock slopes which consist of limestone, with strength and deformability similar to the Wetterstein limestone tested in this study. A transfer to permafrost rock slopes with a different lithology requires more modelling, as the mechanical parameters of the rock mass vary among different rock types and may lead to different model results. To get an impression of this effect, we performed a couple of model test runs with varying values of the mechanical rock mass properties ranging from very low to unrealistically high. However, the selected range of the implemented mechanical properties also covers typical values of a wide range of different rock types (Clauser and Huenges, 1995; Kulatilake et al., 1992; Schön, 2015). We defined four fictitious levels of rock mass strength and deformability which are lower than the one of the Wetterstein limestone used for the presented

models (Section 6.5.1, Section 6.5.2), and six fictitious levels which are higher (Figure 6.12b). Modelling was performed for a rock slope with an inclination of 60° and a mean temperature of -4 °C. In a second step, we examined the pattern of displacements over the full range of slope gradients (30-66°) and temperatures (-0.5 to -4 °C) of the simplified model using a further specific level of high strength (Level 5) for a new set of model runs (Figure 6.12a).

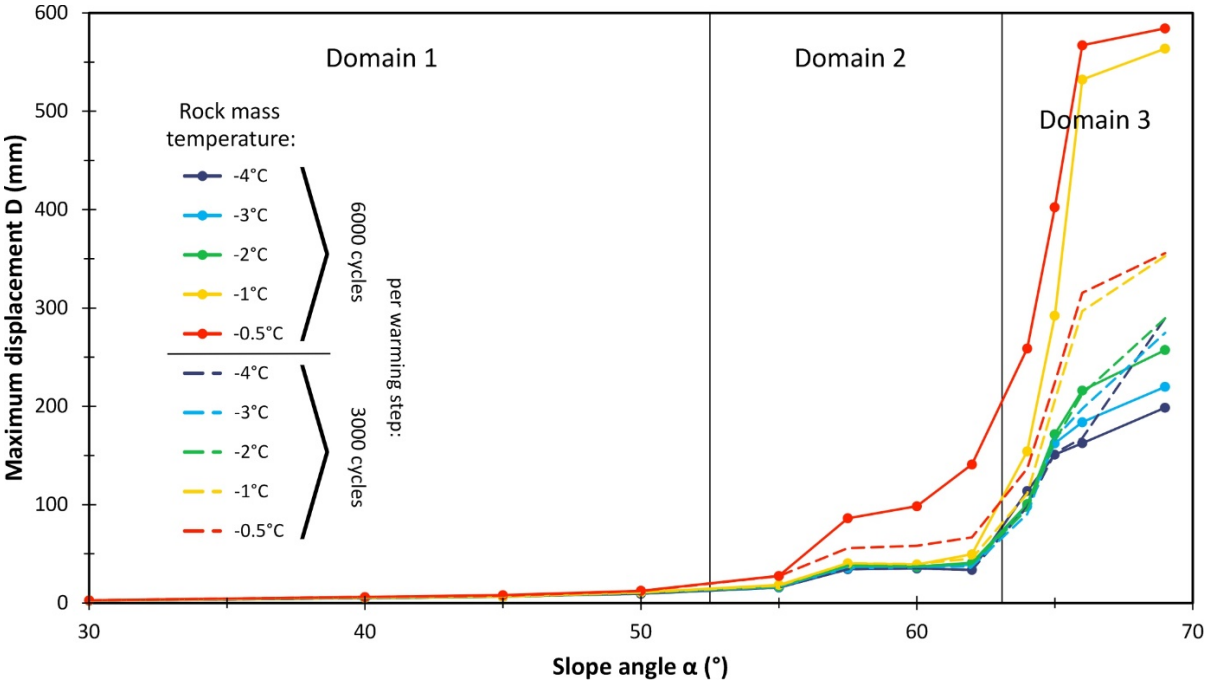

Figure 6.11: Maximum displacements against slope angle for a permafrost rock slope at temperatures between -4 and -0.5 °C.

Dashed lines represent warming steps with 3000 cycles (according to Figure 6.7), while solid lines with circles represent warming steps with the twofold amount of numerical cycles (6000). The three domains relate to a distinct displacement behaviour and are in accordance with the domains presented in Figure 6.7a.

The results of the analysis showed that the displacements mostly remained within the same order of magnitude (Figure 6.12a). This is valid for the model runs with (i) varying strength and deformability at a slope angle of 60° and a temperature of -4 °C (results lie within the dashed blue box), and (ii) the specific strength and deformability level 5 over the entire range of slope angles and temperatures of the simplified model.

a)

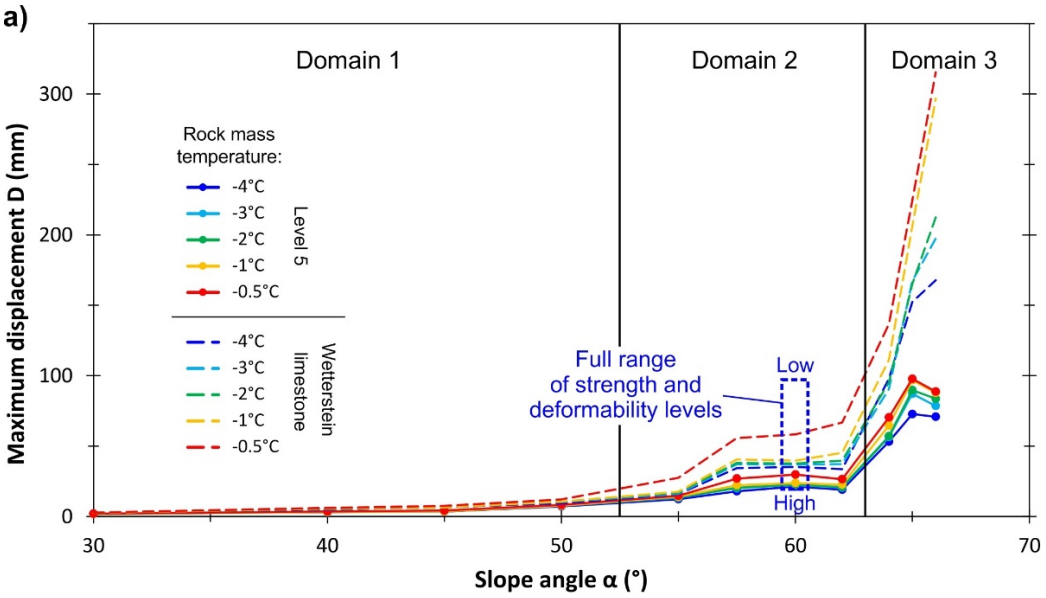

b)

	Strength and deformability level of the rock mass	Mechanical parameter ρ [g/cm³]	K_m [GPa]	G_m [GPa]	c_m [MPa]	σ_{tm} [MPa]	φ_m [°]
Low	-4	2,4	2,5	1,25	0,5	0,125	20
	-3	2,5	5	2,5	1	0,25	30
	-2	2,6	10	5	2	0,5	36
	-1	2,7	15	7,5	3	0,75	42
	0 (Wetterstein limestone: model)	2,7	20,6	9,52	4	0,9	44
	1	2,7	30	14	6	1,5	46
	2	2,7	41	19	8	2	46
	3	2,8	82	38	16	4	49
	4	2,9	164	76	32	8	52
	5 (used for model runs at temperatures from -4 to -0.5°C and slope angles from 30 to 66°)	2,7	200	90	40	9	55
	6	3,0	328	152	64	16	55
High	7	3,1	656	304	128	32	59

Figure 6.12: Maximum block and zone model displacements versus slope angle for different fictitious levels of rock mass strength and deformability and for temperatures between -4 and -0.5 °C.

(a) Dashed lines represent calculations with Wetterstein limestone (according to Figure 6.7), while solid lines with circles represent calculations with a rock type that has a strength and deformability one order of magnitude higher. The dashed blue box defines the range of displacements for all rock mass levels presented in (b), at -4 °C and for a slope gradient of 60°. (b) Mechanical parameters for the distinct rock masses with varying strength and deformability.

7. Synoptic discussion

7.1. The Zugspitze summit crest: A benchmark example for laboratory testing and numerical modelling

This subsection provides a discussion on the first research question of this thesis:

How can we constrain relevant mechanical and thermal conditions of permafrost rock slope instability, using the example of the Zugspitze summit crest?

Geophysical and geotechnical investigation of the mechanical and thermal characteristics of the Zugspitze summit ridge revealed the following main findings:

The study site is characterised by bedrock permafrost close to thawing, which is limited to the core of the crest and the rock layers below 5 m at the north-face. The temperatures of the permafrost body are expected to be in a similar range as at the Zugspitze peak (Gallemann et al., 2017). The derived subsurface temperature field agrees with the modelled thermal field of the Zugspitze peak by Böckli et al. (2011) or Nötzli (2008), and modelled current thermal fields of arbitrary mountain ridge geometries (Nötzli et al., 2007).

Compared to the mean summer air temperature (JJA) between 1991–2019, the summer of 2015 was exceptionally warm (+2.2 °C) at the Zugspitze, while the summer of 2014 (-0.8 °C) was rather cold (Figure 3.3). Due to this contrast, the ER- and SR-inversions of 08/2014 and 08/2015 may be well suited to represent the current, potential close-to-maximum deviation in the spatial permafrost extent at the study site. But still, this representation has to be used with caution due to changing long- and short-term meteorological effects (e.g. precipitation, temperature, evaporation) on the geophysical results (Section 4.4.2.4). Since a slight thermal signal of the contrasting summers of 2014, 2015 and 2016 can be identified with the geoelectrics (in the near-surface layer) and with the geoseismics (in the entire tomographies) (Figure 4.11, Figure 4.12), the derived boundary of permafrost is a good representation of the current situation in the summit crest.

A number of studies have shown that ice fillings can contribute to a higher shear strength of rock joints (e.g. Davies et al., 2001, or Krautblatter et al., 2013) and, thus, reduce shear displacements along fractures. This is valid for discontinuities in permafrost-affected bedrock or in the frozen active layer (during winter), which are mostly filled with ice (Gruber and Haeberli, 2007; Krautblatter and Dräbing, 2014). These fractures in the frozen rock at the study site are probably also mostly ice-filled. The contrast between the observed high displacement rates during summer and the low displacement rates during winter (Figure 4.6) may be a result of this strengthening effect by the ice along discontinuities. This assumption is confirmed by the fact that the period of enhanced fracture displacements (summer) corresponds well with the period of measured positive NSRT (Figure 4.9), and vice versa.

The rock mass is highly fractured, and the main shear zones show a high level of joint persistence and trace lengths. Therefore, the rock slope is likely to be close to or at the advanced stage of destabilisation, in which most of the cohesive intact rock bridges have supposedly been destroyed (Krautblatter et al., 2013). The remaining shear resistance is controlled by the friction along rock-rock-contacts, the creep of ice fillings, and the shear strength of rock-ice-interfaces and ice fillings. While rock-mechanics along rough clean joints are active in unfrozen sections, rock-ice-mechanics along ice-filled joints are active in frozen sections. The latter becomes relevant, since shear zone SZ1 runs in depths not greater than 20 m, and reveals ice-filled fractures at one location (Figure 4.2). A high joint surface roughness and filling with fine cohesive material in some places along the main shear planes may additionally enhance the shear resistance.

7.2. Mechanical response of laboratory rock and ice-filled rock joints to warming/thawing

A number of mechanical laboratory studies demonstrate that unfrozen intact rock has a lower strength and higher deformability than in frozen conditions. At the same time, warming close to melting can reduce the strength of frozen intact rock and (ice-filled) rock joints (Table 6.1). However, the effect of warming on the shear strength of ice-filled rock joints and its relevance for rock slope destabilisation remains poorly understood, since the existing knowledge is based on a negligible number of laboratory studies (Davies et al., 2000; Günzel, 2008, Ladanyi, 2006). Though, the brittle failure of ice fillings presumably constitutes an important final failure mechanism in steep bedrock permafrost, as a number of scars have exposed ice on their surfaces subsequent to failure (e.g. Guerin et al., 2020, Keuschnig et al., 2015, Phillips et al., 2017, or Walter et al., 2020).

The present section contains a short discussion on the second research question:

What is the warming- and thawing-dependent mechanical response of frozen intact rock and ice-filled rock joints at the laboratory scale?

261 constant strain shear tests on rock-ice-rock samples showed that warming from -10 to -0.5 °C causes a decrease in shear strength by 64 to 78 % within rock overburdens of 4 to 15 m. For the first time, natural rock from different permafrost-affected rock walls in the European mountains was used (Sections 5.2 and 5.3). A novel brittle failure criterion was developed which contains a temperature-dependent cohesion and coefficient of friction; these are reduced by 12 % $°C^{-1}$ and by 10 % $°C^{-1}$ respectively due to warming from -8 to -0.5 °C. The failure criterion applies to stress and temperature conditions of more than 90 % of the recently documented failure events in permafrost rock walls in the Mont Blanc Massif (Ravanel and Deline, 2008, 2011; Ravanel et al., 2010, 2017). Further, it is transferable to the accelerating final failure

stage (according to strain rates $4.8 \pm 1.4 * 10^{-3}$ s^{-1}) with rock mass volumes of $\leq 3 * 10^{4}$ m^3, and to a wide variety of rock types relevant for Alpine permafrost rock slope failures.

Most certainly, more laboratory investigations are recommended for the future to better understand the effect of lower strain rates, higher levels of joint surface roughness, and normal stresses above 800 kPa (in the range of the brittle fracture-creep transition) on the shear strength and the failure behaviour of ice-filled rock joints.

The measured mechanical response of the intact rock samples to thawing coincides with the one observed in previous publications. Thawing reduces the uniaxial compressive and tensile strength by 17–22 %, while the dilatational wave velocity decreases by 11 %, and the Poisson´s ratio is not affected. The basic friction angle of frozen unfilled rock joints decreases by 22 % upon thaw.

For a thorough investigation of the different response of various mechanical parameters, more tests with different lithologies are required. In addition, the static Young´s modulus and Poisson´s ratio (derived by destructive uniaxial compression tests) would be capable of providing direct data on the deformability of the intact rock.

7.3. Parameterisation of the numerical stability model

This section addresses research question 3a) of this thesis:

How can we join thermal and mechanical data from the field and the laboratory to develop a numerical stability model for a warming and thawing permafrost rock slope?

The proposed instruction for the set-up of a temperature-dependent mechanical stability model and for modelling (Figure 6.2, Sections 6.3.2 and 6.3.3) presents a useful tool to assess the stability of any permafrost rock slope across the globe, which is subjected to climatic warming. The numerical model of the rock slope under investigation requires a set of thermal, mechanical and geometrical input parameters. The corresponding techniques, applied in this thesis, have a varying spatial coverage of the rock slope (Figure 7.1). While the thermal characterisation includes the analysis of the subsurface temperature field (Figure 7.1a), the mechanical characterisation refers to the determination of mechanical rock and rock joint properties with samples from the field site (Figure 7.1b). The geometrical model input consists of the rock slope topography, the discontinuity network, major shear zones of a potentially failing rock mass, and the possible failure mechanism (Figure 7.1c). The measurement of fracture displacements can help to better assess the reliability of the spatial pattern of instability which is simulated by the numerical model.

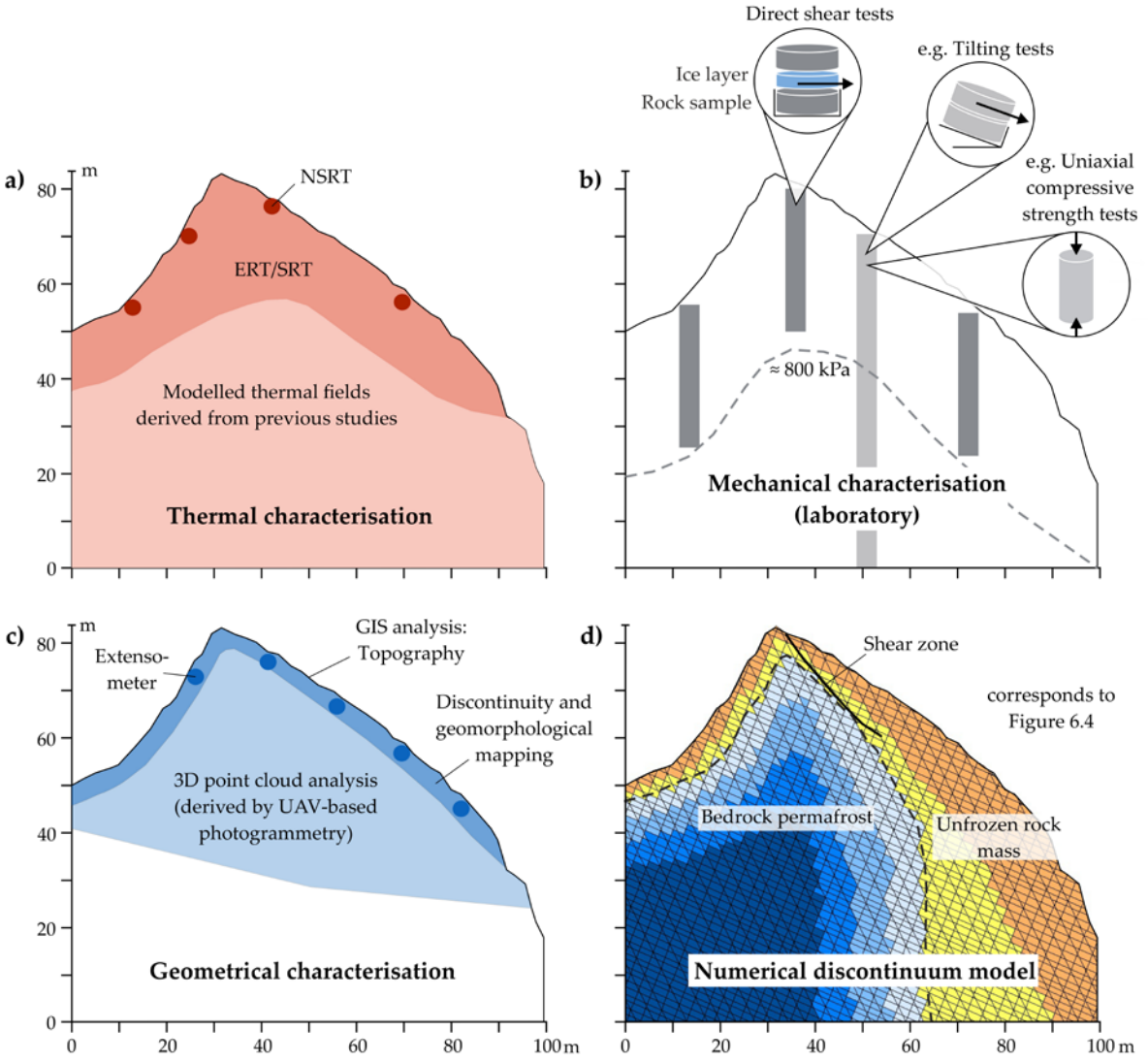

Figure 7.1: Spatial coverage of the applied methods in this thesis.

Techniques for the (a) thermal, (b) mechanical and (c) geometrical characterisation of the Zugspitze summit crest. (d) Resulting numerical discontinuum model, which includes the information of (a)–(c).

While the applied techniques were well suited to provide the required input data for the numerical model, the spatial coverage and temporal resolution of the slope displacement data can be optimised. The latter was based on two acquisition campaigns per year, performed with a digital tape extensometer along selected major fractures or shear zones. Other methods such as continuous crackmeter recordings or multitemporal remote sensing (e.g. digital airborne photogrammetry, DAP) can provide the extensive detection of slope processes or movements over the time. However, repeated DAP resulted to be inappropriate at the study site, since most of the rock surface is covered with permanently moving, loose debris. Hence, in situ measurements were preferably used.

Presently, we are still at the beginning of developing numerical models for the mechanical response of a rock mass to warming/thawing. Therefore, the developed numerical model still

provides a lot potential for improvement. Required adjustments and challenges are discussed below:

Material input parameters

We still have to learn a lot about the mechanical influence of warming and thawing on those rock and rock joint properties which are relevant for implementation in numerical stability models. The laboratory tests of this thesis contribute additional quantitative data, and a step towards a better process understanding: they showed a stronger warming-dependent reduction in mechanical strength (or deformability) for (i) ice-filled rock joints than for ice-free rock joints, and (ii) joint properties than for to intact rock properties (Table 5.1, Table 5.2, Table 6.1 and Table 6.5). As a consequence, the effect of warming on the destabilisation of a permafrost rock slope is expected to result in the highest displacements, if the rock mass has a high joint persistence and ice-filled joints.

More laboratory tests on warming intact rock and rock joints close to the melting point are required to derive mechanical properties for those temperature levels which are currently observed in permafrost rock walls across the European Alps (≥ -4 °C). In this way, they can be utilised as input parameters for modelling the mechanical response of a stepwise warming close below 0 °C. The existing laboratory data (Table 6.1) typically refer to a broader range of subzero-temperatures down to -20 °C or more, and thus do not provide high-resolved data close to 0 °C. Consequently, the stepwise warming above -4 °C in the presented numerical model was calculated by using various temperature-dependent values for the joint cohesion and friction (Table 6.5). However, the input values for the remaining frozen rock and joint parameters were not changed.

Laboratory studies on the normal and shear stiffness of ice-filled joints have not been conducted to this day. As a consequence, the joint stiffness properties implemented in the new model refer to clean joints without ice infill. If laboratory data were available and included in future model runs, the shear stiffness would probably increase (as rock-ice-interlocking and adhesion present a greater resistance than pure friction along rock-rock contacts, Table 6.1), while the normal stiffness would probably reduce (since the compressive strength of ice is one or two orders of magnitude lower than the one of rock, Table 6.1). Currently, we are not able to determine the extent to which the higher shear stiffness may offset the lower normal stiffness. However, it is recommended to study a potential effect in future model runs, ideally based on novel laboratory data.

The GSI rock mass classification system and the Hoek Brown strength criterion were used to determine rock mass properties. Potential effects upon freezing, which can increase the rock mass strength, are mostly ignored in the GSI system. For instance, the suggested determination

of the friction angle after Cai et al. (2004; Figure 5) is based on the temperature-independent Hoek-Brown constant m_i and the *GSI* value, which could only be defined for the unfrozen rock mass currently exposed at the surface of the rock slope. Due to this, the unfrozen internal friction value had to be assigned to both the frozen and the unfrozen rock mass (

Table 6.4), although the frozen angle of internal friction is expected to be larger than the unfrozen one. Triaxial compression tests on intact frozen and unfrozen rock samples may provide data for new model runs.

The joint spacing was set five-times greater than in reality (Table 6.2) due to computational limits defined by UDEC. By doing this, reasonable computation times were achieved and the model still reproduced slope conditions close to reality. Nevertheless, displacements are expected to increase slightly as was shown by Gischig et al. (2011a), and which is an obvious effect due to a reduced rock mass strength (Cai et al., 2004; Figure 7). Though, the comparability among all calculated model stages was not affected by the larger joint spacing as it was kept constant for all calculations.

Thermal regime

So far, the spatial warming pattern for the Zugspitze model is based on the static current temperature field derived from geophysical surveying, NSRT measurements and published thermal models of Böckli et al. (2011), Nötzli et al. (2007) and Nötzli (2008). A task for future studies will certainly be the validation with a heat flow model of the investigated rock slope for different time steps, which may refine the current and the future subsurface temperature field (i.e. the routes of the isothermal curves which separate rock layers from one another each with specific temperature-dependent material properties). Recent thermal modelling approaches at the rock slope scale have been presented by e.g. Lebrouc et al. (2013), Magnin et al. (2017) or Myhra et al. (2019); the first two studies compare modelling with geophysical inversions derived from surveys at the field site. The same is recommended to be done for the scale of the modelled south-slope at the Zugspitze summit crest. Geophysical monitoring of frozen rock is more accurate than thermal modelling as it takes topography, water flow and snow effects into account which are not sufficiently included in thermal models on this scale yet (Haberkorn et al., 2017; Dräbing et al. ,2017a).

Groundwater pressure

In a permafrost rock slope, freezing of ground water in water-filled fissures can block drainage paths. Built-up water pressure can decrease effective normal stress which leads to a decrease in shear strength along potential failure surfaces, and a reduction in slope stability (Wyllie, 2018). Elevated water pressures due to impermeable frozen bedrock may also occur in the permafrost-affected Zugspitze summit crest. It is certainly interesting and important for the

next steps to implement water pressures in the new developed numerical code. So far, there is no detailed knowledge on relevant water pressures in permafrost rock slopes and its effect on slope stability (Krautblatter et al., 2013). Therefore, hydraulic model parameters have to be taken from previous studies which still refer to an unfrozen rock mass. For instance, for their numerical stability model of the permafrost-affected rock wall of the Piz Morteratsch, Switzerland, Fischer et al. (2010) used hydraulic input parameters of an unfrozen rock mass and included a water pressure gradient based on two overlying rock layers with distinct permeability and degree of fissuring. The authors were able to demonstrate that slope stability responded sensitively to the inclusion of elevated water pressure induced by the lower, less permeable rock layer. An inclusion of elevated water pressures in the mechanical model of the Zugspitze will possibly lead to higher displacements near the surface, too, since the underlying permafrost layer may act like the impermeable rock layer in the model by Fischer et al. (2010).

7.4. A comprehensive numerical simulation of rock slope destabilisation

This subsection provides a discussion on research question 3b) of this thesis:

How does the numerical stability model simulate the warming-dependent changes in stability observed at the laboratory scale?

The warming- and thawing-dependent strength reduction, demonstrated in the laboratory tests of this and of previous studies (Table 6.1), could also be simulated by the numerical model for the Zugspitze summit ridge: Rock bridge destruction and warming of ice-filled joints take the slope close to a critical level of stability. As soon as thawing and ice loss set in, the south-face becomes massively destabilised. This is triggered by a slight reduction of the joint cohesion by 0.18 MPa, even though the joint friction angle is increased by 15.8°(Table 6.5).

Numerical modelling revealed that varying properties of the mechanical strength and deformability of the rock mass had a negligible effect on slope stability (even though properties ranged between very low and unrealistically high), since the displacements remained within the same order of magnitude (Figure 6.12). In contrast, a reduction in the joint strength/increase in the deformability induced destabilisation. The numerical analysis demonstrated that, among the joint material properties, the cohesion of ice-filled joints is the most sensitive parameter affected by warming; when thawing sets in and the ice interlayer melts, the increase in the joint friction angle (due to the rougher rock surfaces) cannot compensate the loss in joint cohesion (Table 6.5, Figure 6.5). Failure along a shear plane can be initiated, if joint cohesion due to intact rock bridges is absent, too. However, the degree to which the higher friction compensates the loss in cohesion depends on the joint surface roughness.

Discontinuity mapping at the field site revealed that a number of joints, in particular the bigger shear zones, are filled with fine material ranging from clay-size to gravel-size. Rock slope stability can be considerably affected by filled joints, since due to the low friction of the infill they provide very weak planes available for the initiation of sliding. Hence, the shear strength of an infilled joint is usually lower than a rough, clean joint (Indraratna et al., 1999; Indraratna et al., 2005). For future numerical analyses of rock slope stability, it would be interesting to include detected infilled discontinuities and to adjust appropriate strength parameters for the joints: (i) Bledow and Krautblatter (2010) performed shear tests with infill material from the study site of this thesis and its surroundings, and showed that the shear strength reduced by 50 % or more upon thaw. Other studies (e.g. Arenson and Springman, 2005a, Günzel, 2012, Yamamoto and Springman, 2014, or Yasufuku et al., 2003) demonstrate a similar behaviour for warming frozen sand or other sediment-ice-mixtures. Frozen peak shear strength values lie in a similar range as for the rock-ice-rock samples tested in this study (Sections 5.2 and 5.3). Therefore, the numerical simulation will lead to a similar joint stability and mechanical effect upon warming and thawing as has been shown for discontinuities without fillings of fine material. (ii) If the strength properties of the unfrozen clean joints were substituted by the properties of unfrozen joints filled with clay and/or granular fragments, the typically 0.1–0.4 MPa higher joint cohesion (Wyllie, 2018) would lead to a higher factor of safety. This will probably reduce the maximum displacements in the model, although the friction angle will be lower than for rough clean joints.

The presented model is the first numerical attempt to assess the mechanical response of a permafrost-affected rock slope to warming/thawing. As a consequence, constitutive block or discontinuity models, which are temperature-dependent and proven to be applied for numerical modelling at the rock-slope scale, are still scarce. An important milestone in this context is the work by Krautblatter et al. (2013), who combine different failure criterions to mathematically describe the shear strength of fractures in a permafrost-affected rock slope. The authors present two distinct constellations of various failure criterions for rock- and ice-mechanical processes which alternate (i) temporarily over the failure process and (ii) spatially from the surface to the interior of the model domain (rock slope). Certainly, an interesting future perspective is to improve the presented numerical model by combining different failure criterions in a new comprehensive, constitutive model which accounts for (i) different stages of the failure process and (ii) different ranges of rock overburden (e.g. according to Krautblatter et al., 2013). UDEC allows the user to write new constitutive models in the C++ language and to implement them in the numerical code (Itasca Consulting Group, 2019). For a process which is inactive during a specific model stage (e.g. the creep of ice during the initial stage of rock bridge destruction), the representing failure criterion has to be deactivated by setting input parameters to zero.

Accomplishments and limitations of the presented novel Zugspitze model with regard to (i) and (ii) are discussed as follows:

The different stages of the failure process

The failure process in the numerical model for the Zugspitze is divided chronologically into three stages: 1) the slow preparation of sliding planes (in which intact rock bridges break), 2) the acceleration of displacements along warming ice-filled joints, and 3) the acceleration of dislocations along thawing joints (Table 6.6). All stages are based upon the Mohr-Coulomb plasticity constitutive model. Due to its simplicity, Mohr-Coulomb is advantageous for the initial stage of the model development in which a fundamental understanding of joint response is required before applying more complex joint models (Itasca Consulting Group, 2019). Since process-specific and temperature-dependent input parameters are changed when switching between the stages of the numerical analysis, one single constitutive model is capable of accounting for various stages and processes which act during destabilisation. A limitation of this procedure is that the input parameters mostly represent one single process of shear displacement and failure, although real-world rock slope failure is typically characterised by various processes acting simultaneously; this has already been applied for Stage 2, in which the set of joint parameters accounts for two processes, the brittle failure of ice infillings and the fracture of rock-ice contacts.

Stage 1: For modelling, the joint shear strength during the slow progressive development of new shear planes has been represented by the friction angle and cohesion according to the approach by Jennings (1970). After this, the parameters of fully persistent joints were proportionately increased by the values of the rock mass dependent on the estimated percentages of rock bridges and joints within the rock slope. However, the joint shear strength during Stage 1 may alternatively be described by the frictional resistance of rock-rock-contacts along broken segments, and the fracture toughness of intermediate cohesive unbroken rock segments (Krautblatter et al., 2013).

The friction angle of persistent joints can be determined by Equation 2.3 (Section 2.2). The formula accounts for discontinuities with varying rock overburden and at frozen or unfrozen conditions, since it includes the residual friction angle elevated by the relation between the temperature-dependent joint wall compressive strength (JCS) and normal stress, as well as the joint surface roughness.

The cohesion of a non-persistent joint can inter alia expressed by the fracture toughness of intact rock bridges (see Equation 2.4 after Kemeny, 2003). Applying this failure criterion requires knowledge of the joint and rock bridge persistence (parameters w and a) within the rock

slope, which is not straightforward. In addition, more laboratory data on the frozen and unfrozen Mode II fracture toughness k_{IIC} may be useful, since the available data on rock are still limited to the study of Dwivedi et al. (2000).

Stage 2: Joint cohesion and friction angle for the acceleration of displacements along warming ice-filled joints were modelled with the novel criterion for the brittle failure of ice and rock-ice contacts along ice-filled joints (Section 5.2). A challenge for future improvements is to additionally consider the creep of ice-fillings (derived from Equation 2.1) as well as the shear displacement along rock-rock contacts (Equation 2.3) and discontinuities filled with frozen fine material.

It is impossible to determine the proportions of various failure processes along the joints (e.g. shearing along joints with ice infill, with frozen soil infill or without infill) and their exact location inside the rock slope. Thus, the dominating process which controls destabilisation at the study site, and which will be implemented as representative process in the numerical analysis, will have to be estimated roughly due to discontinuity mapping.

Stage 3: Usually, the cohesion of unfrozen, rough and clean joints is zero (Wyllie, 2018). Values lower than 0.1 MPa have been measured for unfrozen Zugspitze limestone and dolomite (Krautblatter et al., 2013). Accordingly, a joint cohesion of zero was applied to the rock layers in the model which were exposed to thawing. Any cohesion, which has been present in the previous stages, is absent in Stage 3: (i) Intact rock segments are destroyed during Stage 1 due to subcritical and progressive fracture propagation. (ii) Adhesion or interlocking along the rock-ice-interface are lost during Stages 2 and 3 due to warming and thawing of the ice fillings.

The remaining process was the shearing along unfrozen, rough and clean joints simulated by the residual friction only. The friction angle was determined by means of laboratory tilt and Schmidt hammer tests, and Equation 6.10. Alternatively, this process can be simulated by the concept of total friction following Equation 2.3, which also considers the influence of normal stress and joint surface roughness. Future numerical codes may also account for shearing along joints filled with unfrozen fine material (see above).

Different ranges of rock overburden

So far, the implemented material parameters and the corresponding failure processes vary spatially over the model domain dependent on the rock mass temperature. However, Krautblatter et al. (2013) postulate that fracturing of ice and rock-ice contacts mainly occur below a rock overburden of 20 m. At greater depths, higher confinement suppresses brittle failure and may favour creep deformation of ice (Renshaw and Schulson, 2001; Sanderson, 1988). A stress-dependent differentiation of the distinct failure processes has not been applied to the Zugspitze and the simplified model yet, because the model domain is small and processes at

depths greater than 30 m are affected by the fixed boundaries at the sides of the model (Figure 6.5). Therefore, it is assumed that the creep of ice fillings does not play a key role for destabilisation. However, a differentiation into near-surface fracturing along ice-filled joints (using Equation 5.6 for normal stresses of 100–400 kPa, or Equation 6.8 and Equation 6.9 for normal stresses of 100–800 kPa) and creep of ice in greater depths (applying Equation 2.1) is an interesting approach for future models that encompass a larger domain.

7.5. Usability and applicability of the new critical stability thresholds to other Alpine sites

This section provides a discussion on the usability of the new-developed numerical model and on the fourth research question:

Which are the critical slope angles and fracture network orientations for the onset of a warming-dependent slope destabilisation?

Critical thresholds for the failure of Alpine permafrost rock slopes were calculated in the context of a sensitivity analysis of the Zugspitze model with a simplified geometry and warming pattern (Section 6.5.2). The thresholds refer to (i) the slope angle, (ii) the temperature of the rock mass and (iii) the orientation of the fracture network versus the slope face:

(i) Rock slope failure is initiated at slope angles of greater than 50°, and accelerated above a slope gradient of 62°. The greatest relative increase in displacements is observed between 55 and 62° (Domain 2: "First onset of instability").

(ii) The described pattern is more pronounced for warming closer to the melting point (from -2 to -0.5 °C) than for warming from -4 to -2 °C. This difference becomes greatest in Domain 2, with a mean relative increase in displacements being 33 % $°C^{-1}$ higher. Further, a warming from -4 °C to a temperature between -3 and -0.5 °C initiates instability for rock slopes ≥ 50°.

(iii) For anaclinal slopes, the critical slope angles range between 50–62°, and for cataclinal slopes, they range between 55–62°.

The calculated critical slope angles and rock mass temperatures are in accordance with the characteristics of documented rock slope failures in the European Alps, which mostly occurred in areas where permafrost can be expected to be present, and which often showed large amounts of residual ice in the rockfall scars (Fischer et al., 2012; Ravanel et al., 2010; Ravanel et al., 2017). The modelled sensitive temperature range between -3 and -0.5 °C is consistent with the one currently measured in boreholes in permafrost rock walls across the European Alps (Gallemann et al., 2017; Nötzli et al., 2019); further, it is characteristic for warm permafrost areas which involve the release zones for most of the failure events documented in the Swiss, Italian and French Alps.

Can we apply these thresholds to other high-mountain permafrost sites?

The critical thresholds can be applied to warming permafrost rock slopes with (i) ice-filled discontinuities, (ii) slope gradients smaller than 70°, (iii) arbitrary orientations of three joint sets separated from each other by an angle of 45°, and (iv) fractured limestone, which has a strength and deformability similar to the Wetterstein limestone tested in this study.

The critical thresholds can also be applied to a wider range of rock types, which is justified by two facts: Firstly, the shear strength of the ice-filled discontinuities is numerically described by the failure criterion of Mamot et al. (2018, 2020), which is assumed to be valid for the majority of the rocks that are relevant for observed permafrost rock slope failures in the Alps. Secondly, additional model runs were performed to test a potential effect of varying mechanical rock mass properties (ranging from very low to unrealistically high) on the model behaviour. As the displacements remained within the same order of magnitude, the model results may not change significantly if other rock types with distinct strength and deformability are modelled.

Nevertheless, this is still a preliminary assumption, and it is strongly recommended to verify the effect of different rock types on slope stability by thorough modelling in the future. In addition, the new developed brittle failure criterion of Mamot et al. (2018, 2020) is based on shear tests with limestone, mica schist and gneiss. However, the inventory of rock slope failures by Fischer et al. (2012) showed that also granite was among the most frequent rock types, in which failure occurred and which potentially include the fracturing of ice-filled rock joints. Hence, more laboratory tests on granite samples with ice infill are required to study if the measured shear strength falls within the valid range of the new failure criterion. Since granite is not characterised by a pronounced foliation and bands with a concentrated abundance of aligned platy mica (like mica schist or gneiss), it does not represent the expected maximum deviation of potential lithological effects on the shear strength. Therefore, the peak shear strength of granite samples is expected to coincide with the validated range of the failure criterion.

The derived critical stability thresholds can be used to identify single high-mountain rock slopes which are susceptible to fail in future, and can be included in hazard or risk maps. However, the detection of potentially unstable sites at the scale of a mountain range is still a difficult task. For this, a characterisation of the discontinuity pattern and the subsurface thermal field of the investigated rock slopes is essential. But, due to the huge spatial scale, it cannot be derived by means of field work and a numerical thermal model. In contrast, the investigation of such a huge area requires regional photogeologic mapping which is based on high-resolution satellite imagery and digital elevation models available for most of the Earth´s surface. These tools allow the remote measurement of geological surface orientations, and thus,

the characteristics of the fracture network (Loye et al., 2012; Quinn and Ehlmann, 2019). The rock type can be identified due to a regional geological map. Finally, the required data on the permafrost occurrence can be derived from the Alpine Permafrost Index Map by Böckli et al. (2012b). A detailed stability assessment requires even more site-specific input data (i.e. the topography of the model profile, the ground water table or the spatial distribution of displacements), which is not realisable for a quick analysis of a current failure event.

Since time-dependent cycling is not yet implemented in numerical models – and neither it is in the models presented in this thesis – they are still not suited to predict a precise time of rock slope failure. However, a quasi-real simulation of time-dependency can be approached by using measured time series of a site-specific influencing factor (e.g. groundwater pressure, subsurface thermal field, seismic loading, rainfall events, etc.), which is implemented in the model and matched with a specific number of representative numerical cycles (Gischig et al., 2016; Preisig et al., 2016). This procedure can be used for the future assessment of rock slope stability, if the characteristics of the influencing factor vary constantly and in a clearly defined way, such as fluctuations in seasonal groundwater pressure or the water level of a reservoir at the valley bottom. A way to roughly estimate the time of beginning slope failure is to numerically analyse the evolution of the subsurface thermal field of the respective rock slope, since the time of the final stage of accelerated slope destabilisation is induced by the onset of thawing bedrock permafrost or by specific subzero-temperatures close to melting.

8. Conclusion

The presented thesis investigates the effect of climate-induced warming and thawing on the mechanical stability of permafrost rocks at the laboratory scale and at the scale of a high-mountain slope. This work uses multiple laboratory and field techniques to set up, for the first time, a novel 2D numerical discontinuum model that calculates the mechanical stability of a warming and thawing permafrost rock slope. The Zugspitze summit ridge was used as benchmark example to constrain relevant mechanical and thermal conditions of permafrost rock slope instability.

The most important findings of the field work are concluded as follows:

- Combined application of ERT, SRT and NSRT was able to characterise the current extent of permafrost in the summit crest, and to show that the permafrost body is close to thawing.
- Combined geotechnical mapping, kinematic analysis and 3D point cloud analysis (derived from UAV-based photogrammetry) allowed to estimate main shear planes as well as the potential mechanism and volume of an unstable rock mass.
- The rock mass is possibly close to the accelerated stage of rock slope destabilisation which is controlled by (rock-)ice-mechanics along ice-filled joints in frozen sections, and by rock-mechanics along rough clean joints in unfrozen sections.

The rock instability at the Zugspitze summit ridge acts as real-world exemplification of simulated brittle shear failure along rock-ice interfaces in the laboratory, which is still one of the least understood mechanical processes in degrading permafrost rock slopes. The main findings of the laboratory work are summarised as follows:

- 141 shear experiments with limestone-ice-limestone "sandwich" samples were performed at constant strain rates (10^{-3} s^{-1}) to represent the fracturing of ice and rock-ice contacts along ice-filled rock joints during the stage of accelerated rock slope failure (Publication 1: Mamot et al., 2018).
- The tests allowed to develop a novel stress- and temperature-dependent failure criterion. This is valid for normal stress conditions ranging from 100 to 400 kPa (representing 4–15 m of rock overburden), and for temperatures from -8 to -0.5 °C.
- The criterion is based on Mohr-Coulomb and includes a cohesion and friction angle which decrease by 12 % $°C^{-1}$ and by 10 % $°C^{-1}$ upon warming. It applies to stress and temperature conditions of more than 90 % of the recently documented failure events in permafrost rock walls in the Mont Blanc Massif.
- In a second series of 120 shearing tests on simulated ice-filled rock joints in gneiss and mica schist (Publication 2: Mamot et al., 2020), the peak shear strength corresponded well with the novel failure criterion by Mamot et al. (2018).

- The failure criterion is transferable to a wide variety of rock types relevant for permafrost rock slope failures in the Alps, since (i) the tested limestone, gneiss and mica schist cover most of the reported rock types involved in failure events, or those which can be found in the sensitive altitudinal boundary of permafrost, and (ii) the tested mica-rich rocks represent the expected maximum deviation of potential lithological effects on the shear strength.
- The findings of the laboratory tests were transferred to real-world scenarios of rock slope failure: The sudden unloading due to the detachment of a first slab (response within days), and the resulting facilitated warming (within years) of ice-filled rock joints can both induce a significant drop in shear resistance and cause a self-enforced rock slope failure propagation.
- Mechanical tests on frozen and unfrozen intact Wetterstein limestone demonstrated that the deformability and mechanical strength decreases up to 22 % upon thaw. This behaviour lies in the range of similar previous studies.

The Zugspitze summit crest acts as real-world high-mountain permafrost rock slope for the numerical analysis (Publication 3: Mamot et al., 2021). The laboratory tests allowed the parameterisation of the temperature-dependent mechanical properties. The geometry, the fracture network and the thermal field for the numerical model were derived from geotechnical and geophysical reconnaissance of the field site. Main insights from the modelling work are as follows:

- The model contains a subsurface temperature field, characterised by rock layers with varying temperature-dependent mechanical properties, and a procedure of gradual warming.
- A procedure for the input of temperature-dependent mechanical data, the model set-up and the modelling strategy was proposed, and can be used for any permafrost-affected rock slope across the globe, which is subjected to climatic warming.
- The factor of safety decreases to a critical level of stability when rock bridges break and frozen rock and ice-filled joints gradually warm from -4 to -0.5 °C. Rock slope failure is introduced upon thawing of the outermost rock layer as the factor of safety falls below 1.
- Rock slope failure is initiated at slope angles of greater than 50° and is even more intense above a slope gradient of 62°. Within this range, the critical slope angle varies dependent on the orientation of the fracture network versus the slope face. The calculated results agree with inventories of rock slope failures in permafrost areas in the European Alps.

- The increase in displacements intensifies for rock mass temperatures closer to the melting point.
- The derived critical thresholds can be applied to warming permafrost rock slopes with (a) ice-filled joints, (b) limestone equivalent to Wetterstein limestone, or probably most of the rock types relevant for permafrost rock slope failure in the Alps, (c) slope angles smaller than 70° and (d) various orientations of the fracture network consisting of three joint sets.

All in all, this thesis contributes an important step towards the prediction of the mechanical stability of degrading permafrost rock slopes in a warming climate. The proposed and applied procedure for the set-up of the numerical model and for modelling presents a useful tool for engineers and scientists who aim at performing a quantitative and spatially high-resolved stability assessment of a specific field site. The derived critical thresholds make it possible to identify rock slopes susceptible to failure, but their application is still limited and has to be improved in the future.

9. Outlook

Mountain surface air temperature is projected to continue increasing at an average rate of 0.3 °C per decade until the middle of the 21st century. Correspondingly, high-mountain permafrost is expected to continue thawing and degrading within the same time (Beniston et al.; 2018; Hock et al., 2019). Consequently, research progress in the mechanical stability analysis of degrading permafrost rock slopes is increasingly important to assess and reduce the rising risk of failure events to human life, mountain settlements and infrastructure. The required scientific process may include the following incomplete list of next steps structured after the three basic parts of this thesis:

Field work

At the scale of a mountain range, the proposed critical thresholds will be useful for the detection of degrading permafrost rock slopes susceptible to destabilisation or failure, and their implementation in hazard or risk maps. The investigation of such a huge area requires regional photogeologic mapping which is based on high-resolution satellite imagery and digital elevation models available for most of the Earth´s surface. These tools allow the remote measurement of geological surface orientations, and thus, the characteristics of the fracture network (Loye et al., 2012; Quinn and Ehlmann, 2019). The rock type can be identified due to a regional geological map. Finally, the required data on the permafrost occurrence can be derived from the Alpine Permafrost Index Map by Böckli et al. (2012b).

Laboratory work

More testing on mechanical properties of frozen intact rock (e.g. friction angle or cohesion) and rock joints (e.g. joint normal and shear stiffness) at different subzero-temperatures is necessary. By this, a high-resolved database of temperature-dependent material properties can be set up for a better process understanding and for numerical modelling.

To better understand the effect of lower strain rates, higher levels of joint surface roughness, and normal stresses above 800 kPa (in the range of the brittle fracture-creep transition), we need more laboratory tests on the shear strength and the failure behaviour of ice-filled rock joints.

Numerical modelling

Future numerical models should include (i) fracture infill (if detected at the investigated site), (ii) water pressure, (iii) a comprehensive constitutive model which combines different failure criterions and, thus, accounts for different stages of the failure process and different ranges of rock overburden, and (iv) a thermal field which is based on a combination of geophysics and a separate heat flow model for different time steps.

The presented stability model is not yet suited to anticipate the time of rock slope failure. However, the model results showed that at least the beginning of failure can be roughly estimated by the onset of thawing bedrock permafrost or by specific subzero-temperatures close to melting, which both induced the stage of accelerated slope destabilisation. For this, the future evolution of the subsurface thermal field has to be numerically analysed. Alternatively, a quasi-real simulation of time-dependency can be approached by including measured time series of a site-specific influencing factor, for instance, fluctuations in seasonal groundwater pressure. The factor has to vary constantly and in a clearly defined way. Then it can be matched with a specific number of representative numerical cycles (Gischig et al., 2016; Preisig et al., 2016).

This PhD thesis presents the basis for the listed next steps, because it provides a first contribution to a young research field with many gaps and open questions. This will hopefully encourage the future research progress.

10. References

Alava, M. J., Nukala, P. K. V. V. and Zapperi, S. (2006): Statistical model of fracture, Adv. Phys., 55, 349–476, doi: 10.1080/00018730300741518.

Alba-Simionesco, C., Coasne, B., Dosseh, G., Dudziak, G., Gubbins, K. E., Radhakrishnan, R. and Sliwinska-Bartkowiak, M. (2006): Effects of confinement on freezing and melting, Journal of Physics: Condensed Matter, 18, R15-R68, doi: 10.1088/0953-8984/18/6/r01.

Amitrano, D., Gruber, S. and Girard, L. (2012): Evidence of frost-cracking inferred from acoustic emissions in a high-alpine rock-wall, Earth and Planetary Science Letters, 341-344, 86–93, doi: 10.1016/j.epsl.2012.06.014.

Arakawa, M. and Maeno, N. (1997): Mechanical strength of polycrystalline ice under uniaxial compression, Cold regions science and technology, 26, 215–229.

Arenson, L. U. and Springman, S. M. (2005a): Triaxial constant stress and constant strain rate tests on ice-rich permafrost samples, Can. Geotech. J., 42, 2, 412–430, doi: 10.1139/t04-111.

Arenson, L. U. and Springman, S. M. (2005b): Mathematical descriptions for the behaviour of ice-rich frozen soils at temperatures close to 0 °C, Can. Geotech. J., 42, 2, 431–442, doi: 10.1139/t04-109.

Arenson, L. U., Springman, S. M. and Sego, D. C. (2007): The rheology of frozen soils, Applied Rheology, 17, 1–14, doi: 10.3933/ApplRheol-17-12147.

Aydin, A., Basu and A. (2005): The Schmidt hammer in rock material characterization, Engineering Geology, 81, 1–14.

Baer, P., Huggel, C., McArdell, B. W. and Frank, F. (2017): Changing debris flow activity after sudden sediment input: a case study from the Swiss Alps, Geology Today, 33, 6, 216–223, doi: 10.1111/gto.12211.

Bandis, S. C., Lumsden, A. C. and Barton, N. R. (1983): Fundamentals of rock joint deformation, International Journal of Rock Mechanics and Mining Sciences and Geomechanics, 20, 249–268.

Barboux, C., Delaloye, R. and Lambiel, C. (2014): Inventorying slope movements in an Alpine environment using DInSAR, Earth Surface Processes and Landforms, 39, 15, 2087–2099, doi: 10.1002/esp.3603.

Barnes, P. and Tabor, D. (1966): Plastic flow and pressure melting in the deformation of ice I, Nature, 210, 5039, 878-&, doi: 10.1038/210878a0.

Barnes, P., Tabor, D. and Walker, J. C. F. (1971): The friction and creep of polycrystalline ice, Proceedings of the Royal Society London Series A, 324, 127–155.

Barton, N. (1972): A model study of rock-joint deformation, International Journal of Rock Mechanics and Mining Sciences & Geomechanics Abstracts, 9, 579–582, doi: 10.1016/0148-9062(72)90010-1.

Barton, N. (1973): Review of a new shear-strength criterion for rock joints, Engineering Geology, 7, 287–332, doi: 10.1016/0013-7952(73)90013-6.

Barton, N. (2007): Rock quality, seismic velocity, attenuation and anisotropy, Taylor & Francis, London.

Barton, N. (2013): Shear strength criteria for rock, rock joints, rockfill and rock masses: Problems and some solutions, Journal of Rock Mechanics and Geotechnical Engineering, 5, 249–261, doi: 10.1016/j.jrmge.2013.05.008.

Barton, N. R. and Choubey, V. (1977): The shear strength of rock joints in theory and practice, Rock Mechanics, 10, 1–54.

Barton, N., Bandis, S. and Bakhtar, K. (1985): Strength, deformation and conductivity coupling of rock joints, International Journal of Rock Mechanics and Mining Sciences & Geomechanics Abstracts, 22, 121–140, doi: 10.1016/0148-9062(85)93227-9.

Bavarian Agency for Digitisation, High-Speed Internet and Surveying (2006): Digital elevation model of the Zugspitze summit area, Bavarian Agency for Digitisation, High-Speed Internet and Surveying, Munich.

Bayerisches Landesamt für Umwelt (2019): Bavarian Permafrost Map, https://www.umweltatlas.bayern.de/mapapps/resources/apps/lfu_angewandte_geologie_ftz/index.html?lang=de&layers=service_ageo_12&stateId=99aa5c19-cb46-4e51-aa5c-19cb46be5184, last access: 18 October 2019.

Bayerische Zugspitzbahn Bergbahn AG (2019): https://zugspitze.de/de/sommer/aktuell/ seilbahn-zugspitze, last access: 10 September 2019.

Beniston, M., Farinotti, D., Stoffel, M., Andreassen, L. M., Coppola, E., Eckert, N., Fantini, A., Giacona, F., Hauck, C., Huss, M., Huwald, H., Lehning, M., López-Moreno, J.-I., Magnusson, J., Marty, C., Morán-Tejéda, E., Morin, S., Naaim, M., Provenzale, A., Rabatel, A., Six, D., Stötter, J., Strasser, U., Terzago, S. and Vincent, C. (2018): The European mountain cryosphere. A review of its current state, trends, and future challenges, The Cryosphere, 12, 759–794, doi: 10.5194/tc-12-759-2018.

Bhasin, R. and Kaynia, A. M. (2004): Static and dynamic simulation of a 700-m high rock slope in western Norway, Engineering Geology, 71, 213–226, doi: 10.1016/S0013-7952(03)00135-2.

Biskaborn, B. K., Lanckman, J. P., Lantuit, H., Elger, K., Dmitry, S., William, C. and Vladimir, R. (2015): The new database of the Global Terrestrial Network for Permafrost (GTN-P), Earth System Science Data, 7, 245–259, doi: 10.5194/essd-7-245-2015.

Biskaborn, B. K., Smith, S. L., Nötzli, J., Matthes, H., Vieira, G., Streletskiy, D. A., Schoeneich, P., Romanovsky, V. E., Lewkowicz, A. G., Abramov, A., Allard, M., Boike, J., Cable, W. L., Christiansen, H. H., Delaloye, R., Diekmann, B., Drozdov, D., Etzelmüller, B., Grosse, G., Guglielmin, M., Ingeman-Nielsen, T., Isaksen, K., Ishikawa, M., Johansson, M., Johannsson, H., Joo, A., Kaverin, D., Kholodov, A., Konstantinov, P., Kröger, T., Lambiel, C., Lanckman, J.-P., Luo, D., Malkova, G., Meiklejohn, I., Moskalenko, N., Oliva, M., Phillips, M., Ramos, M., Sannel, A. Britta K., Sergeev, D., Seybold, C., Skryabin, P., Vasiliev, A., Wu, Q., Yoshikawa, K., Zheleznyak, M. and Lantuit, H. (2019): Permafrost is warming at a global scale, Nature Communications, 10, 1, 264, doi: 10.1038/s41467-018-08240-4.

Bledow, S. and Krautblatter, M. (2010): The influence of fine-grained fracture infillings on destabilization processes in permafrost-affected rock walls in the Alps, Geophysical Resarch Abstracts.

Böckli, L., Nötzli, J. and Gruber, S. (2011): PermaNET-BY: Untersuchung des Permafrosts in den Bayerischen Alpen. Teilprojekt PermaNET (EU Alpine Space Interreg IVb), Glaciology, Geomorphodynamics & Geochronology, Department of Geography, University of Zurich, Zürich, 60 pp.

Böckli, L., Brenning, A., Gruber, S. and Nötzli, J. (2012a): A statistical approach to modelling permafrost distribution in the European Alps or similar mountain ranges, The Cryosphere, 6, 125–140, doi: 10.5194/tc-6-125-2012.

Böckli, L., Brenning, A., Gruber, S. and Nötzli, J. (2012b): Permafrost distribution in the European Alps. Calculation and evaluation of an index map and summary statistics, The Cryosphere, 6, 807–820, doi: 10.5194/tc-6-807-2012.

Bourg, I. C. and Sposito, G. (2011): Molecular dynamics simulations of the electrical double layer on smectite surfaces contacting concentrated mixed electrolyte (NaCl–CaCl2) solutions, Journal of Colloid and Interface Science, 360, 701–715, doi: 10.1016/j.jcis.2011.04.063.

Bray, M. T. (2013): Secondary creep approximations of ice-rich soils and ice using transient relaxation tests, Cold Regions Science and Technology, 88, 17–36, doi: 10.1016/j.coldregions.2012.12.011.

Budetta, P., Riso, R. de and Luca, C. de (2001): Correlations between jointing and seismic velocities in highly fractured rock masses, Bulletin of the International Association of Engineering Geology - Bulletin de l'Association Internationale de Géologie de l'Ingénieur, 60, 185–192, doi: 10.1007/s100640100097.

Burn, C. R. (2013): Permafrost and periglacial features | Permafrost, in: Encyclopedia of Quaternary Science (Second Edition), Elsevier, Amsterdam, 464–471.

Butkovitch, T. R. (1954): The ultimate strength of ice, Report on the Snow, Ice and Permafrost Research Establishment Project, Res. paper 15, Corps of Engineers, U.S. Army, Wilmette, Illinois.

Cai, M., Kaiser, P. K., Uno, H., Tasaka, Y. and Minami, M. (2004): Estimation of rock mass deformation modulus and strength of jointed hard rock masses using the GSI system, International Journal of Rock Mechanics and Mining Sciences, 41, 3–19, doi: 10.1016/S1365-1609(03)00025-X.

Casagli, N., Frodella, W., Morelli, S., Tofani, V., Ciampalini, A., Intrieri, E., Raspini, F., Rossi, G., Tanteri, L. and Lu, P. (2017): Spaceborne, UAV and ground-based remote sensing techniques for landslide mapping, monitoring and early warning, Geoenvironmental Disasters, 4, 1, 9, doi: 10.1186/s40677-017-0073-1.

Chang, S.-H., Lee, C.-I. and Jeon, S. (2002): Measurement of rock fracture toughness under modes I and II and mixed-mode conditions by using disc-type specimens, Engineering Geology, 66, 79–97, doi: 10.1016/S0013-7952(02)00033-9.

Chayes, F. (1949): A simple point counter for thin-section analysis, American Mineralogist, 34, 1-2, 1–11.

Clague, J. J. and O'Connor, J. E. (2015): Chapter 14 – Glacier-Related Outburst Floods, in: Snow and Ice-Related Hazards, Risks and Disasters, Academic Press, Boston, 487–519.

Clauser, C. and Huenges, E. (1995): Thermal conductivity of rocks and minerals, in: Rock Physics & Phase Relations: A Handbook of Physical Constants, American Geophysical Union, Washington, D. C., 105–126.

Coulomb, C. A. (1776): Essai sur une application des regles de maximis et minimis a quelques problemes de statique, relatifs a l'architecture, Academie Royale des Sciences, Memoires de Mathematique & de Physique, 7, 343–382.

Coulson, J. H. (1970): The effects of surface roughness on the shear strengths of joints, Dissertation, University of Illinois, Urbana, Illinois, USA.

Cox, S. J. D. and Meredith, P. G. (1993): Microcrack formation and material softening in rock measured by monitoring acoustic emissions, Int. J. Rock Mech. Min. Sci. Geomech. Abstr., 30, 1, 11–24, doi: 10.1016/0148-9062(93)90172-A.

Cruden, D. M. (2003): The shapes of cold, high mountains in sedimentary rocks, Geomorphology, 55, 249–261, doi: 10.1016/S0169-555X(03)00143-0.

Davies, M. C.R., Hamza, O., Lumsden, B. W. and Harris, C. (2000): Laboratory measurement of the shear strength of ice-filled rock joints, Annals of Glaciology, 31, 463–467, doi: 10.3189/172756400781819897.

Davies, M. C.R., Hamza, O. and Harris, C. (2001): The effect of rise in mean annual temperature on the stability of rock slopes containing ice-filled discontinuities, Permafrost and periglacial processes, 12, 1, 137–144, doi: 10.1002/ppp.378.

Delaloye, R., Hilbich, C., Lüthi, R., Nötzli, J., Phillips, M. and Staub, B. (2016): Permafrost in Switzerland 2010/2011 to 2013/2014. Glaciological Report (Permafrost) No. 12-15, PERMOS, Fribourg.

Deline, P., Gruber, S., Delaloye, R., Fischer, L., Geertsema, M., Giardino, M., Hasler, A., Kirkbride, M., Krautblatter, M., Magnin, F., McColl, S., Ravanel, L. and Schoeneich, P. (2015): Ice Loss and Slope Stability in High-Mountain Regions, in: Snow and Ice-Related Hazards, Risks and Disasters, Academic Press, Boston, 521–561.

DIN EN ISO 1097-6 (2005): Tests for mechanical and physical properties of aggregates - Part 6: Determination of particle density and water absorption; German version EN 1097-6:2000, 91.100.15, Beuth Verlag GmbH, Berlin.

DIN EN ISO 13755 (2002): Natural stone test methods - Determination of water absorption at atmospheric pressure; German version EN 13755: 2001, 73.020, Beuth Verlag GmbH, Berlin.

DIN EN ISO 16810 (2014): Non-destructive testing - Ultrasonic testing - General principles (ISO 16810: 2012); German version EN ISO 16810: 2014, 19.100, Beuth Verlag GmbH, Berlin.

DIN EN ISO 7500-1 (2018): Metallic materials - Calibration and verification of static uniaxial testing machines - Part 1: Tension/compression testing machines - Calibration and verification of the force-measuring system, Beuth Verlag GmbH, Berlin.

DIN ISO 8576 (2002-06): Optics and optical instruments - Microscopes - Reference systems of polarized light microscopy, 37.020, Beuth Verlag GmbH, Berlin.

Dosch, H., Lied, A. and Bilgram, J. H. (1996): Disruption of the hydrogen-bonding network at the surface of Ih ice near surface premelting, Surface Science, 366, 43–50, doi: 10.1016/0039-6028(96)00805-9.

Dräbing, D. (2016): Application of refraction seismics in alpine permafrost studies. A review, Earth Science Reviews, 155, 136–152, doi: 10.1016/j.earscirev.2016.02.006.

Dräbing, D. and Krautblatter, M. (2012): P-wave velocity changes in freezing hard low-porosity rocks. A laboratory-based time-average model, The Cryosphere, 6, 1163–1174, doi: 10.5194/tc-6-1163-2012.

Dräbing, D., Krautblatter, M. and Dikau, R. (2014): Interaction of thermal and mechanical processes in steep permafrost rock walls: A conceptual approach, Geomorphology, 226, 226–235, doi: 10.1016/j.geomorph.2014.08.009.

Dräbing, D., Haberkorn, A., Krautblatter, M., Kenner, R. and Phillips, M. (2017a): Thermal and mechanical responses resulting from spatial and temporal snow cover variability in permafrost rock slopes, Steintaelli, Swiss Alps, Permafrost and periglacial processes, 28, 140–157, doi: 10.1002/ppp.1921.

Dräbing, D., Krautblatter, M. and Hoffmann, T. (2017b): Thermo-cryogenic controls of fracture kinematics in permafrost rockwalls, Geophysical Research Letters, 44, 8, 3535–3544, doi: 10.1002/2016GL072050.

Dramis, F., Govi, M., Guglielmin, M. and Mortara, G. (1995): Mountain permafrost and slope instability in the Italian Alps. The Val Pola Landslide, Permafrost and periglacial processes, 6, 73–81, doi: 10.1002/ppp.3430060108.

Dwivedi, R. D., Soni, A. K., Goel, R. K. and Dube, A. K. (2000): Fracture toughness of rocks under sub-zero temperature conditions, International Journal of Rock Mechanics and Mining Sciences, 37, 1267–1275.

Eberhardt, E., Stead, D. and Stimpson, B. (1999): Quantifying progressive pre-peak brittle fracture damage in rock during uniaxial compression, International Journal of Rock Mechanics and Mining Sciences, 36, 361–380, doi: 10.1016/S0148-9062(99)00019-4.

Eberhardt, E., Stead, D. and Coggan, J. S. (2004): Numerical analysis of initiation and progressive failure in natural rock slopes—the 1991 Randa rockslide, International Journal of Rock Mechanics and Mining Sciences, 41, 69–87, doi: 10.1016/S1365-1609(03)00076-5.

Etzelmüller, B. (2013): Recent Advances in Mountain Permafrost Research, Permafrost and periglacial processes, 24, 2, 99–107, doi: 10.1002/ppp.1772.

Fellin, W. (2013): Einführung in die Eis-, Schnee- und Lawinenmechanik, Springer Vieweg, Berlin, Heidelberg.

Fenter, P., Cheng, L., Rihs, S., Machesky, M., Bedzyk, M. J. and Sturchio, N. C. (2000): Electrical Double-Layer Structure at the Rutile–Water Interface as Observed in Situ with Small-Period X-Ray Standing Waves, Journal of Colloid and Interface Science, 225, 154–165, doi: 10.1006/jcis.2000.6756.

Fischer, L., Kaeaeb, A., Huggel, C. and Nötzli, J. (2006): Geology, glacier retreat and permafrost degradation as controlling factors of slope instabilities in a high-mountain rock wall. The Monte Rosa east face, Natural Hazards and Earth System Sciences, 6, 5, 761–772, doi: 10.5194/nhess-6-761-2006.

Fischer, L., Amann, F., Moore, J. R. and Huggel, C. (2010): Assessment of periglacial slope stability for the 1988 Tschierva rock avalanche (Piz Morteratsch, Switzerland), Engineering Geology, 116, 1-2, 32–43, doi: 10.1016/j.enggeo.2010.07.005.

Fischer, L., Purves, R. S., Huggel, C., Nötzli, J. and Haeberli, W. (2012): On the influence of topographic, geological and cryospheric factors on rock avalanches and rockfalls in high-mountain areas, Natural Hazards and Earth System Science, 12, 1, 241–254.

Fish, A. M. and Zaretzky, Y. K. (1997): Ice strength as a function of hydrostatic pressure and temperature, in: CRREL Report, 97, 1–13.

Gagnon, R. E. and Gammon, P. H. (1995): Triaxial experiments on iceberg and glacier ice, Journal of Glaciology, 41, 139, 528–540.

Gallemann, T., Haas, U., Teipel, U., Poschinger, A. von, Wagner, B., Mahr, M. and Bäse, F. (2017): Permafrost-Messstation am Zugspitzgipfel: Ergebnisse und Modellberechnungen, Geologica Bavarica, 115, 1–77.

Gambino, G. F. and Harrison, J. P. (2017): Rock engineering design in frozen and thawing rock. Current approaches and future directions, Procedia Engineering, 191, 656–665, doi: 10.1016/j.proeng.2017.05.229.

Girard, L., Beutel, J., Gruber, S., Hunziker, J., Lim, R. and Weber, S. (2012): A custom acoustic emission monitoring system for harsh environments. Application to freezing-induced damage in alpine rock walls, Geosci. Instrum. Method. Data Syst., 1, 2, 155–167, doi: 10.5194/gi-1-155-2012.

Gischig, V., Amann, F., Moore, J. R., Loew, S., Eisenbeiss, H. and Stempfhuber, W. (2011a): Composite rock slope kinematics at the current Randa instability, Switzerland, based on remote sensing and numerical modeling, Engineering Geology, 118, 37–53, doi: 10.1016/j.enggeo.2010.11.006.

Gischig, V. S., Moore, J. R., Evans, K. F., Amann, F. and Loew, S. (2011b): Thermomechanical forcing of deep rock slope deformation. 1. Conceptual study of a simplified slope, Journal of Geophysical Research: Earth Surface, 116, F04010, doi: 10.1029/2011JF002006.

Gischig, V. S., Moore, J. R., Keith, F. E., Amann, F. and Loew, S. (2011c): Thermomechanical forcing of deep rock slope deformation: 2. The Randa rock slope instability, Journal of Geophysical Research, 116, F04011, doi: 10.1029/2011JF002007.

Gischig, V., Preisig, G. and Eberhardt, E. (2016): Numerical Investigation of Seismically Induced Rock Mass Fatigue as a Mechanism Contributing to the Progressive Failure of Deep-Seated Landslides, Rock Mechanics and Rock Engineering, 49, 2457–2478, doi: 10.1007/s00603-015-0821-z.

Glamheden, R. (2001): Thermo-mechanical behaviour of refrigerated caverns in hard rock, Dissertation, Chalmers University of Technology, Göteborg.

Glamheden, R. and Lindblom, U. (2002): Thermal and mechanical behaviour or refrigerated caverns in hard rock, Tunnelling and Underground Space Technology, 17, 341–353.

Glen, J. W. and Perutz, M. Ferdinand (1955): The creep of polycrystalline ice, Proceedings of the Royal Society of London. Series A. Mathematical and Physical Sciences, 228, 1175, 519–538, doi: 10.1098/rspa.1955.0066.

Gobiet, A., Kotlarski, S., Beniston, M., Heinrich, G., Rajczak, J. and Stoffel, M. (2014): 21st century climate change in the European Alps-A review, Science of the Total Environment, 493, 1138–1151, doi: 10.1016/j.scitotenv.2013.07.050.

Gómez-Heras, M., Smith, B. J. and Fort, R. (2006): Surface temperature differences between minerals in crystalline rocks. Implications for granular disaggregation of granites through thermal fatigue, Geomorphology, 78, 3, 236–249, doi: 10.1016/j.geomorph.2005.12.013.

Gruber, S. and Haeberli, W. (2007): Permafrost in steep bedrock slopes and its temperature-related destabilization following climate change, Journal of Geophysical Research, 112, 1–10, doi: 10.1029/2006JF000547.

Gruber, S., Hoelzle, M. and Haeberli, W. (2004a): Permafrost thaw and destabilization of Alpine rock walls in the hot summer of 2003, Geophysical Research Letters, 31, 13, L13504, doi: 10.1029/2004GL020051.

Gruber, S., Hoelzle, M. and Haeberli, W. (2004b): Rock-wall temperatures in the Alps. Modelling their topographic distribution and regional differences, Permafrost and periglacial processes, 15, 3, 299–307, doi: 10.1002/ppp.501.

GTN-P database (2019): http://gtnpdatabase.org/boreholes, last access: 16 October 2019.

Gubler, S., Fiddes, J., Keller, M. and Gruber, S. (2011): Scale-dependent measurement and analysis of ground surface temperature variability in alpine terrain, The Cryosphere, 5, 431–443, doi: 10.5194/tc-5-431-2011.

Gude, M. and Barsch, D. (2005): Assessment of geomorphic hazards in connection with permafrost occurrence in the Zugspitze area (Bavarian Alps, Germany), Geomorphology, 66, 1-4, 85–93.

Guerin, A., Ravanel, L., Matasci, B., Jaboyedoff, M. and Deline, P. (2020): The three-stage rock failure dynamics of the Drus (Mont Blanc massif, France) since the June 2005 large event, Scientific Reports, 10, 17330, doi: 10.1038/s41598-020-74162-1.

Günzel, F. K. (2008): Shear strength of ice-filled rock joints, 9th International Conference on Permafrost, Fairbanks, Alaska, 28 June – 3 July 2008, 581–586.

Günzel, F. K. (2012): Shear strength of rock joints filled with frozen sand, Salekhard, Russia, 25-29 June, 143–148.

Haberkorn, A., Hoelzle, M., Phillips, M. and Kenner, R. (2015): Snow as a driving factor of rock surface temperatures in steep rough rock walls, Cold regions science and technology, 118, 64–75, doi: 10.1016/j.coldregions.2015.06.013.

Haberkorn, A., Wever, N., Hoelzle, M., Phillips, M., Kenner, R., Bavay, M. and Lehning, M. (2017): Distributed snow and rock temperature modelling in steep rock walls using Alpine3D, The Cryosphere, 11, 585–607, doi: 10.5194/tc-11-585-2017.

Haeberli, W. (1992): Construction, environmental problems and natural hazards in periglacial mountain belts, Permafrost and periglacial processes, 3, 2, 111–124, doi: 10.1002/ppp.3430030208.

Haeberli, W. (1999): Hangstabilitätsprobleme im Zusammenhang mit Gletscherschwund und Permafrostdegradation im Hochgebirge, in: Massenbewegungen und Massentransporte in den Alpen als Gefahrenpotential, Relief, Boden, Paläoklima, Borntraeger, Berlin, 11–30.

Hagg, W., Mayer, C., Mayr, E. and Heilig, A. (2012): Climate and glacier fluctuations in the Bavarian Alps in the past 120 years, Erdkunde, 66, 121–142.

Hall, K. and Thorn, C. E. (2014): Thermal fatigue and thermal shock in bedrock: An attempt to unravel the geomorphic processes and products, Geomorphology, 206, 1–13, doi: 10.1016/j.geomorph.2013.09.022.

Hardy, H. R. (2003): Acoustic Emission/Microseismic Activity - Volume 1. Principles, Techniques and Geotechnical Applications, A.A. Balkema Publisher, a member of Swets & Zeitlinger Publishers.

Harris, S. A., French, H. M., Heginbottom, J. A., Johnston, G. H., Ladanyi, B., Sego, D. C. and van Everdingen, R. O. (1988): Glossary of Permafrost and Related Ground-Ice Terms, Technical Memorandum (Associate Committee on Geotechnical Research), 0-660-12540-4.

Harris, C., Vonder Mühll, D., Isaksen, K., Haeberli, W., Sollid, J. L., King, L., Holmlund, P., Dramis, F., Guglielmin, M. and Palacios, D. (2003): Warming permafrost in European mountains, Global and Planetary Change, 39, 3-4, 215–225, doi: 10.1016/j.gloplacha.2003.04.001.

Harris, C., Arenson, L. U., Christiansen, H. H., Etzelmüller, B., Frauenfelder, R., Gruber, S., Haeberli, W., Hauck, C., Hölzle, M., Humlum, O., Isaksen, K., Kääb, A., Kern-Lütschg, M. A., Lehning, M., Matsuoka, N., Murton, J. B., Nötzli, J., Phillips, M., Ross, N., Seppälä, M., Springman, S. M. and Mühll, D. Vonder (2009): Permafrost and climate in Europe. Monitoring and modelling thermal, geomorphological and geotechnical responses, Earth Science Reviews, 92, 117–171, doi: 10.1016/j.earscirev.2008.12.002.

Hasler, A., Gruber, S., Font, M. and Dubois, A. (2011a): Advective Heat Transport in Frozen Rock Clefts. Conceptual Model, Laboratory Experiments and Numerical Simulation, Permafrost and periglacial processes, 22, 4, 378–389, doi: 10.1002/ppp.737.

Hasler, A., Gruber, S. and Haeberli, W. (2011b): Temperature variability and offset in steep alpine rock and ice faces, The Cryosphere, 5, 977–988, doi: 10.5194/tc-5-977-2011.

Hasler, A., Gruber, S. and Beutel, J. (2012): Kinematics of steep bedrock permafrost, Journal of Geophysical Research: Earth Surface, 117, F1, doi: 10.1029/2011JF001981.

Hauck, C. (2013): New Concepts in Geophysical Surveying and Data Interpretation for Permafrost Terrain, Permafrost and periglacial processes, 24, 2, 131–137, doi: 10.1002/ppp.1774.

Hauck, C. and Kneisel, C. (Eds.) (2008): Applied Geophysics in Periglacial Environments, Cambridge University Press, Cambridge.

Heckmann, T., Bimböse, M., Krautblatter, M., Haas, F., Becht, M. and Morche, D. (2012): From geotechnical analysis to quantification and modelling using LiDAR data. A study on rockfall in the Reintal catchment, Bavarian Alps, Germany, Earth Surface Processes and Landforms, 37, 1, 119–133, doi: 10.1002/esp.2250.

Hipp, T., Etzelmüller, B., Farbrot, H., Schuler, T. V. and Westermann, S. (2012): Modelling borehole temperatures in Southern Norway – insights into permafrost dynamics during the 20th and 21st century, The Cryosphere, 6, 553–571, doi: 10.5194/tc-6-553-2012.

Hipp, T., Etzelmüller, B. and Westermann, S. (2014): Permafrost in Alpine Rock Faces from Jotunheimen and Hurrungane, Southern Norway, Permafrost and periglacial processes, 25, 1, 1–13, doi: 10.1002/ppp.1799.

Hobbs, P. V. (1974): Ice Physics, Oxford University Press, Oxford, New York.

Hock, R., Rasul, G., Adler, C., Cáceres, B., Gruber, S., Hirabayashi, Y., Jackson, M., Kääb, A., Kang, S., Kutuzov, S., Milner, A., Molau, U., Morin, S., Orlove, B. and Steltzer, H. (2019): High Mountain Areas, in: IPCC Special Report on the Ocean and Cryosphere in a Changing Climate, edited by: Pörtner, H.-O., Roberts, D. C., Masson-Delmotte, V., Zhai, P., Tignor, M., Poloczanska, E., Mintenbeck, K., Alegría, A., Nicolai, M., Okem, A., Petzold, J., Rama, B., Weyer, N. M., 131-202.

Hoek, E. and Brown, E. T. (1997): Practical estimates of rock mass strength, International Journal of Rock Mechanics and Mining Sciences, 34, 1165–1186, doi: 10.1016/S1365-1609(97)80069-X.

Hoek, E., Carranza-Torres, C. and Corkum, B. (2002): Hoek-Brown failure criterion - 2002 Edition, Proceedings of the 5th North American Rock Mechanics Symposium (NARMS), edited by: Hammah, R., Bawden, W., Curran, J., and Telesnicki, M., University of Toronto Press, Toronto, Ont., Canada, 1, 267–273.

Huang, D., Cen, D., Ma, G. and Huang, R. (2015): Step-path failure of rock slopes with intermittent joints, Landslides, 12, 5, 911–926, doi: 10.1007/s10346-014-0517-6.

Huggel, C. (2009): Recent extreme slope failures in glacial environments. Effects of thermal perturbation, Quaternary Science Reviews, 28, 1119–1130, doi: 10.1016/j.quascirev.2008.06.007.

Huggel, C., Zgraggen-Oswald, S., Haeberli, W., Kääb, A. and Polkvoj, A. (2005): The 2002 rock/ice avalanche at Kolka/Karmadon, Russian Caucasus: assessment of extraordinary avalanche formation and mobility, and application of QuickBird satellite imagery, Natural Hazards and Earth System Science, 5, 173–187.

Huggel, C., Salzmann, N., Allen, S., Caplan-Auerbach, J., Fischer, L., Haeberli, W., Larsen, C., Schneider, D. and Wessels, R. (2010): Recent and future warm extreme events and high-mountain slope stability, Philosophical Transactions of the Royal Society A: Mathematical, Physical and Engineering Sciences, 368, 1919, 2435–2459, doi: 10.1098/rsta.2010.0078.

Huggel, C., Allen, S., Deline, P., Fischer, L., Nötzli, J. and Ravanel, L. (2012a): Ice thawing, mountains falling - are alpine rock slope failures increasing?, Geology Today, 28, 3, 98–104, doi: 10.1111/j.1365-2451.2012.00836.x.

Huggel, C., Clague, J. J. and Korup, O. (2012b): Is climate change responsible for changing landslide activity in high mountains?, Earth Surface Processes and Landforms, 37, 1, 77–91, doi: 10.1002/esp.2223.

Inada, Y. and Yokota, K. (1984): Some studies of low temperature rock strength, International Journal of Rock Mechanics and Mining Sciences & Geomechanics Abstracts, 21, 145–153, doi: 10.1016/0148-9062(84)91532-8.

Indraratna, B., Haque, A. and Aziz, N. (1999): Shear behaviour of idealized infilled joints under constant normal stiffness, Géotechnique, 49, 331–355, doi: 10.1680/geot.1999.49.3.331.

Indraratna, B., Welideniya, H. S. and Brown, E. T. (2005): A shear strength model for idealised infilled joints under constant normal stiffness, Géotechnique, 55, 215–226, doi: 10.1680/geot.2005.55.3.215.

Itasca Consulting Group, I. (2016): 3DEC, Minneapolis.

Itasca Consulting Group, I. (2019): UDEC - Universal Distinct Element Code. User´s Manual, Minneapolis.

Jaboyedoff, M., Couture, R. and Locat, P. (2009): Structural analysis of Turtle Mountain (Alberta) using digital elevation model. Toward a progressive failure, Geomorphology, 103, 5–16, doi: 10.1016/j.geomorph.2008.04.012.

Jaeger, J. C., Cook, N. G. and Zimmerman, R. W. (2007): Fundamentals of rock mechanics, 4th Edition, Blackwell Publishing Ltd., Malden, USA, Oxford, UK, Carlton, Australia.

Jarvis, A., Reuter, H. I., Nelson, A. and Guevara, E. (2008): Hole-filled seamless SRTM data V4: available from http://srtm.csi.cgiar.org.

Jellinek, H. H. G. (1959): Adhesive properties of ice, Journal of Colloid Science, 14, 268–280.

Jennings, J. (1970): A mathematical theory for the calculation of the stability of open cast mines, Symposium on the theoretical background to the planning of open pit mines, Johannesburg, Republic of South Africa, 87–102.

Jerz, H. and Poschinger, A. von (1995): Neuere Ergebnisse zum Bergsturz Eibsee-Grainau, Geologica Bavarica, 99, 383–398.

Jia, H., Xiang, W. and Krautblatter, M. (2015): Quantifying rock fatigue and decreasing compressive and tensile strength after repeated freeze-thaw cycles, Permafrost and periglacial processes, 26, 368–377, doi: 10.1002/ppp.1857.

Jones, S. J. and Glen, J. W. (1968): The mechanical properties of single crystals of ice at low temperatures, International Association of Hydrological Sciences Publ., 79, 326–340.

Kemeny, J. (2003): The Time-Dependent Reduction of Sliding Cohesion due to Rock Bridges Along Discontinuities. A Fracture Mechanics Approach, Rock Mechanics and Rock Engineering, 36, 27–38, doi: 10.1007/s00603-002-0032-2.

Kenner, R., Bühler, Y., Delaloye, R., Ginzler, C. and Phillips, M. (2014): Monitoring of high alpine mass movements combining laser scanning with digital airborne photogrammetry, Geomorphology, 206, 492–504, doi: 10.1016/j.geomorph.2013.10.020.

Keuschnig, M., Hartmeyer, I., Höfer-Öllinger, G., Schober, A., Krautblatter, M. and Schrott, L. (2015): Permafrost-Related Mass Movements. Implications from a Rock Slide at the Kitzsteinhorn, Austria, in: Engineering Geology for Society and Territory - Volume 1: Climate Change and Engineering Geology, edited by: Lollino, G., Manconi, A., Clague, J., Shan, W., Chiarle, M., Springer International Publishing, Cham, 255–259.

Keuschnig, M. (2016): Long-term monitoring of permafrost-affected rock walls. Towards an automatic, continuous electrical resistivity tomography (AERT) monitoring for early warning systems, Dissertation, Technical University of Munich, Munich, Germany.

Keuschnig, M., Krautblatter, M., Hartmeyer, I., Fuss, C. and Schrott, L. (2017): Automated Electrical Resistivity Tomography Testing for Early Warning in Unstable Permafrost Rock Walls Around Alpine Infrastructure, Permafrost and periglacial processes, 28, 1, 158–171, doi: 10.1002/ppp.1916.

Kodama, J., Goto, T., Fujii, Y. and Hagan P. (2013): The effects of water content, temperature and loading rate on strength and failure process of frozen rocks, International Journal of Rock Mechanics and Mining Sciences, 62, 1–13.

Körner, H. and Ulrich, R. (1965): Geologische und felsmechanische Untersuchungen für die Gipfelstation der Seilbahn Eibsee-Zugspitze, Geologica Bavarica, 55, 404–421.

Krautblatter, M. (2009): Detection and quantification of permafrost change in alpine rock walls and implications for rock instability, Dissertation, University of Bonn, Bonn, Germany.

Krautblatter, M. and Dräbing, D. (2014): Pseudo 3-D wave refraction seismic monitoring of permafrost in steep unstable bedrock, Journal of Geophysical Research, 119, 1–13.

Krautblatter, M., Verleysdonk, S., Flores-Orozco, A. and Kemna, A. (2010): Temperature-calibrated imaging of seasonal changes in permafrost rock walls by quantitative electrical resistivity tomography (Zugspitze, German/Austrian Alps), Journal of Geophysical Research - Earth Surface, 115, 1–15.

Krautblatter, M., Huggel, C., Deline, P. and Hasler, A. (2012): Research Perspectives on Unstable High-alpine Bedrock Permafrost. Measurement, Modelling and Process Understanding, Permafrost and periglacial processes, 23, 1, 80–88, doi: 10.1002/ppp.740.

Krautblatter, M., Funk, D. and Günzel, F. K. (2013): Why permafrost rocks become unstable: a rock-ice-mechanical model in time and space, Earth Surface Processes and Landforms, 38, 876–887.

Kulatilake, P. H. S. W., Ucpirti, H., Wang, S., Radberg, G. and Stephansson, O. (1992): Use of the distinct element method to perform stress analysis in rock with non-persistent joints and to study the effect of joint geometry parameters on the strength and deformability of rock masses, Rock Mechanics and Rock Engineering, 25, 253–274, doi: 10.1007/BF01041807.

Kveldsvik, V., Einstein, H. H., Nilsen, B. and Blikra, L. Harald (2008): Numerical Analysis of the 650,000 m2 Åknes Rock Slope based on Measured Displacements and Geotechnical Data, Rock Mechanics and Rock Engineering, 42, 689-728, doi: 10.1007/s00603-008-0005-1.

Ladanyi, B. (2006): Creep of frozen slopes and ice-filled rock joints under temperature variation, Canadian Journal of Civil Engineering, 33, 719–725, doi: 10.1139/l05-112.

Lauber, U. and Goldscheider, N. (2014): Use of artificial and natural tracers to assess groundwater transit-time distribution and flow systems in a high-alpine karst system (Wetterstein Mountains, Germany), Hydrogeology Journal, 22, 1807–1824, doi: 10.1007/s10040-014-1173-6.

Lebrouc, V., Schwartz, S., Baillet, L., Jongmans, D. and Gamond, J. F. (2013): Modeling permafrost extension in a rock slope since the Last Glacial Maximum. Application to the large Séchilienne landslide (French Alps), Geomorphology, 198, 189–200, doi: 10.1016/j.geomorph.2013.06.001.

Lepique, M. (2008): Empfehlung Nr. 10 des Arbeitskreises 3.3 "Versuchstechnik Fels" der Deutschen Gesellschaft für Geotechnik e. V. Indirekter Zugversuch an Gesteinsproben – Spaltzugversuch, Bautechnik, 85, 9, 623–627, doi: 10.1002/bate.200810048.

Lockner, D. (1993): The role of acoustic emission in the study of rock, International Journal of Rock Mechanics and Mining Science & Geomechanics Abstracts, 30, 7, 883–899, doi: 10.1016/0148-9062(93)90041-B.

Loke, M. H. (2019): Res2Dinv. Geoelectrical Imaging 2D & 3D, Geotomo Software Sdn Bhd.

Loye, A., Pedrazzini, A., Theule, J. I., Jaboyedoff, M., Liébault, F. and Metzger, R. (2012): Influence of bedrock structures on the spatial pattern of erosional landforms in small alpine catchments, Earth Surface Processes and Landforms, 37, 13, 1407–1423, doi: 10.1002/esp.3285.

Luethi, R., Gruber, S. and Ravanel, L. (2015): Modelling transient ground surface temperatures of past rockfall events. Towards a better understanding of failure mechanisms in changing periglacial environments, Geografiska Annaler: Series A, Physical Geography, 97, 753–767, doi: 10.1111/geoa.12114.

Magnin, F., Deline, P., Ravanel, L., Nötzli, J. and Pogliotti, P. (2015): Thermal characteristics of permafrost in the steep alpine rock walls of the Aiguille du Midi (Mont Blanc Massif, 3842 m a.s.l), The Cryosphere, 9, 109–121, doi: 10.5194/tc-9-109-2015.

Magnin, F., Krautblatter, M., Deline, P., Ravanel, L., Malet, E., and Bevington, A. (2015): Determination of warm, sensitive permafrost areas in near-vertical rockwalls and evaluation of distributed models by electrical resistivity tomography, Journal of Geophysical Research: Earth Surface, 120, 745–762, doi: 10.1002/2014JF003351.

Magnin, F., Josnin, J.-Y., Ravanel, L., Pergaud, J., Pohl, B. and Deline, P. (2017): Modelling rock wall permafrost degradation in the Mont Blanc massif from the LIA to the end of the 21st century, The Cryosphere, 11, 1813–1834, doi: 10.5194/tc-11-1813-2017.

Mamot, P., Weber, S., Schröder, T. and Krautblatter, M. (2018): A temperature- and stress-controlled failure criterion for ice-filled permafrost rock joints, The Cryosphere, 12, 3333–3353, doi: 10.5194/tc-12-3333-2018.

Mamot, P., Weber, S., Lanz, M. and Krautblatter, M. (2020): Brief communication. The influence of mica-rich rocks on the shear strength of ice-filled discontinuities, The Cryosphere, 14, 1849–1855, doi: 10.5194/tc-14-1849-2020.

Mamot, P., Weber, S., Eppinger, S. and Krautblatter, M. (2021): A temperature-dependent mechanical model to assess the stability of degrading permafrost rock slopes, Earth Surface Dynamics, 9, 1125–1151, doi: 10.5194/esurf-9-1125-2021.

Marinos, P. and Hoek, E. (2000): GSI: A Geologically Friendly Tool for Rock Mass Strength Estimation. ISRM International Symposium, International Society for Rock Mechanics and Rock Engineering, Melbourne, Australia.

Marmy, A., Rajczak, J., Delaloye, R., Hilbich, C., Hoelzle, M., Kotlarski, S., Lambiel, C., Nötzli, J., Phillips, M., Salzmann, N., Staub, B. and Hauck, C. (2016): Semi-automated calibration method for modelling of mountain permafrost evolution in Switzerland, The Cryosphere, 10, 2693–2719, doi: 10.5194/tc-10-2693-2016.

MathWorks (2017): Statistics and machine learning toolbox, regression, model building and assessment, coefficient standard errors and confidence intervals: https://ch.mathworks.com/help/stats/coefficient-standard-errors-and-confidence-790, last access: 3 April 2017.

Matsuoka, N. and Murton, J. (2008): Frost weathering. Recent advances and future directions, Permafrost and periglacial processes, 19, 2, 195–210, doi: 10.1002/ppp.620.

McColl, S. T. and Dräbing, D. (2019): Rock Slope Instability in the Proglacial Zone. State of the Art, in: Geomorphology of Proglacial Systems: Landform and Sediment Dynamics in Recently Deglaciated Alpine Landscapes, Springer International Publishing, Cham, 119–141.

Mejía Camones, L. A., Vargas, E. d. A., de Figueiredo, R. P. and Velloso, R. Q. (2013): Application of the discrete element method for modeling of rock crack propagation and coalescence in the step-path failure mechanism, Engineering Geology, 153, 80–94, doi: 10.1016/j.enggeo.2012.11.013.

Mellor, M. (1973): Mechanical properties of rocks at low temperatures, 2nd International Conference on Permafrost, Yakutsk, Siberia, 13-28 July 1973, 334–344.

Mergili, M., Jaboyedoff, M., Pullarello, J. and Pudasaini, S. P. (2020): Back calculation of the 2017 Piz Cengalo–Bondo landslide cascade with r.avaflow: what we can do and what we can learn, Natural Hazards and Earth System Sciences, 20, 505–520, doi: 10.5194/nhess-20-505-2020.

Micheletti, N., Chandler, J. and Lane, S. N. (2015): Structure from motion (SFM) photogrammetry.

Miller, H. (1962): Der Bau des westlichen Wettersteingebirges, Zeitschrift deutsche geologische Gesellschaft, 113, 409–425.

Mittaz, C., Hoelzle, M. and Haeberli, W. (2000): First results and interpretation of energy-flux measurements over Alpine permafrost, Annals of Glaciology, 31, 275–280, doi: 10.3189/172756400781820363.

Mohr, O. (1900): Welche Umstände bedingen die Elastizitätsgrenze und den Bruch eines Materials?, Zeitschrift des Vereins deutscher Ingenieure, 44, 1524–1530.

Moore, J. R., Gischig, V., Katterbach, M. and Loew, S. (2011): Air circulation in deep fractures and the temperature field of an alpine rock slope, Earth Surface Processes and Landforms, 36, 15, 1985–1996, doi: 10.1002/esp.2217.

Müller, J., Gärtner-Roer, I., Kenner, R., Thee, P. and Morche, D. (2014a): Sediment storage and transfer on a periglacial mountain slope (Corvatsch, Switzerland), Geomorphology, 218, 35–44, doi: 10.1016/j.geomorph.2013.12.002.

Müller, J., Gärtner-Roer, I., Thee, P. and Ginzler, C. (2014b): Accuracy assessment of airborne photogrammetrically derived high-resolution digital elevation models in a high mountain environment, ISPRS Journal of Photogrammetry and Remote Sensing, 98, 58–69, doi: 10.1016/j.isprsjprs.2014.09.015.

Murton, J. B., Peterson, R. and Ozouf, J.-C. (2006): Bedrock Fracture by Ice Segregation in Cold Regions, Science, 314, 1127–1129, doi: 10.1126/science.1132127.

Murton, J., Kuras, O., Krautblatter, M., Cane, T., Tschofen, D., Uhlemann, S., Schober, S. and Watson, P. (2016): Monitoring rock freezing and thawing by novel geoelectrical and acoustic techniques, Journal of Geophysical Research - Earth Surface, 121, 2309–2332, doi: 10.1002/2016JF003948.

Mutschler, T. (2004): Neufassung der Empfehlung Nr. 1 des Arbeitskreises "Versuchstechnik Fels" der Deutschen Gesellschaft für Geotechnik e. V. Einaxiale Druckversuche an zylindrischen Gesteinsprüfkörpern, Bautechnik, 81, 10, 825–834, doi: 10.1002/bate.200490194.

Myhra, K. S., Westermann, S. and Etzelmüller, B. (2017): Modelled Distribution and Temporal Evolution of Permafrost in Steep Rock Walls Along a Latitudinal Transect in Norway by CryoGrid 2D, Permafrost and periglacial processes, 28, 1, 172–182, doi: 10.1002/ppp.1884.

Myhra, K. Sæterdal, Westermann, S. and Etzelmüller, B. (2019): Modeling Conductive Heat Flow Between Steep Rock Walls and Talus Slopes – Thermal Processes and Geomorphological Implications, Frontiers in Earth Science, 7, 192, doi: 10.3389/feart.2019.00192.

Nechad, H., Helmstetter, A., Guerjouma, R. El and Sornette, D. (2005): Creep rrupture in heterogeneous materials, Physical Review Letters, 94, 45501, doi: 10.1103/PhysRevLett.94.045501.

Necsoiu, M., Onaca, A., Wigginton, S. and Urdea, P. (2016): Rock glacier dynamics in Southern Carpathian Mountains from high-resolution optical and multi-temporal SAR satellite imagery, Remote Sensing of Environment, 177, 21–36, doi: 10.1016/j.rse.2016.02.025.

Nötzli, J. (2008): Modeling transient three-dimensional temperature fields in mountain permafrost, Dissertation, University of Zurich, Zurich.

Nötzli, J. and Gruber, S. (2009): Transient thermal effects in Alpine permafrost, The Cryosphere, 3, 85–99, doi: 10.5194/tc-3-85-2009.

Nötzli, J., Gruber, S., Kohl, T., Salzmann, N. and Haeberli, W. (2007): Three-dimensional distribution and evolution of permafrost temperatures in idealized high-mountain topography, Journal of Geophysical Research: Earth Surface, 112, F02S13, doi: 10.1029/2006JF000545.

Nötzli, J., Hilbich, C., Hauck, C., Hoelzle, M. and Gruber, S. (2008): Comparison of Simulated 2D Temperature Profiles with Time-Lapse Electrical Resistivity Data at the Schilthorn Crest, Switzerland, 9th International Conference on Permafrost, Fairbanks, Alaska, 28 June – 3 July 2008.

Nötzli, J., Gruber, S. and Poschinger, A. von (2010): Modellierung und Messung von Permafrosttemperaturen im Gipfelgrat der Zugspitze, Deutschland, Geographica Helvetica, 65, 2, 113–123.

Nötzli, J., Pellet, C. and Staub, B. (Eds.) (2019): PERMOS 2019. Permafrost in Switzerland 2014/2015 to 2017/2018. Glaciological Report (Permafrost) No. 16–19, Cryospheric Commission of the Swiss Academy of Sciences, 104 pp., doi: 10.13093/permos-rep-2019-16-19.

Osasan, K. S. and Afeni, T. B. (2010): Review of surface mine slope monitoring techniques, Journal of Mining Science, 46, 177–186, doi: 10.1007/s10913-010-0023-8.

Paterson, W. S. B. (1994): The Physics of Glaciers, Butterworth Heinemann, Oxford.

Pellet, C., Hilbich, C., Marmy, A. and Hauck, C. (2016): Soil Moisture Data for the Validation of Permafrost Models Using Direct and Indirect Measurement Approaches at Three Alpine Sites, Frontiers in Earth Science, 3, 91, doi: 10.3389/feart.2015.00091.

Phillips, M., Haberkorn, A., Dräbing, D., Krautblatter, M., Rhyner, H. and Kenner, R. (2016): Seasonally intermittent water flow through deep fractures in an Alpine Rock Ridge. Gemsstock, Central Swiss Alps, Cold regions science and technology, 125, 117–127, doi: 10.1016/j.coldregions.2016.02.010.

Phillips, M., Wolter, A., Lüthi, R., Amann, F., Kenner, R. and Bühler, Y. (2017): Rock slope failure in a recently deglaciated permafrost rock wall at Piz Kesch (Eastern Swiss Alps), February 2014, Earth Surface Processes and Landforms, 42, 3, 426–438, doi: 10.1002/esp.3992.

Pläsken, R., Keuschnig, M. and Krautblatter, M. (2020): Permafrost rocks and high-alpine infrastructure. Interrelated, interconnected, interacting, Geomechanics and Tunnelling, 13, 628–633, doi:10.1002/geot.202000028.

Pogliotti, P., Guglielmin, M., Cremonese, E., Di Morra Cella, U., Filippa, G., Pellet, C. and Hauck, C. (2015): Warming permafrost and active layer variability at Cime Bianche, Western European Alps, The Cryosphere, 9, 647–661, doi: 10.5194/tc-9-647-2015.

Pogrebiskiy, M. and Chernyshev, S. (1977): Determination of the permeability of the frozen fissured rock massif in the vicinity of the Kolyma hydroelectric power station, Cold Regions Research and Engineering Laboratory, 634, 1–13.

Poisel, R. and Preh, A. (2004): Rock slope initial failure mechanisms and their mechanical models, Felsbau, 22, 2, 40–45.

Preisig, G., Eberhardt, E., Smithyman, M., Preh, A. and Bonzanigo, L. (2016): Hydromechanical Rock Mass Fatigue in Deep-Seated Landslides Accompanying Seasonal Variations in Pore Pressures, Rock Mechanics and Rock Engineering, 49, 2333–2351, doi: 10.1007/s00603-016-0912-5.

Quinn, D. P. and Ehlmann, B. L. (2019): A PCA-Based Framework for Determining Remotely Sensed Geological Surface Orientations and Their Statistical Quality, Earth and Space Science, 6, 8, 1378–1408, doi: 10.1029/2018EA000416.

Radd, F. J. and Oertel, D. H. (1973): Experimental pressure studies of frost-heave mechanisms and the growth-fusion behaviour of ice, Yakutsk, USSR, 13-28 July, 377–383.

Ravanel, L. and Deline, P. (2008): La face ouest des Drus (massif du Mont-Blanc): évolution de l´instabilité d´une paroi rocheuse dans la haute montagne alpine depuis la fin du petit age glaciaire, Géomorphologie: relief, processus, environnement, 4, 261–272.

Ravanel, L. and Deline, P. (2011): Climate influence on rockfalls in high-Alpine steep rock-walls. The north side of the Aiguilles de Chamonix (Mont Blanc massif) since the end of the 'Little Ice Age', Holocene, 21, 2, 357–365, doi: 10.1177/0959683610374887.

Ravanel, L. and Deline, P. (2015): Rockfall Hazard in the Mont Blanc Massif Increased by the Current Atmospheric Warming, in: Engineering Geology for Society and Territory - Volume 1: Climate Change and Engineering Geology, edited by: Lollino, G., Manconi, A., Clague, J., Shan, W., Chiarle, M., Springer International Publishing, Cham, 425–428.

Ravanel, L., Allignol, F., Deline, P., Gruber, S. and Ravello, M. (2010): Rock falls in the Mont Blanc Massif in 2007 and 2008, Landslides, 7, 4, 493–501.

Ravanel, L., Magnin, F. and Deline, P. (2017): Impacts of the 2003 and 2015 summer heatwaves on permafrost-affected rock-walls in the Mont Blanc massif, Science of the Total Environment, 609, 132–143, doi: 10.1016/j.scitotenv.2017.07.055.

Rempel, A. W., Wettlaufer, J. S. and Worster, M. G. (2004): Premelting dynamics in a continuum model of frost heave, Journal of Fluid Mechanics, 498, 227–244.

Renshaw, C. E. and Schulson, E. M. (2001): Universal behaviour in compressive failure of brittle materials, Nature, 412, 6850, 897–900, doi: 10.1038/35091045.

Rentsch, W. and Krompholz, G. (1961): Zur Bestimmung elastischer Konstanten durch Schallgeschwindigkeitsmessungen, Bergakademie - Zeitschrift für Bergbau, Hüttenwesen und verwandte Wissenschaften, 13, 7-8, 492–504.

Rode, M., Schnepfleitner, H. and Sass, O. (2016): Simulation of moisture content in alpine rock-walls during freeze–thaw events, Earth Surface Processes and Landforms, 41, 13, 1937–1950, doi: 10.1002/esp.3961.

Ryzhkin, I. A. and Petrenko, V. F. (1997): Physical Mechanisms Responsible for Ice Adhesion, The Journal of Physical Chemistry B, 101, 6267–6270, doi: 10.1021/jp9632145.

Sanderson, T. J. O. (1988): Ice Mechanics. Risks to offshore structures, Graham & Trotman, London.

Sass, O. (2005): Rock moisture measurements. Techniques, results, and implications for weathering, Earth Surface Processes and Landforms, 30, 3, 359–374, doi: 10.1002/esp.1214.

Sättele, M., Krautblatter, M., Bründl, M. and Straub, D. (2016): Forecasting rock slope failure. How reliable and effective are warning systems?, Landslides, 13, 737–750, doi: 10.1007/s10346-015-0605-2.

Scandroglio, R., Dräbing, D., Offer, M., and Krautblatter, M. (2021): 4D quantification of alpine permafrost degradation in steep rock walls using a laboratory-calibrated electrical resistivity tomography approach, Near Surface Geophysics, 19, 241–260, doi: 10.1002/nsg.12149.

Scholz, C. H. (1968): Microfracturing and the inelastic deformation of rock in compression, Journal of Geophysical Research, 73, 4, 1417–1432, doi: 10.1029/JB073i004p01417.

Schön, J. H. (2015): Physical properties of rocks. Fundamentals and principles of petrophysics, Elsevier.

Schrott, L. and Sass, O. (2008): Application of field geophysics in geomorphology: Advances and limitations exemplified by case studies, Geomorphology, 93, 1-2, 55–73.

Schulson, E. M. and Duval, P. (2009): Creep and Fracture of Ice, Cambridge University Press.

Senfaute, G., Duperret, A. and Lawrence, J. A. (2009): Micro-seismic precursory cracks prior to rock-fall on coastal chalk cliffs. A case study at Mesnil-Val, Normandie, NW France, Natural Hazards and Earth System Sciences, 9, 1625–1641, doi: 10.5194/nhess-9-1625-2009.

Shea, W. T. and Kronenberg, A. K. (1993): Strength and anisotropy of foliated rocks with varied mica contents, Journal of Structural Geology, 15, 1097–1121, doi: 10.1016/0191-8141(93)90158-7.

Shiotani, T., Fujii, K., Aoki, T. and Amou, K. (1994): Evaluation of progressive failure using AE sources and improved b-value on slope model tests, Progress in AE, VII, 529–534.

Shiotani, T., Li, Z., Yuyama, S. and Ohtsu, M. (2001): Application of the AE improved b-value to quantitative evalutation of fracture proces in concrete materials, Journal of AE, 19, 118–133.

Sjøgren, B., Øfsthus, A. and Sandberg, J. (1979): Seismic classification of rock mass qualities, Geophysical Prospecting, 27, 2, 409–442, doi: 10.1111/j.1365-2478.1979.tb00977.x.

Sornette, D. (2006): Critical Phenomena in Natural Sciences, Springer Verlag, Berlin.

SRTM DEM Digital Elevation Database (2020): http://srtm.csi.cgiar.org/, last access: 14 February 2020.

Stead, D., Eberhardt, E. and Coggan, J. S. (2006): Developments in the characterization of complex rock slope deformation and failure using numerical modelling techniques, Engineering Geology, 83, 217–235, doi: 10.1016/j.enggeo.2005.06.033.

Sturzenegger, M. and Stead, D. (2009): Close-range terrestrial digital photogrammetry and terrestrial laser scanning for discontinuity characterization on rock cuts, Engineering Geology, 106, 163–182, doi: 10.1016/j.enggeo.2009.03.004.

Supper, R., Ottowitz, D., Jochum, B., Römer, A., Pfeiler, S., Kauer, S., Keuschnig, M. and Ita, A. (2014): Geoelectrical monitoring of frozen ground and permafrost in alpine areas. Field studies and considerations towards an improved measuring technology, Near Surface Geophysics, 12, 1, 93–115, doi: 10.3997/1873-0604.2013057.

Telford, W. M., Geldart, L. P. and Sheriff, R. E. (1990): Applied Geophysics, Second Edition, Cambridge University Press, Cambridge.

Tipler, P. A. and Mosca, G. (2015): Physik für Wissenschaftler und Ingenieure, Springer Spektrum, 7th Edition, Springer, Berlin.

Tse, R. and Cruden, D. M. (1979): Estimating joint roughness coefficients, International Journal of Rock Mechanics and Mining Sciences & Geomechanics Abstracts, 16, 5, 303–307, doi: 10.1016/0148-9062(79)90241-9.

Ulrich, R. and King, L. (1993): Influence of mountain permafrost on construction in the Zugspitze mountains, Bavarian Alps, Germany, 6th International Conference on Permafrost, 5–9 July 1993, Beijing, China, International Permafrost Association, Potsdam, 625–630.

Ulusay, R. (2015): The ISRM Suggested Methods for Rock Characterization, Testing and Monitoring: 2007-2014, Springer International Publishing, Cham, Heidelberg, New York, Dordrecht, London.

Ulusay, R. and Karakul, H. (2016): Assessment of basic friction angles of various rock types from Turkey under dry, wet and submerged conditions and some considerations on tilt testing, Bulletin of Engineering Geology and the Environment, 75, 1683–1699, doi: 10.1007/s10064-015-0828-4.

Vidal, H. (1953): Neue Ergebnisse zur Stratigraphie und Tektonik des nordwestlichen Wettersteingebirges und seines nördlichen Vorlandes, in: Zur Geologie der Bayerischen Alpen und des Alpenvorlandes, Geologica Bavarica, Akademische Buchdruckerei F. Straub, München, 56–88.

Voigtländer, A., Scandroglio, R. and Krautblatter, M. (2014): Entwicklung geotechnischer Felsparameter des Kitzsteinhorner Kalkglimmerschiefers, Abschlussbericht zum Forschungs- und Entwicklungsvertrag der TU München und AlpS-GmbH, München.

Walter, F., Amann, F., Kos, A., Kenner, R., Phillips, M., Preux, A. de, Huss, M., Tognacca, C., Clinton, J., Diehl, T. and Bonanomi, Y. (2020): Direct observations of a three million cubic meter rock-slope collapse with almost immediate initiation of ensuing debris flows, Geomorphology, 351, 106933, doi: 10.1016/j.geomorph.2019.106933.

Weber, S., Beutel, J., Faillettaz, J., Hasler, A., Krautblatter, M. and Vieli, A. (2017): Quantifying irreversible movement in steep, fractured bedrock permafrost on Matterhorn (CH), The Cryosphere, 11, 567–583, doi: 10.5194/tc-11-567-2017.

Weber, S., Faillettaz, J., Meyer, M., Beutel, J. and Vieli, A. (2018): Acoustic and Microseismic Characterization in Steep Bedrock Permafrost on Matterhorn (CH), Journal of Geophysical Research: Earth Surface, 123, 6, 1363–1385, doi: 10.1029/2018JF004615.

Weber, S., Beutel, J., Da Forno, R., Geiger, A., Gruber, S., Gsell, T., Hasler, A., Keller, M., Lim, R., Limpach, P., Meyer, M., Talzi, I., Thiele, L., Tschudin, C., Vieli, A., Vonder Mühll, D. and Yücel, M. (2019): A decade of detailed observations (2008–2018) in steep bedrock permafrost at the Matterhorn Hörnligrat (Zermatt, CH), Earth System Science Data, 11, 1203–1237, doi: 10.5194/essd-11-1203-2019.

Wegmann, M. (1998): Frostdynamik in hochalpinen Felswänden am Beispiel der Region Jungfraujoch - Aletsch, Dissertation, ETH Zurich, Zurich, Switzerland.

Wegmann, M. and Gudmundsson, G. Hilmar (1999): Thermally induced temporal strain variations in rock walls observed at subzero temperatures, in: Advances in Cold-Region

Thermal Engineering and Sciences, edited by: Hutter, K., Wang, Y., Beer, H., Springer, Berlin, Heidelberg, 511–518.

Welkner, D., Eberhardt, E. and Hermanns, R. L. (2010): Hazard investigation of the Portillo Rock Avalanche site, central Andes, Chile, using an integrated field mapping and numerical modelling approach, Engineering Geology, 114, 278–297, doi: 10.1016/j.enggeo.2010.05.007.

Wyllie, D. C. (2018): Rock slope engineering. Civil applications, Taylor & Francis Group, Boca Raton.

Yamamoto, Y. and Springman, S. M. (2014): Axial compression stress path tests on artificial frozen soil samples in a triaxial device at temperatures just below 0 °C, Can. Geotech. J., 51, 1178–1195, doi: 10.1139/cgj-2013-0257.

Yang, Z. Y., Lo, S. C. and Di, C. C. (2001): Reassessing the Joint Roughness Coefficient (JRC) Estimation Using Z2, Rock Mechanics and Rock Engineering, 34, 243–251, doi: 10.1007/s006030170012.

Yasufuku, N., Springman, S. M., Arenson, L. U. and Ramholt, T. (2003): Stress-dilatancy behaviour of frozen sand in direct shear, International Conference on Permafrost, Zurich, Switzerland, 21-25 July, 1253–1258.

Zhang, X.-P. and Wong, L. Ngai Yuen (2013): Crack Initiation, Propagation and Coalescence in Rock-Like Material Containing Two Flaws. A Numerical Study Based on Bonded-Particle Model Approach, Rock Mechanics and Rock Engineering, 46, 5, 1001–1021, doi: 10.1007/s00603-012-0323-1.

Zhang, K., Cao, P., Meng, J., Li, K. and Fan, W. (2015): Modeling the Progressive Failure of Jointed Rock Slope Using Fracture Mechanics and the Strength Reduction Method, Rock Mechanics and Rock Engineering, 48, 2, 771–785, doi: 10.1007/s00603-014-0605-x.

Abbreviations

AE	Acoustic Emission
ALS	Airborne Laser Scanning
APIM	Alpine Permafrost Index Map
a.s.l.	above sea level
CGIAR	Consultative Group on International Agricultural Research
CSI	Consortium for Spatial Information
CV	Coefficient of variation
DEM	Digital Elevation Model
DP	Digital Photogrammetry
DAP	Digital aerial photogrammetry
e.g.	exempli gratia, for example
EM	Electromagnetic Induction
ERT	Electrical Resistivity Tomography
FS	Factor of Safety
GNT-P	Global Terrestrial Network for Permafrost
GPR	Ground Penetrating Radar
GPS	Global Positioning System
GSI	Geological Strength Index
i.e.	id est, that is
ISRM	International Society for Rock Mechanics and Rock Engineering
JCS	Joint wall Compressive Strength
JRC	Joint Roughness Coefficient
LiDAR	Light Detection and Ranging
MAAT	Mean Annual Air Temperature
MAD	Mean absolute deviation
NSRT	Near-surface Rock Temperature
PDF	Probability density function
SAR	Synthetic Aperture Radar
SRT	Seismic Refraction Tomography
SRTM	Shuttle Radar Topography Mission
TLS	Terrestrial Laser Scanning
UAV	Unmanned Aerial Vehicle
UDEC	Universal Distinct Element Code
VHR	optical Very High Resolution
1D, 2D, 3D	one-, two, three-dimensional

Symbols

A	Arhenius factor
R^2	Coefficient of determination
μ	Coefficient of friction
ρ	Density
V_D	Dilatational wave velocity
D	Disturbance factor
K	Elastic bulk modulus
G	Elastic shear modulus
m_i, m_b, s	Hoek Brown constant
c	Joint cohesion
φ_b, φ_r	Joint friction angle (basic, residual)
k_n	Joint normal stiffness
k_s	Joint shear stiffness
k_{CII}	Mode II Fracture toughness
σ	Normal stress
Ω	Ohm
υ	Poisson´s ratio
ϕ	Porosity
N	Probability distribution function
p	Probability of rejecting the null hypothesis (H_0) although it is true
R	Schmidt hammer rebound hardness for unweathered, sawn surfaces
r	Schmidt hammer rebound hardness for weathered surfaces
τ	Shear strength
r	Specimen radius
ε'	Strain rate
T	Temperature
σ_c	Uniaxial compressive strength
σ_{tm}	Uniaxial tensile strength
W	Water content
E	Young´s modulus

List of figures

List of tables